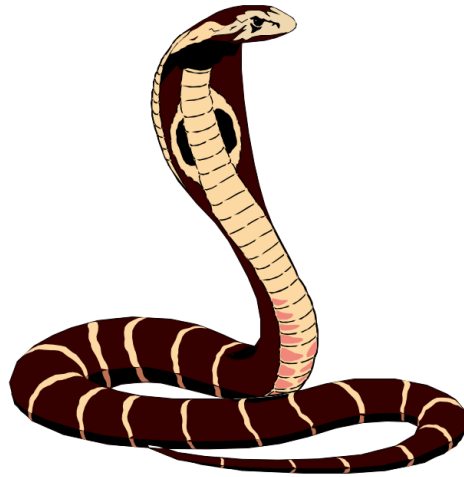


# The COBRA Extended Demonstrator – Conception, Characterization, Commissioning



Dissertation  
zur Erlangung des akademischen Grades  
eines Doktors der Naturwissenschaften

vorgelegt von  
**Robert Temminghoff**  
geboren in Gelsenkirchen

Lehrstuhl für Experimentelle Physik IV  
Fakultät Physik  
TU Dortmund

– 2019 –

Der Fakultät Physik der TU Dortmund zur Erlangung des akademischen Grades eines Doktors der Naturwissenschaften vorgelegte Dissertation.

1. Gutachter: Prof. Dr. Kevin Kröninger

2. Gutachter: Prof. Dr. Wolfgang Rhode

Vorsitzender der Prüfungskommission: Prof. Dr. Heinz Hövel

Weiteres Mitglied der Prüfungskommission: PD Dr. Ilya Akimov

Datum des Einreichens der Arbeit: 26. September 2019

Datum der mündlichen Prüfung: 06. Dezember 2019

## Kurzfassung

Der neutrinolose doppelte  $\beta$ -Zerfall ist ein hypothetischer Kernzerfall dessen Nachweis grundlegende Fragen über bislang unbekannte Eigenschaften von Neutrinos liefern und auf Physik jenseits des Standard Modells der Teilchenphysik hindeuten würde. Das COBRA Experiment sucht nach diesem Zerfall mit Hilfe von CdZnTe Halbleiter-Detektoren. In dieser Arbeit wird ein wesentlich verbesserter Aufbau des Experiments, genannt *Extended Demonstrator (XDEM)*, präsentiert. Um diesen zur verwirklichen, wurden wichtige Eigenschaften der verwendeten Detektoren in Labormessungen bestimmt. Außerdem wurden Simulationen durchgeführt um Aufschluß über die Wahrscheinlichkeit einen doppelten  $\beta$ -Zerfall zu detektieren zu erhalten und eine Abschätzung des Hintergrundes durch andere Prozesse zu erreichen. Darauf basierend wurden Daten analysiert, welche über mehr als ein halbes Jahr am LNGS Untergrundlabor in Italien aufgezeichnet wurden. Im Vergleich zu früheren Versionen des COBRA Experiments wurde der Hintergrund um mehr als einen Faktor 30 reduziert bei gleichzeitiger Steigerung der Wahrscheinlichkeit ein Signal zu messen um 50%. Es wurden keine Hinweise auf neutrinolosen doppelten  $\beta$ -Zerfall gefunden. Stattdessen wurden untere Grenzen für die Halbwertszeit der Zerfälle von  $^{116}\text{Cd}$  und  $^{130}\text{Te}$  aufgestellt, welche  $t_{1/2}^{116\text{Cd}} \geq 2.7 \cdot 10^{21}$  yr und  $t_{1/2}^{130\text{Te}} \geq 8.8 \cdot 10^{21}$  yr betragen. Dies sind die stärksten Grenzen auf diese Halbwertszeiten die im Rahmen des COBRA Experiments bestimmt wurden.

## Abstract

Neutrinoless double  $\beta$ -decay is a hypothetical nuclear decay whose detection would shed light on unknown properties of the neutrino and physics beyond the Standard Model of particle physics. The COBRA experiment is searching for this decay using CdZnTe semiconductor detectors. In this work, a major upgrade of the experiment is presented, called extended demonstrator (XDEM). For this, important parameters of the detectors were determined in laboratory measurements. Furthermore, simulations were used to estimate the signal efficiency and potential background from other nuclear processes. Based on this, data taken over the course of more than half a year at the LNGS underground laboratory in Italy were analyzed. Compared to earlier versions of COBRA, the background is reduced by more than a factor of 30. At the same time, the signal efficiency is improved by 50%. No signs for neutrinoless double  $\beta$ -decay were detected. Instead, lower limits on the half-lives of  $^{116}\text{Cd}$  und  $^{130}\text{Te}$  were set at  $t_{1/2}^{116\text{Cd}} \geq 2.7 \cdot 10^{21}$  yr and  $t_{1/2}^{130\text{Te}} \geq 8.8 \cdot 10^{21}$  yr. These are the strongest limits set on these half-lives in the context of COBRA.



# Contents

<b>1</b>	<b>Introduction</b>	<b>1</b>
<b>2</b>	<b>Neutrino Physics and Double <math>\beta</math>-Decay</b>	<b>3</b>
2.1	$\beta$ -decays . . . . .	4
2.2	The Weak Force . . . . .	5
2.3	From First Detection to Oscillations . . . . .	6
2.4	Neutrino Masses . . . . .	9
2.5	Known Unknowns . . . . .	11
2.6	Neutrinoless Double- $\beta$ Decay . . . . .	12
2.6.1	BSM-Theories Giving Rise to $0\nu\beta\beta$ -Decay . . . . .	15
2.6.2	Phase-Space Factors and Nuclear Matrix Elements . . . . .	16
2.6.3	Considerations for a $0\nu\beta\beta$ -Experiment . . . . .	18
2.6.4	Status of Searches for $0\nu\beta\beta$ -decay . . . . .	20
<b>3</b>	<b>The COBRA Experiment</b>	<b>25</b>
3.1	CdZnTe as Radiation Detector . . . . .	25
3.2	The COBRA Demonstrator Setup . . . . .	37
3.3	Physics with the COBRA Demonstrator . . . . .	41
<b>4</b>	<b>The COBRA XDEM Upgrade and Improvements to the Demonstrator</b>	<b>45</b>
4.1	Changes to the Demonstrator Setup and General Infrastructure . . . . .	46
4.2	The COBRA Extended Demonstrator . . . . .	49
4.2.1	Larger Detectors . . . . .	49
4.2.2	Read-Out Electronics . . . . .	54
4.2.3	High-Voltage Supply . . . . .	58
4.2.4	Modifications to Shielding and Infrastructure . . . . .	61
<b>5</b>	<b>Large CdZnTe Detectors for the XDEM</b>	<b>63</b>
5.1	Interaction Depth in CPqG Detectors . . . . .	63

## Contents

5.2	Characterization of XDEM Detectors . . . . .	68
5.2.1	Working Point . . . . .	73
5.2.2	Mobility-Lifetime Product . . . . .	77
5.2.3	Efficiency . . . . .	78
5.2.4	Energy Resolution . . . . .	82
5.2.5	Current-Voltage Characteristics . . . . .	85
5.2.6	Conclusion of Characterization Measurements . . . . .	92
<b>6</b>	<b>Simulations for the XDEM phase</b>	<b>93</b>
6.1	Efficiency Calculations . . . . .	93
6.2	Background Estimation . . . . .	96
<b>7</b>	<b>Performance of the XDEM</b>	<b>105</b>
7.1	Data-Taking Conditions . . . . .	105
7.2	Linearity, Energy Resolution, Interaction Depth & Multiplicity . . . . .	107
7.3	Stability . . . . .	115
7.4	Analysis of the Low-Background Spectrum . . . . .	119
7.5	Search for $0\nu\beta\beta$ -decays . . . . .	126
7.6	Discussion and Outlook . . . . .	130
<b>8</b>	<b>Conclusion</b>	<b>133</b>
	<b>Acknowledgments</b>	<b>II</b>
	<b>Bibliography</b>	<b>XXXI</b>
<b>A</b>	<b>Measurement of Radioisotopes in Materials Used for XDEM</b>	<b>XXXII</b>
<b>B</b>	<b>Peak Contents in Background Spectrum</b>	<b>XXXIX</b>
<b>C</b>	<b>Zn Content of CdZnTe Detectors</b>	<b>XL</b>
<b>D</b>	<b>PCB Design</b>	<b>XLII</b>
	<b>List of Publications and Conference Contributions</b>	<b>XLVII</b>
	<b>List of (Co-)Supervised Theses</b>	<b>XLIX</b>

# 1 Introduction

Modern particle physics, as described by the Standard Model (SM), successfully explains a vast number of phenomena in the microscopic world. It predicts experimental results with remarkable accuracy. Still, it is empirically known that the SM is not able to explain all observed phenomena. One striking example is gravity, which is well understood through the theory of general relativity. Yet, it is unknown how gravity can be reconciled with the SM. There is also the case of Dark Matter, which is believed to make up a large fraction of matter in our universe. Dark Matter could in principle be explained viably in terms of elementary particles, but so far no direct signs of Dark Matter have been found in the laboratory.

One interesting way to look for physics beyond the SM is by studying neutrinos. Neutrinos are nearly massless elementary particles which barely interact with matter. The confirmation that neutrinos have in fact mass is often seen as a hint of such physics, as neutrino masses were not predicted by the SM. The existence of massive neutrinos and potential beyond Standard Model (BSM) physics could also give rise to a nuclear process called neutrinoless double  $\beta$ -decay ( $0\nu\beta\beta$ ). If this decay is indeed realized in nature, it would be incredibly rare.  $0\nu\beta\beta$ -decay is associated with half-lives of at least  $10^{26}$  yr. Many different approaches are employed to search for this decay. One of these is to use CdZnTe semiconductor crystals. These can act as source and detector for  $0\nu\beta\beta$ -decay at the same time. This concept is used by the COBRA experiment.

COBRA is currently still in an R&D-phase in which the viability of the idea is validated. It is operated at the Laboratori Nazionali del Gran Sasso (LNGS) underground laboratory in Italy. The aim of this thesis is to introduce a major upgrade of COBRA called the XDEM. The conception of the XDEM project will be presented, characterization measurements to test the concept's realizability will be shown and the commissioning of the actual experiment will be described, culminating in an analysis of first data taken with the XDEM setup.

The work will be organized as follows. First, an overview of the field of neutrino physics and  $0\nu\beta\beta$ -decay in particular will be given in chapter 2. In chapter 3 it will be shown how CdZnTe detectors can be used to search for  $0\nu\beta\beta$ -decay together with a

## 1 Introduction

short summary of the COBRA experimental apparatus and results recently achieved with it. The XDEM upgrade will then be introduced in chapter 4. Modifications to the existing COBRA setup, which made it possible to measure events at low energies not accessible before, are also described there. Central to the upgrade are novel CdZnTe detectors which are extensively characterized in chapter 5. Simulations used to better understand the behavior of the detectors in the underground setup are shown in chapter 6. Finally, in chapter 7 data acquired over more than half a year with the XDEM setup will be presented. In chapter 8 all results will be summarized.

The results presented in this work were achieved by the author in collaboration with other members of COBRA. All work conducted at the LNGS was only possible as part of a team. Much planning for this work took place at TU Dortmund together with Lucas Bodenstein-Dresler [BD18], Hannah Jansen and Jan Tebrügge. Furthermore, the scientific results could not have been accomplished by the author alone. This is especially true for laboratory measurements presented in chapter 5: The analysis of interaction depth relied on data taken by Katja Rohatsch at TU Dresden [Roh16]. Characterization measurements were done at TU Dortmund with Lucas Bodenstein-Dresler [BD18], who performed some of the measurement, and Inga Höfman [Hö18], who adopted the efficiency-analysis for the test setup in Dortmund. Stefan Zatschler provided some ROOT-scripts which were the basis for evaluating spectra acquired in this campaign. Pre-studies, which are not presented here, but delivered valuable experience for later laboratory work, were conducted by Marcus Albrecht [Alb16], Klaus David [Dav16], Christian Schleich [Sch16] and Jan-Hendrik Arling [Arl16]. In chapter 6 simulations are presented which required to implement an accurate description of the XDEM setup into a simulation framework. This was done in collaboration with Christian Herrmann [Her16], who was also involved in the simulation of some background sources [Her18].

Some parts of this work were already published in Refs. [Tem17; Tem16; BD+18] and presented at various conferences (see chapter D).

## 2 Neutrino Physics and Double $\beta$ -Decay

Neutrinos are ubiquitous elementary particles. Coming from the sun, about 40 trillion of them cross this sheet of paper each second. Yet, their interaction probability with ordinary matter is so small, that nearly all of them will pass through it. This is because neutrinos only interact via the weak force. They are also astonishingly light, about six order of magnitude lighter than electrons. Thus, they present an interesting object to study.

Even though the neutrino was proposed already in 1930 [Pau30] as a solution to the long-standing question how energy and momentum can be conserved in  $\beta$ -decays, there are still many questions surrounding it. Among those are their absolute mass and whether they are Majorana- or Dirac-fermions, i. e. if they are their own anti-particles or not. As neutrinos are the only fermions without electric charge, they are the only elementary particles for which this can not be trivially determined. The SM describes the state-of-the-art of modern particle physics and thus also that of neutrino physics. Its particle content is shown in Figure 2.1. Three generations of neutrinos are included and labeled in analogy to their charged lepton counterparts  $\nu_e$ ,  $\nu_\mu$  and  $\nu_\tau$ .

The study of the weak force and the quest to detect neutrinos from various sources have accompanied the development of today's understanding of the SM. It predicted that neutrinos are massless, which fitted experimental data for a long time. But it became clear from experiments with solar and reactor neutrinos, that this assumption does not hold. Neutrinos are in fact massive, giving first direct evidence for the existence of physics beyond the SM. Also, even if their exact masses are still unknown, the smallness of neutrino masses seems puzzling.

Today, many neutrino properties are measured with high precision, while others are still completely unknown. Their determination is the ongoing task of a large number of experiments. The following sections will explain the role of neutrinos in the SM of particle physics. The focus will be on the experimental milestones reached to obtain the present knowledge. Then, the field of  $0\nu\beta\beta$ -decay will be covered.  $0\nu\beta\beta$ -decay is a hypothetical nuclear decay that may help to answer open questions in the neutrino sector and push open the window to BSM physics.

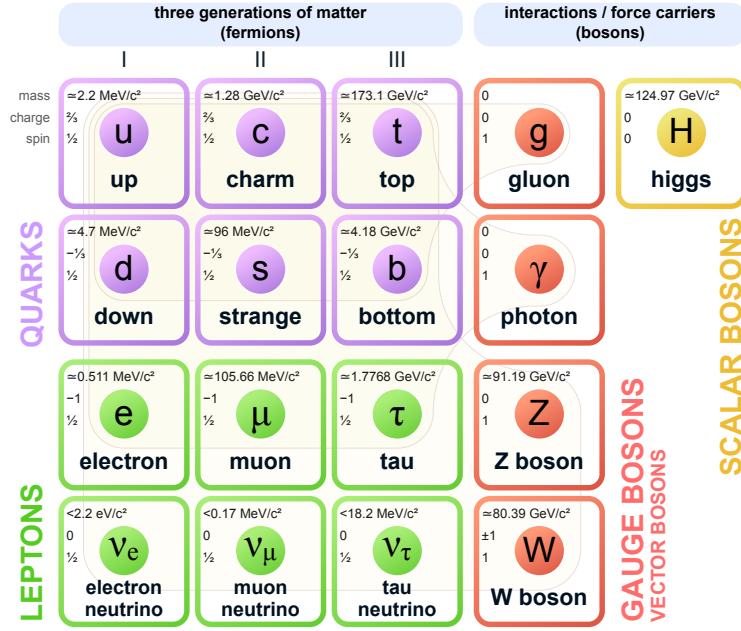


Figure 2.1: Elementary particles in the Standard Model of particle physics with some of their key properties. Adapted from Ref. [Mis06].

## 2.1 $\beta$ -decays

As the study of neutrinos originated in the study of  $\beta$ -decays and  $0\nu\beta\beta$ -decay is in many respects similar to ordinary  $\beta$ -decay, it will be useful to introduce some terminology regarding this phenomenon. The simplest case is the  $\beta^-$ -decay of the free neutron

$$n \rightarrow p^+ + e^- + \bar{\nu}_e, \quad (2.1)$$

where an anti-neutrino  $\bar{\nu}_e$  is emitted together with an electron to obey conservation laws. While the free proton is assumed to be stable, inside nuclear matter it can decay via a similar process  $p^+ \rightarrow n + e^+ + \nu_e$  called  $\beta^+$ -decay. If there is a non-zero probability for an electron from the atomic shell to be present in the nucleus electron capture (EC)  $p^+ + e^- \rightarrow n + \nu_e$  is also possible. In this case the vacancy in the shell is subsequently filled and X-rays or Auger electrons are emitted. Neutron-rich nuclei undergo  $\beta^-$ -decay while proton-rich undergo  $\beta^+$ -decay or EC. There are also nuclei unstable to several forms of  $\beta$ -decay. In general, a  $\beta$ -decay has not to leave the final state nucleus in its ground state. If the nucleus is left in an excited state, it will relax

into the ground state shortly after by emitting one or several  $\gamma$ -rays or shell electrons.

If the angular momenta of the initial and the final state nucleus are the same, which implies anti-parallel spins of the electron and the neutrino, the decay is called a Fermi or super-allowed decay. Its strength is given by the weak vector coupling  $g_V$ . Contrary, if the spins of electron and neutrino are parallel, one speaks of a Gamow-Teller or allowed transition. Here, the strength is governed by the weak axial-vector coupling  $g_A$ . Furthermore, forbidden transitions are transitions in which the difference in total angular momentum is larger than zero. Depending on its value they are classified as first-forbidden, second-forbidden, and so forth. If the parity of initial state and final state nucleus is the same a decay is called non-unique, or unique if the parity is different.

## 2.2 The Weak Force

Not only  $\beta$ -decays, but also many other particle decays are governed by the weak force. A first theoretical description of the weak force was based on four-fermion vertices [Fer34], in contrast to modern understanding. While this theory works quite well to describe  $\beta$ -decay, it breaks down at higher energies. It was initially not clear how to resolve this and it took many years to develop a more mature theory.

An important step was the discovery of the mediators of the weak force, the  $Z$ - and the  $W^\pm$ -bosons. These bosons couple to fermions at two-fermion vertices and also have boson-boson interactions. Because of their high mass the effective range of the weak interaction is very short. This explains both why Fermi's theory is a good approximation at low energies and why the weak force is so much weaker than other fundamental forces at scales larger than about the size of an atomic nucleus.

Another important discovery was that parity is not conserved in weak decays. This was first seen in Kaon decays [LY56] and shortly after confirmed by studying the asymmetry of electrons coming of  $\beta$ -decays of a polarized sample of  $^{60}\text{Co}$  in a switchable magnetic field [Wu+57]. This led to the  $V$ - $A$ -theory which describes weak interactions as mixture of vector- and axial-vector currents [FGM58]. This implies that only neutrinos with helicity  $h = -1$  (called left-handed) and only anti-neutrinos with  $h = 1$  (called right-handed) participate in weak interactions. Helicity is defined as

$$h = \frac{\vec{s} \cdot \vec{p}}{|\vec{s} \cdot \vec{p}|}, \quad (2.2)$$

with spin  $\vec{s}$  and momentum  $\vec{p}$ . This was experimentally demonstrated [GGS58] shortly after the  $V$ - $A$ -theory had been suggested. It was also realized, that the descriptions of

the electromagnetic and the weak force can be unified into the electroweak force [Wei67]. Today the electroweak theory is one of the pillars of the SM.

### 2.3 From First Detection to Oscillations

While assuming the existence of neutrinos solved the problem of  $\beta$ -decay – and later also of pion- and muon-decay – for many years direct experimental evidence for the existence of neutrinos was missing. This changed in 1956, when for the first time electron anti-neutrinos were unambiguously detected at the Savannah River nuclear power plant, where they were produced in large numbers in the reactor [Cow+56]. The inverse beta decay (IBD) reaction  $\bar{\nu} + p^+ \rightarrow \beta^+ + n$ , which has a tiny cross section of about  $1 \cdot 10^{-44} \text{ cm}^2$ , was observed by making use of the signal from positron annihilation as well as neutron capture after a neutrino was captured in a segmented scintillation detector.

Today it is known that there are three different flavor of neutrinos. First evidence for the muon neutrino came from an experiment at the Brookhaven Alternating Gradient Synchrotron (AGS) in 1962 [Dan+62]. The experiment made use of neutrinos produced by an accelerator, by focusing an intense proton beam on a beryllium target. This produced a large number of charged pions which decay according to  $\pi^\pm \rightarrow \mu^\pm + \nu_\mu/\bar{\nu}_\mu$ . The  $\nu_\mu$  entered a spark chamber, where they subsequently produced muons via a reaction similar to IBD, which could be detected in the chamber. Finally, in 2001 the observation of the tau-neutrino using a similar beam-dump experiment and nuclear emulsion plates was announced by the DONUT collaboration [Kod+01]. Several experiments at the Large Electron-Positron Collider (LEP) found that the number of light ( $m_\nu \leq m_Z/2$ ) neutrinos is  $N_\nu = 2.9840 \pm 0.0082$  [Sch+06]. Thus, the three flavor picture was confirmed.

Beside neutrinos from reactors or accelerators, another strong source of neutrinos on Earth is the sun. In the sun nuclear fusion occurring in the  $pp$ - and CNO-cycles produces neutrinos in huge quantities. The solar neutrino flux on Earth is about  $6.5 \cdot 10^{10}/(\text{cm}^2 \text{ s})$  [GLZ18], giving rise to the number quoted at the beginning of this chapter. Whereas nuclear fission reactors produce anti-electron neutrinos, the sun produces electron neutrinos. Their detection requires a different<sup>1</sup> detection technique [Pon91], e.g. making use of the reaction  $\nu_e + {}^{37}\text{Cl} \rightarrow {}^{37}\text{Ar} + e^-$ . Based on this reaction, the Homestake Experiment [DHH68] was conceived, in which a

---

<sup>1</sup>In fact, a similar technique was used earlier at a reactor site to establish that neutrinos are different from anti-neutrinos [Dav55].

large tank filled with 615 tons of  $\text{C}_2\text{Cl}_4$  was placed about 1500 m underground in a mine. Argon was extracted from the tank and its  $^{37}\text{Ar}$ -concentration was determined by radio-chemical methods. After many years of data-taking, a production rate of  $2.56 \pm 0.22 \cdot 10^{-36}$  captures/(target atom · second) was measured [Cle+98]. This was later confirmed by other experiments using Gallium [Abd+94; Cri+99] and water based targets [Hir+89]. This number was much lower than predicted by theoretical calculations, a discrepancy which became known as the *Solar neutrino puzzle* [BD76].

While it had been believed that this discrepancy was due to a not well enough understood solar model, it eventually became clear, that it was in fact due to the nature of the emitted neutrinos. This conclusion was reached by observing neutrinos not coming from the sun, but produced in the interaction of cosmic-rays with Earth's atmosphere, which have much higher energy and consists of all three neutrino flavor. By observing charged-current interactions of the form  $\nu + N \rightarrow \nu + X$  large water based Čerenkov-detectors like Kamiokande were able to distinguish between  $\nu_e$  and  $\nu_\mu$  interactions and found a smaller than expected  $\nu_e/\nu_\mu$  ratio [Fuk+94]. This deficit can be explained by neutrino oscillations [Pon57; Pon58; Pon68], i. e. the possibility of a neutrino to change its flavor after it has traveled a certain distance. This is similar to a mechanism that was observed earlier in neutral mesons [Chr+64].

The probability for the simplified case of two-flavor oscillations is given by

$$P_{a \rightarrow b} = \sin^2(2\Theta) \sin^2\left(\frac{1.27\Delta m^2(\text{eV}^2)L(\text{km})}{E_\nu(\text{GeV})}\right), \quad (2.3)$$

where  $\Delta m^2$  is the squared mass difference between neutrino eigenstates,  $L$  the distance traveled and  $E_\nu$  the energy of the neutrino and  $\Theta$  is the mixing angle which governs the oscillations strength between neutrino flavors. With this, the Kamiokande results can be explained by assuming that  $\nu_\mu$  oscillate into another flavor on their way through the atmosphere. This assumption was later confirmed by the Super-Kamiokande experiment [Fuk+98]. This experiment was able to measure the zenith angle of incoming neutrinos and could thus measure  $P_{a \rightarrow b}$  as a function of  $L$ . At the same time, the Sudbury Neutrino Observatory (SNO) was able to distinguish between different neutrino flavors by observing neutral- and charged-current reactions on heavy water [Ahm+02]. This led to the award of a Nobel Prize for the discovery of neutrino oscillations to the heads of those experiments<sup>2</sup>.

---

<sup>2</sup>Actually, it turned out that the explanation for these results is slightly more complicated than simple neutrino oscillations, see Ref. [Smi16].

Table 2.1: Currently accepted values of neutrino mixing parameters taken from Ref. [Tan+18]. The sign of  $\Delta m_{21}$  is known, the one of  $\Delta m_{32}$  is not.  $\Delta m_{32}^2 \cong \Delta m_{31}^2$  is assumed. The exact definition depends on the (unknown) mass ordering.

Parameter	Value
$\sin^2(\Theta_{12})$	$0.307 \pm 0.013$
$\sin^2(\Theta_{23})$	$0.536^{+0.023}_{-0.028}$
$\sin^2(\Theta_{13})$	$0.0218 \pm 0.0007$
$\Delta m_{21}^2$	$(7.53 \pm 0.18) \cdot 10^{-5} \text{ eV}^2$
$\Delta m_{32}^2 \cong \Delta m_{31}^2$	$(2.444 \pm 0.034) \cdot 10^{-3} \text{ eV}^2$

In general, neutrino mixing parameters can be described by the Pontecorvo–Maki–Nakagawa–Sakata Matrix (PMNS matrix) [NSS62]:

$$\begin{pmatrix} \nu_e \\ \nu_\mu \\ \nu_\tau \end{pmatrix} = \begin{pmatrix} U_{e1} & U_{e2} & U_{e3} \\ U_{\mu1} & U_{\mu2} & U_{\mu3} \\ U_{\tau1} & U_{\tau2} & U_{\tau3} \end{pmatrix} \begin{pmatrix} \nu_1 \\ \nu_2 \\ \nu_3 \end{pmatrix}. \quad (2.4)$$

This matrix describes the relation between the mass and the flavor eigenstates in the  $\nu$ -sector, analogously to the Cabibbo–Kobayashi–Maskawa Matrix (CKM matrix) in the quark sector, which describes the mixing between up- and down-type quarks. Unlike in the PMNS matrix, in the CKM matrix the diagonal elements are dominant. This implies a much greater relative impact of oscillation phenomena in the neutrino sector. A common parameterization of the PMNS matrix is given by

$$\begin{pmatrix} c_{12}c_{13} & s_{12}c_{13} & s_{13}e^{-i\delta} \\ -s_{12}c_{23} - c_{12}s_{23}s_{13}e^{i\delta} & c_{12}c_{23} - s_{12}s_{23}s_{13}e^{i\delta} & c_{13}s_{23} \\ s_{12}s_{23} - c_{12}c_{23}s_{13}e^{i\delta} & -c_{12}s_{23} - s_{12}c_{23}s_{13}e^{i\delta} & c_{13}c_{23} \end{pmatrix} \begin{pmatrix} e^{i\rho} & 0 & 0 \\ 0 & e^{i\sigma} & 0 \\ 0 & 0 & 1 \end{pmatrix} \quad (2.5)$$

where  $c_{ij} = \cos(\Theta_{ij})$  and  $s_{ij} = \sin(\Theta_{ij})$ , while  $\delta$  is the so-called  $CP$ -phase and  $\rho$  and  $\sigma$  are (unknown) Majorana phases. Currently accepted values of the mixing parameters are given in Table 2.1. Today’s values come from a variety of different experiments, measuring  $\nu$ -fluxes from reactors [Ade+18], accelerators [Ada+17; Abe+18] and the atmosphere at different baselines. The value of  $\delta$  is not known with great precision. A fit to data from different experiments gives  $215^{+40}_{-29}^\circ$  [Est+19], with a value of zero also excluded by individual experiments. This hints at much larger  $CP$ -violation than in the quark sector [GLZ18].

## 2.4 Neutrino Masses

As neutrino mixing parameters are large but also often not well known, there is no unique way to define neutrino masses that is useful in any case. Mass eigenstates of course have a definite mass. But what is usually observed are flavor eigenstates. As the frequency of neutrino oscillations is proportional to  $\Delta m_{ij}^2$ , it follows, that at least two mass eigenstates must have non-zero mass. But oscillations experiments are insensitive to the absolute neutrino mass-scale, which is still unknown. Different approaches to determine the neutrino mass-scale lead to different observables [WZ13]. Converting them into one another requires precise knowledge of the PMNS matrix elements. Some common definitions will be shortly explained here:

- Neutrino oscillations depend on the *mass differences squared* of two neutrino types  $\Delta m_{ij}^2 = (m_i - m_j)^2$ .
- What is usually measured in direct mass measurements involving  $\beta$ -decays is the *average anti-electron neutrino mass squared*  $m_{\bar{\nu}_e}^2 = \sum_i |U_{ei}|^2 m_{\nu_i}^2$ .
- Cosmology is sensitive to *sum of masses* of all neutrino types  $m_{\text{tot}} = \sum_i m_{\nu_i}$ .
- As the mass splittings are known from oscillation experiments, the absolute neutrino mass scale is often parameterized as the *mass of the lightest neutrino*  $m_{1,3} = m_{\text{lightest}}$ , depending on whether  $\nu_1$  or  $\nu_3$  is in fact the lightest mass eigenstate .
- As  $0\nu\beta\beta$ -decay is potentially sensitive to the Majorana phases, the observed quantity is different from the one probed in direct mass measurements and called *effective neutrino mass*:

$$m_{\beta\beta}^2 = \left| \sum_i U_{ei}^2 m_{\nu_i} \right|^2. \quad (2.6)$$

One approach [Fer34] to determine  $m_{\bar{\nu}_e}^2$  is to precisely measure the region close to the maximum electron energy released in a  $\beta$ -decay, called the endpoint. In this region a characteristic shift and a shape distortion of the spectrum are present if  $m_{\bar{\nu}_e}^2 > 0$ . The relative size of this effect is larger the smaller the  $Q$ -value is. Also corrections to the spectrum from electronic and nuclear effects should be as small as possible and well understood. Furthermore, the half-life of the isotope used should not be impractically large or small. These conditions are fulfilled by the super-allowed decay  ${}^3\text{H} \rightarrow {}^3\text{He} + e^- + \bar{\nu}_e$  with a  $Q$ -value of 18.6 keV and  $t_{1/2} = 12.3\text{yr}$ . The

best limits on  $m_{\bar{\nu}_e} \leq 2 \text{ eV}$  were achieved with this isotope in the Troitsk- and the Mainz-experiments [Ase+11; Kra+05]. Both experiments were based on a technique called magnetic adiabatic collimation with electrostatic filtering (MAC-E-filter). A MAC-E-filter can qualitatively be understood as a high-pass filter for electron energies. These filters have the advantage of both a high acceptance for electrons isotropically emitted from the source and good energy resolution. Furthermore, they are not affected by the overwhelming number of electrons with energy far away from the endpoint. With significant improvements, the same idea is used for the Karlsruhe Tritium Neutrino (KATRIN) experiment. KATRIN started data-taking in 2018 and should be able to increase the sensitivity on  $m_{\bar{\nu}_e}^2$  by an order of magnitude<sup>3</sup>.

Project8 [Ali+17] is another experiment to determine  $m_{\bar{\nu}_e}^2$  using tritium. Project8 aims at the detection of the energy-dependent frequency of cyclotron radiation emitted by electrons from tritium decay trapped in a magnetic bottle. Similar sensitivities as for KATRIN are envisioned and ultimately it might be possible to reach a sensitivity on  $m_{\bar{\nu}_e}^2$  of 40 meV. The Electron capture in  $^{163}\text{Ho}$  experiment (EChO) [Gas+17] on the other hand uses the EC of  $^{163}\text{Ho}$ , which has a very low endpoint of 2.8 keV. Its disadvantage is that multiple decay channels exist. Thus, a calorimetric measurements of all non-neutrino emissions is required. This is done by employing an array of cryo-bolometers. Again, the goal is to reach a similar sensitivity as KATRIN.

It is also possible to deduce  $m_{\bar{\nu}_e}^2$  from observations of supernovae based on the difference in arrival times for neutrinos of different energy. This has been done with  $\bar{\nu}_e$  from the supernova SN1987A [SB88]. Due to the limited statistics, only a comparatively high limit of  $m_{\bar{\nu}_e}^2 \leq 5.8 \text{ eV}$  [PRTV10] could be set. Because of improvements in both quality and quantity of neutrino detectors since then, the observation of another nearby supernova would allow measure  $m_{\bar{\nu}_e}$  with much higher sensitivity [Sch17].

A source of information on  $m_{\text{tot}}$  comes from cosmology. Due to the fact that neutrinos were produced in large number during the Big Bang, their mass affected structure formation in the early universe. Hence,  $m_{\text{tot}}$  can be incorporated into the cosmological standard model and extracted from a fit to various cosmological data sets. If data from the Planck satellite on the cosmic microwave background (CMB) are used, an upper limit of  $m_{\text{tot}} \leq 0.59 \text{ eV}$  is obtained [Col+16]. If additional data are taken into account limits in the order of 0.1 eV to 0.2 eV are reached. Unlike direct mass measurements, the limits from cosmology depend on details of the model and so these values are often treated with caution. On the other hand, if direct and indirect measurements would come into tension at some point, this would be evidence for BSM-physics.

---

<sup>3</sup>Early results [Ake+19] give  $m_{\bar{\nu}_e}^2 < 1.1 \text{ eV}$ .

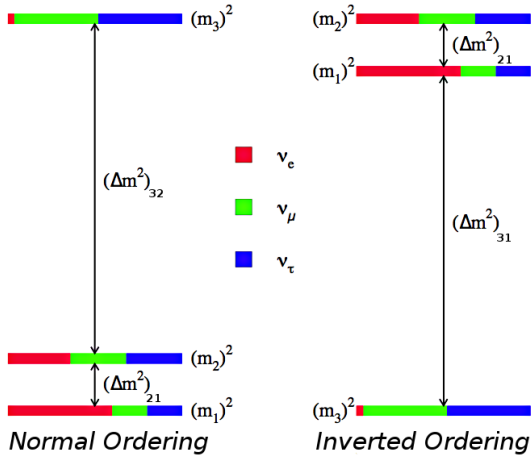


Figure 2.2: Mixing of weak- and mass- neutrino eigenstates and mass splittings for normal and inverted hierarchy. The colored bars indicate the portion of weak eigenstates in each mass eigenstate.  $\nu_2$  is made up of nearly equal parts of all weak states.  $\nu_1$  has a much larger fraction of  $\nu_e$  and  $\nu_3$  nearly no  $\nu_e$  component. The mass splittings are not shown to scale. Adapted from Ref. [Cah+13].

The so-called mass ordering, i.e. the relative size of  $m_{1,2,3}$ , also has not been determined so far. As it is known that  $\Delta m_{21} > 0$  and  $\Delta m_{21}^2 \ll \Delta m_{32}^2$ , it is clear that  $m_1 < m_2$ . Given the values of Table 2.1, this leaves open two possible scenarios<sup>4</sup>. One is the so-called *normal hierarchy* where  $m_1 < m_2 < m_3$ . The other is called *inverted hierarchy* where  $m_3 < m_1 < m_2$ . As they can not be distinguished with the given precision it is often assumed that  $m_{32}^2 = m_{31}^2$ . The two scenarios of normal and inverted hierarchy are graphically depicted in Figure 2.2. A global fit combining data from different sources [Est+19] favors the normal hierarchy. But no running experiment alone gives a strong preference for either due to a degeneracy with matter effects and  $\delta$ . Thus, the ordering has to be determined by a combination of next-generation experiments.

## 2.5 Known Unknowns

Even though many interesting neutrino properties were deduced since the first detection of the neutrino, some are also still unknown. Among these open questions are whether neutrinos are Dirac- or Majorana-fermions, if there are exactly three neutrino flavors, and the absolute mass scale and ordering.

Besides these fundamental questions, there are also a number of rather long standing experimental anomalies. Among these are the *gallium anomaly*, the *reactor anomaly*, and an excess of  $\nu_e$  and  $\bar{\nu}_e$  events in accelerator-based experiments [AA+18]. All of them might be interpreted as evidence for so-called sterile (not participating in weak

<sup>4</sup>The case of *degenerate hierarchy* where  $m_1 \cong m_2 \cong m_3$  is increasingly disfavored by experimental data, as this requires the absolute mass-scale to be much higher than the individual mass-splittings.

interactions) neutrinos seen in oscillations at short baselines. As only left-handed neutrinos participate in weak interactions of the SM, sterile neutrinos may be right-handed. Different BSM-theories predict them in a wide mass range [Dre13]. As these anomalies do not point into a consistent direction they can neither confirm nor rule out the existence of sterile neutrinos.

A question that is hard to settled by oscillation experiments is that of the Dirac- or Majorana-character of neutrinos. Due to the  $V$ - $A$ -nature of weak interactions, results of experiments demonstrating that the neutrino is different from the anti-neutrino [Dav55] can be explained by assuming they just have different helicity and thus can not be used to judge the Dirac/Majorana questions. At the same time, this question has important bearing for BSM-models, as many of them favor one possibility over the other. For example, the popular seesaw-mechanism, which gives an explanation for the smallness of neutrino masses, predicts Majorana character. The observation of  $0\nu\beta\beta$ -decay could be the only viable way to settle this questions<sup>5</sup> and give insights to other BSM-physics by being the currently most sensitive probe for  $\Delta L = 2$  lepton number violating processes. Furthermore it has sensitivity to the absolute neutrino mass-scale and hierarchy.

## 2.6 Neutrinoless Double- $\beta$ Decay

Today, the search for  $0\nu\beta\beta$ -decay is a very active field in neutrino physics. Although this decay has been searched for since several decades it has not been found yet. In this section, important milestones in this search will be reviewed and the current status of the field will be summarized. First, its theoretical motivation will be laid out starting with the closely related SM-process of two-neutrino double  $\beta$ -decay ( $2\nu\beta\beta$ )-decay

$${}^A_Z X \rightarrow {}^A_{Z+2} Y + e^- + e^- + \bar{\nu}_e + \bar{\nu}_e. \quad (2.7)$$

$2\nu\beta\beta$ -decay is depicted on the left side of Figure 2.3. It occurs whenever there is a nucleus which has isobars with lower energy, but the decay to the nearest neighboring nucleus is energetically forbidden, while a decay to the next-to-nearest neighbor is possible as shown in Figure 2.4. This situation arises due to the mass splitting in even/even and odd/odd nuclei, i. e. nuclei with an even or odd number of both protons

---

<sup>5</sup>Another way could be the detection of the cosmic neutrino background. The capture rate of such neutrinos from the cosmic neutrino background depends on their Dirac/Majorana nature [LLS14]. It remains to be shown that this is indeed feasible. An even more challenging idea is the detection of quadruple  $\beta$ -decay [HR13].

## 2.6 Neutrinoless Double- $\beta$ Decay

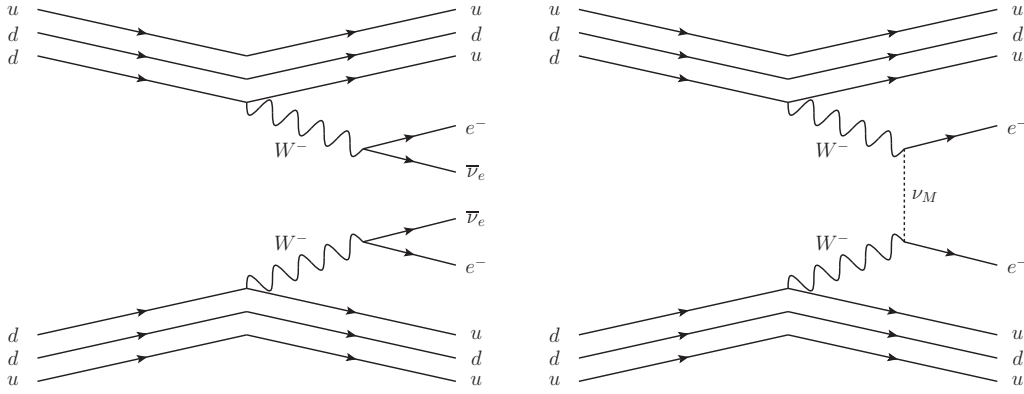


Figure 2.3: Feynman graphs for  $2\nu\beta\beta$ - and  $0\nu\beta\beta$ -decay at quark level.  $\nu_M$  denotes a Majorana neutrino. Drawn with JAXODRAW [BT04] after Ref. [AEE08].

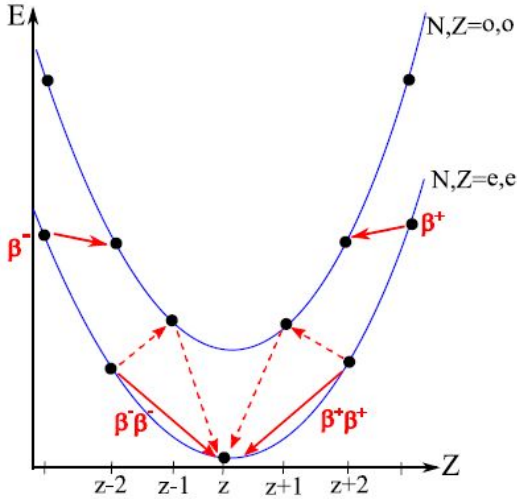


Figure 2.4: Total energy of isobaric nuclei near the point of lowest energy. The upper line represent nuclei with an odd number of protons and neutrons, generally of higher energy, the lower line those with an even number of both. Sometimes a single  $\beta$ -decay is energetically not allowed, while two decays lead to a final state with lower energy. Taken from Ref. [Koe12].

and neutrons. As the odd/odd situation is in general energetically unfavorable, an even/even nucleus can in some cases not decay into an odd/odd nucleus via  $\beta$ -decay. But two quasi-simultaneous  $\beta$ -decays are possible. The decay was first described in 1935 [GM35]. As a second-order weak process half-lives  $t_{1/2}$  greater than  $10^{17}$  yr were predicted. In general,  $t_{1/2}$  is given by

$$\left(t_{1/2}^{2\nu}\right)^{-1} = G_{2\nu} |M_{2\nu}^2| \quad (2.8)$$

where  $G_{2\nu}$  is the phase-space, representing the decay-kinematics and  $M_{2\nu}$  is the nuclear matrix element (NME), representing the nuclear physics aspect. Both depend on

the nucleus of interest. Even though  $2\nu\beta\beta$ -decay is very rare, it has been observed in more than ten different nuclei. The earliest evidence came from geochemical experiments [IR50] in 1950, while the first direct detection was made with the decay of  $^{82}\text{Se}$  in 1987 [EHM87] having  $t_{1/2} \approx 10^{20}$  yr. As the two outgoing neutrinos cannot be observed in practice,  $2\nu\beta\beta$ -decay has a continuous energy spectrum. It is also possible for a double-beta decay to leave the final state nucleus in an excited state. In general these decay modes are even rarer and have only been observed for a small number of nuclei. Most data exists for the decay of  $^{100}\text{Mo}$  to the  $0_1^+$  state of  $^{100}\text{Ru}$  [Bel+10], which is two orders of magnitude less likely to occur than the decay into the ground state.

Aside from the ordinary  $2\nu\beta\beta$ -decay, one can also consider that a decay of the form

$${}^A_Z\text{X} \rightarrow {}^A_{Z+2}\text{Y} + e^- + e^- \quad (2.9)$$

exists as shown in the right in Figure 2.3. This so-called  $0\nu\beta\beta$ -decay was first described in 1939 [Fur39] and has not been detected yet. As no neutrinos would be emitted in this decay, the total energy is taken away by the electrons. Consequently the energy spectrum only consists of a line at the  $Q$ -value and could thus be distinguished from the two-neutrino decay as shown in Figure 2.7. This process would violate the total lepton number  $L$ , so that  $\Delta L = 2$ .

Besides the standard  $0\nu\beta\beta$ -decay, there is also the possibility for similar processes like

$${}^A_Z\text{X} \rightarrow {}^A_{Z-2}\text{Y} + e^+ + e^+ \quad (0\nu\beta^+\beta^+) \quad (2.10)$$

$${}^A_Z\text{X} + e^- \rightarrow {}^A_{Z-2}\text{Y} + e^+ \quad (0\nu EC/\beta^+) \quad (2.11)$$

$${}^A_Z\text{X} + e^- + e^- \rightarrow {}^A_{Z-2}\text{Y} \quad (0\nu EC/EC) \quad (2.12)$$

whose two-neutrino analogues have only been observed in three nuclei so far [Apr+19a]. They usually have an even smaller rate than the two electron decay<sup>6</sup>. As total lepton number is not associated with a global symmetry, many BSM theories predict such lepton number violating processes.

---

<sup>6</sup>Especially the positron emitting modes suffer from a restricted phase space. The case of neutrinoless double-electron capture ( $0\nu EC EC$ ) is somewhat complicated, because with nothing else in the final state except for the nucleus, energy and momentum conservation can not be satisfied. This makes it necessary to either allow for the emission of an additional particle like an X-ray or have a transition where there is an excited state of the final states nucleus with exactly the right energy to absorb the energy of the decay [Win55]. In this case there might be a resonant rate enhancement [BRJ83].

### 2.6.1 BSM-Theories Giving Rise to $0\nu\beta\beta$ -Decay

From a theoretical perspective, the simplest realization of  $0\nu\beta\beta$ -decay is the exchange of light neutrinos, as shown on the right of Figure 2.3. In this model, the outgoing neutrino emitted in one beta-decay is re-absorbed as an incoming anti-neutrino in the other beta-decay. Obviously, for this to be possible the neutrino needs to be massive to have a chance of being absorbed with the correct helicity but also to be a Majorana particle. As such, a detection of  $0\nu\beta\beta$ -decay would answer several questions about the neutrino's fundamental character.

Besides this mechanism,  $0\nu\beta\beta$ -decay is also present in models involving heavy neutrinos, an enlarged Higgs sector and left-right symmetric as well as supersymmetric theories [Rod11; DHP12]. Independent of the underlying mechanism, the so-called *black-box* or Schechter-Valle theorem [SV82] implies, that any theory allowing for lepton-number violation produces a Majorana-mass term in higher order. Even if the contribution of higher order terms would be small, the existence of  $0\nu\beta\beta$ -decay is thus directly connected to the Majorana character of neutrinos.

Models in which a massless or light boson couples to neutrinos are a special case. In these models one or more so-called Majorons  $M^0$  are emitted

$${}^A_Z\text{X} \rightarrow {}^A_{Z+2}\text{Y} + e^- + e^- + M^0. \quad (2.13)$$

Due to the additional boson the spectrum would be continuous but of different shape than that of  $2\nu\beta\beta$ -decay. For light neutrino exchange, the half-life can be calculated similar to Equation 2.8. Only an additional factor accounting for the helicity flip has to be considered so that

$$\left(t_{1/2}^{0\nu}\right)^{-1} = G_{0\nu} |M_{0\nu}^2| \frac{m_{\beta\beta}^2}{m_e} \quad (2.14)$$

with  $G_{0\nu}$  and  $M_{0\nu}$  qualitatively similar to Equation 2.8, and  $m_{\beta\beta}$  as introduced in Equation 2.6. Due to the dependence on  $m_{\beta\beta}$  an observation of this decay can be interpreted as a measurement of the absolute neutrino mass scale.

It is possible to parametrize  $m_{\beta\beta}$  either as a function of the mass of the lightest neutrino  $m_{\text{lightest}}$  or as the sum of the neutrino masses  $m_{\text{tot}}$ , as is shown in Figure 2.5. Due to the uncertainty in the  $\Delta m_{ij}^2$ ,  $\Theta_{ij}$  and the unknown Majorana phases, such a parametrization is ambiguous. Especially, it depends on the mass ordering. In general, for a given  $m_{\text{lightest}}$  or  $m_{\text{tot}}$  the inverted mass ordering gives  $m_{\beta\beta}$  higher by about one order of magnitude, leading to a two orders of magnitude shorter half-life. In case of normal mass ordering, for some values of  $m_{\text{lightest}}$  a cancellation of different terms

## 2 Neutrino Physics and Double $\beta$ -Decay

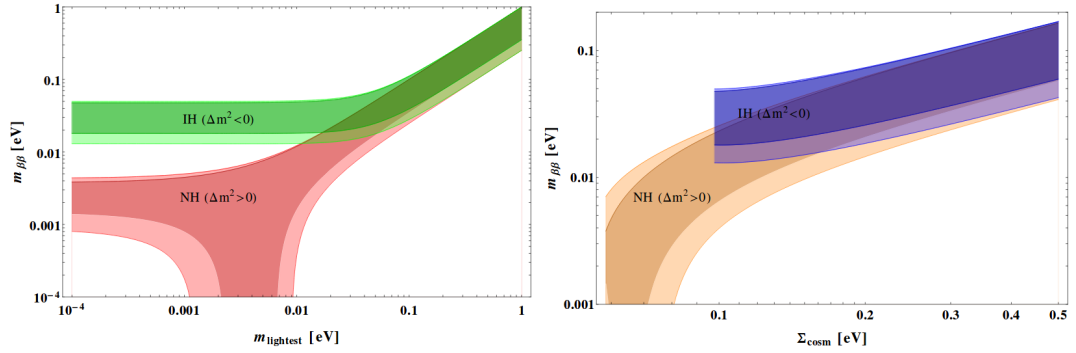


Figure 2.5:  $m_{\beta\beta}$  as a function of the mass of the lightest neutrino and as a sum of the neutrino masses for normal ordering (NH) and inverted ordering (IH). Each band represents the ambiguity from the unknown Majorana phases, while the shaded bands additionally include  $3\sigma$  uncertainties of the PMNS matrix elements.  $\Sigma_{cosm}$  is equivalent to  $m_{tot}$ . Taken from Ref. [DMV14].

in  $m_{\beta\beta}$  can occur, leading to arbitrary low  $m_{\beta\beta}$  and making a detection practically impossible. Thus, from an experimental point of view, the inverted ordering would be preferable. It would make detection of  $0\nu\beta\beta$ -decay much easier if the neutrino is truly a Majorana-particle and allow to rule out Majorana-character with a null results from a sufficiently sensitive experiment. So far no such experiment exists.

### 2.6.2 Phase-Space Factors and Nuclear Matrix Elements

Although small deviations exist between the results from different groups, there seems to be a general agreement on how to calculate  $G_{0\nu}$  [KI12; MPS14]. Contrary, the calculation of  $M_{0\nu}$  is much more complicated. As nuclei are strongly coupled many-body systems, calculations from first principles are currently only possible in light nuclei with a small number of nucleons [SSS18]. For heavier nuclei, simplifications have to be used in the form of nuclear models. Each model generally predicts a slightly different  $M_{0\nu}$ . One example is the nuclear shell model (NSM), which only takes a small number of nucleons into account, but treats these with their full correlations. A complementary approach is taken by quasiparticle random phase approximation (QRPA), which includes many more nuclear orbitals at the price of simplifying their correlations. These models have both been used for a long time, with the NSM predicting often smaller  $M_{0\nu}$ . The interacting boson model (IBM) models the nucleus in terms of creation- and annihilation-operators of bosons. It is quite distinct from the aforementioned models and used less often. A comparison of NMEs calculated in different models for the

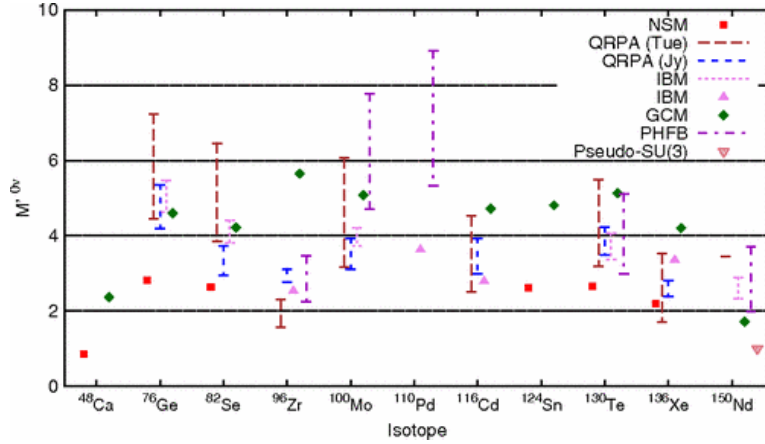


Figure 2.6: Nuclear matrix elements of a number of isotopes calculated in different theoretical frameworks according to Ref. [DRZ11]. Although newer calculations might be available for some data-points in recent years, the picture has not changed fundamentally. Note also, that this is not taking into account any uncertainty in the value of  $g_A$ .

exchange of a light Majorana neutrino can be found in Figure 2.6. Large disparities up to a factor of three exist for the same isotope. The present situation would thus not allow to unambiguously extract  $m_{\beta\beta}$  from a measurement of  $t_{1/2}$ .

Additionally, all models rely on knowledge about the value of the weak vector coupling  $g_V$  and axial-vector coupling  $g_A$ . In pure leptonic interactions  $g_A = g_V = 1$ , but this is only true for point-like particles. The value  $g_V$  is assumed to be protected by the conserved vector current hypothesis [GZ55; FGM58], but the value of  $g_A$  is at best partly conserved. The so-called free value of  $g_A^{\text{free}} = 1.27$  is obtained from data on the decay of the free neutron [Tan+18]. However, with this value it is not possible to reproduce the measured strength of Gamow-Teller  $\beta$ -transitions for more complex<sup>7</sup> systems [Wil73]. Lower values  $g_A^{\text{eff}}$  are often expressed as a quenching factor  $q = g_A^{\text{eff}}/g_A^{\text{free}}$  [MP+96]. There are a number of effects discussed in the literature that can lead to quenching. These effects are mainly related to various approximations used in the theoretical calculations and complex interactions in the nuclear medium, which may have different influences on different nuclear models [Suh17b]. Regardless of the considered model, quenching is found to be necessary not only in the context

<sup>7</sup>Recently calculations became available, that include more nuclear correlations and meson-exchange currents [Gys+19]. These calculations seem to agree with experimental data on  $\beta$ -decay without the need for modifying  $g_A$ . But they are so far only possible for comparatively light nuclei or special cases like the doubly-magic  $^{100}\text{Sn}$ . They remain yet to be applied and tested in the context of double-beta decay.

of ordinary unique and non-unique single  $\beta$ -decays, but also for higher-forbidden and  $2\nu\beta\beta$ -decays. For  $2\nu\beta\beta$ -decay, there seems to be a dependence on the nuclear mass number  $A$ . For heavy nuclei, such as  $^{136}\text{Xe}$ , quenching factors between 0.4 and 1.0 are reported. The study of  $g_A^{\text{eff}}$  in non-unique forbidden decays is also of interest. For these more complicated decays, not only the rate, but also the spectral shape depends on  $g_A$ , making them a highly sensitive probe for quenching [HKS17].

The intermediate momentum exchanged in neutrinoless transitions is much higher due to the emitted and reabsorbed neutrino and so many more intermediate states can be excited. Consequently, it is not clear how the results obtained from  $\beta$ - and  $2\nu\beta\beta$ -decays relate to the calculation of NMEs for  $0\nu\beta\beta$ -decay.  $M_{0\nu}$  depends roughly on  $g_A^2$  and  $t_{1/2}$  depends on  $M_{0\nu}^{-2}$ , so that  $t_{1/2} \propto g_A^{-4}$ . Thus, a small deviation, from  $g_A^{\text{free}}$  leads to a severe<sup>8</sup> suppression in rate of  $0\nu\beta\beta$ -decay. For example, assuming  $q = 0.9$  leads to a decrease in rate of about 35%, while  $q = 0.5$  results in more than an order of magnitude decrease.

Summarizing, a large amount of uncertainty is involved in relating the decay rate to the neutrino mass scale. The prospects of measuring a potential  $0\nu\beta\beta$ -decay with a given detector vary wildly depending on assumptions on the theoretical side. From a fundamental perspective, it would be ideal to use the sensitivity on  $m_{\beta\beta}$  to compare different experiments. Due to the nature of different BSM-model, the simple light neutrino mass-mechanism might not be responsible for  $0\nu\beta\beta$ -decay if it exists. Even if this mechanism is responsible, there is still a large uncertainty associated with the matrix-elements. Thus, instead of values of  $m_{\beta\beta}$  half-lives will be reported here. In this way, a comparison of the potential to detect  $0\nu\beta\beta$  for different detection technologies is independent of the shortcomings of the nuclear models and lacking knowledge about BSM particle physics.

### 2.6.3 Considerations for a $0\nu\beta\beta$ -Experiment

If  $0\nu\beta\beta$ -decay exists, it has a very low rate. Thus, its detection presents an experimental challenge. In this section, some considerations for the design of a suitable experiment will be discussed. The most basic question is which isotopes to use<sup>9</sup>. A list of relevant properties of some of the most interesting isotopes is given in Table 2.2. It can be deduced from Equation 2.14, that  $G_{0\nu}$  and  $M_{0\nu}$  should be as large as possible. But

---

<sup>8</sup>In reality, the dependence is more complicate, making the effect smaller than naïvely assumed [Suh17a], but in any case considerable.

<sup>9</sup>Here only  $\beta^-\beta^-$ -candidates are considered, as other modes are associated with much larger half-lives [MS13] but similar considerations apply in these cases.

Table 2.2: List of isotopes unstable against double beta-decay.  $Q$ -values from Ref. [Hua+17], natural abundances  $a$  from Ref. [BW11], phase-space factors for  $0\nu\beta\beta$ -decay  $G_{0\nu}$  from Ref. [KI12] and  $2\nu\beta\beta$ -decay half-lives  $t_{1/2}^{2\nu}$  from Ref. [Bar15]

Isotope	$Q$ -value [keV]	$a$ [%]	$G_{0\nu}$ [ $10^{-15}/\text{yr}$ ]	$t_{1/2}^{2\nu}$ [ $10^{20}$ yr]
$^{48}\text{Ca}$	4 263	0.2	24.8	$0.44 \pm 0.06$
$^{76}\text{Ge}$	2 039	7.8	2.7	$16.5 \pm 1.4$
$^{82}\text{Se}$	2 998	8.7	10.2	$0.92 \pm 0.07$
$^{100}\text{Mo}$	3 035	9.8	15.9	$0.071 \pm 0.004$
$^{116}\text{Cd}$	2 814	7.5	16.7	$0.29 \pm 0.01$
$^{130}\text{Te}$	2 528	34.1	14.2	$6.9 \pm 1.3$
$^{136}\text{Xe}$	2 459	8.9	14.6	$21.9 \pm 0.6$

as seen in the previous section, it is hard to reliably predict  $M_{0\nu}$ . As the available phase-space is a function of the  $Q$ -value, it follows that the  $Q$ -value should be as high as possible. Based on this, a lot of isotopes can be ruled out that are not listed in Table 2.2.

The sensitivity of an counting experiment searching for a peak over a given background  $B$  in a spectrum can be approximated as

$$t_{1/2} \propto a\epsilon\sqrt{\frac{Mt}{\Delta EB}} \quad (2.15)$$

which in the limit of  $B \rightarrow 0$  becomes

$$t_{1/2} \propto a\epsilon Mt, \quad (2.16)$$

with  $a$  the abundance of the isotope of interest,  $\epsilon$  the signal efficiency,  $M$  the source mass,  $t$  the measurement time and  $\Delta E$  the energy resolution.

To make  $a$  as large as possible, either one chooses an element with a large natural abundance of the candidate isotope like tellurium with its high  $^{130}\text{Te}$  content or isotopic enrichment is used. In case of very low natural abundance, like for  $^{48}\text{Ca}$ , enrichment is very demanding. Due to their chemical properties some isotopes like the noble gas  $^{136}\text{Xe}$  can be enriched more easily.

Besides a larger phase space, a large  $Q$ -value is also beneficial in achieving a low background  $B$ . If background from  $\gamma$ -rays is considered, a natural criterion is to aim for a  $Q$ -value significantly above 2615 keV, where there is a prominent  $\gamma$ -line from the decay of  $^{208}\text{Tl}$ . This line is often quoted as the highest energetic line with notable intensity from a long-lived naturally occurring isotope. A similar line of

thought can be constructed for background from  $\beta$ -decays, where there is e. g.  $^{214}\text{Bi}$  with  $Q^{\beta^-} = 3270$  keV. However,  $\beta$ -decays are of lesser importance as a background as electrons can be easily shielded if the background source is external to the detector.

Besides that, to reach a very low background it is necessary to shield an experiment from external radiation as much as possible. This can be done by using a passive shield surrounding the detector, like lead, copper, or very pure water. To reduce the flux of cosmic rays active elements that veto external radiation or a massive overburden are employed.

To reach a high efficiency  $\epsilon$  many modern experiments use a *source=detector* approach. For this, an isotope is suited to be used exclusively or in a large fraction as the construction material for a particle detector is chosen. This requires that a suitable technology exists to do this. Another choice is to embed the isotope into the detector material, e. g. by dissolving it in liquid scintillator. Again, the number of isotopes usable this way is limited due to the chemistry involved.

The choice of detection technology also determines energy resolution  $\Delta E$ . Scintillators generally have rather poor resolution of about 10 % full-width-at-half-maximum (FWHM) at the Q-value. The best resolution is achieved with semiconductors approaching 0.1 % FWHM. Energy resolution is especially important as every experiment will suffer from an irreducible background due to  $2\nu\beta\beta$ -decay if the resolution is not good enough, as shown in Figure 2.7. The ratio of signal events  $S_{0\nu}$  from  $0\nu\beta\beta$ -decay to background events  $B_{2\nu}$  from  $2\nu\beta\beta$ -decay can be approximated [EV02] as

$$\frac{S_{0\nu}}{B_{2\nu}} = \frac{m_e}{7Q} \left( \frac{Q}{\Delta E} \right)^6 \frac{t_{1/2}^{2\nu}}{t_{1/2}^{0\nu}} \quad (2.17)$$

with the electron mass  $m_e$ . In this regard, also the  $2\nu\beta\beta$ -decay half-life  $t_{1/2}^{2\nu}$  is of interest, although  $t_{1/2}^{2\nu}$  and  $t_{1/2}^{0\nu}$  are actually not totally independent, as factors like phase-space are similar. As  $S_{0\nu}/B_{2\nu}$  falls with energy resolution to the power of six, this background can effectively mitigated with sufficient resolution.

Because of these often competing considerations no clearly best candidate isotope can be identified. Instead, there are numerous experimental approaches to search for  $0\nu\beta\beta$ -decay, each relying on different advantages of certain isotopes.

#### 2.6.4 Status of Searches for $0\nu\beta\beta$ -decay

In this section some concluded, ongoing and planned experiments to search for  $0\nu\beta\beta$ -decay will be presented. The first direct detection experiments for  $0\nu\beta\beta$ -decay

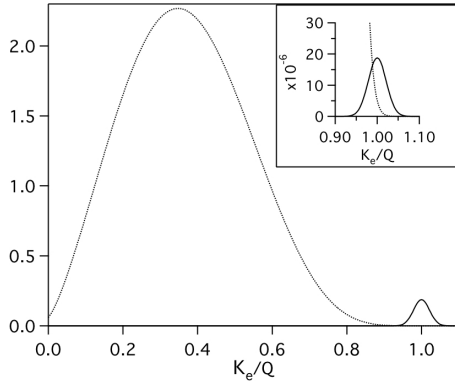


Figure 2.7: Energy spectrum of  $0\nu\beta\beta$ - and  $2\nu\beta\beta$ -decay.  $2\nu\beta\beta$ -decay (dashed line) produces a continuous spectrum as the neutrinos escape the detector.  $0\nu\beta\beta$ -decay (solid line) produces a peak at the  $Q$ -value. The inset shows how both spectra overlap due to resolution effects. Taken from Ref. [EV02].

used Geiger counters. They reached half-life sensitivities from  $10^{15}$  yr to  $10^{19}$  yr. No significant signal was found with this technique [Bar10]. Geochemical experiments present indirect searches. They aim to extract the final state isotopes from very old ores with known age. These experiments are very sensitive due to the long time of exposure and found first evidence for  $2\nu\beta\beta$ -decay [Bar10]. But as it is not possible to distinguish between  $2\nu\beta\beta$ - and  $0\nu\beta\beta$ -decay in this way, modern experiments focus on direct detection.

One popular choice is the use of Ge-diodes. They have excellent energy resolution and can be produced with masses up to some kilogram per crystal. Important results [Vas+90] were obtained with detectors enriched in  $^{76}\text{Ge}$  to more than 80% such as the International Germanium Experiment (IGEX) and the Heidelberg-Moscow (HdM) experiment. Both used a small number of individual detectors in a shielding made up of lead and copper. IGEX was able to obtain a limit of  $t_{1/2}^{76\text{Ge}} \geq 1.57 \cdot 10^{25}$  yr at 90% confidence level (C.L.) [Aal+02b]. HdM initially reported  $t_{1/2}^{76\text{Ge}} \geq 1.9 \cdot 10^{25}$  yr at 90% C.L. [KK+01b]. Later a part of the collaboration claimed to have found positive evidence [KK+01a] for the decay at the level of  $3\sigma$ , subsequently raised to  $6\sigma$  [KKK06] based on the same data. This was met with skepticism [ZDT02; Aal+02a; Bak+05] but it took many years for other germanium-based experiments to produce independent results to settle the matter.

These are the Germanium Detector Array (GERDA) and MAJORANA. The GERDA concept is focused on a low-Z shielding to reduce cosmogenic activation and active veto techniques. MAJORANA uses a more conventional shielding, but a novel method to produce copper underground to reduce cosmogenic activation. Both experiments employ a total detectors mass of tens of kilogram and rely on pulse-shape discrimination (PSD) to distinguish signal and background events. The highest limit for the  $0\nu\beta\beta$ -decay

of  $^{76}\text{Ge}$  so far was set by GERDA at  $t_{1/2}^{76\text{Ge}} \geq 9.0 \cdot 10^{25}$  yr. This clearly refutes the evidence claimed in Ref. [KK+01a]. Both experiments were able to reach a background at the level  $10^{-3}$  cts/kg/keV/yr, among the lowest in the field.

The collaborations plan to merge and build a larger array of HPGe detectors called Large Enriched Germanium Experiment for Neutrinoless Double Beta Decay (LEGEND), which combines ideas from both concepts. The first stage called LEGEND-200 [Abg+17] is already under construction. It will use the shielding infrastructure of GERDA. LEGEND will also re-use detectors from both experiments in addition to some new ones. The concept is aiming at a total detector mass of 200 kg and significant background reduction. A second stage is intended to cover the parameter space of the inverted mass ordering completely.

Because of easy enrichment  $^{136}\text{Xe}$  is another commonly used isotope. The most stringent half-life limit in the field of  $0\nu\beta\beta$ -decay of  $t_{1/2}^{136\text{Xe}} \geq 1.1 \cdot 10^{26}$  comes from the KamLAND-Zen-experiment [Gan+16] using  $^{136}\text{Xe}$ . In this experiment, over 340 kg of  $^{136}\text{Xe}$  were dissolved in an organic scintillator surrounded by ultra-pure water. In this way low external backgrounds are achieved, but background from  $2\nu\beta\beta$ -decay is significant because of poor energy resolution. Consequently, in the recently started KamLAND-Zen-800 stage, twice the isotope mass and a cleaner detector will be used, but ultimately the energy resolution shall be improved [Gan18].  $^{136}\text{Xe}$  is also itself a scintillator and can thus be used to construct a detector, e.g. a time projection chamber (TPC). A TPC allows to not only measure the energy, but also topological features of a decay to reduce background. This approach is followed by EXO-200 [Alb+18a], which used around 200 kg of liquid Xenon and reached a background of  $1 \cdot 10^{-3}$  cts/kg/keV/yr. In the planned next-generation Enriched Xenon Observatory (nEXO) [Alb+18b] experiment, the EXO idea will be scaled up to several tons of  $^{136}\text{Xe}$  to cover the complete inverted mass ordering.

The ultimate technique for background reduction using xenon would be to tag the final state barium nucleus through fluorescence imaging [JMN16]. This is possible in principle but has not yet shown to be feasible on a large scale. With barium tagging  $2\nu\beta\beta$ -decay would be the only concern in terms of background. A TPCs based on gaseous xenon like used in the Neutrino Experiment with a Xenon TPC (NEXT)-experiment seems to be promising in this regard [Her15]. Because of their very large fiducial mass up to multiple tons, current and future xenon based Dark Matter experiments are also able to perform competitive searches for  $0\nu\beta\beta$ -decay [Aal+16]. The detection of  $0\nu ECEC$ -decay of  $^{124}\text{Xe}$  with a Dark Matter detector is in fact the rarest ( $t_{1/2} = (1.8 \pm 0.5) \cdot 10^{22}$  yr) nuclear process directly measured to this date [Apr+19b].

$^{130}\text{Te}$  is used in  $\text{TeO}_2$  bolometers. The challenge in using bolometers lies in the necessary operational temperatures of about 10 mK. As those bolometers usually have a mass of less than a kilogram, arrays of them are used. The recent state-of-the-art experiment using this technology is the Cryogenic Underground Observatory for Rare Events (CUORE). The total detector mass of CUORE is close to a ton, including over 200 kg of  $^{130}\text{Te}$ . The shielding is made up of about 70 t of lead. The energy resolution is slightly inferior to HPGe detectors, but the background is higher than with the previously presented approaches, coming mainly from  $\alpha$ -decays near the detector surface [Ald+18]. The best limit obtained by CUORE is  $t_{1/2}^{130\text{Te}} \geq 1.3 \cdot 10^{25}$  yr. The goal is to reach a sensitivity of  $9 \cdot 10^{25}$  yr after several years of operation.

To substantially lower the background, the basic technology of COURE is planned to be enhanced in the CUORE Upgrade with Particle IDentification (CUPID) project [Gro19]. Particle identification would allow to distinguish between  $\alpha$ -particles and electrons. This can be achieved by making use of the fact, that  $\alpha$ -particles have a much lower light production in scintillators than electrons. This technique is well established in Dark Matter experiments [Ang+12]. But  $\text{TeO}_2$  is not a scintillator. Thus, CUPID will either use  $\text{Li}_2\text{MoO}_4$  crystals instead, which have good scintillating properties, or  $\text{TeO}_2$  and use Cerenkov radiation. Cerenkov radiation can also be used as  $\alpha$ -particles with energy around the  $Q$ -value are below the Cerenkov-threshold, but electrons are not. This option would technically be much more challenging. In either case, a ton-scale experiment with a background of  $10^{-4}$  cts/kg/keV/yr is envisioned to cover the inverted mass hierarchy.

One notable exception from the *source=detector* approach is the Neutrino Ettore Majorana Observatory (NEMO)-3 [Arn+05]. In this experiment, the sources are employed in the form of thin foils of the isotope of interest. The detector itself is more akin to a design used in collider experiments, with a tracker and a separate calorimeter surrounding the source foil in a sandwich geometry. This design has the advantage of being able to use a large variety of isotopes at the same time 6.9 kg of  $^{100}\text{Mo}$ , slightly smaller amounts of  $^{82}\text{Se}$ ,  $^{116}\text{Cd}$  and  $^{130}\text{Te}$  and various isotopes in amounts of some gram were used. NEMO allowed a detailed investigation of many  $2\nu\beta\beta$ -decays and could set comparatively high limits for  $0\nu\beta\beta$ -decays not accessible with other technologies. Super-NEMO is a plan to extend the concept to sensitivities up to  $1 \cdot 10^{26}$  yr.

In conclusion, the search for double-beta decay saw an enormous increase in sensitivity of nearly ten orders of magnitude over several decades. While no conclusive evidence for  $0\nu\beta\beta$ -decay could be found,  $2\nu\beta\beta$ -decay was detected in many isotopes with half-lives known at the percent-level [Bar15]. Especially since it was realized that neutrinos

Table 2.3: List of finished, currently running and proposed double  $\beta$ -experiments. As NEMO-3 is not a *source=detector* experiment no comparable value for  $B$  can be given. For future experiments, the number are given according to the outlined goals as far as available. Energy Resolution  $\Delta E$  is given as relative FWHM resolution. Limits on  $t_{1/2}$  are given at 90% C.L.

Experiment	Isotope	$M_{iso}$ [kg]	$\Delta E$ [%]	$B$ [cts/kg/keV/yr]	$t_{1/2}$ Limit [yr]
<b>Already Finished</b>					
Solotvina [Dan+03]	$^{116}\text{Cd}$	0.09	7.7	$3.7 \pm 1.0 \cdot 10^{-2}$	$1.7 \cdot 10^{23}$
AURORA [Bar+18]	$^{116}\text{Cd}$	0.3	6.0	$1.4 \pm 0.1 \cdot 10^{-1}$	$2.2 \cdot 10^{23}$
NEMO-3 [Arn+15]	various	various	$\approx 4$	-	$1.1 \cdot 10^{24}$
HdM [KK+01b]	$^{76}\text{Ge}$	9.4	0.21	$6 \pm 1 \cdot 10^{-2}$	$1.9 \cdot 10^{25}$
IGEX [Aal+02b]	$^{76}\text{Ge}$	7.2	0.2	$1.7 \cdot 10^{-1}$	$1.6 \cdot 10^{25}$
CUORICINO [Ald+18]	$^{130}\text{Te}$	11	0.3	$2.0 \pm 0.2 \cdot 10^{-1}$	$2.8 \cdot 10^{24}$
<b>Currently Running</b>					
GERDA [Ago+18; Zsi18]	$^{76}\text{Ge}$	25.3	0.13	$0.6_{-0.3}^{+0.4} \cdot 10^{-3}$	$9.0 \cdot 10^{25}$
MAJORANA [Alv+19]	$^{76}\text{Ge}$	27.3	0.12	$4.7 \pm 0.8 \cdot 10^{-3}$	$2.7 \cdot 10^{25}$
CUORE [Ald+18]	$^{130}\text{Te}$	206	0.3	$1.4 \pm 0.2 \cdot 10^{-2}$	$1.3 \cdot 10^{25}$
KamLAND-Zen [Gan+16]	$^{136}\text{Xe}$	345	11	$0.4 \cdot 10^{-3}$	$1.1 \cdot 10^{26}$
EXO-200 [Alb+18a]	$^{136}\text{Xe}$	74.7	2.9	$1.6 \pm 0.2 \cdot 10^{-3}$	$1.8 \cdot 10^{25}$
CUPID-0 [Azz+18]	$^{82}\text{Se}$	5.2	0.77	$3.6_{-1.4}^{+1.9} \cdot 10^{-3}$	$2.4 \cdot 10^{24}$
<b>Planned or Under Construction</b>					
SNO+ [OG18]	$^{130}\text{Te}$	$\approx 1000$	$\approx 15$	$\approx 1 \cdot 10^{-6}$	$1.9 \cdot 10^{26}$
CUPID [Gro19]	$^{100}\text{Mo}$	253	0.2	$\approx 1 \cdot 10^{-4}$	$\approx 1.5 \cdot 10^{27}$
LEGEND-200 [Abg+17]	$^{76}\text{Ge}$	$\approx 175$	$\approx 1.3$	$\approx 2 \cdot 10^{-4}$	$1 \cdot 10^{27}$
nEXO [Alb+18b]	$^{136}\text{Xe}$	3366	-	$\approx 3 \cdot 10^{-4}$	$9.2 \cdot 10^{27}$
Super-NEMO [Bar+17]	$^{82}\text{Se}$	100	$\approx 4$	-	$\approx 1 \cdot 10^{26}$

are massive particles, the effort to search for  $0\nu\beta\beta$ -decay has been intensified. Its detection could help to answer many questions surrounding the origin of neutrino masses and their fundamental properties. Running experiments already cover large parts of the degenerate mass ordering. Future ton-scale experiments might tackle the inverted mass ordering with novel ideas to reach lower backgrounds and larger detector masses. An overview of notable experiments mentioned can be found in Table 2.3. A further approach to search for  $0\nu\beta\beta$ -decay is the **C**admium-**Z**inc-**T**elluride **0**-neutrino **D**ouble-**B**eta **R**esearch **A**pparatus (COBRA)-experiment based on  $^{116}\text{Cd}$  and  $^{130}\text{Te}$ , which will be extensively covered in the next chapter

## 3 The COBRA Experiment

Cadmium-Zinc-Telluride (CdZnTe) is a direct band-gap semiconductor that is a very attractive material for the construction of ionizing-radiation detectors as it can achieve good energy resolution and a high detection efficiency. This is a result of its high atomic number and high density as well as large number of charge carriers generated in each interaction. Due to its large band gap operation at room temperature is possible. These properties make CdZnTe an interesting choice for a large range of applications from the use in hand-held spectrometers,  $\gamma$ -cameras for nuclear safety applications, dosimetry, national security or medical applications such as dental imaging or SPECT devices. It is also used in astrophysical sciences and high energy physics [SG01; Sch+01; Sor+09].

CdZnTe is of interest for double  $\beta$ -decay because all of its three constituting elements contain candidate isotopes for neutrinoless double  $\beta$ -decay ( $0\nu\beta\beta$ ). As explained in section 2.6. the most promising ones are  $^{116}\text{Cd}$  and  $^{130}\text{Te}$ . This makes it possible to construct a *source=detector* experiment using CdZnTe. This is the approach of the **C**admium-**Z**inc-**T**elluride **0**-neutrino **D**ouble-**B**eta **R**esearch **A**pparatus (COBRA). In this chapter, some of the practical consequences and challenges in working with CdZnTe as radiation detector will be introduced, the general idea of the COBRA experiment will be described and its key results will be summarized.

### 3.1 CdZnTe as Radiation Detector

The basic principle behind the operation of semiconductors as radiation detectors is simple. If radiation interacts with a semiconductor, charged primary or secondary particles ionize atoms along their track and electron-holes pairs are created. If voltage is applied across the detector they start to drift. Eventually, electrons and holes can be collected at the electrodes. Their number is proportional to the energy of incoming radiation. This basic process is the same for all semiconductors, but details vary with the choice of material.

### 3 The COBRA Experiment

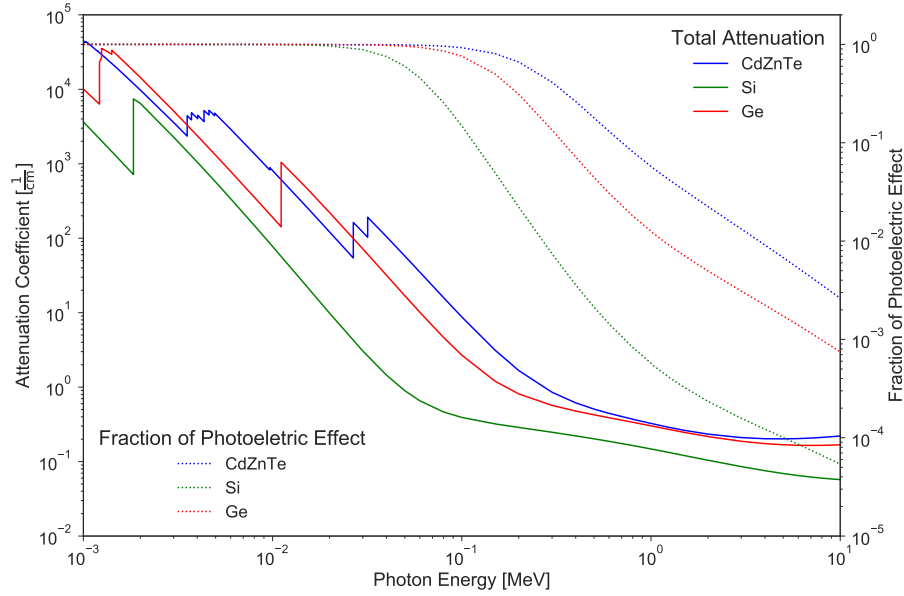


Figure 3.1: Attenuation coefficients for  $\gamma$ -rays for CdZnTe, Si and Ge. The dashed line shows the relative contribution of the photoelectric effect. Data taken from Ref. [Ber+].

In Figure 3.1 one can easily see the advantage of CdZnTe over other semiconductors like Ge and Si in detecting photons. Not only the total attenuation  $\mu$  is higher, but also the fraction induced by photoelectric effect, which rises as  $\mu_{PE} \propto Z^n$  where  $n$  is 4 to 5. The photoelectric effect is the most relevant for the identification of  $\gamma$ -lines.

Beside this fundamental property, detector size, detection efficiency, and energy resolution are also of great importance. An illustration of their effect on  $\gamma$ -spectra is given in Figure 3.2. Three spectra are shown, which were taken with a NaI scintillation detector, an HPGe detector and a CdZnTe detector together with a  $^{137}\text{Cs}$ -source. All spectra are normalized to the maximum of the peak. The NaI detector is large but has poor energy resolution. Its full-energy peak is thus very broad but the height of the Compton continuum is low compared to the peak. The HPGe detector has very good resolution. The resolution of the CdZnTe detector is right in the middle of the two, but the detector is rather small, so the Compton continuum is the highest compared to the peak. In summary, CdZnTe can not achieve the resolution of the HPGe detector, nor the detection efficiency of the NaI detector. But it still offers a good compromise in resolution, while being also very easy to handle and detection efficiency can be enlarged by using a detector array instead of single device.

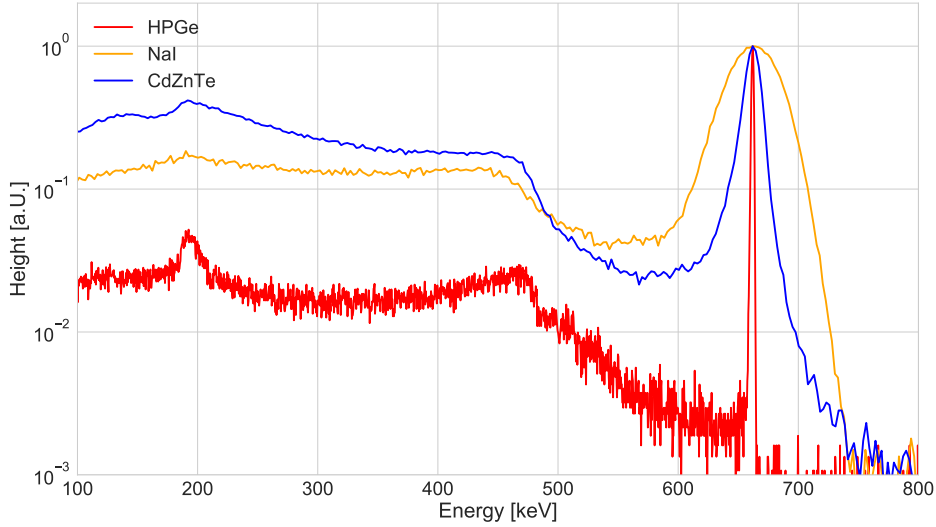


Figure 3.2: Spectrum of  $^{137}\text{Cs}$  taken with a NaI, a CdZnTe and a HPGe detector at TU Dortmund showing the different response of each detector type.

CdZnTe naturally contains a number of isotopes that are of interest from the point of view of nuclear and particle physics. An overview is given in Table 3.1. Beside double-beta isotopes,  $^{113}\text{Cd}$  is of interest as it undergoes a fourfold-forbidden non-unique  $\beta^-$ -decay. Its spectral shape is highly sensitive to the value of  $g_A$  (see subsection 2.6.2). At the current stage, COBRA uses all elements in their natural abundance. This makes COBRA an interesting experiment to search for the decay of  $^{116}\text{Cd}$ . It has the highest  $Q$ -value of all double-beta isotopes in CdZnTe and a reasonable natural abundance, allowing the construction of a *source=detector* experiment. Even though measuring double  $\beta$ -decays requires the detection of electrons instead of photons, the high density of CdZnTe yields a higher interaction probability also in this case. But, as has been pointed out, energy resolution and detection efficiency also need to be as high as possible.

To achieve this it is crucial to produce high-quality CdZnTe crystals, which is a topic of ongoing research. Some basic traits of CdZnTe important for this will be quickly reviewed. Its stoichiometric composition is usually given as  $\text{Cd}_{0.9}\text{Zn}_{0.1}\text{Te}$ . CdZnTe may be thought of as an alloy of CdTe with small amounts of ZnTe in a zincblende lattice. The exact fraction of Zn varies among manufacturers and crystals<sup>1</sup>. In general,

<sup>1</sup>A discussion of the Zn content of the COBRA detectors can be found in Appendix C.

### 3 The COBRA Experiment

Table 3.1: Unstable, naturally occurring isotopes in CdZnTe.  $Q$ -values taken from Ref. [Hua+17], natural abundances  $a$  from Ref. [BW11].

Isotope	Decay Modes	$Q$ -Value [keV]	$a$ in Cd <sub>0.9</sub> Zn <sub>0.1</sub> Te [%]
<sup>106</sup> Cd	$\beta^+\beta^+$ , $\beta^+/\text{EC}$ , EC/EC	$2775.4 \pm 1.6$	0.59
<sup>108</sup> Cd	EC/EC	$271.8 \pm 1.6$	0.41
<sup>113</sup> Cd	$\beta^-$	$323.8 \pm 0.3$	5.50
<sup>114</sup> Cd	$\beta^-\beta^-$	$544.8 \pm 0.3$	12.96
<sup>116</sup> Cd	$\beta^-\beta^-$	$2813.5 \pm 0.1$	3.37
<sup>64</sup> Zn	$\beta^+/\text{EC}$ , EC/EC	$1095.0 \pm 0.8$	2.41
<sup>70</sup> Zn	$\beta^-\beta^-$	$997.1 \pm 2.1$	0.03
<sup>120</sup> Te	$\beta^+/\text{EC}$ , EC/EC	$1730.8 \pm 3.0$	0.05
<sup>123</sup> Te	EC	$51.9 \pm 0.1$	0.45
<sup>128</sup> Te	$\beta^-\beta^-$	$866.6 \pm 0.9$	15.84
<sup>130</sup> Te	$\beta^-\beta^-$	$2527.51 \pm 0.01$	16.90

Table 3.2: Some of the most important physical properties of common semiconductors at room temperature. Ge and CdZnTe are used to search for double-beta decay. Si and HgI<sub>2</sub> are included as a examples for low- $Z$  and high- $Z$  semiconductors. Values compiled from Refs. [Sor+09; Dev+06].

	Si	Ge	CdZnTe	HgI <sub>2</sub>
Avg. atomic number $\bar{Z}$	14	32	58	62
Density [g/cm <sup>3</sup> ]	2.33	5.33	5.78	6.4
Band gap [eV]	1.12	0.67	1.57	2.13
Pair creation energy $\varepsilon$ [eV]	3.62	2.96	4.6	4.2
Fano factor $F$	0.06	0.06	0.10	0.12
Resistivity $\rho$ [ $\Omega$ cm]	$10^4$	50	$10^{10}$	$10^{13}$
Mobility-lifetime (electrons) $\mu_e\tau_e$ [cm <sup>2</sup> /V]	$\geq 1$	$\geq 1$	$10^{-3}$ to $10^{-2}$	$10^{-4}$
Mobility-lifetime (holes) $\mu_h\tau_h$ [cm <sup>2</sup> /V]	1	$\geq 1$	$10^{-5}$	$10^{-5}$

the addition of Zn results in a larger band gap which increases the resistivity  $\rho$  of the material and reduces the amount of defects. Furthermore, CdZnTe suffers much less from polarization effects present in pure CdTe and is thus better suited for large and long-term stable detectors. Some basic material properties are presented in Table 3.2 in comparison to other commonly used semiconductors. One can see some of the already mentioned advantages of the material. But the mobility-lifetime product  $\mu\tau$  in CdZnTe is lower than in other materials, an issue that will be discussed more deeply later.

Due to its high resistivity, CdZnTe is sometimes referred to as a semi-insulator. To achieve high resistivity the Fermi level has to be very close to the middle of the

band-gap. Impurities in CdZnTe cause a shift of the Fermi level, which needs to be compensated by dopants like In or Al [Sch+01]. Another consequence of the high resistivity is that only a small voltage  $V_{dep}$  suffices to deplete a CdZnTe detector. The depletion depth [Li+06] in a semiconductor is given by

$$W = \sqrt{2\epsilon_0\epsilon_r\rho\mu V_{dep}} \quad (3.1)$$

where  $\epsilon_0$  is the vacuum permittivity and  $\epsilon_r \approx 10.9$  the dielectric constant of the material. The mobility  $\mu$  is  $10^2 \text{ cm}^2 \text{ s/V}$  to  $10^3 \text{ cm}^2 \text{ s/V}$  depending on the type of charge carrier, and  $\rho$  is about  $10^{10} \Omega \text{ cm}$ . These values result in a voltage far below 1 V necessary to deplete a CdZnTe crystal with a thickness of 1 cm.

A challenge associated with CdZnTe is that it is currently not possible to grow crystals with the same size or quality as Ge or Si. This is mainly due to the ternary nature of CdZnTe and fundamental properties of its constituents. The largest detectors today [Che+18] have a volume of about  $24 \text{ cm}^3$ .  $6 \text{ cm}^3$  devices are readily available from commercial suppliers. A number of different growth techniques exist, the most important ones today are the high-pressure Bridgman method and the traveling heater method.

For the high-pressure Bridgman method, the individual elements are melted at temperatures above  $1100^\circ\text{C}$  and high pressure is applied to reduce vaporization. The method provides a high growth rate and it is possible to produce ingots with a mass of several kg. But the yield of large high-quality detectors is typically low [Sch+01]. For the traveling heater method, the temperature is much lower and crystals grow from a seed out of a tellurium-rich solution. The traveling heater method is able to consistently produce high quality crystals, but the growth rate is only a few mm/d. Usually these crystals are equipped with contacts made from Au or Pt to form functional detectors. Besides crystal growth, surface treatment also has a big influence on the final detector performance [Zhe+11].

More or less regardless of the growth method, the main problems of CdZnTe detectors are Te inclusions [Car+06] and spatially extended defects like grain boundaries. These problems produce non-uniform detector response [ALL02] and limit energy resolution. The problem of Te inclusions is hard to overcome: The melt of the crystal always tends to be enriched in Te during the growth process. This is because Cd is more volatile and evaporates at high temperatures and Te has a retrograde solubility [Awa+10].

Even though CdZnTe can be operated at room temperature, the performance of detectors is influenced by temperature. Optimal performance is often found at a

### 3 The COBRA Experiment

temperature slightly above 0 °C [Daw+09a]. Cooling detectors has been shown to lower leakage current as well as improving the electron mobility-lifetime product [Li+07]. This makes it necessary to control the temperature if stable long-term operation is desired.

The energy resolution  $\Delta E$  at a given energy  $E$  is an important criterion in the detection of ionizing radiation and can be understood as a combination of three different parts

$$\Delta E = \sqrt{\Delta E_{\text{stat}}^2 + \Delta E_{\text{el}}^2 + \Delta E_{\text{CCE}}^2}. \quad (3.2)$$

The first term reflects the statistical nature of charge carrier generation. It can be expressed as  $\Delta E_{\text{stat}}^2 = (2.355)^2 (F \cdot E / \varepsilon)$  with the Fano factor  $F$  [Fan47] as a measure of the correlation between created charge carries, and the pair creation energy  $\varepsilon$ . As this factor is rooted in the quantum mechanical nature of ionizing radiation,  $\Delta E_{\text{stat}}$  poses a lower limit on energy resolution. It is about 0.2 % full-width-at-half-maximum (FWHM) at 662 keV and 0.06 % at 2814 keV in CdZnTe, similar to other semiconductors and much better than for scintillators.

While  $\Delta E_{\text{el}}$  can in principle be very small, in conventional designs it is often at least of the same magnitude as  $\Delta E_{\text{stat}}$ . As it represents an energy independent contribution from electronic noise, it often limits energy resolution at low energies. The most important contribution at high energies is typically  $\Delta E_{\text{CCE}}$ , which refers to effects of charge collection efficiency. It includes variations in the number of created charge carriers due to inhomogeneities in the detector material, but also due to its bulk properties like charge carrier trapping, resulting in an effective loss of charge carriers. Taking all this into account energy resolutions at the level of few percent FWHM can be achieved.

CdZnTe suffers from a low charge carrier mobility  $\mu$  and lifetime  $\tau$ , although exact values differs among different detectors. While the mean drift length for electrons is in the cm-range, the drift length of holes is orders of magnitude smaller. This limits detector dimensions to the same level if no further measures are taken. Even below these ranges, some fraction of charge carrier will be lost due to trapping. Consequently, the ratio of holes to electrons differs depending on the path traveled. This means the signal height produced by radiation of given energy will depend on the position of an interaction relative to the electrodes.

Furthermore, the weaker effect of electron trapping will lead to another slight depth-dependence of the signal. If only a single type of charge carrier is considered, the effect of their finite mobility and lifetime on the produced signal can be analyzed by using

the Hecht equation [Hec32]

$$q = q_0 \frac{\mu\tau V}{d^2} (1 - \exp(-d^2/\mu\tau V)) \quad (3.3)$$

where  $q$  is the measured charge,  $q_0$  is the initially generated charge,  $V$  is the potential difference between cathode and anode and  $d$  is the distance the charge carriers have to travel. The measured charge starts noticeably to decline if  $d^2$  is comparable to  $\mu\tau V$ . Given the values in Table 3.2, an operational voltage of 1 000 V and  $d = 1$  cm,  $\approx 95\%$  of the initially generated electrons can be measured, but only 1% of the holes. Equation 3.3 also shows why CdZnTe need to be operated at much higher voltages than what is needed for depletion according to Equation 3.1. Simple planar electrode designs do not compensate for this effect. They can still be used if only X-rays are to be detected, as these only penetrate a few mm into the material. But they are not suited for large volume detectors needed to have a high detection efficiency for  $\gamma$ -rays or double-beta decay.

An overview of many of the currently used techniques to do so can be found in the literature [Zha+13; RS92] and only some of the most important ones will be shortly discussed here in the context of a low-background experiment. In principle, there are several ways to overcome the limitation imposed by hole trapping. But only single-polarity charge sensing achieved by using electronic circuits or special electrode designs turns out to be practical if high detection efficiency is desired. All other approaches rely on rejecting events that are severely affected by trapping instead of avoiding it.

The idea to employ single-polarity charge sensing was originally conceived in the context of gas-filled ionization chambers. They are similar to CdZnTe detectors, in that ions move much slower than electrons due to their higher mass. To overcome this, an additional grid – called Frisch-grid – is placed close to the anode. Before charge carriers pass this grid, charges are induced on this grid. As ions are repelled from the grid because of the potential difference, basically only electrons produce a signal on the actual anode.

The Shockley-Ramo theorem [Sho38; Ram39] is a helpful tool to understand the effect of electrode geometry more quantitatively. The theorem states that the charge  $q$  induced on an electrode by a moving point charge  $q_0$  is

$$q = -q_0 \cdot \phi_0(x) \quad (3.4)$$

with the so-called weighting-potential  $\phi_0(x)$ . Thus, knowing the number of charge carriers generated in an interaction, the induced charge  $q$  is completely determined

### 3 The COBRA Experiment

by  $\phi_0$ .  $\phi_0$  can be calculated by assuming unit potential on the electrode of interest and zero potential for all other electrodes and then calculating the electric field in this special case. The application to this theorem with regard to electrode design in semiconductors is discussed in detail in Ref. [He01]. The basic idea of all approaches is to create a region in the detector insensitive to the drift of holes, similar to what the Frisch-Grid achieves in ionization chambers.

A design very similar to the original Frisch-grid idea is the *virtual* Frisch-grid. This approach works by placing a conductive ring around the lateral sides of a crystal, close to the anodes. As this ring is only capacitively coupled, charge carriers induce a signal on it without being collected. This allows to separate the induced portion of the signal and with this the influence of the holes. With this approach, excellent energy resolution below 1% [Bol+16] is reported. Its best suited for detectors with one side much longer than the other two and needs some amount of inactive material close to the detector. This makes it not ideal for a low-background experiment.

Another common design for a large number of use cases are pixelated anodes [Zha+12; CM13; Bil+17]. With this design, an energy resolution of 0.5% to 1.0% can be achieved. Additionally it offers good spatial resolution. In fact, both properties are connected, as the spatial resolution allows to correct for material non-uniformity, which would otherwise limit resolution. Their operational principle is the so-called small pixel effect [Dot+94; Esk+95]. It occurs if the anode dimension is much smaller than the detector thickness. In this case,  $\phi_0$  only extends into a small fraction of the crystal, causing only charge carriers which are very close to the anode, and thus mainly electrons, to contribute. The best spectroscopic performance is achieved in general with this design. But it also has a number of drawbacks, such as the need for a large number of read-out channels with very low noise to actually achieve this performance. This is once again problematic in the context of low-background experiments.

Besides those two designs, there are a number of other techniques like the drift-strip detector [PBJ98; Kuv+10], or the strengthened electric field technique [Fu+15b]. Most of them are either optimized for niche applications or still in an experimental status and not further discussed here.

The approach taken by COBRA to overcome hole trapping is called the co-planar-grid (CPG). The CPG has the advantage of being a relatively simple design. In principle, only one additional signal has to be read-out compared to a planar geometry. It was first applied to CdZnTe detectors by in 1994 [Luk94]. The energy resolution was initially reported to be 5% FWHM at 662 keV. Today an energy resolution below 2% FWHM can be achieved with the CPG design [Amm+09a].

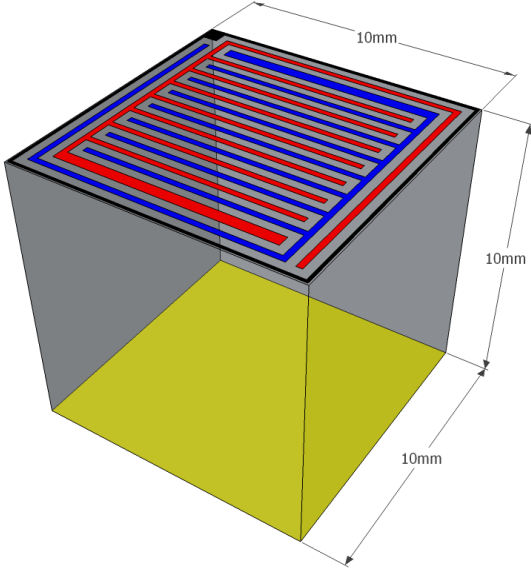


Figure 3.3: Schematic depiction of a CPG detector. The CPG itself is seen on the top in red and blue. The cathode is shown in yellow. Taken from Ref. [Fri+13].

The CPG makes use of two anodes, called the collecting anode (CA) and the non-collecting anode (NCA). The CA is usually on zero potential and the NCA on a slightly negative potential. This way, in the ideal case all charges are collected at the CA. The potential difference between the two anodes is called grid bias (GB), while the one between the cathode and the CA is called bulk voltage (BV). The two anodes are placed on the same face of the detector (hence the name co-planar) in an interlocked, comb-shaped pattern, which can be seen in Figure 3.3. Many detectors also feature an additional electrode surrounding the actual CPG, called guard-ring, which is usually not read-out but only used to create a homogeneous electrical field at the detector boundaries and hence improve energy resolution and detection efficiency.

$\phi_0(x)$  of a simplified CPG design can be seen in Figure 3.4. A charge moving along the x-direction homogeneously induces a fraction of the total charge during most of its drift. Only very close to the anode of interest, the contribution becomes much larger (when close to an anode) or smaller (between two anodes). The consequence of this is, that such a charge will induce the same amount on both the CA and NCA during most of its drift and only in the region close to the anodes a difference exists. At the end of the drift, all electrons move to the CA due to the potential difference between CA and NCA and holes move towards the cathode. As a consequence, if one takes the difference signal from the two anodes, the contribution from the central part containing the hole signal is the same and will cancel. Only the portion of the drift very close to the anodes, where  $\phi_0$  is different for CA and NCA, will contribute to the difference. This means, that with a CPG single-polarity charge-sensing can be achieved, as the

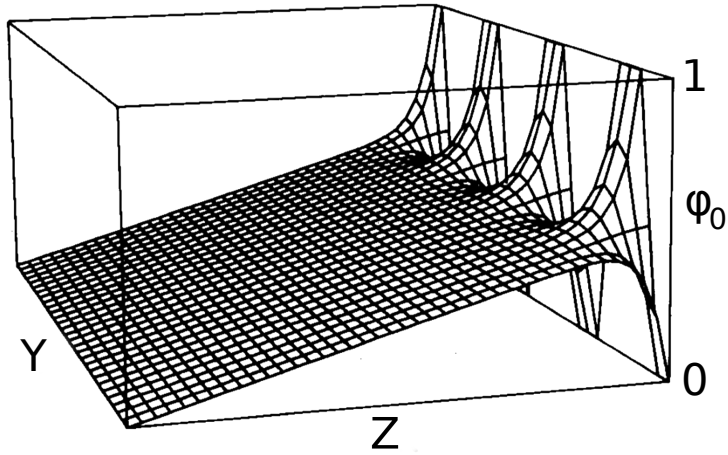


Figure 3.4: Weighting potential  $\phi_0$  for one of the anodes in a simple CPG design. Modified after Ref. [Luk94].

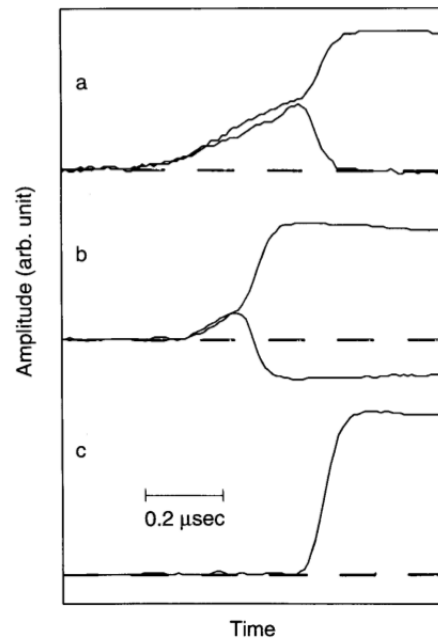


Figure 3.5: Examples of signal wave-forms on CA and NCA for different drift lengths (a,b) and the difference signal (c). The depth dependence of CA and NCA signal can clearly be seen, the difference signals looks approximately like a step function. Taken from Ref. [Luk95].

contribution from holes cancels out.

Figure 3.5 shows how the shapes of the CA and NCA signals differs depending on the starting position of the drift. In Figure 3.5(a) a long drift is seen, in (b) the charges start much closer to the anodes. The difference signal is seen in (c). Because the drift part is removed, the difference signal always looks similar independent of drift length.

Quantitatively, the energy  $E$  deposited in a CPG detector can be calculated as

$$E \propto A_{CA} - A_{NCA} = A_{\text{DIFF}}, \quad (3.5)$$

where  $A_{CA/NCA}$  is the pulse height measured on the respective anodes and  $A_{\text{DIFF}}$  their difference. The relative height of signals varies from a pure CA-signal if an interaction takes place close to the cathode and holes are immediately collected to opposite equal size if the interaction is close to the anodes. The second case is a special effect. While electrons drift to the CA as usual, holes drift towards the NCA instead of the cathode and so the CPG principle is no longer working as intended. The difference signal will be nearly doubled in amplitude, as twice as many charges are collected than one would expect purely from electrons. This so-called energy-doubling effect is mostly unwanted and can lead to reduced spectroscopic performance.

Another detrimental effect is that of electron trapping. In CPG detectors, it is possible to correct for this effect, as has already been pointed out in 1995 [Luk95]. This can be done by introducing a weighting factor  $0.5 < w < 1$  to Equation 3.5 so that

$$E \propto A_{CA} - wA_{NCA}, \quad (3.6)$$

which results in  $A_{NCA}$  being systematically under-weighted. This idea is called differential-gain method. A detailed discussion of the method is found in Ref. [Fri+13]. The reason for this is that near the anodes  $A_{NCA}$  takes on the largest values compared to signals originating far away from the anodes, which are most affected by trapping due to their long drift distance. By using  $w$  the detector response is homogenized. Signals not affected by trapping are artificially lowered and thus more equal to those affected. The use of  $w$  can improve the spectral response of a detector significantly, especially if  $\mu_e\tau_e$  is small.

One can also make use of the depth-dependence in CdZnTe by constructing a quantity that is independent of energy and is only sensitive to depth. Such a method<sup>2</sup> was first published by He *et al.* [He+96]. With this, a CPG detector gets spatial resolution in a single dimension. This can be used to study the performance of a detector<sup>3</sup> as function of depth and allows the removal of signals from regions with poor performance<sup>4</sup>. Such regions are typically found close to the anodes. In the case of COBRA, it is interesting

---

<sup>2</sup>A timing-based approach is given e.g. in Ref. [Fu+15a] but proved to be less accurate and more complex to implement [Teb16].

<sup>3</sup>Depth determination can also be used as an alternative approach for trapping correction. In Ref. [Arl16] both methods were shown to give similar results at least for COBRA style detectors.

<sup>4</sup>It is also useful for imaging applications [Hon+04].

### 3 The COBRA Experiment

to remove regions contributing to background above average (see section 3.3).

The method works as follows: The signal at the cathode  $A_{\text{CATH}}$  is a function of the interaction depth  $z_0$  and the energy  $E$ , i. e.  $A_{\text{CATH}} \propto z_0 \cdot E$ . The difference signal of the two anodes  $A_{\text{DIFF}}$  is constructed to only depend on the energy  $A_{\text{DIFF}} \propto E$ . The depth of an interaction  $z_0$  is then computed by taking the ratio  $\frac{A_{\text{CATH}}}{A_{\text{DIFF}}} \propto z_0$ . Charge conservation implies that the magnitude of  $A_{\text{CATH}}$  is equal to the magnitude of the sum of both anodes [Ger+06; Car+07]. Thus, the cathode signal does not need to be explicitly read-out for this method to work.  $z_0$  can be written as

$$z_0 = \frac{A_{\text{CATH}}}{A_{\text{DIFF}}} = \frac{A_{\text{CA}} + A_{\text{NCA}}}{A_{\text{CA}} - A_{\text{NCA}}} \quad (3.7)$$

and depends only on signals measured anyway to determine the energy of an event. By construction, the physically allowed depth-range is  $0 \leq z_0 \leq 1$  without taking resolution and higher order effects into account.

For a real detector, additional effects cause a deviation from the idealized behavior presented so far. If two interactions happen simultaneously the method will give their average interaction depth. In general, charge-carrier statistics, crystal non-uniformities and so on lead to a finite depth resolution in the order of mm. Furthermore, charge carrier trapping can cause events to fall outside of the depth-range given above. The effect of electron trapping can be compensated to first order. An analytical correction for Equation 3.7 was derived in Ref. [Fri+13]. In analogy to the trapping correction for energy determination, its effect is strongest close to the cathode, where the drift length is maximal.

The reasoning is closely related to that used to derive the differential-gain method. Both methods make use of the same weighting factor  $w$ . The trapping corrected interaction depth  $z_{tc}$  is given by

$$z_{tc} = \lambda \ln \left( 1 + \frac{1}{\lambda} \frac{A_{\text{CA}} + A_{\text{NCA}}}{A_{\text{CA}} - A_{\text{NCA}}} \right), \quad (3.8)$$

where  $\lambda$  is the mean trapping length.  $\lambda$  can be expressed as a function of  $w$

$$\lambda = \frac{1 + w}{1 - w}. \quad (3.9)$$

This correction is effective for shifting near-electrode events into the range  $0 \leq z_0 \leq 1$  and can thus make depth determination more accurate.

In summary, CdZnTe is an interesting option for a double-beta decay experiment.

It is made up of several isotopes of interest and shows favorable characteristics as a radiation detector. Problems with crystal growth and quality exist, limiting the size of available detectors, but both have become significantly better in recent years. With the right choice of read-out technique, high-resolution detectors with comparatively large volumes are possible .

The CPG approach is suitable for a low-background experiment. It allows to overcome hole trapping with a minimal amount of additional read-out channels, minimizing the need for inactive and potentially radioactive material close to the detectors and offers reasonably good energy resolution. The interaction depth method further presents a possibility to reduce background, by vetoing near-electrode events. Furthermore, the CPG is well understood and CdZnTe with this anode design can be bought off-shelf. This makes detector deployment easy. Together, these advantages motivate the use of CdZnTe for the COBRA experiment.

## 3.2 The COBRA Demonstrator Setup

The idea to use CdZnTe to search for  $0\nu\beta\beta$ -decay was proposed in 2001 [Zub01]. First results with an overground setup were quickly achieved [KMZ03] and soon after an underground setup followed [Blo+07]. Beside CPG detectors, different designs of pixelated detectors were investigated [Sch+11]. Ultimately,  $1\text{ cm}^3$  CPG detectors turned out to offer the best compromise between the different requirements. The most advanced version of COBRA using CPG detectors is the so-called *Demonstrator* setup. Its construction started in 2011 and was completed in 2013. It is described in detail in Ref. [Ebe+16d] and references therein. As the extended demonstrator (XDEM), is largely based on the Demonstrator, its most important features shall be explained here.

The COBRA Demonstrator is located at the Laboratori Nazionali del Gran Sasso (LNGS) underground laboratory [Bel88] in Italy in a small building formerly used by the Heidelberg-Moscow experiment. The LNGS is located under the Gran Sasso mountain range at an altitude of about 960 m above sea level and has an rock overburden equivalent to 3 800 m of water<sup>5</sup>. The muons flux at the LNGS has been determined to be  $(3.41 \pm 0.01) \cdot 10^{-4}/(\text{m}^2\text{ s})$  [Bel+12]. This corresponds to a reduction by about six orders of magnitude compared to the surface. In Figure 3.6, the muon flux of the LNGS is compared to other underground laboratories and the surface.

---

<sup>5</sup>As the laboratory is placed under a mountain the attenuation of the cosmic ray flux is less then for a site of equal depth under a flat overburden. The corresponding depth under a flat overburden is calculated to be about 3 100 m of water equivalent [MH06].

### 3 The COBRA Experiment

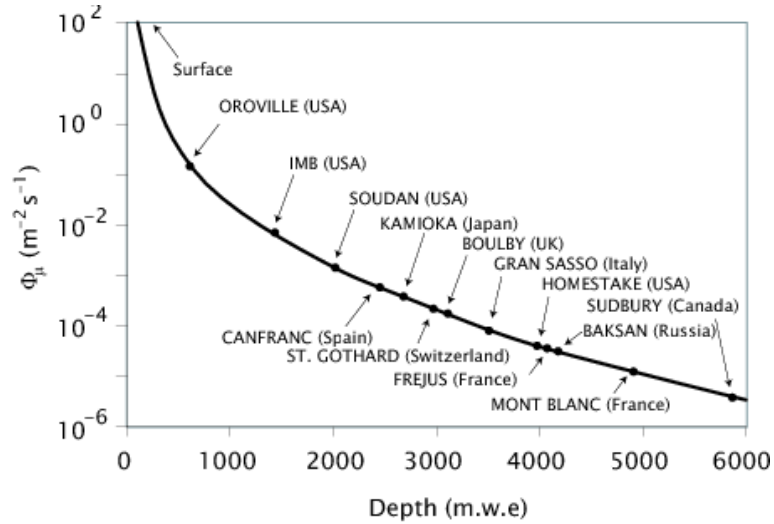


Figure 3.6: Overview of muon flux at different underground laboratories around the world as a function of their depth and the flux at the surface of Earth for comparison. The LNGS is labeled as *Gran Sasso*. Taken from Ref. [Car+04].

At the depth of the LNGS, the hadronic component of cosmic rays is completely stopped and neutrons are mostly produced by  $(\alpha, n)$ -reactions in the surrounding rock [Heu95]. The flux of thermal neutrons is  $(3.06 \pm 0.02) \cdot 10^{-6}/(\text{cm}^2 \text{ s})$ . As  $^{113}\text{Cd}$  has a very large cross-section of about 20 000 b [Wis+02] for the interaction with thermal neutrons, they present an important concern in term of background. The flux of fast neutrons is  $(0.23 \pm 0.07) \cdot 10^{-6}/(\text{cm}^2 \text{ s})$  [Bel+89]. The flux of  $\gamma$ -rays is in the range of  $0.2/(\text{m}^2 \text{ s})$  to  $0.3/(\text{m}^2 \text{ s})$  [Haf+11], mainly caused by the decay chains of  $^{238}\text{U}$ ,  $^{235}\text{U}$  and  $^{232}\text{Th}$  or the decay of  $^{40}\text{K}$ . These decay chains also produce Radon. Its activity inside the COBRA building is about  $80 \text{ Bq}/\text{m}^3$ .

To shield the experiment from these background sources, a multi-layer shielding is employed for COBRA. The first part consists of 7 cm thick polyethylen (PE) loaded with 2.7% by weight of boron. PE is a good moderator for neutrons as it has a high hydrogen content, while  $^{10}\text{B}$  has a high cross section of about 3 840 b to capture thermal neutrons. As neutrons can not only hit a detector directly, but also interact with surrounding materials and produce secondary radiation, this part of the shielding is the outermost. Directly below this, 2 mm thick steel-sheets are placed as an electromagnetic interference (EMI) shield to reduce electronic noise. The remaining parts only shield the detectors: A gas-tight enclosure made up of metal and polymethylmethacrylat (PMMA) to keep Radon from the vicinity of the detectors. 15 cm of standard lead, 5 cm of low-activity lead and finally 5 cm of electro-formed copper are used to attenuate  $\gamma$ -rays

by at least four orders of magnitude at all relevant energies. The mix of lead and copper is chosen for two reasons: On the one hand, lead shields radiation effectively. But, as it can have high contents of uranium, thorium and especially  $^{210}\text{Pb}$ , it is a source of radiation itself. The activity of  $^{210}\text{Pb}$  is below 3 Bq/kg for the low-activity lead, but even this would be too high close to the detectors. Copper, on the other hand, is less effective for shielding purposes and may easily be activated by cosmic rays. But it can be produced with minimal impurities through electro-forming. It can thus be used to shield to residual activity from the lead. The total mass of this inner shielding is about 2.5 ton. The whole shielding is constantly flushed with  $\text{N}_2$  evaporated from a Dewar containing  $\text{LN}_2$  with the help of an ohmic heater and purified by a charcoal filter to keep Radon away from the detectors [WZ05].

Another important aspect is the contamination with radio-isotopes of the materials surrounding the detectors. This requires careful selection prior to installation. The detectors are placed in holder structures made up of polyoxymethylene (POM), which is in general low in impurities. Thin polyimide-based flexible printed circuit boards (PCBs) – known to be very clean [Ceb+15] – are used to carry the signal traces. Specially designed coaxial cables are used for the supply of high-voltage. Mechanical and electrical connection between detectors, PCBs and cables is achieved with two different products, silver based LS 200 lacquer by FERRO GMBH with high conductivity and conventional glue, such as UHU HART, for good mechanical strength.

The detectors themselves have a size of  $1 \times 1 \times 1 \text{ cm}^3$ , a mass of about 5.9 g and were produced by EV PRODUCTS. They are placed in four layers consisting of  $4 \times 4$  detectors each. In sum, 64 detectors with a total mass of about 378 g are installed. To prevent degradation of the detector performance by exposure to moisture and oxygen the detectors are coated with a clear lacquer called GLYPTAL which also protects them mechanically.

The signals from the detectors are fed into pre-amplifiers which serve multiple purposes. First, the currents coming from the detectors are converted to proportional voltage signals using CREMAT CR-110 REV. 2 charge-sensitive amplifiers [Inca]. These devices are quoted to have a constant equivalent noise charge (ENC) of about 200 electrons RMS or 2.4 keV for a typical CdZnTe detector. Additionally, the ENC has a slope of about 4 electrons RMS/pF of capacitance connected to the input. This is why it is important to keep the input capacitance as low as possible. They also have a short rise time of about 7 ns and are thus well suited for semiconductor detectors. The signals are then converted into a pair of differential signals for robust transmission over commercial Cat.6 Ethernet cables for further processing in another part of the

### 3 The COBRA Experiment

COBRA building. The pre-amplifiers are also used to couple GB to NCA channels and filter both GB and BV to reduce noise. Moreover, it is possible to inject test charges into the pre-amplifiers.

The signals from the pre-amplifiers are further amplified and converted back to single-ended signals by linear amplifiers. These have a configurable gain between 0.5 to 89, usually operated at 11. The signals are then digitized by STRUCK SIS 3300 flash-analog-digital-converters (FADCs) [Sys]. They allow to sample the signal with a frequency of 100 MHz and a digital resolution of 12 bit. The duration of the digitized signals is 10.24  $\mu$ s. The FADCs have a two-bank system allowing for dead-time free read-out. They were adapted to better match the input from the linear amplifiers by the electrical workshop at TU Dortmund. In Ref. [Ebe+16d] it was estimated that the read-out electronics described here cause an energy resolution of at least 0.3% FWHM.

An overview of the complete signal flow and the auxiliary infrastructure is given in Figure 3.7. The voltages needed to operate the detectors are supplied by several devices from ISEG, while the low-voltage for the pre-amplifiers is delivered by a WIENER MPOD supply. The linear amplifiers are housed in two NIM crates with a third one usually reserved for auxiliary electronics like a BERKLEY NUCLEONICS PB-5 precision pulse generator, while the FADCs are housed in VME crates. The pre-amplifiers are furthermore cooled by a JULABO FL 601 cooling unit, as they produced considerable waste heat. This device keeps them at a temperature below 20°C in normal operation. With this unit the detectors are also cooled to some extent, which benefits their performance.

The digitization of the complete signal pulse of both CA and NCA from the detectors has several advantages. For once, it is possible to apply advanced digital filter techniques to optimize energy resolution. Off-line pulse processing allows to vary parameters like gain or weighting factor  $w$  of each detector at any time after the data is stored. Digitization is also useful for pulse-shape analysis (PSA) to differentiate between signal and background pulses. In the context of COBRA PSA, based cuts were developed to reduce the rate of events caused by interactions near the lateral-side walls of the detectors as well as multiple interactions within a detector. In addition, unphysical events caused by electrical interference or malfunctions of the electronics can be identified in this way. Details about how this technique is employed in COBRA can be found in Refs. [Fri+14; Zat14; Zat16].

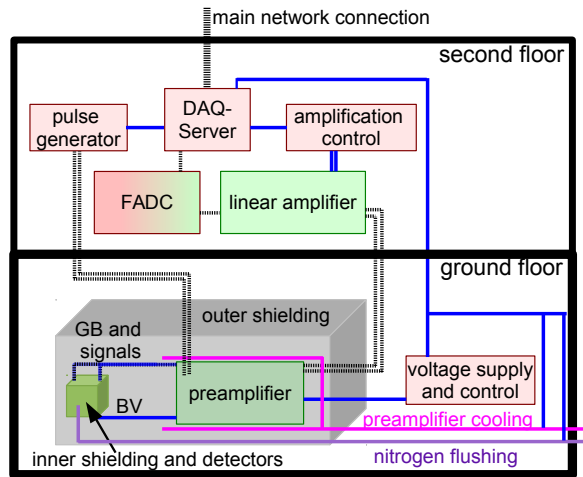


Figure 3.7: Schematic of the COBRA infrastructure at the LNGS showing the different components described in the text. Taken from Ref. [Ebe+16d].

### 3.3 Physics with the COBRA Demonstrator

Its granularity, good shielding, the low activity of the construction materials and the use of cuts allow the COBRA Demonstrator to reach a low background and perform several interesting measurements. The status of the Demonstrator in 2015, the beginning of this thesis, will be presented to establish a baseline for the XDEM upgrade.

As no other low-background experiments using CdZnTe detectors exists one of the primary goals of the Demonstrator was to show that stable data-taking over several years is possible using this technology. The stability of the setup was investigated with the help of variations in rate of the decay of  $^{113}\text{Cd}$  over two years in Ref. [Ebe+16b]. Even though the rate for a few detectors was found to change by more than 10% per year, the overall rate for all 48 detectors considered in this analysis changed only by a factor of  $0.995 \pm 0.004$ . It was thus deemed negligible for a  $0\nu\beta\beta$ -experiment where other uncertainties are usually much larger.

Another important goal was to show that a low-background can be achieved. This is evidently shown by fact, that the rare decay of  $^{113}\text{Cd}$  ( $t_{1/2} \approx 8 \cdot 10^{15}$  yr) makes up about 98% of all recorded events. Besides this decay, only few features are recognizable in the background spectrum<sup>6</sup>, namely the 511 keV annihilation peak, a  $\gamma$ -line at 1275 keV associated with  $^{22}\text{Na}$  and a  $\gamma$ -line at 1461 keV from the decay of  $^{40}\text{K}$ . Furthermore, two broad  $\alpha$ -peaks originating from the decay of  $^{190}\text{Pt}$  with  $t_{1/2} \approx 5 \cdot 10^{11}$  yr and a

<sup>6</sup>If data-taking periods in which the  $\text{N}_2$  flushing failed are also taken into account, two additional lines at 352 keV and 609 keV – belonging to the  $^{222}\text{Rn}$  progenies  $^{214}\text{Pb}$  and  $^{214}\text{Bi}$  – can be detected.

### 3 The COBRA Experiment

Table 3.3: Background indices and half-life limits for various isotopes obtained with 234.7 kg d of data [Ebe+16c] taken with the COBRA Demonstrator.

Isotope	Background [cts/kg/keV/yr]	$T_{1/2} \geq [10^{21} \text{ yr}]$
$^{114}\text{Cd}$	213.9	1.6
$^{128}\text{Te}$	65.5	1.9
$^{70}\text{Zn}$	45.1	$6.8 \cdot 10^{-3}$
$^{130}\text{Te}$	3.6	6.1
$^{116}\text{Cd}$	2.7	1.1

$Q$ -value of  $(3\,268.6 \pm 0.6)$  keV [Bra+17], and of  $^{210}\text{Po}$  with a  $Q$ -value of 5 407.5 keV can be identified.

These  $\alpha$ -peaks are tightly clustered around interaction depths corresponding to the electrodes. Platinum is part of the electrodes and  $^{190}\text{Pt}$  has an abundance of about 0.1 % in natural platinum. The contamination with  $^{210}\text{Po}$  likely results from the plate-out of  $^{222}\text{Rn}$  and its daughter isotopes, especially at the cathode, which is at a high negative potential attracting positively ions. After applying an interaction-depth cut, most remaining events originate from  $\alpha$ - and  $\beta$ -decays at or very near to the lateral detector surface. These particles lose a part of their energy in the coating and a small dead layer on top of the detector before being measured. This assumption is supported by the absence of clear peaks in the energy spectrum and no single origin in terms of interaction depth. At the same time, PSA based cuts which are designed to remove such events are highly effective in reducing the remaining background in this region.

Concerning the search for  $0\nu\beta\beta$ -decay, an analysis was performed based on an exposure of 234.7 kg d acquired between September 2011 and February 2015 with up to 61 detectors [Ebe+16c]. The results of this analysis are summed up in Table 3.3. The strongest limit was obtained for  $^{130}\text{Te}$  due to its high abundance, while the lowest background was achieved for  $^{116}\text{Cd}$ . This analysis presented the most sensitive search for the decay  $^{114}\text{Cd}$  of any counting experiment so far.

These results show that the mentioned goals of the Demonstrator setup could be reached, operating for several years with backgrounds at the level of only few cts/kg/keV/yr. The available exposure has more than doubled since the last analysis in Ref. [Ebe+16c]. Work is ongoing to develop new and improved cuts to produce a more sensitive search for  $0\nu\beta\beta$ -decay with this larger data-set. Also the possibility to search for other more exotic decay modes is investigated [Vol18]. Nevertheless, it is clear that the existing setup is too small to produce limits comparable to state-of-the-art experiments mentioned in section 2.6. Also, an even lower background is needed to be

### *3.3 Physics with the COBRA Demonstrator*

competitive in the field of double  $\beta$ -decay. Lowering the background while increasing detection efficiency and keeping other important parameters at least at the same level is the goal of the XDEM setup described in the coming chapters.



## 4 The COBRA XDEM Upgrade and Improvements to the Demonstrator

During the course of this work the experimental setup of COBRA at the Laboratori Nazionali del Gran Sasso (LNGS) has been modified in many ways. The largest part of this concerned the extended demonstrator (XDEM) upgrade. This made it necessary to enlarge nearly every aspect of the existing infrastructure beginning with the shielding, over low- and high-voltage distribution, and read-out electronics. But most importantly additional detectors were installed. Besides, the original demonstrator setup has been modified in preparation for a special run with trigger-thresholds as low as possible. Furthermore, major maintenance concerning the  $N_2$ -flushing had to be carried out and the system was substantially changed. In all of this lay some major challenges:

1. On-site work at the LNGS was limited to some weeks per year, thus all work needed to be prepared as much as possible beforehand in the COBRA home institutes.
2. Any changes are constrained by the limited space available in the underground laboratory.
3. All works should disturb the existing experiment as little as possible to not lose precious time for data-taking.
4. As COBRA is a low-background experiment, great care had to be taken not to contaminate any part of the setup. These efforts were somewhat limited by the lack of access to clean-room facilities in the COBRA building.
5. All materials used in the vicinity of the detectors had to be selected to be as free as possible of radioactive contamination (see Appendix A).

## 4.1 Changes to the Demonstrator Setup and General Infrastructure

For several years, there had been numerous issues with the N<sub>2</sub>-flushing system described in Ref. [Ale07]. These resulted in sudden increases of humidity as seen in Figure 4.1. As their cause initially was unclear, most parts of the system have been exchanged. The Dewar containing the liquid N<sub>2</sub> was exchanged in February 2016. This was necessary, as it lost its vacuum insulation and nitrogen was boiling off much too quickly. The failure became noticeable in 2014 already, but was for some time mitigated by switching to a shorter fill-cycle. In 2015 the situation became worse, leading to a large fraction of time without proper N<sub>2</sub>-flushing.

Unfortunately, the repeated cooling and warming up of the Dewar and all parts nearby caused leaks in the piping. New hoses and new electrical wires with lower resistance to power the heater were installed in June 2016. This led to a stable behavior for several months, in which a new instrumentation was produced in the mechanical workshop at TU Dortmund. This was installed in December 2017, but the pipe used to fill liquid N<sub>2</sub> into the Dewar burst upon the first filling. After another replacement had been produced the humidity inside the setup has been acceptable. No more modifications have been done, even though no fill-level read-out and no redundant heating is currently available.

Another set of changes concerned the power infrastructure. The heater used to evaporate the liquid N<sub>2</sub>, initially powered by the same device as the pre-amplifiers, is now powered by its own RIGOL DP711 power supply. This was done to eliminate any electrical connection between the pre-amplifiers and the outside of the setup and to deliver more power to the heater. Furthermore, the number of uninterruptible power supplies has been raised to accommodate the additional electronics needed for the XDEM as described in the next section and so far unprotected devices.

To allow for easier synchronization of data taken with the different flash-analog-digital-converters (FADCs) a common 100 MHz clock was installed. To synchronize the FADCs artificially injected pulses are being used, as described e. g. in Ref. [Tim15]. Even though a high number of pulses is injected, the FADCs show some clock-drift between injections, limiting synchronization accuracy to a few milliseconds. To improve this, a STRUCK SIS3820 CLOCK-DISTRIBUTOR, was installed in March 2018. Even though the device could be successfully integrated into the FADC infrastructure, it did not solve the synchronization issue. It appears to be caused by the data acquisition (DAQ) software and could so far not be solved.

## 4.1 Changes to the Demonstrator Setup and General Infrastructure

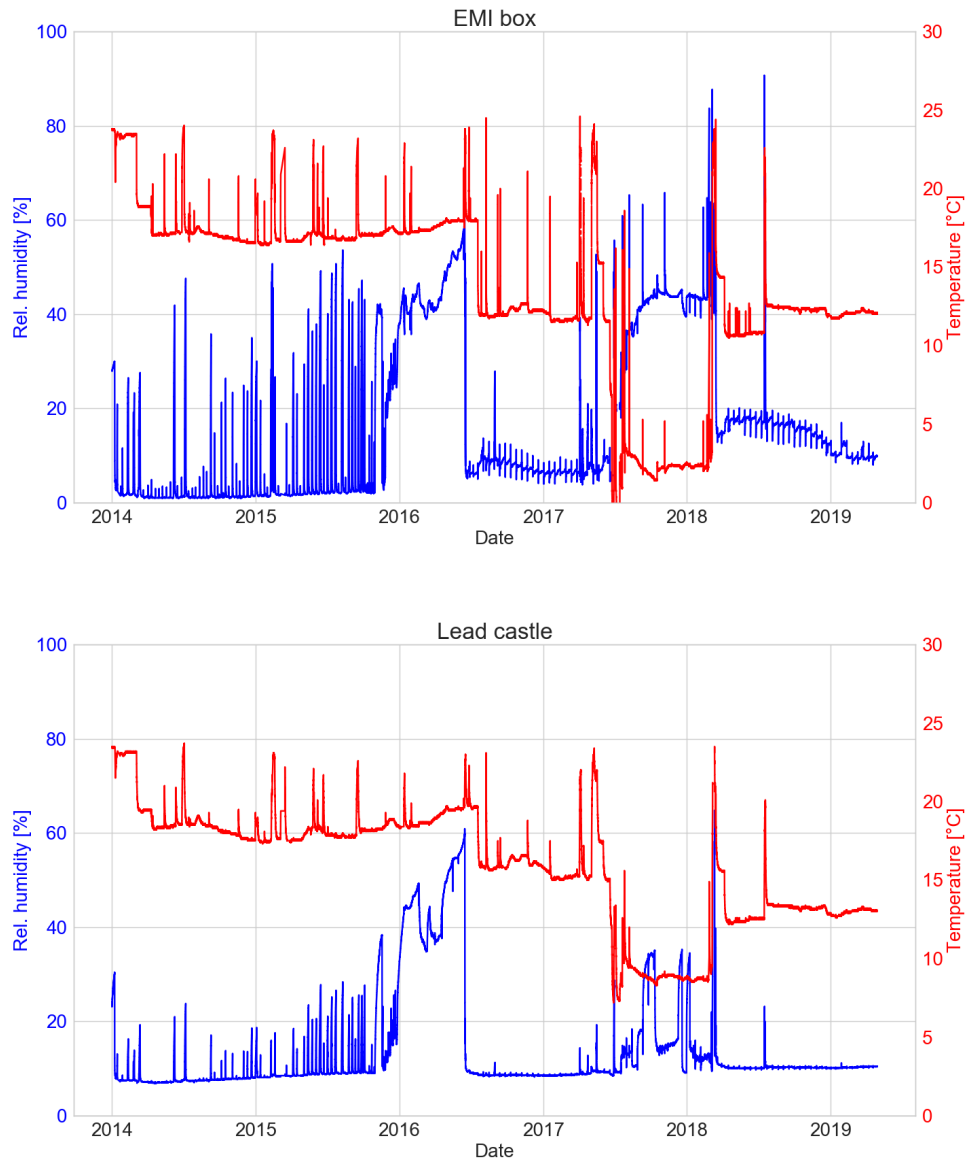


Figure 4.1: Temperature and humidity inside the LNGS setup measured at two different locations, corresponding loosely to the pre-amplifiers (EMI box) and the detectors (Lead castle) over a time of more than five years. In general, the temperature is lower at the EMI box location, as this is where the cooling plates are placed and humidity is lower near the lead castle, as it is enclosed by the gas-tight enclosure. The bi-weekly fill cycle of the dewar can be seen clearly as spikes in the humidity in the upper panel.

Another important change to the setup was made as a preparation for a special run with low trigger thresholds. The final goal for this was an in-depth investigation of the shape of the  $\beta$ -spectrum of  $^{113}\text{Cd}$ . The shape of this fourfold-forbidden decay is highly sensitive to  $g_A^{\text{eff}}$ , presenting a possibility to study  $g_A^{\text{eff}}$  in a Cadmium isotope. Based on calculations of the shape in Ref. [HKS17], it turned out that a lot of the discrimination power for different values of  $g_A^{\text{eff}}$  lays in the low energy region, motivating the use of low trigger-thresholds.

There were several investigations of the decay  $^{113}\text{Cd}$  in the past, with the aim of measuring the half-life and the  $Q$ -value of the decay. A recent measurement of  $^{113}\text{Cd}$  spectral shape can be found in Ref. [Bel+07], where a  $\text{CdWO}_4$  scintillator with a mass of about 0.4 kg and poor energy resolution was used. The decay was also investigated by COBRA with only eleven detectors [Daw+09a] which had a better resolution, but used thresholds between 100 keV and 150 keV. Consequently, the aim of the new study was to make use of the larger number of detectors with good resolution operated at thresholds as low as possible.

To reach these low thresholds, the idea was to reduce the temperature of the pre-amplifiers and the detectors, switch off detectors affected most by noise and eliminate or isolate noise sources. Prior to this, the temperature near the amplifiers was slightly below  $20^\circ\text{C}$ . The colling device is situated outside of the COBRA building a few meters away from the pre-amplifiers. As the colling liquid and the pre-amplifiers are not perfectly isolated, the bath temperature at the device has to be much lower than the temperature that can be reached near the amplifiers. As the bath temperature was already only at some  $^\circ\text{C}$  above zero, a further reduction was not possible using pure water as colling liquid. Consequently, it was exchanged for the ethylene glycol based cooling liquid JULABO THERMAL G in April 2017. This allowed to reach bath temperatures down to  $-20^\circ\text{C}$ . After the exchange temperatures around  $3^\circ\text{C}$  in the EMI-box and around  $9^\circ\text{C}$  near the detectors were reached. Lower temperatures were not used for a prolonged duration to avoid condensation, as seen in Figure 4.1.

The power distribution for the pre-amplifiers was also modified, with individual channels supplying layer 1 and 2 individually and layer 3 and 4 together. This reduced the number of possible pathways for noise to spread across several pre-amplifiers. Furthermore, a  $^{152}\text{Eu}$ -source was purchased to have additional  $\gamma$ -lines close to the trigger thresholds for calibration.

After these changes were implemented, the average threshold that could be reached was 83.9 keV. Some detectors could even be operated with thresholds below 70 keV. This can be compared to thresholds around 200 keV before. The analysis of the data

has been carried out by other members of the collaboration, results are summarized in Ref. [BD+18]. They indicate serious quenching in the analyzed models for this decay, for example  $q^{ISM} = 0.720 \pm 0.017$ .

## 4.2 The COBRA Extended Demonstrator

After the Demonstrator Setup described in the previous chapter was completed and the results from this phase showed the general feasibility to construct a low-background experiment with CdZnTe detectors, the experiments next stage was planned. The two goals of this next phase, coined XDEM, were to show that a further reduction in background is possible<sup>1</sup> and that the approach can be scaled up to a larger array. Thus, the basic idea was to design a new detector array which would also be the atomic building block of a large scale COBRA experiment. In this section, new detectors used for the XDEM project will be described, the necessary read-out electronics and high-voltage distribution will be explained and modifications to the shielding and general infrastructure are outlined.

### 4.2.1 Larger Detectors

A key element to reach both goals is to use larger detectors than in the Demonstrator phase. A larger detector of similar geometry will have a beneficial surface-to-volume ratio, reducing the influence of surface contamination, the main background in the Demonstrator phase. Also, fewer auxiliary components like cables and holders are needed per unit detector mass, reducing possible background sources. This ties in with the goal of scaling the experiment up at a later stage, because larger individual detectors make it easier to instrument a given total detector mass. Further beneficial is the improved intrinsic efficiency to detect double  $\beta$ -decays, as well as potentially improved efficiency for fiducial volume cuts, important to maximize the sensitivity of the experiment, as seen from Equation 2.15.

The state-of-the art for CdZnTe detectors in terms of volume at the time of planning was about  $6 \text{ cm}^3$ , a sixfold increase compared to the Demonstrator phase. Such detectors had already been investigated with a CPG anode design by other academical groups [Bol+11], showing excellent performance with pixelated anodes [Zha+12], and were used in commercial  $\gamma$ -ray imaging systems like POLARIS [Mic; Incb]. Because of

---

<sup>1</sup>The goal stated initially was to prove that a background index of  $1 \cdot 10^{-3} \text{ cts/kg/keV/yr}$  can be reached, although considering the size of the planned new detector array, it is practically not possible to demonstrate such a low background due to statistical considerations.

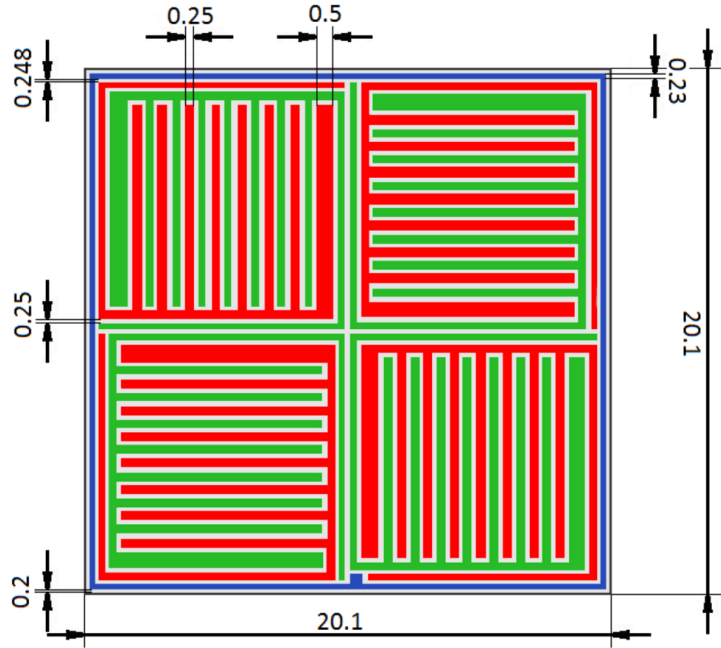


Figure 4.2: Schematic of the CPqG anode grid with dimensions in mm. The guard ring is shown in blue and the two sets of anodes in green and red respectively, while uncovered areas are shown in white. Taken from Ref. [Arl16]

this,  $6 \text{ cm}^3$  CdZnTe detector seemed like a good choice for the XDEM. Nine of such detectors with exact dimensions of  $20 \times 20 \times 15 \text{ mm}^3$  can fit into a detector holder with the same side length as a  $16 \times 1 \text{ cm}^3$  detector layer of the Demonstrator while having nearly the same total mass as the complete 64 detector array. Consequently, a  $3 \times 3$ -layer of  $6 \text{ cm}^3$  detectors was foreseen for the XDEM.

An important question was how to scale up the anode structure of the detectors. One option is to simply enlarge the CPG to fit the face of a larger crystal, as has been done e. g. in Ref. [Bol+11]. This option will henceforth be called *single-grid*. There are some disadvantages to this approach, namely that the leakage currents and the electrical capacitance will scale up by the same factor as the grid itself and thus degrade performance. The other option is to leave the CPG at approximately  $1 \text{ cm}^2$  in area and instead employ four individual CPGs, called sectors or sub-grids, to cover the whole face, from hereon called *co-planar-quad-grid (CPqG)*. This approach has been used by some groups already [HSR05; Stu07; Ma+14]. A schematic of the CPqG can be seen in Figure 4.2. In Figure 4.3 detectors with these two different designs and a volume of  $6 \text{ cm}^3$  each are shown alongside an  $1 \text{ cm}^3$  detector as used for the Demonstrator.

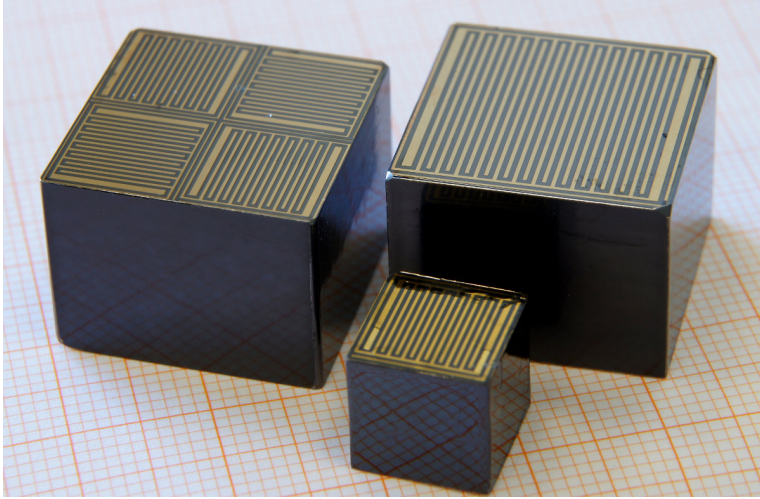


Figure 4.3: Three different types of CdZnTe detectors as used in COBRA [Geh17]. The small detector is similar to the Demonstrator type detectors. On the top-left a large CPqG detector as used in the XDEM can be seen. The large single-grid type on the upper right was investigated, but not used in the low-background setup.

Beside not having the drawbacks of the single-grid, the CPqG allows for an individual calibration in each sector, mitigating negative effects of crystal inhomogeneities like a very simple pixelated detector. Furthermore, it allows to veto interactions taking place in more than one sector. The main drawback is that a four times higher number of read-out channels per detector is needed. This is in contrast to the original motivation of using larger detectors. Another concern was that the use of multiple grids on a single crystal could lead to unwanted effects such as charge-sharing between grids.

Eventually, as it was not obvious which of these two approaches is better suited for the XDEM, a number of studies had been conducted within the COBRA collaboration to determine the best solution. A total of eight test detectors were purchased from two manufacturers, REDLEN and EV PRODUCTS/KROMEK, using different anode designs. The spectroscopic performance and current-voltage (I-V) characteristics of the first four detectors from 2014 was initially investigated in Refs. [Arl14; The14]. These early results showed that the energy resolution of the single-grid approach was up to 8%. On the other hand, challenges anticipated with the quad-grid approach turned out to be solvable: Two CPqG detectors from this batch were irradiated with a highly collimated  $\gamma$ -source [Roh16], as a means to examine the issue of charge-sharing. Based on these results, in Ref. [Tem17] it has been concluded that the count-rate at the border between two sectors deviates not more than 5% from the mean count-rate. Deviations

in the reconstructed energy were found to be small compared to usual resolution-effects. The same issue was also tackled with another approach [Tem15] by comparing results from measurements to Monte Carlo (MC) simulations for energy deposition in a single (sub-)grid as well as multiple (sub-)grids of the CPqG. No signs for charge-sharing were found this way. The results for one CPqG detector were summarized in Ref. [Ebe+16a].

The conclusion of these investigations was, that with the single-grid approach it seemed not possible to produce detectors with sufficient energy resolution for COBRA. On the other hand, a single-grid detector that produced no usable spectrum at all could be successfully reworked<sup>2</sup> into a quad-grid detector, which produced a spectrum with a resolution of about 4% FWHM. On the other hand, no indications for charge-sharing across multiple grids was found at a level which would diminish considerably the full-energy detection efficiency. But it also became clear, that standard algorithms to calculate the interaction depth in CPG detectors do not work in CPqGs, an issue that could eventually be resolved and will be dealt with in section 5.1 of this work. Based on all these results, it was decided that CPqG detectors would be used for the XDEM.

The detectors tested in 2014 did not feature a guard-ring similar to the small detectors. With the CPqG design, it is possible to have a homogeneous electrical potential at the detector boundaries even without a guard-ring because of the rotated grids seen in Figure 4.2. A guard-ring was then re-introduced in the REDLEN detectors purchased in 2015, as it was realized that it could be used to reach a very significant background reduction. This idea was not actually new<sup>3</sup>, but the focus of the research within the COBRA collaboration had primarily been on making pulse-shape analysis (PSA) fruitful. But while re-examining results obtained with a pixelated detector in Ref. [Koe12], it was realized that the potential for background suppression using the guard-ring could actually be larger than possible with PSA. This was demonstrated using a 1 cm<sup>3</sup> in Ref. [Teb16] and using a 6 cm<sup>3</sup> CPqG detector in Ref. [Arl16]. The results are summarized in Ref. [Arl+17]. A suppression factor of 5300 for  $\alpha$ -particles directed at a lateral side of the detector was reported, with an efficiency loss of only about 15%. Both results are significantly better than what could be achieved with PSA. The suppression of external  $\beta$ -radiation should similarly also be possible if the guard-ring signal is recorded, but results obtained in Ref. [BD18] were not completely conclusive.

Finally, a total of ten detectors were purchased for the XDEM, five from EV PROD-

---

<sup>2</sup>There also has been work by another group on a so called virtual CPG [Esp+17], where one is able to modify anode geometry without the need for a mechanical rework and recent results showed the superior performance of a virtual CPqG over a virtual CPG on the same crystal.

<sup>3</sup>See e.g. test measurements in Ref. [Tem13], but more importantly Ref. [Teb16]. A similar idea might now also be adopted by other experiments [Ban+19]

## 4.2 The COBRA Extended Demonstrator

UCTS and five from REDLEN, with their properties summarized in Table 4.1. The two main differences between detectors from the two manufacturers are the type of coating and the electrode metalization. For the metalization, REDLEN uses a process where only gold is needed, while the electrodes of EV detectors also contain platinum. As already successfully used for the Demonstrator, *Glyptal* is used as coating varnish for EV detectors. REDLEN offered no similar low-background coating solution. Thus, these detectors were coated in Dortmund with an epoxy called 20-3001 by EPOXIES, ETC. [Epo]. This produced was found to have only very little contamination with radioisotopes. Great care had been taken not to contaminate the coating during application. All work was conducted under a laminar flow hood and detectors were cleaned, in this order, with acetone, isopropyl alcohol and ultra-pure water before and after application of the coating. When not used, the detectors were stored under N<sub>2</sub> atmosphere in a desiccator to prevent exposure to radon and other detrimental substances in the air. The approximate coating thickness is 60 μm for EV and 160 μm for REDLEN detectors. A visual comparison is given in Figure 4.4.

Table 4.1: List of detectors purchased for the XDEM. Detector 694242-R was not installed into the LNGS setup for reasons given in the text. Energy resolution was measured at 662 keV by the respective manufacturers. Detector and coating masses for EV detectors were given by the manufacturer (except detector mass for 694242-R), the ones for REDLEN detectors were measured in Dortmund.

Manufacturer	ID	Coating	FWHM [%]	M <sub>det</sub> [g]	M <sub>coating</sub> [g]
EV	694318-1	Glyptal	2.4 to 2.9	34.15	0.06
EV	694318-2	Glyptal	1.8 to 2.1	35.08	0.07
EV	694318-3	Glyptal	2.0 to 2.8	34.57	0.06
EV	694253-2	Glyptal	1.9 to 3.7	33.84	0.07
EV	694242-R	Glyptal	2.0 to 2.2	35.45 ± 0.01	0.06
REDLEN	109026	Epoxy	2.0 to 2.0	35.50 ± 0.01	0.14 ± 0.01
REDLEN	109032	Epoxy	2.0 to 2.2	35.50 ± 0.01	0.13 ± 0.01
REDLEN	109033	Epoxy	1.9 to 2.1	35.50 ± 0.01	0.14 ± 0.01
REDLEN	109034	Epoxy	1.9 to 2.0	35.50 ± 0.01	0.12 ± 0.01
REDLEN	109031	Epoxy	3.7 to 4.5	35.50 ± 0.01	0.16 ± 0.01

Important criteria for the performance of all detectors will be evaluated in chapter 5. For detector EV 694242-R the manufacturer forgot to apply vacuum sealing during shipment to Dortmund so that it was exposed to radon. Also, the metalization on the cathode was partly missing indicating low adhesion. Because of these problems and the results of chapter 5 it was decided to exclude 694242-R from the final XDEM setup.



Figure 4.4: Comparison of GLYPTAL coating (left) applied by EV and epoxy coating applied by the author (right). The coating on the left seems much more in-homogeneous and small inclusions are visible in a number of spots.

The total mass of the installed detectors is 315.1 g. They are shown in Figure 4.5. Their positions in the layer are indicated in Figure 4.6.

The selected detectors were installed during two weeks in March 2018 into the LNGS setup. Great care was taken to keep the detectors as clean as possible when assembling the detector layer given the restrictions explained at the beginning of this chapter. The detectors were stored under  $N_2$  atmosphere when no work was carried out on them and also immediately after they were installed into the shielding, which has not been opened again since then. The performance of the detector array at the LNGS and possible background sources will be discussed in chapter 7.

#### 4.2.2 Read-Out Electronics

The original idea of the XDEM was to feature a substantial change of read-out electronics. Instead of the system based on discrete circuits described in chapter 3, a highly integrated system should have been used to be suitable for scaling up<sup>4</sup> the experiment to a much larger number of detectors at a later stage. Also, a much smaller system would likely have a reduced content of radioisotopes and could thus be placed closer to the detectors, which has the potential to lower noise and hence improve resolution. However, the existing system worked well in terms of energy resolution and PSA capabilities. Thus, the challenge was to find a solution which is

---

<sup>4</sup>The power consumption of the Demonstrator setup was already at the order of few kW.

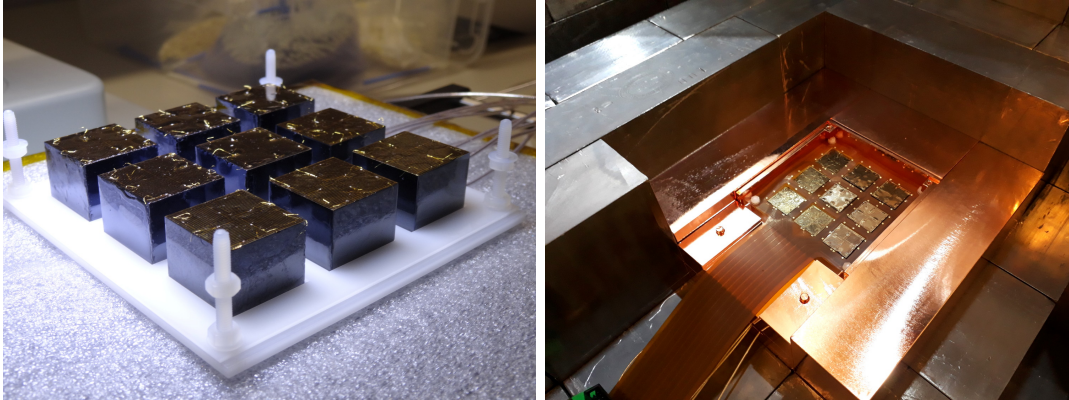


Figure 4.5: XDEM detectors placed in the POM holder (left) and installed into the shielding (right).

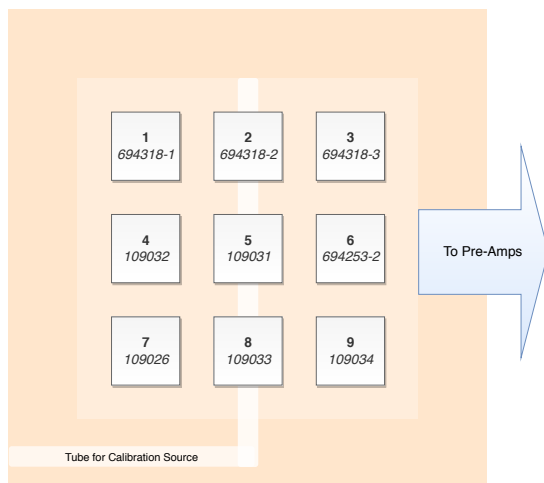


Figure 4.6: Schematic of detector positions in the detector holder. The pathway of cables to the pre-amplifiers and the tube guiding the calibration source are indicated.

much more integrated, while keeping the physics performance at a similar level. Both of these considerations could in principle be fulfilled by the IDE3421 application-specific integrated circuit (ASIC) from the Norwegian company IDEAS. This system was successfully used together with a pixelated CdZnTe and achieved an energy resolution far below 1% FWHM at 2615 keV [ZH12].

Its basic features make the system reasonably well suited to be used in the context of COBRA:

- 130 channels in total, 128 for negative charges i. e. anode channels. The complete XDEM layer with nine CPqG detectors can be read-out with a single ASIC.
- Maximum sampling frequency of 80 MHz with 14-bit ADCs
- 160 memory cells resulting in a total sample length of 2  $\mu$ s

#### 4 The COBRA XDEM Upgrade and Improvements to the Demonstrator

- Programmable gains and trigger thresholds
- Power consumption of 270 mW

Due to the fact that the system was originally intended to be used with pixelated detectors, it also possesses some properties which are not optimal for COBRA. One is the fact that triggering is only possible for a single channel, its nearest neighbors or all channels at once, but not for a group of all channels belonging to a single CPqG detector. Nevertheless, a first proof-of-principle test at IDEAS in Oslo was successful [Teb16]. Consequently, a testing system including some auxiliary components was purchased to be tested in-depth for the XDEM project. This was done as part of this thesis, but also in two bachelors theses [BD15; Alb16].

In practice, working with the system in Dortmund proved to be cumbersome, as both the ASIC itself, as well as the GAMMAPROCESSOR software based on LABVIEW used for read-out repeatedly required regular updates and lacked proper documentation. Testing functions integrated in GAMMAPROCESSOR showed a large variation of noise across channels, and very low gain in about one third of them. The complete system furthermore suffered from as 'freezing' of the software, i. e. the need for a complete restart to continue data-taking. Still, if a detector was connected to the channels which were supposed to be functional, GAMMAPROCESSOR showed that the system was in principle operational, as indicated by the two spectra with and without a  $^{137}\text{Cs}$ -source present shown in Figure 4.7.

An updated version of the circuit solved some of these problems, but also introduced new ones. Ultimately, it was decided to not use the ASIC-based system for the XDEM at this point. Instead a conventional system as employed in the Demonstrator was used again.

Two of the three pre-amplifiers needed for the XDEM<sup>5</sup> were already available from the Demonstrator construction. For the newly produced device the printed circuit board (PCB) material was switched from standard FR-4 to ROGERS 4350B, better suited<sup>6</sup> for high signal frequencies [Cor]. Also, a single new high-voltage filter was needed, as discussed in subsection 4.2.3. The flexible polyimide PCB carrying the signal traces had to be completely redesigned to accommodate a much higher channel density.

---

<sup>5</sup>nine channels for each of the nine detector are needed if the guard-ring signal is also recorded, resulting in a total of 81, while 32 channels are available per pre-amplifiers

<sup>6</sup>The actual impact of this change is hard to determine, as the device suffered from problem with the ground connection. For details see Ref. [BD18].

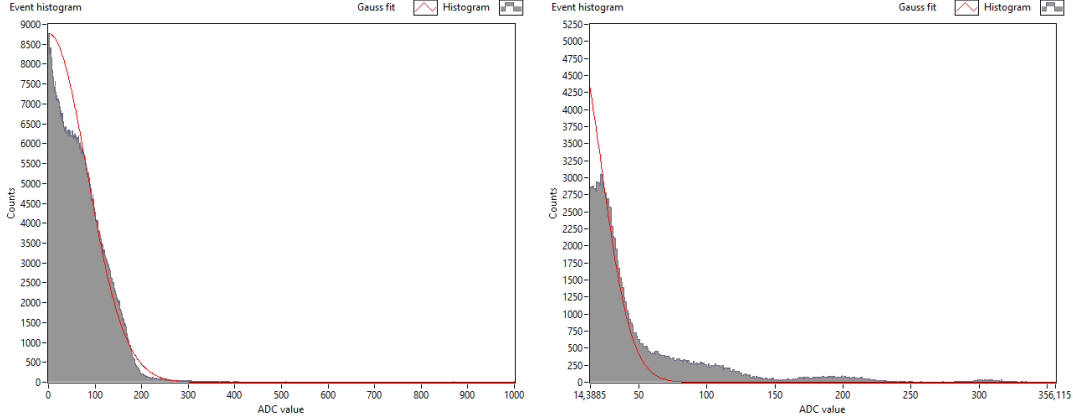


Figure 4.7: Spectrum obtained in GAMMAPROCESSOR a  $1\text{ cm}^3$  CdZnTe detector in planar read-out mode, on the left without and on the right with a  $^{137}\text{Cs}$ -source present. The high number of counts in region of low ADC values can be attributed to electronic noise, while the small bump on the right around  $\approx 200$  ADC values is likely an indication of the full-energy peak.

As the charge-sensitive pre-amplifiers are very susceptible to their total input capacitance, traces were design to have a capacitance as small as possible. This meant to minimize trace width, maximize trace spacing and avoid guiding traces in parallel on both sides of the PCB. The final design featured traces with a width and spacing of both  $100\text{ }\mu\text{m}$ ,  $35\text{ }\mu\text{m}$  thickness and rigid end on the PCB to accommodate connectors. The flexible PCB is connected via short wires to another PCB fixed at the gas-tight enclosure and acting as a feed-through. On the other side of the enclosure, flat-band cables connect the second PCB to the pre-amplifiers. While this design lead to slightly longer cables as well as more connections than strictly necessary, it ensured some adjustability, which was helpful in construction of the setup. Details of the design can be found in Appendix D.

The detector electrodes were connected to the flexible PCB via  $50\text{ }\mu\text{m}$  thick gold wires, fixed with a silver-based epoxy well suited for low-background applications [Abg+16] called TRA-DUCT 2902 by TRA-CON, INC.. Such a connection is exemplary shown in Figure 4.8. It has high mechanical strength, thus no additional glue is necessary. Gluing of the wires to the electrodes was done under a laminar-flow hood at TU Dortmund, connection to the PCB was done underground at the LNGS just before installing the detectors into the setup.

Even with the conventional electronics, some challenges were encountered. First of all, the pre-amplifiers are highly susceptible to electrical noise if any one of their



Figure 4.8: Connection of gold wire and anode of a test detector with conductive silver-based epoxy.

ground connections is not done well. Adjusting all the cables and connectors to achieve this is a time consuming and error-prone task, as has already been pointed out in Refs. [Teb16; Geh17]. Furthermore, the design of signal traces proved to be quite complicated due to the combination of a large number of channels, restricted space, low-background considerations and little possibilities to test components prior to the final assembly inside the LNGS setup. This led to some errors in signal routing, that were only corrected in July 2018.

The power consumption of the linear amplifiers turned out to be too high for a standard NIM crate if all eleven modules needed for the XDEM were operated within one crate. This resulted in non-linear behavior and worsened signal quality, which unfortunately was not immediately recognized. An exemplary measurement of the non-linearity of one FADC, acquired with signals from a pulse generator, is shown in Figure 4.9. This was solved by installing a second crate in October 2018. As a consequence, only test data was taken until October 2018 and the results presented in chapter 7 include only data taken after this date.

### 4.2.3 High-Voltage Supply

For the XDEM it was necessary to slightly deviate from the voltage-distribution design of the Demonstrator due to the fact, that the larger XDEM detectors need a higher

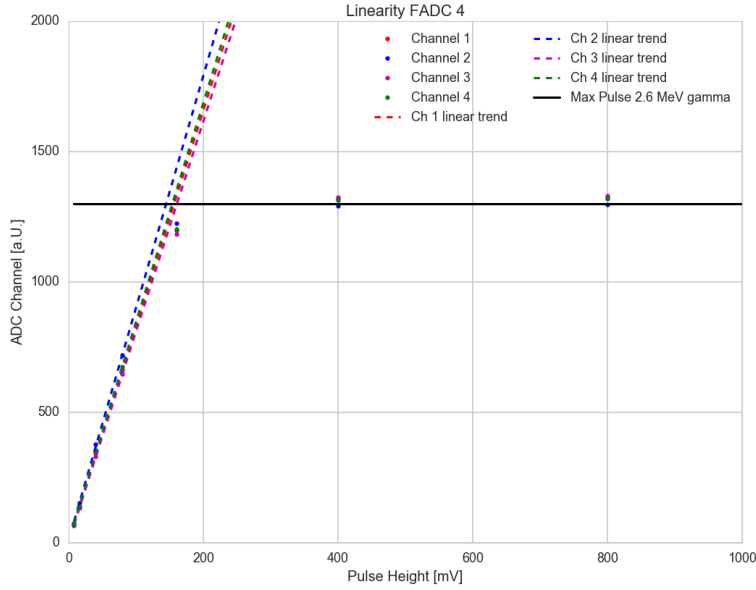


Figure 4.9: Measurement of the non-linearity caused by insufficient current delivered to the linear amplifiers in the XDEM setup measured with injected pulses injected of varying amplitude. For small pulse heights the relationship is linear, but reaches saturation around 200 mV and is non-linear in a transition region. The ADC channel in which a 2.6 MeV  $\gamma$ -ray would approximately be registered is indicated by a black line, showing that the non-linearity can only be seen in the high-energy region of a spectrum.

bulk voltage (BV) to reach their working point, as explained in subsection 5.2.1. On the other hand, fewer channels are needed: Nine times BV and grid bias (GB) each, compared to 64 times BV and GB each for the demonstrator.

To power the XDEM detectors, an ISEG EDS 181 30n high-voltage supply with 24 channels is used. Each channel can deliver voltages up to  $-3$  kV with a maximum ripple of 5 mV. The device is used for both BV and GB simultaneously. Its output is a proprietary connector from REDEL which needs to be converted to the FCT FMV high-voltage contacts at the pre-amplifiers. This is done by first using a so-called *break-out box* by ISEG which converts the REDEL connector to more common SHV connectors. From there, a chain of cables with SHV on one end and FCT FMV on the other end, manufactured in the TU Dortmund electronics workshop, is used. The cables of this chain are rated to withstand the maximum voltage delivered by the high-voltage supply. Each individual cable is further equipped with a ferrite-core to suppress high-frequency signals.

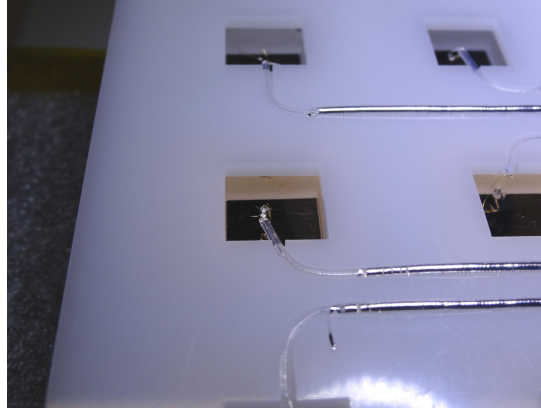


Figure 4.10: Close-up photograph of high-voltage contacts of XDEM detectors.

Coming from the high-voltage filters in the pre-amplifiers, voltage is delivered to the detectors by miniature coaxial cables of type 2275090 by MEDIKABEL GMBH rated for voltages up to 6 kV. Small grooves were laser-cut in the polyoxymethylene (POM) detector holders to guide cables to the detectors, as seen in Figure 4.10. There, they are connected using once again conductive epoxy and gold wire.

The design of the high-voltage filters itself also had to be modified. All resistors and capacitors were exchanged for models rated for operation at voltages of at least 3 kV. The spacing between individual channels, as well as ground wires and wires on negative potential, was increased as much as possible. Despite these changes, it turned out after the XDEM installation, that this design was not able to withstand the voltages needed to operate the detectors at their working point. In fact, this was only possible for two detectors, which were running at 1 800 V and 2 200 V, while for other detectors the BV had to be reduced to values as low as 800 V – clearly too low to achieve reasonable performance – and two detectors even had to be switched off completely.

As this situation was not satisfactory, a new HV filter PCB was produced. This included an additional cut-out, already employed for eight-channel pre-amplifiers in the laboratory, below the two contact points of the capacitors which were subject to the largest voltage drop. The contact pads on the PCB were changed from lead-based ones to gold pads providing a more even surface and great care was taken to make sure no dust or remnants of solder flux were left on the board, all to minimize the possibility of conductive channels across the surface. The new PCB was also placed in its own housing, as opposed to the older versions which were included in the same housing as the pre-amplifiers, to give as much protection from sparking as possible. These changes proved to be effective – tests at TU Dortmund were successfully conducted far above

any voltage needed to operate any of the detectors. Finally, operation at the working points determined in the laboratory was possible at the LNGS. Only for the three detectors needing a BV of 2 600 V in the time between July 2018 and April 2019 the voltage was kept at only 2 200 V to ensure stable data taking. In May 2019 the highest voltages were finally raised to 2 600 V.

### 4.2.4 Modifications to Shielding and Infrastructure

To accommodate the additional detectors and electronics for the XDEM, several changes had to be made to the shielding and auxiliary infrastructure. An important consideration for these changes was to keep the original Demonstrator setup unchanged as much as possible to not risk degrading its performance. At the same time, the XDEM should share as many parts as possible with the Demonstrator to make the upgrade both easier to conduct and cheaper. An extensive account of the planning and production of a large fraction of the new parts is given in Refs. [BD15; BD18] by Lucas Bodenstein-Dresler. Many of the ideas for possible improvements and information about details of the original design were coming from Jan Tebrügge and Daniel Gehre. The re-arrangement and extension of the lead-castle was largely planned by Hannah Jansen. Consequently, only a short account will be given here, focusing on what is relevant for the results presented later in this work.

To make use of much of the original shielding, the new detectors were placed very close to the old ones, only separated by a few millimeters of copper. In this way, only a small amount of new shielding material is necessary, which is beneficial, as the copper parts of the Demonstrator are now in the deep underground for several years and thus most long-lived unstable isotopes produced through cosmogenic activation have already decayed. All new parts were produced from copper stored at the Felsenkeller underground laboratory in Dresden, which has an overburden of about 140 m of water equivalent, to suppress cosmogenic activation. They were then machined by the mechanical workshop in Dresden, with the aim to minimize time above ground. Tools that came into direct contact with the copper were all new to prevent cross-contamination from other parts machined earlier.

The finished parts were sent to POLIGRAT in Munich for electro-polishing. This process removes a very thin layer of the copper on top of the pieces, shown to remove Radon-daughters effectively [ZW12], and produces a very smooth surface which makes it harder for new contaminants to settle on the it [Yan+16]. The total time between when the copper was fetched from the Felsenkeller until it was brought deep underground again at the LNGS was about four months. The resulting cosmogenic activation will

be discussed in section 6.2. Additional lead parts were machined from a stock available at TU Dresden. The original shielding had a size of  $60 \times 60 \times 60 \text{ cm}^3$ . Its footprint was kept, but its height was raised to 70 cm to account for the additional 5 cm of height occupied by the XDEM detectors and another 5 cm filled with spare lead bricks.

All parts of the shielding as well as the POM used for the detector holder were extensively cleaned in an ultrasonic bath with cleaning agents and ultra-pure water in the chemical laboratory of the LNGS. Once underground, they were again cleaned with acetone, isopropyl alcohol and ultra-pure water.

To accommodate the additional feed-through for the XDEM wiring, a new radon-tight housing made up of 15 mm thick polymethylmethacrylat (PMMA) was constructed at the mechanical workshop of the faculty of Biochemical and Chemical Engineering in Dortmund. At all joints, sealing tape made from ethylene-propylene-diene-monomer (EPDM) rubber was placed to make the housing more gas tight.

As three additional pre-amplifiers were installed for the XDEM, the cooling system had also to be enlarged correspondingly. For this, the same flow-distributor from OVENTROP as for the Demonstrator was used, only that the new device has eight outlets instead of five. The design of the cooling plates themselves was also completely adopted.

One issue that became apparent, was the production of excessive waste heat due to the installation of additional electronics. This led to temperatures of about  $46^\circ\text{C}$  at the DAQ computers and  $39^\circ\text{C}$  at the VME crates. These values were thought to be dangerous, as they could lead to instabilities of the electronics or shorten the live-time of components like the FADCs, which are rated for a maximum operational temperature of  $40^\circ\text{C}$ . Also, working became very uncomfortable due to this. To tackle this issue, the upper part of the building was connected to a water-cooling system run by the LNGS and equipped with fans to remove warm air. As a result, the temperature dropped by about  $10^\circ\text{C}$ .

Based on the results presented in this chapter, the XDEM could be successfully commissioned in November 2018. Results from data acquired with the XDEM setup at the LNGS will be presented in chapter 7, while chapter 5 will focus on the characterization of the detectors introduced above.

# 5 Large CdZnTe Detectors for the XDEM

The decision to use significantly larger detectors with a novel CPqG anode design including an instrumented guard-ring constitutes the key element of the XDEM upgrade. But it made also it necessary to re-evaluate the methods used to interpret detector-data in the framework of COBRA. An especially pressing concern was to establish that calculation of the interaction depth is still possible, as it is crucial for a low background. The first section of this chapter will deal with an adaptation of the standard algorithm to do this and an experimental verification of this new method.

Furthermore, it was necessary to characterize the detectors foreseen to be used for the final XDEM setup. This will be the content of the second section of this chapter. The most important points were first, the determination of the so-called working point of each detector, i. e. the combination of grid bias and bulk voltage at which optimal performance is achieved, and second, an estimation of the relative detection-efficiency of each device (results based on Monte Carlo-simulations to determine their absolute efficiency are presented in section 6.1). Based on the results of the working point determination, the mobility-lifetime product  $\mu_e\tau_e$  is calculated. Furthermore, the energy resolution of the detectors is determined, hinting at their performance in the underground setup. current-voltage (I-V) characteristics were also measured and the influence of leakage currents on the detector performance is estimated.

## 5.1 Interaction Depth in CPqG Detectors

The task of adopting the interaction depth algorithm for CPqG designs was covered partly in a number of theses [Rö14; The14; Tem15]. The results shown in this work are largely based on Ref. [Tem17]. The measurements on which Ref. [Tem17] is based were kindly provided by the COBRA group at TU Dresden.

The interaction depth calculation presented in chapter 3 cannot be used in the exact same manner for the CPqG detectors of the XDEM, as for the single-grid CPGs. But

it can be extended quite easily, which was first shown in Ref. [HSR05]. The basic idea is that even though drifting charge carriers will in general induce some charge on all grids, due to charge conservation the total amount of charge induced is the same regardless of the anode design. With this in mind, Equation 3.7 can be modified

$$z_0 = \sum_i \frac{(A_{CA}^i + A_{NCA}^i)}{(A_{CA}^i - A_{NCA}^i)} \quad (5.1)$$

i. e. the individual CA and NCA pulse heights are exchanged for the corresponding sums over all grids  $i = 1, 2, 3, 4$ .

It is also possible to include the effect of electron trapping into this formula, as it is done in Equation 3.8, although this is more complicated, as the weighting factor  $w$  is in general different for all sectors. But trapping only needs to be considered in sectors where charges actually drift, and not in those in which charges are only induced on the grid. If a single interaction takes place<sup>1</sup> in some sector  $j$ , then the other sectors will have no influence and Equation 3.8 becomes

$$z_{tc} = \lambda_j \ln \left( 1 + \frac{1}{\lambda_j} \sum_i \frac{(A_{CA}^i + A_{NCA}^i)}{(A_{CA}^i - A_{NCA}^i)} \right) . \quad (5.2)$$

where  $\lambda_j$  is just

$$\lambda = \frac{1 + w_j}{1 - w_j} . \quad (5.3)$$

Even though Equation 5.1 is known in the literature and was also investigated by the COBRA collaboration before, it lacked experimental verification. Measurements done by the collaboration and in other groups always used a source that irradiated the detector homogeneously and could thus only conclude that the obtained depth distributions looked similar in the cases of CPG and CPqG detectors. But an assignment of a spatially limited interaction to a reconstructed depth could not be tested in this way. Also the depth resolution could not be tested. Fortunately, an automated detector scanning apparatus with a strong collimated source was available at TU Dresden. Measurements with a suitable detector had already been performed for a different purpose [Roh16], which could be re-used to study the interaction depth method further.

The measurements were conducted with a REDLEN detector at a BV of 1 300 V and a GB of 100 V. The source was a 90 MBq <sup>137</sup>Cs  $\gamma$ -source<sup>2</sup>. The collimator consisted

---

<sup>1</sup>In the case of multiple interaction it is possible to use an energy-weighted average of the  $w$  as an approximation.

<sup>2</sup>More information about the use of <sup>137</sup>Cs for detector tests is given in the next section.

of lead with a thickness of up to 6 cm. The opening for the  $\gamma$ -rays had an area of about  $1 \text{ mm}^2$ . The whole device could be moved electronically to allow for automated measurements with the source in many different positions. The same setup was also used to scan detectors for the COBRA Demonstrator and is described in detail in Ref. [Sö11].

For the measurements used here, the source was moved between the electrodes (z-direction) of the detector in increments of 1 mm, starting and ending slightly above and below the crystal to make sure its whole length is covered. As there was no method available to determine to exact position of the detector relative to the source, the first and last of these scanning points did exactly fall into the first mm of the detector, but usually only covered it partly. Thus, the relative position between source and detector has an uncertainty of 1 mm. But the uncertainty of the relative position between two scanning points will be much smaller. In the analysis only events which deposited their full energy of  $(662 \pm 30) \text{ keV}$ , taking into account the finite energy resolution, are considered in order to discard external backgrounds and photons that scattered inside the collimator. Furthermore, only single-sector events were considered, i. e. all events with interactions detected in more than a single sector were discarded.

An example of the interaction depth calculated for a single measurement point with Equation 5.1 (*conventional* in red) and Equation 5.2 (*trapping corrected* in blue) can be seen in Figure 5.1. This point is very close to the cathode and thus the reconstructed depth of every event should be close to 1, but not higher than that as such values would represent an unphysical location outside of the detector. One can see that with both formulas, the results produce a peak around the expected positions of the source and a relatively flat background distributed over all interaction depths. This is mainly caused by multiple quasi simultaneous interactions inside the detector, e. g. through Compton scattering, which produces a depth that is an average of all single interactions. The peak width is given largely by the size of the collimator opening, which is only slightly smaller than the width of about  $\Delta z = 0.1 \approx 1.5 \text{ mm}$ .

In the case of the trapping corrected reconstruction one can see that the distribution falls of much steeper near the cathode. In general, just from this single measurement point it can be concluded, that the interaction depth formula given above is able to reproduce the expected position of the source.

From the single measurements it is also possible to determine the mean interaction depth at each position and directly compare it to the relative position of the collimator to test the linearity of the method. To extract the mean a Gaussian function is used to describe the peak itself, while the flat continuum background is described by a

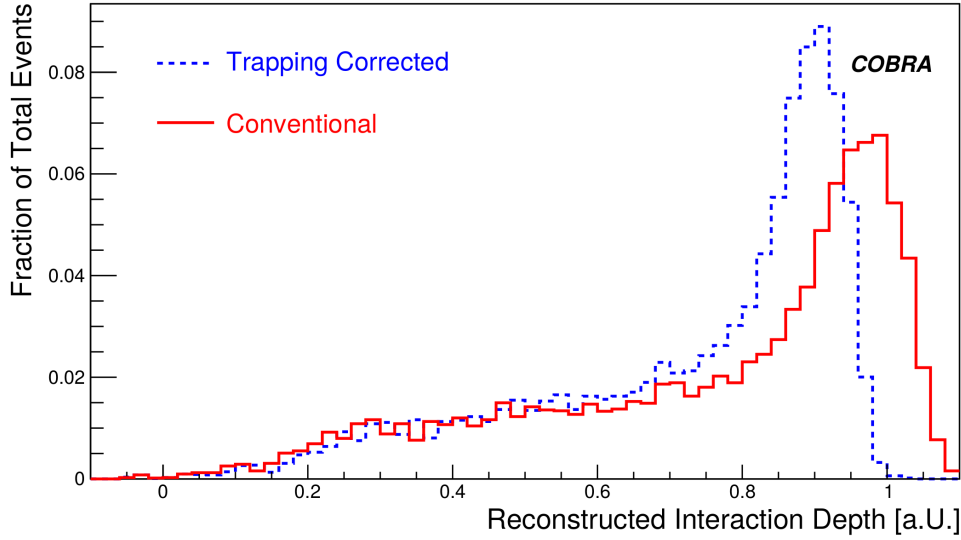


Figure 5.1: Interaction-depth distribution for a single scanning point close to the anode with a REDLEN detector with and without trapping correction applied. Reproduced from Ref. [Tem17].

polynomial function. This compound function is then fitted to the data and the mean value of the Gaussian together with its uncertainty is taken as the mean interaction depth. This quantity is plotted against the collimator position. The result can be seen in Figure 5.2. Again, both formulas are shown and the colors are the same as above. Both formulas indicate a fairly linear behavior in the center of the detector with deviations mostly near the electrodes ( $z = 0$  or  $1$ ).

In both cases, the mean interaction depth is a bit higher than a linear relation would predict near the anode and a bit lower near the cathode. This can be understood as a cut-off effect: Even if the center of the beam is exactly aimed at for example the cathode ( $z = 0$ ), only photons arriving above the cathode can interact with the detector and so the average of detected events lies above  $z = 0$ . This leads to a kind of S-shaped curve in Figure 5.2. But for the purpose at hand, it is enough to notice that it can still be well approximated by a linear curve for the most part of the detector, especially if one takes into account the finite position resolution, which is larger than deviations from linearity.

It is also possible to compare CPG and CPqG detector designs with this approach. The overall behavior of both detectors is rather similar, which verifies the results of earlier measurements with an un-collimated source. Only close to the the electrodes,

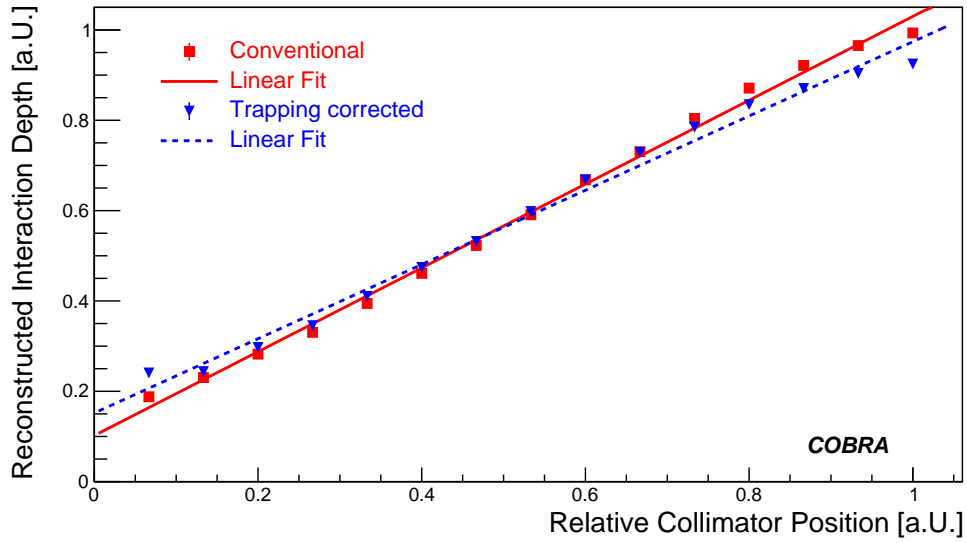


Figure 5.2: Mean interaction-depth as a function of the collimator position with and without trapping correction. A linear fit is overlaid in both cases. The uncertainties are smaller than the marker-size and can not be seen here. Reproduced from Ref. [Tem17].

the CPqG design tends to give slightly higher (near the anodes) or lower (near the cathode) values.

Overall, it can be concluded, that the interaction depth reconstruction is also possible with the CPqG design and is only slightly less accurate than for a conventional CPG. The trapping correction also produces the intended effect and thus it can be used as a valuable tool for background reduction, although it might be necessary to adjust the exact cut values.

## 5.2 Characterization of XDEM Detectors

In this section the essential characterization measurements of the XDEM detectors will be presented. The goal of these measurements is to identify optimal working conditions for each detector, determine the most suitable detectors for the underground setup and get an overview of the performance of these detectors. Although the measurements presented here were used partly to choose the best detector for the XDEM, for most results an average value of all XDEM detectors is reported for easier comparison in later chapters. As already mentioned in subsection 4.2.1, the excluded detector is EV 694242-R. The results are prefaced by a short overview of the laboratory measurement setup and the methods used to evaluate the above mentioned criteria.

In general, the idea of the laboratory setup<sup>3</sup> – schematically shown in Figure 5.3 – is to replicate the LNGS setup as closely as possible. The same type of FADC and linear-amplifier is used. The pre-amplifiers are similar, but smaller with only eight channels and slightly different connectors are used.

Both the grid bias (GB) and the bulk voltage (BV) are provided by an ISEG SHQ224 high-voltage supply. The two channels of the device are ideal to operate a single detector with the same voltage across all four sectors<sup>4</sup>. If a detector requires different voltages across the sectors, a custom build voltage divider is used. This can be useful if noise in a single sector becomes excessive above a certain voltage, but the other sectors can be operated at a much higher value with significantly enhanced performance. The SHQ224 provides many useful features like a precise measurement of the current flowing through the channels, defined voltage ramps, and the possibility for remote controlling the voltages, which allows the working point determination and measurements of I-V curves to be done in an automated manner.

The detector under test and the pre-amplifier are placed in an electromagnetic interference (EMI) shielding box built at the mechanical workshop in TU Dortmund. It features a chute for feeding-through the cables similar to the one used at the LNGS. The detector itself is placed under an air-tight polymethylmethacrylat (PMMA) box, which is constantly flushed with nitrogen to protect it from moisture, oxygen and radon. Unused detectors are stored in a similar box outside the EMI box and are also constantly flushed. The laboratory is air-conditioned to a temperature around 22 °C.

---

<sup>3</sup>Many details about these devices can be found in the references given earlier regarding the COBRA setup at the LNGS.

<sup>4</sup>This mode is generally foreseen for the operation at the LNGS, as it requires fewer voltage channels and introduces less uncertainties about the differences between the sectors on a single detector, which can be a concern if the energy measured by the whole detector is to be determined

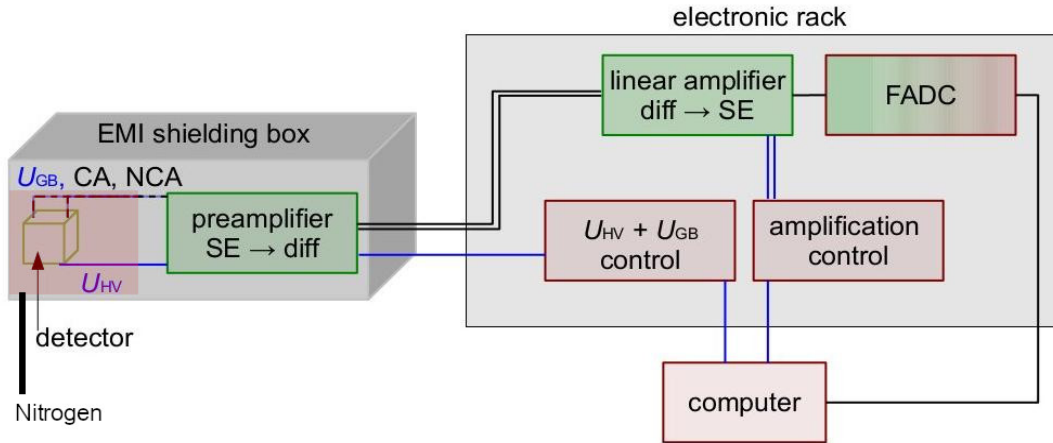


Figure 5.3: Main components of the detector test setup at TU Dortmund. Adapted from Ref. [Ebe+16a].

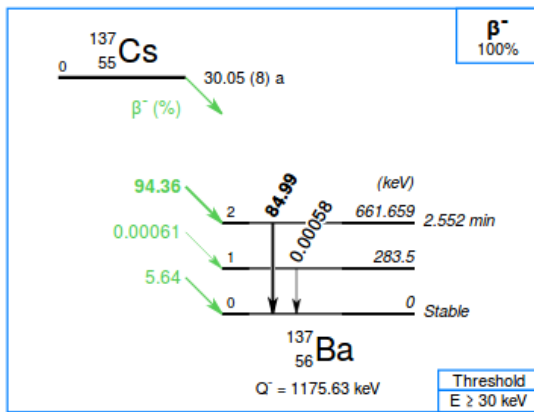


Figure 5.4: Decay scheme of  $^{137}\text{Cs}$ . Only the de-excitation  $\gamma$ -ray with an energy of 662 keV is used for the measurements presented here. Taken from Ref. [Bec19].

Spectroscopic measurements are done with a  $^{137}\text{Cs}$ -source. The decay scheme of this isotope can be seen in Figure 5.4. The only part of interest here is the de-excitation from the second excited state to the ground-state. Additional  $\gamma$ -lines are emitted with an intensities far below the per mille level. The electrons from the initial  $\beta^-$ -decay are shielded within the source itself. This makes  $^{137}\text{Cs}$  effectively a mono-energetic  $\gamma$ -ray source. It is thus ideal for a simple, quasi-automatic evaluation of the spectra. The nominal activity of the source at the time of production was 370 kBq, but it was never calibrated. The date of production is also not precisely known. The present day activity can only roughly be estimated to be about 260 kBq.

The pulse-shapes acquired with this setup are stored on a computer and later processed using the standard COBRA software MANTICORE [Sch11]. It is important to notice, that the calculation of the energy  $E$  deposited in a detector is more involved

than Equation 3.5 would suggest. Effects from the amplifiers also have to be taken into account. In the most general case,  $E$  is given by

$$E = c_1(A_{\text{CA}} - c_2 w A_{\text{NCA}}) + c_3 \quad (5.4)$$

where in addition to  $w$  and  $c_1$ , two additional calibration factors  $c_{2,3}$  appear.  $c_2$  takes into account that the gain of the CA and the NCA channel in the amplifiers will usually not be equal. Correcting this allows for a more accurate determination of  $w$  and the interaction depth. The factor  $c_3$  can be used to compensate a possible offset in energy, but this factor is small for energies of interest here.  $c_2$  is usually estimated by matching the rise of the CA- and NCA-amplitudes, as these should be equal if the gain of each channel is the same. This correction is only done once for the laboratory measurements, as the same pre-amplifier is used for all detectors.

The actual calibration involved three iterations of pulse-shape processing, as calibration parameters are applied on the level of individual pulses prior to processing them.

1. A set of identical initial parameters is used.
2. The ideal weighting factor  $w$  giving the best energy resolution is determined.
3. The spectrum is calibrated using the known energy of the  $\gamma$ -line of  $^{137}\text{Cs}$ .

Only spectra calibrated in this way are used for further analysis. In total, nearly 3000 individual spectra were evaluated in the characterization campaign.

The exact analysis performed on these spectra depends on the intended purpose of the measurement, but a common peak-shape model was used in all of them. This model is based on a well established model used for HPGe detectors [SK16] and is sometimes referred to as *hypermet*-function [CM97]. It can be divided into three parts: First, a Gaussian modeling the main part of the peak

$$g(E) = \frac{S_g}{\sqrt{2\pi}\sigma} \cdot \exp\left(\frac{-(E - \mu)^2}{2\sigma^2}\right) \quad (5.5)$$

where  $S_g$  is the (normalized) height of the Gaussian,  $\sigma$  is the square-root of its variance,  $\mu$  is the central value corresponding to the nominal energy of the  $\gamma$ -line and  $E$  is the energy at which the function is evaluated. It further includes a *tail* to describe the asymmetric peak-shape towards lower energies caused by electron trapping. This tail

is of the form

$$t(E) = \frac{S_t}{2\beta} \cdot \exp\left(\frac{E - \mu}{\beta} + \frac{\sigma^2}{2\beta^2}\right) \cdot \operatorname{erf}\left(\frac{E - \mu}{\sqrt{2}\sigma} + \frac{\sigma}{\sqrt{2}\beta}\right) \quad (5.6)$$

with  $S_t$  the height of the tail and  $\beta$  controlling its slope. Finally, a part called the *shelf* is introduced, which accounts for a constant background  $B$  not belonging to the investigated  $\gamma$ -line and a higher continuum background  $A$  at energies below the full energy of the line. This stems from multiple Compton-scattering inside the detector or scattering under small angles outside of it and deposition of the remaining energy in the detector afterwards. The transition between a continuum background at low energies and a constant background is of the form

$$b(E) = \frac{A}{2} \cdot \operatorname{erf}\left(\frac{E - \mu}{\sqrt{2}\sigma}\right) + B. \quad (5.7)$$

The total *hypermet*-function is given by  $h(E) = g(E) + t(E) + b(E)$  and shown in Figure 5.5 after being fitted to data acquired with one of the XDEM detectors. The total function can be seen to give a quite good fit to the data over most of the energy range, especially in the peak region. Towards higher energies, an additional tail appears in the data, that is not well reproduced by the function, but the fraction of entries in this region is tiny. The tail towards lower energies is well reproduced. Sometimes, this tail is not very prominent, either if the overall energy resolution is bad washing out details, or the tail is virtually not present in the first place, due to electron trapping being very small. In these cases, the fitting algorithm falls back to a simple model without a tail. If the fall-back were not implemented, the tail-parameters can sometimes only be fitted with large uncertainty, which would cause unnecessary hurdles in later steps like integration. Depending on this, either only the Gaussian or the Gaussian plus the tail are interpreted as a signal.

Other peak models were also used in the context of COBRA for fitting spectra with a single peak, all using a similar form for the background. A simple Gaussian is usually not able to fit spectra of an arbitrary detector well enough and is only used for testing purposes. In Refs. [Tem15; Ebe+16c] a double-Gaussian model was used, in which a one Gaussian is used to model the central part of the peak and a second, broader but smaller, Gaussian is used to describe the tails to both sides<sup>5</sup>. The drawback of this model is that it does not incorporate the asymmetric effect of electron trapping.

---

<sup>5</sup>The rationale for using this model is, that even a single detector can actually have varying energy resolutions as a function of the interaction depth and because of this, the overall peak shape can look like a broad, small peak overlaid with a narrow, high peak.

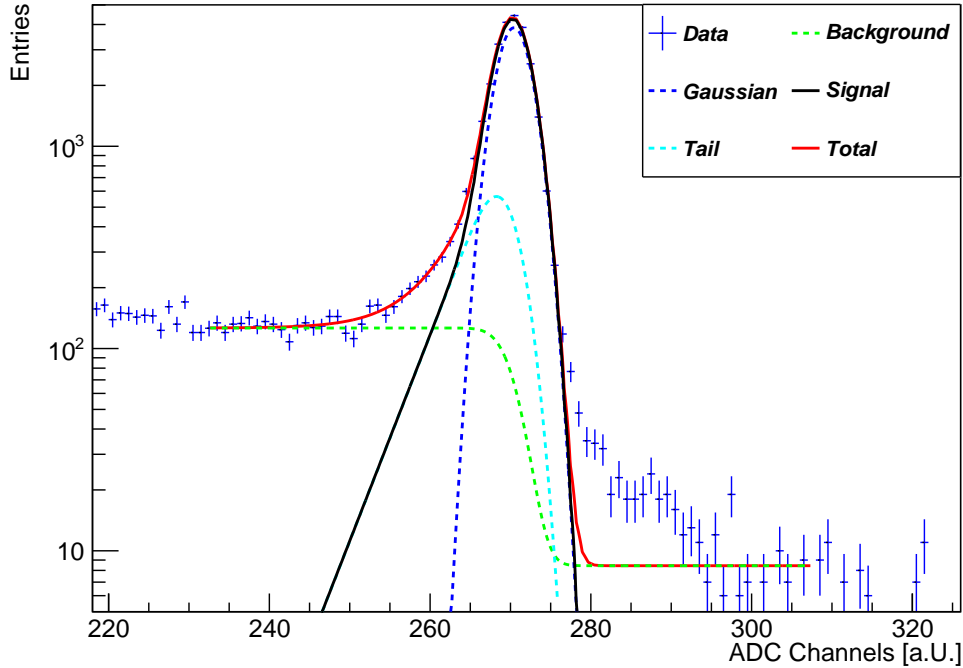


Figure 5.5: Uncalibrated spectrum showing the  $^{137}\text{Cs}$ -peak and a fit of a *hypermet*-function with its various components to this peak. Fits like this are used to compute quantities like energy resolution and efficiency in this work.

Usually it can only be fitted well if the height-ratio of the two Gaussians is fixed. In Ref. [Roh16] another combination of Gaussians was used – a different variance was allowed for both sides of the peak. With this, an asymmetric peak shape can be reproduced. The drawbacks are that it is hard to motivate this model with regard to physics at the microscopic scale and that the complete shape is essentially still Gaussian over each side of the peak, neglecting that the tail might well have a different slope than the central portion. All of these function were also fitted as a test to a spectrum obtained with sector 3 of detector REDLEN 109033, giving the following results for the goodness-of-fit:

$$\text{Simple Gaussian: } \chi_{\text{red}}^2 = 14.1$$

$$\text{Double Gaussian: } \chi_{\text{red}}^2 = 8.3$$

$$\text{Two Sided Gaussian: } \chi_{\text{red}}^2 = 9.2$$

$$\text{Hypermet: } \chi_{\text{red}}^2 = 1.4$$

These show a clear preference for the *Hypermet* function. Only for a few detectors a double Gaussian could also be shown to give a good fit [Tem15]. Notwithstanding, the *Hypermet* function is found to describe the peak shape well in most cases and will thus be used in this work.

### 5.2.1 Working Point

The ideal combination of GB and BV – the so-called working point – has to be determined for each detector individually, as it depends on a number of device specific quantities. As the determination is quite time consuming, establishing the working point in the low-background setup would be impracticable. It is also essential for all the following measurements, as these are influenced by the chosen voltages.

In the case of BV, two<sup>6</sup> opposite effects are governing detector performance [Ini+08]. The first is the charge collection efficiency (CCE), which is generally rising with BV. For a given value of  $\mu\tau$  the mean drift length  $\mu\tau V$  increases linearly, which improves detection efficiency and energy resolution and reduces tailing.

The second effect is the leakage current between cathode and the anodes. This effect also increases with BV, although in general not linearly, which will be further illuminated in subsection 5.2.5. A higher leakage current leads to larger noise and thus a worse energy resolution. As a consequence there is an interplay between the two effects and the optimal value of BV has to be experimentally determined.

A similar relationship also exists for GB, where the voltage must be high enough to effectively separate CA and NCA, i. e. for all field lines<sup>7</sup> to end on the CA, so that no charge sharing occurs [Bol+05]. Charge sharing has little effect on resolution, but a much stronger effect on detection efficiency, as events suffering from charge sharing can basically be reconstructed to appear as any amount of charge smaller than the true one. In general  $E_{ideal} \propto A_{CA} - A_{NCA}$  and if some charge  $\delta A$  is shared this becomes

$$E_{Shared} \propto (A_{CA} - \delta A) - (A_{NCA} + \delta A) = A_{Diff} - 2\delta A. \quad (5.8)$$

If  $\delta A$  is small, charge sharing will only produce a tail towards low energies in the full-energy peak resulting in an apparent lower CCE, while if  $\delta A$  is large enough, events might even completely fall out of the peak, which appears as a lower detection efficiency  $\epsilon_{Det}$ . Thus, GB has to be high enough to avoid charge sharing. On the other hand, the

<sup>6</sup>Depletion is not a concern, as calculated in section 3.1.

<sup>7</sup>A very simplified picture would suggest that any potential difference between the anodes should be enough to achieve this. In reality due to the finite surface resistivity and space charge effect, this is not the case, as shown in Ref. [Arl16].

energy doubling effect explained in section 3.1 affects a region of the detector whose size is given by the ratio of GB to BV, so a large GB will cause a larger region to be affected by this effect, rendering it virtually unusable. At the same time, the leakage current between CA and NCA also increases with voltage, decreasing resolution.

Furthermore, there is also some interplay between GB and BV: The amount of charge sharing depends not only on GB, but also on the ratio of GB to BV as both affect the electric field lines. As a consequence, the working point has to be determined by testing each combination of GB and BV separately. Simply scanning both independently is not sufficient. To get a good compromise of accuracy and time needed for the measurement campaign, BV is varied in steps of 200 V ranging from 1 000 V to 3 000 V and GB is varied in steps of 20 V from 20 V to 120 V. Each individual measurement had a duration of 180 s for data-taking and 90 s for changing the voltage. Thus, without taking into account the time necessary for data-analysis and possible failures, each determination took about 5 hours.

As no single criterion exists to define the ideal detector configuration, a combination adopted from Equation 2.15 will be used here. If the efficiency to detect a  $\gamma$ -quantum with an energy of 662 keV is taken as a proxy to detect a double-beta decay at its  $Q$ -value, then the (relative) sensitivity  $s$  can be defined as

$$s = \frac{\epsilon_{\text{rel}}}{\sqrt{\Delta E}}. \quad (5.9)$$

with the  $\epsilon_{\text{Detrel}}$  calculated as the ratio between a given configuration to the one with the highest count-rate. The energy resolution  $\Delta E$  is taken as the relative full-width-at-half-maximum (FWHM) resolution<sup>8</sup>. Finally,  $s$  is calculated from these quantities according to the formula above. The working point is then defined as the combination of GB and BV where  $s$  averaged over all four sectors of a detector is maximal. In case of ambiguity, the point with lower voltage was picked as working point. The process is graphically sketched in Figure 5.6.

The resulting voltages for each detector can be found in Table 5.1. Most of them show similar results, especially concerning GB. One notable exception is detector EV 694253-2, for which it was not possible to operate one particular sector above 30 V GB. Thus this sector was limited to that voltage, while the other three sectors were optimized separately, resulting in an optimal GB of 60 V for them. For EV 694242-R it was not possible to operate any sector above 35 V.

---

<sup>8</sup>Contrary to what is done for the more detailed investigation of the energy resolution in the next subsection, here only the  $\sigma$  of the Gaussian part of the peak-shape function is used as a simplified approach to determine the energy resolution.

## 5.2 Characterization of XDEM Detectors

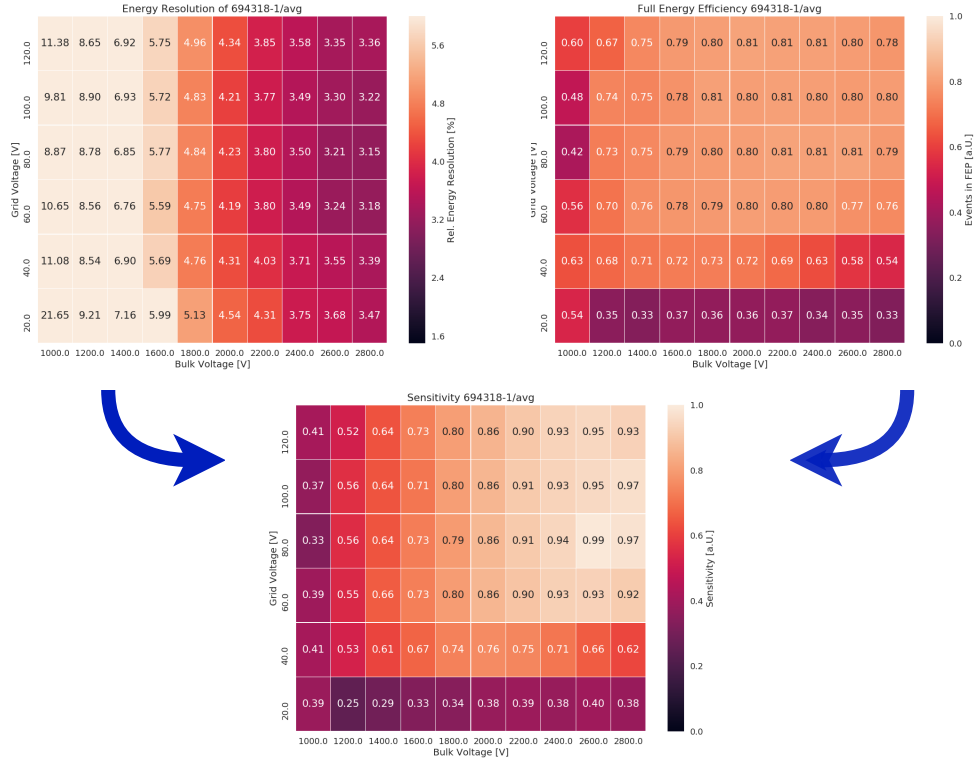


Figure 5.6: The relative energy resolution in terms of FWHM in percent (upper left) and the detection efficiency normalized to the measurement with the largest peak area (upper right) are calculated for each GB/BV combination. From these two the  $s$  criterion normalized to the highest value in each sector is calculated (lower panel). The GB/BV combination corresponding to the largest value of  $s$  is the optimal working point of the detector.

Table 5.1: Optimal working point for each detector and mean values for both eV and REDLEN detectors as well as detectors selected for the XDEM

eV	GB [V]	BV [V]	REDLEN	GB [V]	BV [V]
694242-R	35	2200	109026	60	2200
694253-2	60/30	1800	109031	80	2200
694318-1	80	2600	109032	60	2000
694318-2	80	2600	109033	60	1800
694318-1	80	2600	109034	60	2000
mean	$73 \pm 10$	$2\,400 \pm 300$	mean	$65 \pm 8$	$2\,000 \pm 100$
mean XDEM	$69 \pm 11$	$2\,200 \pm 300$			

The average BV turned out to be  $(2\,200 \pm 300)$  V. On average, the voltage needed to operate the REDLEN detectors with optimal performance is 20% lower than for the eV detectors. Expressed as a field strength, which makes a comparison to detectors of different size easier, the result is  $(1\,467 \pm 200)$  V/cm. This is slightly higher than the value of 1 275 V/cm determined for the Demonstrator detectors. The results are also in agreement with a rule-of-thumb derived from the experience of earlier experiments stating that a least 1 000 V/cm are needed, as no device has a working point below this value.

The average GB is  $(69 \pm 11)$  V. Here again, the mean value needed for the REDLEN detectors is somewhat lower, but actually both values agree within their uncertainties. The mean is also very close to the Demonstrator average of 70 V. This indicates, that a GB of 60 V to 80 V seems universally to be a good value, except for detectors where excessive noise prevents the use of comparable voltages, like EV 694242-R and one sector of 694253-2.

In the context of COBRA, several theses covered the topic of working point determination, as it is crucial to detector operation both in the laboratory and at the LNGS. For the Demonstrator detectors, measurements are described in two works [Wes12; Geh17]. Various 6 cm<sup>3</sup> detector were investigated in Dresden [Roh16] and in Dortmund [Arl14]. Although the methodology was similar to what is used here, some notable differences exists, including peak parameterization and optimization criteria.

Compared to earlier campaigns, in this work also much higher BVs are used. First, due to their larger size the 6 cm<sup>3</sup> detector require a higher voltage to achieve the same electric field strength. Furthermore, results from other groups with similarly large detectors indicated that a very high BV of up to 3 kV is beneficial for the detector performance [Zha+12]. Earlier studies by COBRA were largely restricted to voltages of 1 500 V, which may have limited the detector performance<sup>9</sup>.

In Ref. [Roh16] the optimal ratio between GB and BV was stated to be  $\frac{GB}{BV} = \frac{1}{15}$ . The optimal ratio found here is much smaller,  $\frac{GB}{BV} = \frac{(69 \pm 11) \text{ V}}{(2\,200 \pm 300) \text{ V}} \approx \frac{1}{32}$ . This discrepancy might be caused by the limited maximum BV used in Ref. [Roh16]. The GB values obtained also tended to be higher. In terms of field strength the ratio determined in this work is actually close to unity. If 0.05 cm is used as the distance between two anode rails and 1.5 cm as the distance between the cathode and the anode grids the result is  $\frac{GB_{\text{field}}}{BV_{\text{field}}} = \frac{(1\,380 \pm 220) \text{ V/cm}}{(1\,467 \pm 200) \text{ V/cm}} = 0.94 \pm 0.20$ . This result seems to be somewhat

---

<sup>9</sup>The optimal BV for a number of 1 cm<sup>3</sup> detectors is exactly 1 500 V or slightly below. This in principle leaves open the possibility, that the real optimal value without an artificial voltage limit would be even higher.

intuitive, as it means that from the point of view of forces acting upon charge carriers moving through a detector, no potential difference is clearly dominating, although of course these field strengths are not constant throughout the detector.

A general tendency of the optimization based on to the  $s$  criterion instead of the energy resolution is, that slightly lower BV values are preferred. This may be due to the fact that, for most detectors the efficiency only increases little above a given BV, while the resolution often keeps improving more steadily. But due to the definition of  $s$  the resolution is not as strongly weighted as the efficiency in the final results, shifting the optimum to lower values. This behavior also results in a fairly stable<sup>10</sup> working point – small changes in BV or GB do not produce dramatically different results. In general, a stable working point could be found for all detectors, with special treatment needed for only a single detector.

### 5.2.2 Mobility-Lifetime Product

Based on the approach presented in Refs. [Fri+13; Zat14] it is also possible to calculate the mobility-lifetime product for electrons  $\mu_e\tau_e$  based on the optimal weighting factor  $w$  at a the working point. In this reference it is shown that the mean trapping length  $\lambda$  can be expressed purely as a function of  $w$  as explained in section 3.1.  $\mu_e\tau_e$  can be calculated as

$$\mu_e\tau_e = \frac{L^2\lambda}{V_{\text{eff}}} \quad (5.10)$$

with the detector length  $L$ , assumed to be  $(1.50 \pm 0.03)$  cm in this case<sup>11</sup>, and  $V_{\text{eff}} = BV - \frac{1}{2}GB$  the mean potential difference between the anodes and the cathode. For  $w$ , an average across all four sectors  $\bar{w}$  of a CPqG is used, which allows to calculate an uncertainty based on the uncertainty of the mean.

In Table 5.2 the results are shown. The uncertainty on  $\mu_e\tau_e$  is calculated by adding the uncertainties on  $\bar{w}$  and  $L$  in quadrature. The results show a clear distinction between the two manufacturers, with eV detectors having much lower values. The obtained range of values is  $0.75 \cdot 10^{-2} \text{ cm}^2/\text{V}$  to  $1.83 \cdot 10^{-2} \text{ cm}^2/\text{V}$  and the average is  $(1.25 \pm 0.44) \text{ cm}^2/\text{V}$ . This is compatible with the value of  $1.1 \text{ cm}^2/\text{V}$  from Ref. [Fri+13], based on Demonstrator detectors. In Ref. [Amm+09b] a sample of 29 REDLEN detectors with a size of  $1 \text{ cm}^3$  was investigated and a mean value of  $\mu_e\tau_e = 2.2 \cdot 10^{-2} \text{ cm}^2/\text{V}$

<sup>10</sup>Another reason for this stability is the use of a trapping correction via the introduction of a weighting factor  $w$ , which partly compensates the loss in energy resolution due to increased trapping when the BV is lowered.

<sup>11</sup>The uncertainty is based on the maximum difference in detector weights translated into a maximum variation in detector dimensions, assumed to be equal among all three dimensions.

## 5 Large CdZnTe Detectors for the XDEM

was found<sup>12</sup>. This is higher than the mean value of the REDLEN detectors of  $\mu_e\tau_e = (1.65 \pm 0.09) \cdot 10^{-2} \text{ cm}^2/\text{V}$  measured here. In Ref. [Che+08] a somewhat lower value of  $\approx 1.3 \cdot 10^{-2} \text{ cm}^2/\text{V}$  was reported for crystal grown by traveling-heater method. The characterization of an early CPqG test detector from REDLEN [Tem17] yielded  $\mu_e\tau_e = 1.4 \cdot 10^{-2} \text{ cm}^2/\text{V}$ .

In summary, the determination of the  $\mu_e\tau_e$  product shows that the crystal quality of the XDEM detectors should be on par with the quality of the Demonstrator detectors, with a significant advantage of the REDLEN devices over the EV devices. In both cases  $\mu_e\tau_e$  values are reached, which are seen as a sign of high-quality crystals. Given these differences, the lower BVs needed for optimal operation of REDLEN detector is likely caused by the fact that the same mean free path length for electrons can be achieved with lower voltages.

Table 5.2: Calculated  $\mu_e\tau_e$  coefficients for all ten detectors based on the average optimal weighting factor  $\bar{w}$  at the working point.

EV	$\bar{w}$	$\mu_e\tau_e$ [ $10^{-2} \text{ cm}^2/\text{V}$ ]	REDLEN	$\bar{w}$	$\mu_e\tau_e$ [ $10^{-2} \text{ cm}^2/\text{V}$ ]
694242-R	$0.83 \pm 0.02$	$1.08 \pm 0.05$	109026	$0.89 \pm 0.04$	$1.70 \pm 0.10$
694253-2	$0.76 \pm 0.14$	$0.94 \pm 0.18$	109031	$0.87 \pm 0.03$	$1.47 \pm 0.05$
694318-1	$0.80 \pm 0.03$	$0.78 \pm 0.04$	109032	$0.87 \pm 0.04$	$1.64 \pm 0.09$
694318-2	$0.77 \pm 0.03$	$0.66 \pm 0.04$	109033	$0.87 \pm 0.05$	$1.83 \pm 0.13$
694318-3	$0.75 \pm 0.04$	$0.62 \pm 0.04$	109034	$0.87 \pm 0.04$	$1.61 \pm 0.09$
mean		$0.81 \pm 0.16$	mean		$1.65 \pm 0.09$
<b>XDEM</b>		$1.25 \pm 0.44$			

### 5.2.3 Efficiency

To perform a meaningful analysis of low-background data to search for double  $\beta$ -decay, it is necessary to know the probability to measure such a decay close to its  $Q$ -value. To calculate the efficiency  $\epsilon$  effects of an idealized detector have to be taken into account as well as effects of any individual detector, causing  $\epsilon$  to be below that of an ideal device. To do this, the intrinsic efficiency to measure a neutrinoless double  $\beta$ -decay at its full energy  $\epsilon_{\text{int}}$  is taken from Monte Carlo simulations (presented in section 6.1). The relative efficiency of each individual detector  $\epsilon_{\text{Det}}$  is taken from measurements which are shown here have to be combined. To achieve a high accuracy in these measurements,

<sup>12</sup>The reference reports no uncertainty on the result. It also reported a much lower value for EV detectors based on earlier measurements, but gives no detailed information.

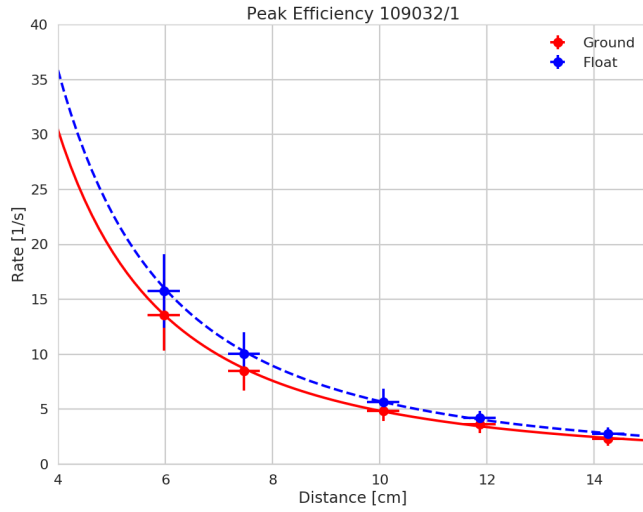


Figure 5.7: The measured rate of events with an energy around 662 keV  $R$  from a  $^{137}\text{Cs}$ -source as a function of the distance between source and detector  $r$ . The case of a floating guard-ring is shown in blue and the case of a grounded guard-ring in red. The fit function is of the form  $R(r) = a/r^2$ .

the detection efficiency is measured for five different distances between source and detector for 15 minutes each. For every distance, the rate of events  $R$  is plotted against the distance  $r$  and a function of the form

$$R(r) = \frac{a}{r^2} \quad (5.11)$$

is fitted to the data, with  $a \propto \epsilon_{\text{Det}}$ , shown in Figure 5.7 for a single sector.  $R$  is calculated by integrating the signal part of peak-shape function described above over its entire range and the result is divided by the measurement time.

This method is adapted from Ref. [Wes12], where it was used for the Demonstrator detectors. For 6 cm<sup>3</sup> CPqG detectors, it was already tested earlier in Dortmund [Dav16]. The same data-set analyzed here was already the subject of Ref. [Hö18], where the method is also explained in great detail. Some points are varied here to be consistent with the other measurements presented, mainly concerning the fit procedure of the  $\gamma$ -spectra.

One crucial point shall be stressed again: The activity of the used  $^{137}\text{Cs}$  source is not well known. As a consequence, the data can only be used to determine relative efficiencies between detectors. This is sufficient, as the detection efficiency for double-

beta decays has to be taken from simulations anyway, but an assumption has to be made for the efficiency of at least one detector to compute a total result. In Ref. [Ebe+16c] it was assumed that the detector with the highest relative efficiency is fully efficient, i. e.  $\epsilon_{\text{Det}} = 1$ . The same assumption is made here. A further advantage of using only relative efficiencies is, that uncertainties related to activity or emission probability cancel out. Thus, only detector size variations and statistical uncertainties are taken into account.

The results for every sector in the case of a floating guard ring are shown in Table 5.3 and for a grounded guard ring in Table 5.4. If the guard ring is left on floating potential, charges from the complete detector volume drift to the CA and the efficiency is maximal. If the guard ring is on ground potential, some charges will end up on it. This reduces efficiency but is also the reason for the reduction of surface related backgrounds. This is way in low-background operation a grounded guard ring will be used. It is nevertheless interesting to judge the loss in signal efficiency by grounding the guard ring. The uncertainty quoted for the mean of the detectors is based only on differences between sectors, as these are usually larger than the uncertainties of the efficiencies of the individual sectors. It can be seen, that both the variations among sectors and among detectors are quite large, more than a factor of two for the sectors of EV 694318-3, and nearly 40% between the least efficient detector EV 694318-3 and the most efficient detector REDLEN 109034.

Table 5.3: Uncorrected detection efficiencies calculated for the case of a floating guard-ring prior to normalization.

Detector	$\epsilon_{\text{Det}}^{\text{float}}$ [a.U.]				
	Sector 1	Sector 2	Sector 3	Sector 4	Mean
<b>eV</b>					
694242-R	$0.90 \pm 0.06$	$1.21 \pm 0.03$	$1.39 \pm 0.02$	$1.36 \pm 0.02$	$1.22 \pm 0.16$
694253-2	$1.18 \pm 0.03$	$1.15 \pm 0.03$	$0.94 \pm 0.04$	$1.18 \pm 0.03$	$1.11 \pm 0.09$
694318-1	$1.19 \pm 0.06$	$1.21 \pm 0.03$	$1.39 \pm 0.02$	$1.36 \pm 0.02$	$1.27 \pm 0.06$
694318-2	$1.14 \pm 0.12$	$1.00 \pm 0.10$	$0.95 \pm 0.09$	$0.94 \pm 0.11$	$1.01 \pm 0.12$
694318-3	$0.59 \pm 0.01$	$0.90 \pm 0.02$	$1.36 \pm 0.02$	$1.05 \pm 0.02$	$0.98 \pm 0.23$
<b>Redlen</b>					
109026	$1.09 \pm 0.02$	$1.17 \pm 0.01$	$1.11 \pm 0.02$	$1.12 \pm 0.02$	$1.12 \pm 0.03$
109031	$1.23 \pm 0.06$	$1.18 \pm 0.07$	$1.15 \pm 0.07$	$1.12 \pm 0.07$	$1.17 \pm 0.08$
109032	$1.22 \pm 0.01$	$1.26 \pm 0.02$	$1.30 \pm 0.02$	$1.26 \pm 0.01$	$1.26 \pm 0.03$
109033	$1.10 \pm 0.12$	$1.21 \pm 0.06$	$1.20 \pm 0.05$	$1.28 \pm 0.05$	$1.20 \pm 0.11$
109034	$1.33 \pm 0.06$	$1.22 \pm 0.03$	$1.30 \pm 0.02$	$1.38 \pm 0.02$	$1.31 \pm 0.02$

Table 5.4: Uncorrected detection efficiencies calculated for the case of a grounded guard-ring prior to normalization.

Detector	$\epsilon_{\text{Det}}^{\text{ground}}$ [a.U.]				
	Sector 1	Sector 2	Sector 3	Sector 4	Mean
<b>eV</b>					
694242-R	$0.90 \pm 0.05$	$1.18 \pm 0.02$	$1.38 \pm 0.02$	$1.37 \pm 0.02$	$1.21 \pm 0.17$
694253-2	$1.00 \pm 0.06$	$1.03 \pm 0.08$	$0.91 \pm 0.07$	$1.00 \pm 0.07$	$0.99 \pm 0.08$
694318-1	$1.09 \pm 0.02$	$1.13 \pm 0.03$	$1.13 \pm 0.03$	$1.10 \pm 0.01$	$1.11 \pm 0.03$
694318-2	$1.22 \pm 0.09$	$0.92 \pm 0.07$	$0.90 \pm 0.07$	$0.87 \pm 0.08$	$0.98 \pm 0.14$
694318-3	$0.57 \pm 0.01$	$0.82 \pm 0.02$	$1.18 \pm 0.02$	$0.99 \pm 0.02$	$0.89 \pm 0.20$
<b>Redlen</b>					
109026	$1.04 \pm 0.01$	$1.08 \pm 0.01$	$1.06 \pm 0.02$	$1.09 \pm 0.01$	$1.07 \pm 0.02$
109031	$1.08 \pm 0.02$	$0.95 \pm 0.02$	$0.96 \pm 0.01$	$1.02 \pm 0.02$	$1.00 \pm 0.05$
109032	$1.03 \pm 0.02$	$1.02 \pm 0.01$	$1.00 \pm 0.01$	$1.07 \pm 0.02$	$1.03 \pm 0.03$
109033	$1.05 \pm 0.04$	$0.99 \pm 0.04$	$0.96 \pm 0.04$	$1.09 \pm 0.04$	$0.98 \pm 0.08$
109034	$1.18 \pm 0.02$	$0.99 \pm 0.01$	$1.09 \pm 0.02$	$1.21 \pm 0.02$	$1.12 \pm 0.08$

Furthermore,  $\epsilon_{\text{Det}}$  is corrected for different detector masses by dividing  $\epsilon_{\text{Det}}$  by the mass-ratio between a given detector and the mean mass of all detectors. This is necessary, as a smaller detector has a smaller probability to capture a photon. For double  $\beta$ -decay, this factor is already taken into account when calculating the number of source atoms.

The remaining effect is a reduction of the fraction of full-energy event, much smaller than the linear reduction in the total number of events with varying detector mass. This was tested for the decay of  $^{116}\text{Cd}$  with a simulation of different detector sizes. A size of  $1.95 \times 1.95 \times 1.45\text{cm}^3$  was compared to a size of  $2.05 \times 2.05 \times 1.55$ , which corresponds to a increase in volume of about 18%. This increase in volume only results in a increase in  $\epsilon_{\text{int}}$  of 1.9%, so an order of magnitude less compared to the volume effect. The maximum deviation in volume of the XDEM detector is smaller than 5%, resulting a negligible error by not taking this additional effect into account.

For the calculation of  $\epsilon_{\text{Det}}$ , devices are compared on a detector level. The results for the case of the guard-ring on ground potential are shown in Table 5.5. It should be noted that the relative values are normalized to the detector with the highest efficiency regardless of the guard ring potential, which is REDLEN 109034 with a floating guard-ring. This is done in order to account for the loss in signal efficiency by using the guard ring. The obtained values for  $\epsilon_{\text{Det}}$  are in the range of  $0.69 \pm 0.15$  to

## 5 Large CdZnTe Detectors for the XDEM

$0.91 \pm 0.13$ , so there is a significant difference among them. The mean value for all EV detectors is  $\epsilon_{\text{Det}}^{\text{eV}} = 0.80 \pm 0.07$  and for all REDLEN detectors is  $\epsilon_{\text{Det}}^{\text{Redlen}} = 0.79 \pm 0.03$ , so the averages are compatible. The mean value for all detectors finally used for the XDEM setup at the LNGS is  $\epsilon_{\text{Det}} = 0.78 \pm 0.04$ . This is somewhat lower than the mean value of all ten detectors, because the most efficient detector<sup>13</sup> with a grounded guard-ring, EV 694242-R, is not included in the XDEM. If the guard-ring is in floating mode the efficiency of the XDEM detectors is increased to  $\epsilon_{\text{int}}^{\text{float}} = 0.88 \pm 0.07$ . This is coincidentally very close to the value of 0.89 obtained for the Demonstrator detectors in Ref. [Ebe+16c].

The efficiency loss introduced by using the guard-ring in grounded mode is 11%, a bit lower than the value of  $14.7 \pm 0.1\%$  measured in Ref. [Arl+17] with a Redlen CPqG from the 2015 batch. As only a single sector was used in this publication, both values can still be said to be in agreement, taking into account the large variations seen in Table 5.3 and Table 5.4. The final efficiency  $\epsilon_{\text{tot}}$  based on the relative efficiency measurements presented here, intrinsic efficiencies presented in section 6.1 and cut-efficiencies is calculated in section 7.5.

Table 5.5: Mass corrected relative efficiencies for the cases of a grounded guard-ring. Detector 694242-R is not used for the XDEM and consequently not included for the XDEM mean.

EV	$\epsilon_{\text{Det}}$	REDLEN	$\epsilon_{\text{Det}}$
694242-R	$0.91 \pm 0.13$	109026	$0.80 \pm 0.02$
694253-2	$0.78 \pm 0.06$	109031	$0.76 \pm 0.04$
694318-1	$0.87 \pm 0.02$	109032	$0.78 \pm 0.02$
694318-2	$0.75 \pm 0.11$	109033	$0.77 \pm 0.05$
694318-3	$0.69 \pm 0.15$	109034	$0.84 \pm 0.06$
mean	$0.80 \pm 0.07$	mean	$0.79 \pm 0.03$
<b>XDEM</b>	$0.78 \pm 0.04$		

### 5.2.4 Energy Resolution

Besides its importance for determining the working point, the energy resolution  $\Delta E$  is an interesting quantity to study in its own right, because it is directly connected to the sensitivity to detect neutrinoless double  $\beta$ -decay ( $0\nu\beta\beta$ )-decay. Even if during the

<sup>13</sup>The high efficiency of this particular detector in operation with a grounded guard-ring may be related to its low GB, which also results in a small volume of the detector affected by the use of the guard-ring.

characterization measurements resolution is only evaluated at 662 keV and not at the actual  $Q$ -value, it already gives a hint at the final performance of the XDEM. Because of the importance of resolution, a FWHM value at 662 keV below 4% was set as a quality criterion for detector purchase. This value was chosen, as a significantly worse resolution not only reduces sensitivity, but calibration becomes increasingly difficult, as peaks can no longer be separated.

Besides that, experience from the 6 cm<sup>3</sup> test-detectors has shown that CPG detectors with  $\Delta E$  above several percent are often affected by a number of further problems, like low efficiency or large noise. As the resolution is also reported by the manufacturers themselves, it is also possible to compare it to Dortmund measurements as a check of quality.

The data used for resolution measurement is identical to the efficiency determination in subsection 5.2.3 for the closest distance, as these are high-statistics data taken with already known working point<sup>14</sup>. Only the case of a grounded guard-ring is analyzed in detail, as this mode of operation is used in the low-background setup. To calculate the FWHM, the full-energy peak is fitted and then points to the left and right of the center at which the height of the function is reduced to 1/2 are determined. This works independent of the amount of tailing. The uncertainties here are purely based on the uncertainty on the mean of sector FWHM, as this is typically much larger than the uncertainty from individual fits.

Table 5.6: Average FWHM resolution for all tested detectors at an energy of 662 keV

EV	FWHM [%]	REDLEN	FWHM [%]
694242-R	$8.3 \pm 4.5$	109026	$2.0 \pm 0.1$
694253-2	$3.5 \pm 1.7$	109031	$2.0 \pm 0.1$
694318-1	$2.7 \pm 0.1$	109032	$2.0 \pm 0.1$
694318-2	$2.2 \pm 0.1$	109033	$2.1 \pm 0.1$
694318-3	$2.4 \pm 0.3$	109034	$2.0 \pm 0.1$
mean	$3.8 \pm 2.1$	mean	$2.0 \pm 0.1$
<b>XDEM</b>	$2.3 \pm 0.4$		

The results for each detector, expressed as the mean and uncertainty of the mean over all sectors, can be found in Table 5.6. It can be seen that all detectors, except for EV 694242-R, are compliant with the 4% quality criterion. Indeed, REDLEN 109031, which was intended to be only a mechanical sample and should have the worst resolution

<sup>14</sup>A possible dependence on the distance between source and detector, or equally the data-rate, was tested with one detector, but none was found

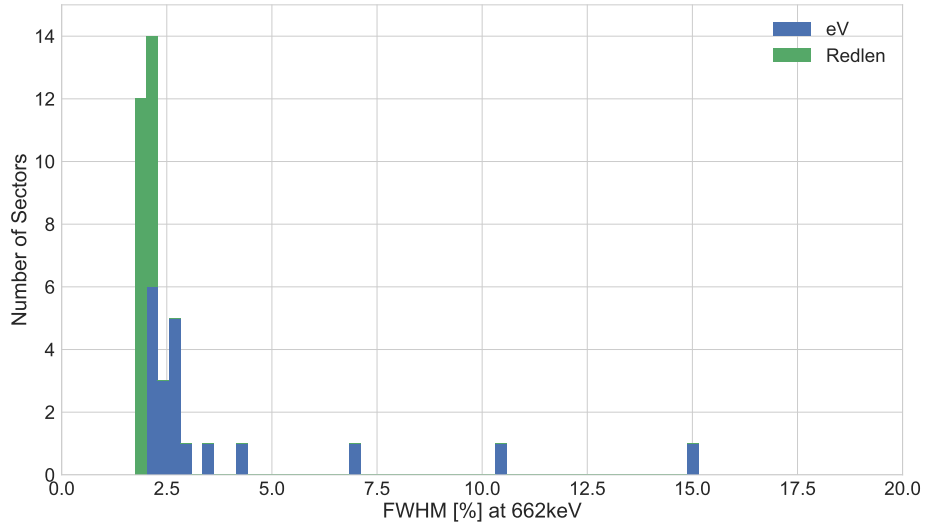


Figure 5.8: Energy resolution at 662 keV on the level of individual sectors as a stacked histogram.

according to REDLEN, shows one of the best resolutions. Many detectors are able to reach  $\Delta E \approx 2.0\%$ , vastly better than the quality criterion.

In Figure 5.8 the results are histogrammed on the basis of individual sectors. It can again be seen that most sectors cluster above 2.0%, but some rather extreme outliers towards higher values exist. The averages for both manufacturers and for all detectors included in the XDEM are given in Table 5.6. The high mean and uncertainty of the EV detectors are mainly driven by 694242-R, but are significantly higher than the REDLEN values even without it. Overall, the mean value is far below the quality criterion and also below the average resolution of the Demonstrator detectors of 2.78% [Wes12]. This is quite surprising, given both the much larger size of the new detectors and the experimental CPqG anode.

In summary it can be concluded that nine detectors exist which are compatible with the quality criteria and can thus be used for the XDEM. Furthermore, it can be anticipated that the energy resolution of the XDEM should at least be comparable to that of the Demonstrator, if not better.

### 5.2.5 Current-Voltage Characteristics

Besides direct measurement of a detectors spectroscopic properties, an often used technique for characterization is the I-V characteristic. For CPG detectors, both the bulk- (between cathode and anodes) and the grid-leakage (between CA and NCA) currents are of interest. Such measurements can provide information about the electrical properties of the crystal bulk, surface and contacts. It is usually necessary to observe currents over a wide range of voltages – which is not trivial due to the high resistivity of the material – and then to fit the data to some known function. Direct information can also be extracted, like the absolute value of leakage currents at a given voltage to assess its contribution to the noise and ultimately the energy resolution<sup>15</sup>. Often, high leakage currents are associated with either crystal defects, which form regions of lower resistivity, or a large amount of charge carrier traps shifting the Fermi level [Sch+01].

To simplify the measurement process, sectors of a detector are not treated individually, but the total current between all grids, or between the cathode and all anodes, is measured. Also, no distinction is made between bulk and surface currents, i. e. between the current flowing through the CdZnTe itself and across its surface. This is in principle possible if the guard-ring is treated separately but would increase measurement complexity. Because of this, the reported leakage currents are larger than what each individual sector would measure during real operation. Only about one quarter of the total current contributes in each sector minus surface leakage blocked by the guard-ring. Nevertheless, as this affects all detectors in the same way, it does not impede the possibility to compare devices quantitatively.

The number of voltage steps was slightly adjusted during the characterization campaign to speed-up the process. For all measurements the step-width was at least 25 V bulk I-V and 5 V for grid I-V. Usually, a range of 0 V to 3 000 V was considered for bulk measurements, except for detector 694318-3, where voltage was initially limited to 2 600 V. Grid I-V curves were always taken in the range 0 V to 120 V.

The current and voltage reported by the ISEG SHQ224 are averaged over ten individual measurements. Uncertainties of the device itself are given by the manufacturer to be well below 0.1% of the absolute value in the case of voltage, and 0.05% of the absolute value plus a constant value of 2 nA in case of current. These are negligibly small – the relative term gives ( $\pm 0.05$  nA for an absolute current of 100 nA) and the

---

<sup>15</sup>Different sources of noise are combined in quadrature, so that a contribution like the leakage current quickly becomes dominant if it is increased only by a moderate degree.

constant term affects all individual measurements in the same way<sup>16</sup>. Only the finite precision of 0.1 nA is of interest, which is also generally small compared to the absolute value.

Another limitation is, that very small currents ( $\leq 2$  nA) can not be detected at all. This gives further reason not to treat all four sectors and the guard-ring individually, as this would decrease the currents even further. To observe the behavior of the electrical contacts, it is necessary to take I-V-curves in the range of some Volts, as the difference of the work function between the CdZnTe and the metal of the contact is on the order of some eV. Thus, it is not possible to observe this with the given equipment. In fact, for some detectors the current only becomes measurable well above 1000 V.

The bulk I-V curves of the detectors 109031 (red) and 694242-R (green) are shown as two examples in Figure 5.9. In Figure 5.9 grid I-V curves from the same detectors are shown. The size of leakage currents differs by almost an order of magnitude between the detectors in both cases. The increase in voltage is also rather different.

The grid I-V curves show similar behavior. Astonishingly, at small bias voltages the leakage currents of 694242-R are a bit lower than for 109031, but due to the super-linear increase of 694242-R, at a voltage of 120 V the difference between the two detectors is almost 200 nA. While these two are extreme cases, they exemplify that each detector shows a unique behavior and important features in some I-V curves are completely absent from other ones. With regard to the results from subsection 5.2.1 this shows that an increase in voltage is in general not reflected by a proportional increase in noise. The behavior is more complex and detector dependent.

A common function<sup>17</sup> to parameterize bulk I-V curves is

$$I = aV^b \tag{5.12}$$

where  $b$  is called the ohmicity, as a value of 1 would represent a perfect ohmic resistor, and  $a$  is some normalization factor [Sch+01]. Some authors also applied a more detailed theory [Bol+02] based on the interfacial layer-thermionic-diffusion model. This model treats the detectors as a metal-semiconductor-metal system. This more complex model is not applied here, as it requires assumptions about several unknown parameters.

---

<sup>16</sup>If the values presented here are to be compared to values obtained with another measurement device, this should be taken into account.

<sup>17</sup>I-V curves with two clearly different regimes, e.g. a linear part at low voltages and a quadratic part at higher voltages, are also sometimes reported, but such an effect is not included in the fit here, as it is not easy to define the exact point of transition in a rigorous manner.

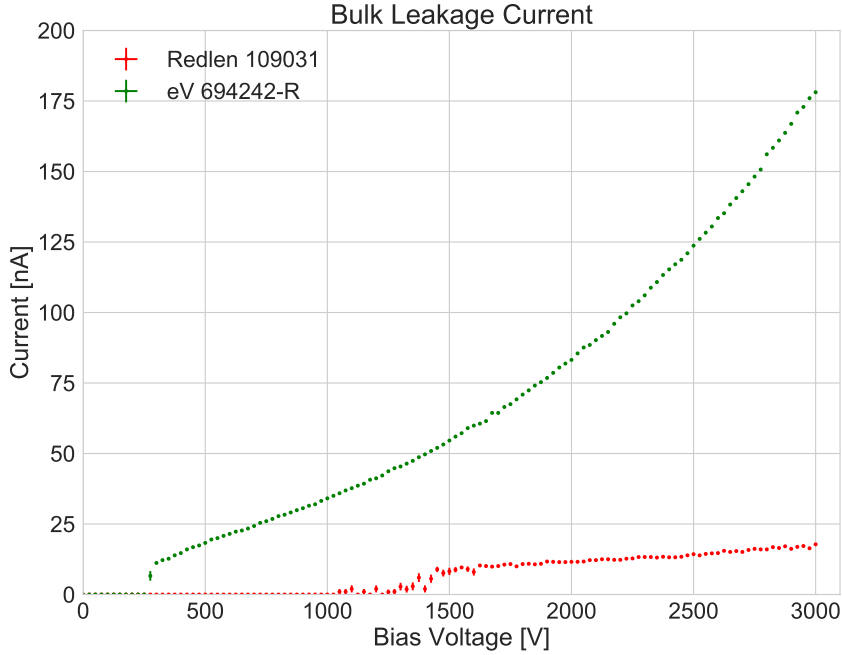


Figure 5.9: Bulk leakage currents as a function of applied voltage for EV 694242-R (green) and REDLEN 109031 (red).

Also, bias voltages have to be varied in a wide range from  $1 \cdot 10^{-2}$  V to  $1 \cdot 10^{-4}$  V to gather information about all components of this model, which is not possible to do here given the limitations described above. But the model of Ref. [Bol+02] makes two qualitative predictions about the behavior of the detectors. First, at bias voltages considered here, the bulk leakage current is not determined by the bulk resistivity of the CdZnTe, but in fact diffusion limited. This means, that the current will be lower in this regime than expected from the bulk resistivity. Second, if the bias voltage is further increased leakage currents rise exponentially. The increase is governed by the properties of the non-conductive layer between the CdZnTe and the metal interfaces. The non-conductive layer is supposed to form by oxidization of the CdZnTe surface. The exponential increase in currents is due to a lowering of the barrier height at this interface with rising voltage. In general, the effect should be stronger if the non-conductive layer is thicker.

Due to the fact that the minimal voltage at which a current is measurable varies, the fit to Equation 5.12 was conducted in two different ways. In the first version, the complete range of accessible voltages is considered to extract the maximum amount of

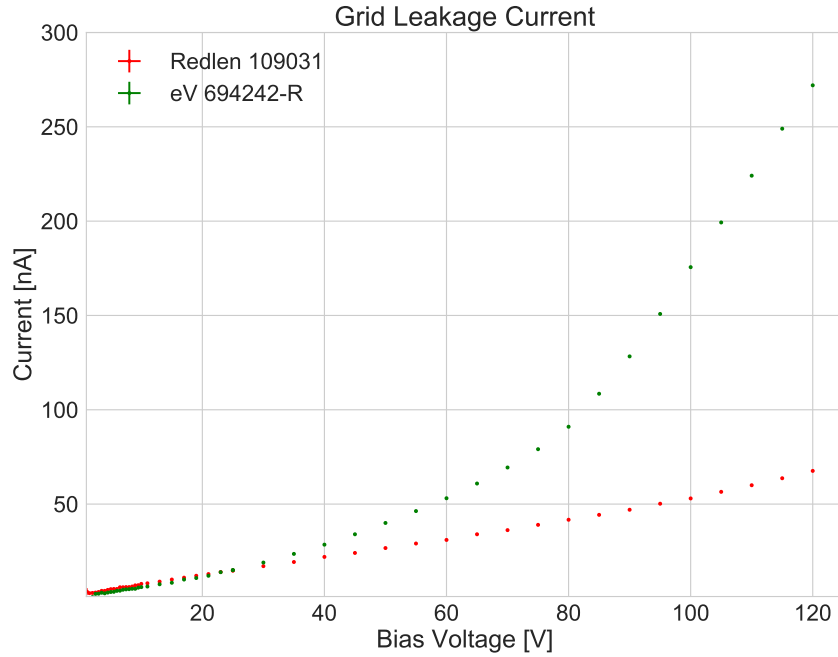


Figure 5.10: The same as Figure 5.9, but for grid leakage currents.

information from the I-V curves. This lowest voltages with a measurable current vary from 125 V for 694253-2 and 1 600 V for 109033 and 109034. This makes a comparison between different detectors difficult, which is why a second fit was conducted with a fixed threshold of 1 500 V. This is high enough for nearly all detectors to produce a measurable current and still comprises half the voltage range, especially all value used for actual detector operation.

An example of such these fits can be seen in Figure 5.11, where a bulk I-V curve of detector 694253-2 is shown, with the complete fit as a green dashed line and the restricted fit above 1 500 V as a blue dot-dashed line. It can be seen that no fit is able to reproduced the data well at all voltages, but the overall agreement is better for the complete fit, while it is better for higher voltages in the restricted case. What is noticeable regardless of the chosen fit range, is that there is a big deviation from ohmicity in both cases, making the detectors quite imperfect conductors.

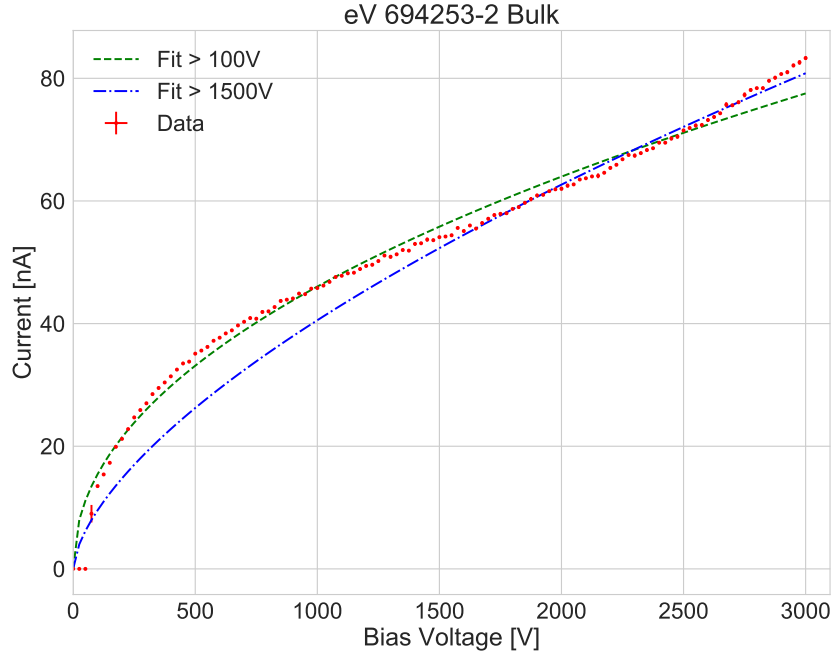


Figure 5.11: Bulk I-V curve for eV 694253-2 shown with two different fits of the form  $I = aV^b$ . In one case all values above a voltage of 100 V are used for the fit, while in the other case only values above 1 500 V are used. In both cases the fit is rather poor for this detector.

Results of the fits from all detectors are summarized in Table 5.7. The parameter  $a$  is not quoted, as it has no straight-forward interpretation. Beside the fit parameter  $b$ ,  $\chi_{\text{red}}^2$  is given as a measure of goodness-of-fit. Usually,  $\chi_{\text{red}}^2$  is smaller for the restricted range. But I-V curves that can not be fitted well with Equation 5.12 over the whole range still have a comparatively large  $\chi_{\text{red}}^2$  even in the restricted case.

The REDLEN detectors all produce  $b \approx 1$ , with a slight tendency to be lower and the lowest value being  $0.89 \pm 0.02$ . At the same time, the fits tend to be rather good with the values of  $\chi_{\text{red}}^2$  being the range of 0.4 to 2.0. EV detectors 694318-2 and 694318-3 behave similarly, but the remaining three detectors show a large deviation from this, with  $b$  far from 1 and  $\chi_{\text{red}}^2$  between 4.0 to 427.3, indicating that it is not possible to reproduce the shape of their I-V curve with Equation 5.12. Some detectors show a quasi exponential increase at high voltages. This exponential rise may be seen as an example of the rise in voltage due to lowering of the barrier height at the metal-semiconductor surface. If this is the case, it can be concluded that the non-conductive oxide layer at

the surface should be much thicker for e. g. 694242-R than for 109031.

Table 5.7: Results from the fit described in the text for all potential XDEM detectors for two different fit ranges. In each case the value of the parameter  $b$  and its corresponding uncertainty and  $\chi_{\text{red}}^2$  are given.

	$b_{\text{tot}}$	$\chi_{\text{red}}^2$	$b_{\geq 1500\text{V}}$	$\chi_{\text{red}}^2$
<b>eV</b>				
694242-R	$1.52 \pm 0.02$	135.3	$1.77 \pm 0.02$	4.6
694253-2	$0.48 \pm 0.01$	14.9	$0.63 \pm 0.01$	4.3
694318-1	$0.36 \pm 0.02$	427.3	$0.22 \pm 0.01$	4.0
694318-2	$0.94 \pm 0.01$	0.9	$1.00 \pm 0.01$	0.7
694318-3	$0.71 \pm 0.01$	3.6	$0.90 \pm 0.01$	0.8
<b>Redlen</b>				
109026	$0.95 \pm 0.01$	0.8	$1.00 \pm 0.01$	0.6
109031	$1.00 \pm 0.02$	0.8	$1.02 \pm 0.02$	0.8
109032	$0.93 \pm 0.02$	0.9	$0.96 \pm 0.02$	0.8
109033	$0.93 \pm 0.02$	0.5	$0.92 \pm 0.02$	2.0
109034	$0.92 \pm 0.02$	0.4	$0.89 \pm 0.02$	0.5

For the grid I-V curves, no similar widely used function exists in the literature, probably due to the fact that many different anodes designs are in use. Consequently, these curves are not fitted. Nevertheless, it can be noted that all curves have a tendency to look like an exponential increase, but with very different slopes. Two examples are given in Figure 5.9, where it can be seen that 109031 rises nearly linearly over the entire range, while the exponential increase is clearly visible for 694242-R.

The results for both bulk and grid I-V curves are summarized in Table 5.8. There, measured currents of the bulk and the grid are given once at the working point, and at 1500 V for the bulk and 60 V for the grid. The working-point current is the value that matters most for the final detector performance, while it is easier to compare devices at fixed parameters. The mean values for both EV and REDLEN are also presented. In general, the current for REDLEN detectors are rather low and well below 20 nA at the working point for the bulk and around 30 nA for the grid. Detector 109031 with a grid current of  $(49.0 \pm 0.1)$  nA is the only exception.

For these detectors, the grid leakage current is clearly dominating the contribution of leakage currents to noise. Leakage currents of EV detectors are all much higher. In the most extreme case of detector 694318-1 the bulk current is  $(118.6 \pm 0.2)$  nA. For these detectors, sometimes the bulk and sometimes the grid leakage is dominant. But, while both are in general higher, the tendency is much stronger for the bulk current.

## 5.2 Characterization of XDEM Detectors

This conclusion is independent of whether the current is measured at the working point or at a fixed voltage. Looking at the mean values for both manufacturers at a fixed voltage, bulk currents for EV detectors are five times higher than for REDLEN detectors, while the difference is only a little over 50% for grid currents.

Table 5.8: Leakage currents for grid and bulk for two voltages.

	$I_{\text{Bulk}}$ at WP	$I_{\text{Grid}}$ at WP	$I_{\text{Bulk}}$ at 1 500 V	$I_{\text{Grid}}$ at 60 V
<b>eV</b>				
694242-R	$98.3 \pm 0.1$	$23.6 \pm 0.2$	$54.6 \pm 0.3$	$53.1 \pm 0.2$
694253-2	$58.7 \pm 0.1$	$36.0 \pm 0.0 / 79.0 \pm 0.2$	$54.1 \pm 0.2$	$79.0 \pm 0.2$
694318-1	$118.6 \pm 0.2$	$52.8 \pm 0.1$	$106.3 \pm 0.2$	$41.2 \pm 0.1$
694318-2	$24.0 \pm 0.2$	$43.0 \pm 0.0$	$14.2 \pm 0.2$	$29.9 \pm 0.1$
694318-3	$42.3 \pm 0.3$	$71.0 \pm 0.0$	$25.7 \pm 0.1$	$49.5 \pm 0.2$
Mean	$68.4 \pm 17.6$	$45.3 \pm 8.0$	$51.0 \pm 15.9$	$50.5 \pm 8.2$
<b>Redlen</b>				
109026	$17.3 \pm 0.2$	$29.7 \pm 0.1$	$12.8 \pm 0.2$	$29.7 \pm 0.1$
109031	$14.2 \pm 0.3$	$49.0 \pm 0.1$	$10.4 \pm 0.2$	$37.7 \pm 0.1$
109032	$14.2 \pm 0.4$	$33.5 \pm 0.2$	$9.8 \pm 1.1$	$33.5 \pm 0.2$
109033	$10.8 \pm 0.2$	$31.0 \pm 0.1$	$8.2 \pm 1.3$	$31.0 \pm 0.1$
109034	$13.0 \pm 0.1$	$31.0 \pm 0.1$	$9.7 \pm 1.0$	$31.0 \pm 0.1$
Mean	$13.9 \pm 1.1$	$34.8 \pm 3.6$	$10.2 \pm 0.7$	$32.6 \pm 1.4$

In conclusion, one can say that I-V characteristics of the detectors are all rather different, especially among EV detectors. This is true for both the shape of the curves as well as the absolute currents measured at a given voltage. Large deviations from ohmicity for the EV detector hints at issues with their contacts, i.e. a large oxide layer. Compared to the resistivity given in Table 3.2, the apparent bulk resistivity measured here seem to about one order of magnitude larger, e.g.  $1.2 \cdot 10^{-11} \Omega/\text{cm}$  for 109033 at 1 500 V. Bulk leakage currents vary much more than grid leakage currents.

Although there is no complete correlation between leakage currents and energy resolution, it is striking that the three detector with the worst resolution are also outliers in term of leakage currents. All of them are EV detectors. 694242-R has the worst resolution and the second highest bulk leakage current. 694253-2 has the second worst resolution and shows a high leakage current at least in one sector and also one of the highest bulk leakage currents. 694318-1 also has rather bad resolution and shows high bulk leakage even at low BV. Those three detectors also show the largest deviation from ohmicity, as well as the largest  $\chi_{\text{red}}^2$ . It is thus likely that their bad performance is related to contact issues. A further indication for this assumption

is that the cathode of 694242-R obviously has only low adhesion to the CdZnTe and the electrode design of this device is considered experimental by the manufacturer, as mentioned in subsection 4.2.1.

### 5.2.6 Conclusion of Characterization Measurements

The measurements presented in this section each provide information about the XDEM detectors informing the decision which of them can be used for the XDEM underground setup and about the possible performance of it. The determination of the working point was a necessary step in order to achieve optimal performance both in the laboratory and the underground setup.

It turned out, that a sufficient number of devices exists, that pass the quality criteria and behave reasonably well for a stable long-term operation. As a general trend, the REDLEN detectors show a better energy resolution while needing lower voltages to achieve this, while the detection efficiency is fairly equal among both manufacturers, but has a quite large variation across individual detectors. The behavior of the energy resolution can at least partly be explained by looking at the leakage current measurements. EV detectors in general have much higher bulk- and moderately higher grid-leakage currents, which degrades the energy resolution. The shape of the I-V-curves of some EV detector might also hint at issues with their electrodes. This effect is enhanced by the fact that these detectors need higher voltages for the bulk to achieve optimal performance, which is compatible with lower values of  $\mu_e\tau_e$  found here. Overall, a similar or better spectroscopic performance should be anticipated for the XDEM than has been achieved with the demonstrator.

## 6 Simulations for the XDEM phase

Monte Carlo (MC) simulations are a helpful tool to gain a better understanding of the detectors themselves as well as low-background spectra acquired with the XDEM. In this chapter, MC simulations are used to determine the detection efficiency  $\epsilon_{\text{int}}$  for neutrinoless double  $\beta$ -decay ( $0\nu\beta\beta$ ). They are also used to generate background projections based on externally measured activities of various materials used in the XDEM. All simulations shown here were performed with the COBRA toolkit VENOM [Koe12; Ned14] based on Geant4 [Ago+03; All+16].

### 6.1 Efficiency Calculations

As there is no way to introduce  $\beta$ -emitters with a mono-energetic spectrum near the  $Q$ -value of e. g.  $^{116}\text{Cd}$  homogeneously and with a sufficient activity in to the detector material the intrinsic efficiency  $\epsilon_{\text{int}}$  of a detector can only be simulated. Intrinsic efficiency means the efficiency based on the material properties and geometry alone, i. e. the fraction of events that deposit all their energy inside the detector, regardless of what is eventually measured in reality. This does not take into account effects due to the finite energy resolution, charge transport, or possible inactive regions of the detector, but is a value common to all detectors of same the material and geometry.

In earlier works performed in the context of the Demonstrator, some uncertainty surrounded this topic, as the obtained value was not the same in all versions of GEANT4. Here, the most recent GEANT4 version at the time of simulation, 10.4, is used. To test for systematic effects caused by various approximations needed to perform a simulation in a limited amount of time, a number of parameters are varied. One of these is the so-called *physics list*. This list encodes physical processes by means of tabulated, measured cross sections and interpolations. Several of physics lists are available, as GEANT4 is used for a large range of applications requiring precision at different energy scales. Most of the physics list are optimized for high-energies found at particle colliders. They are thus of no interest for this work.

Two lists considered here are the LBE, and the SHIELDING list. The SHIELDING

list was originally designed to be used in the simulation of shieldings for ionizing radiation, especially at particle accelerators. This task is related to the task at hand and thus the SHIELDING list is sometimes recommended to be used for the simulation of low-background underground experiments [Geab]. The LBE list on the other hand is based on the *Underground Advanced* example simulation code for an imaginary underground experiment, delivered as part of GEANT4 itself. In addition, for every physics list it is possible to change the electromagnetic part individually to several different models, called *EM options* [Geaa]. Six EM options suitable in this context are considered here.

All physics lists and EM options make use of approximations of the underlying physical laws. In particular, they make use of cuts in the low energetic part, i. e. particles below a certain energy are simply stopped instead of propagated further. As the energy loss of a charged particle per single interaction get increasingly small, a large number of steps would have to be computed that have little influence on the final result if not cut is used. To be independent of the material through which the particle propagates, cuts in GEANT4 are expressed in terms of the (remaining) range of the particle in a material. If for example a cut of 1 mm is used, the particle will be propagated until its remaining range is below 1 mm irregardless of whether it is propagating in air or lead. If the cut is set to a value much lower than any dimension of interest (like detector size), this should give a valid approximation of the real physical laws. But a too large value influences the results. Here, the range-cuts for both electrons and photons were varied in a large range from 1 nm to  $10^7$  nm, but only exemplary for the SHIELDING list. This is done in order to test for systematic effects from a variation of these cuts.

The simulated detector geometry is a single crystal of dimensions  $20 \times 20 \times 15$  mm<sup>3</sup> divided into four sectors of exactly equal size. No coating or electrodes are implemented. This setup is somewhat simplified compared to the real XDEM setup, but as only internal decays within the detector volume are simulated, it should be sufficient. As the range of electrons from  $\beta$ -decay in CdZnTe is rather short, multi-detector events will not play a significant role. Furthermore, such events will likely be disregarded in a real analysis to reduce background. For each simulation, the efficiency was calculated based on the total energy deposition in a detector  $\epsilon_{\text{Sum}}$ , and interactions in a single sector  $\epsilon_{\text{Single}}$ . For each configuration,  $10^6$  events are simulated.

The initial-state kinematics are not calculated by GEANT4 itself, but are provided by a so-called event generator. For double-beta decay, two different options currently exist in VENOM. One is the internal generator of VENOM, DBGEN. The other possibility

Table 6.1: Full energy detection efficiencies for the decay of the five  $0\nu\beta^-\beta^-$  isotopes, simulated with standard EM options and the DECA0 generator and two different physics lists. The uncertainties of the individual simulations from statistics alone are below 0.001. The uncertainty of the mean is given as the difference between the two models added in quadrature to the statistical uncertainty.

Isotope	$\epsilon^{\text{Single}}$			$\epsilon^{\text{Sum}}$		
	LBE	SHIELDING	MEAN	LBE	SHIELDING	MEAN
$^{70}\text{Zn}$	0.905	0.908	$0.907 \pm 0.003$	0.935	0.937	$0.936 \pm 0.002$
$^{114}\text{Cd}$	0.963	0.964	$0.964 \pm 0.001$	0.976	0.976	$0.976 \pm 0.001$
$^{116}\text{Cd}$	0.625	0.636	$0.631 \pm 0.011$	0.710	0.719	$0.714 \pm 0.009$
$^{128}\text{Te}$	0.921	0.925	$0.923 \pm 0.004$	0.946	0.949	$0.947 \pm 0.003$
$^{130}\text{Te}$	0.671	0.680	$0.676 \pm 0.009$	0.750	0.757	$0.753 \pm 0.007$

is to use the DECA0 code<sup>1</sup>, which is widely used in the field of double  $\beta$ -decay.

Sizable variations of the efficiency up to 1.8% come from the changed physics list, as can be seen in Table 6.1. The effect is especially pronounced for isotopes with a high  $Q$ -value, like  $^{116}\text{Cd}$  or  $^{130}\text{Te}$ , and becomes negligible at low  $Q$ -values like in the case of  $^{114}\text{Cd}$ . Some, but not all, EM options also produce significant changes in the results. The GOUDSMIT-SAUNDERSON option in particular results in an efficiency slightly below 1% smaller than other options. The results of all other options are in agreement. As five out of six options basically give the same results, the slight deviation using GOUDSMIT-SAUNDERSON will be neglected.

No systematic difference is found using the two event generators. The range cuts only have an influence if cut values similar to the dimensions of the detector itself are chosen. As this is never the case if standard options are used and in line with expectations, their influence is consequently ignored in the further discussion. In the end, the total efficiency uncertainty is calculated by adding in quadrature the statistical uncertainties and the difference between the two physics lists. The results are given in Table 6.1.

All values are close to the ones obtained by the same author with standard settings of GEANT4 10.00 in Ref. [Tem15]. Compared to the results for  $1\text{ cm}^3$  detectors stated in Ref. [Ebe+16c], the efficiency of the XDEM detectors is only marginally higher for  $^{114}\text{Cd}$ . For low energies it is close to unity in both cases anyway. But it is about 15% higher for  $^{116}\text{Cd}$ , reflecting the larger detector size and showing again their principal advantage.

<sup>1</sup>Here, a version of the code ported to C++ is used instead of the original FORTRAN code, which can be found at [Mau]

## 6.2 Background Estimation

A model of the energy spectrum is important for a low-rate experiment, as it allows for a quantitative understanding of the background. An analysis of its most important components may hint at ways to lower the background. In particular, a such a model is important to disentangle signal and background contributions if a signal is indeed found, especially if the signal one is looking for is not simply a peak, e. g. in the case of two-neutrino double  $\beta$ -decay ( $2\nu\beta\beta$ )-decays.

To create such a model, one needs both good knowledge of background sources and reliable MC simulations to estimate the detector response in presence of these sources. Information about possible sources are usually obtained by measuring the activity of a given sample, e. g. a part of the shielding, with an external detector like a HPGe  $\gamma$ -spectroscopy system or via inductively coupled plasma mass spectrometry (ICP-MS). If the material is very common, information might also be available from databases [Loa+16], or even as part of 'common knowledge' in the literature, e. g. Ref. [Heu95]. External background sources can also be parameterized as fluxes and are usually available for underground laboratories like LNGS, see section 3.2. Measurements done as part of the XDEM project and relevant results from earlier campaigns can be found in Appendix A. If only upper limits are reported there, these are taken as a conservative estimate of the true value. For MC simulations the VENOM framework – as laid out in the previous section – is used together with the *Shielding* physics list.

The status of the background model as presented here is incomplete. Not all potential background sources are taken into account at this point. This is due to the large number of possible sources one has to considered and which all need to be properly implemented into the MC-model. Running a simulation can be time consuming as in some cases a large number of events needs to be simulated to achieve statistically meaningful results. For example, the simulation of the  $^{232}\text{Th}$ - and  $^{238}\text{U}$ -chains in this work comprise  $10^{11}$  events each. Also, most earlier works focused on either the Demonstrator-array or a future large-scale experiment [Hei14] with different geometry and background sources and hence can not be used here. Consequently, the development of the XDEM model so far focused on parts that are expected to give the biggest contribution. This is either because of their vicinity to the detectors (detector coatings and holder) or because of the large mass (shielding) and for which it is known that some contamination with radioisotopes is present.

A detailed account of the modeling of background contributions from the detector-coating, -holder, and  $2\nu\beta\beta$ -decays is given in Ref. [Her18]. The results from this work

are incorporated here into a larger mode. They are combined with results obtained for various components of the shielding that will be discussed in the following. Uncertainties will be only briefly discussed here. The activity of every isotope in each component has its own uncertainty of up to 50%. Sometimes only limits or averages values are known, or the activity has to be guessed based on values from the literature. Finally, the measured samples do not have to be a perfect representation of the finally installed parts. Thus, values presented here are only intended to give a rough indication of the real background.

For background estimation, the shielding is divided in four parts, for each of which a different level of information is available:

1. Parts of copper shielding produced for the XDEM: Together with the XDEM parts, a sample measured at the OBELIX detector [Loa+15] was produced, which was used to search for contamination by long-lived decay chains, but also cosmogenic activation. Exposure to cosmic rays of this sample was the same as for the XDEM parts. The exposure history is summarized in subsection 4.2.4.
2. Parts of copper shielding produced for the Demonstrator: These parts were produced from the same copper stock as the XDEM parts, but the exposure to cosmic rays was different. Thus, the same level of contamination by decay-chains can be assumed, but cosmogenic activation is conservatively estimated to be 50% higher than for XDEM parts. The combined mass of all copper parts is 79 kg.
3. Parts from ultra low activity (ULA) lead: The activity of  $^{210}\text{Pb}$  was certified to be  $A(^{210}\text{Pb}) = (3.4 \pm 2.6) \text{ Bq/kg}$ . The contamination with long-lived isotopes is taken from the literature. The mass of ULA lead parts is 267 kg.
4. Standard lead: Here, the activity is scaled up from measurements of the ULA lead. The mass of standard lead parts is 2212 kg

For copper it is of special interest to look for cosmogenic activation products, as production rates in copper are comparatively high and saturation activities up to 1 mBq/kg can be reached for isotopes like  $^{60}\text{Co}$ . Results from a search for commonly isotopes produced by activation can be found in Table 6.2. The considered isotopes all have half-lives between more than a month and about five years. Isotopes with much shorter half-life are usually not of interest, as their activity quickly declines when they are brought underground, while isotopes with much longer half-life are not produced in large enough number to have a significant activity.

## 6 Simulations for the XDEM phase

Table 6.2: Relevant products of cosmogenic activation on copper. The production rate  $R$  from Ref. [LH09] is used to estimated an activity  $A_{\text{calc}}$ .  $A_{\text{meas}}$  represents activities measured in a sample of the copper used for the XDEM with the OBELIX detector.  $t_{\text{exp}}^{\text{eff}}$  is the exposition time giving the best fit of  $R$  to  $A_{\text{meas}}$ .

Isotope	$t_{1/2}$	$R$ [1/kg/d]	$A_{\text{calc}}$ [mBq/kg]	$A_{\text{meas}}$ [mBq/kg]	$\frac{A_{\text{calc}}}{A_{\text{meas}}}$	$t_{\text{exp}}^{\text{eff}}$ [d]
$^{54}\text{Mn}$	312 d	$18.6 \pm 1.8$	$0.05 \pm 0.01$	$<0.02$	$<2.5$	$<40$
$^{56}\text{Co}$	77 d	$19.9 \pm 2.6$	$0.15 \pm 0.02$	$0.07 \pm 0.02$	$2.1 \pm 0.7$	48
$^{58}\text{Co}$	71 d	$142.6 \pm 7.8$	$1.14 \pm 0.06$	$0.29 \pm 0.06$	$3.9 \pm 0.8$	20
$^{60}\text{Co}$	5.3 yr	$181 \pm 16$	$0.09 \pm 0.01$	$<0.02$	$<4.5$	$<27$

The measured activities  $A_{\text{meas}}$  of the copper sample are contrasted with calculated activities  $A_{\text{calc}}$  based on production rates  $R$  measured in Ref. [LH09] and an exposure to cosmic rays at sea level for about  $t_{\text{exp}} = 120$  days. This is the time between taking the copper stock out of the Felsenkeller underground laboratory in Dresden where it was stored and when it was brought deep underground into the LNGS.  $^{46}\text{Sc}$ ,  $^{57}\text{Co}$  and  $^{59}\text{Fe}$  were considered in Ref. [LH09], but not searched for in the measurements. These isotopes have either a small production rate ( $^{46}\text{Sc}$ ), low energetic  $\gamma$ -rays ( $^{57}\text{Co}$ ) or short half-life ( $^{59}\text{Fe}$ ). Only for  $^{56}\text{Co}$  and  $^{58}\text{Co}$  a significant activity could be measured, with  $A_{\text{meas}}(^{56}\text{Co}) = (0.07 \pm 0.02)$  mBq/kg and  $A_{\text{meas}}(^{58}\text{Co}) = (0.29 \pm 0.06)$  mBq/kg. These are corrected for the activity at the start of the measurement.

One can see that  $A_{\text{calc}}$  is always bigger by a factor of two to five than  $A_{\text{meas}}$ . The measured activities can also be converted into an effective exposure time  $t_{\text{exp}}^{\text{eff}}$ , which is the time that would result in an activity of  $A_{\text{meas}}$  if exposure would have taken place under worst-case conditions and with the given production rates. The values obtained this way are  $20 \text{ d} \leq t_{\text{exp}}^{\text{eff}} \leq 48 \text{ d}$ .

The measured results can also be compared to results obtained with a copper sample exposed to cosmic rays for 41 days in Ref. [Coa+16]. There, higher activities for all isotopes are reported. This gives further indication for the assumption that activation did not take place with rates  $R$  as given in Table 6.2 for the full 120 days. Literature values for  $R$  vary by over a factor of two in some cases (see e.g. Ref. [Bau+15]) and the true rate might be lower than reported in Ref. [LH09]. Furthermore, the shallow overburden of the workshops reduced the cosmic ray flux, resulting in a smaller  $R$  than reported in the literature. In conclusion, the combination of quick processing under a shallow overburden and long-term underground storage beforehand resulted in a small activities of cosmogenic activation products.

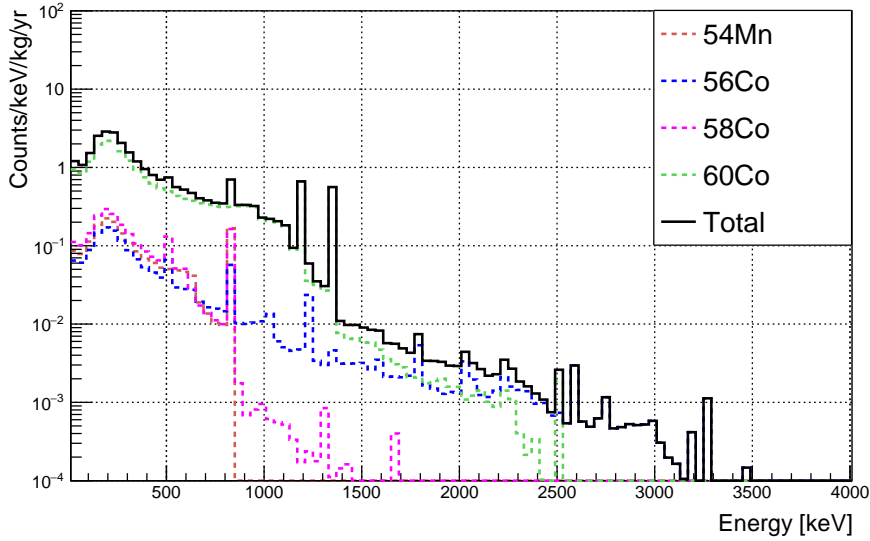


Figure 6.1: Simulated spectrum of the background contribution of various isotopes produced through cosmogenic activation of the copper shielding. The rates of each decay are based on externally measured activities.

As the half-life of the considered isotopes is comparable to the measurement duration of the XDEM, one also has to take into account their decay between the time the parts were brought underground and the start of the experiment  $t_{cool}$ , as well as their decay during measurement time  $t_{meas}$ . Here,  $t_{cool} = 180$  d is assumed. The XDEM was installed in late March 2018 and full data-taking started in early November 2018 (the reasons are given in subsection 4.2.1). Also,  $t_{meas} = 3$  yr is assumed.

For the copper part already installed for the Demonstrator a 50% higher activity at start and  $t_{cool} = 180$  d + 6 yr is assumed. 6 yr are roughly the time between installation of the first Demonstrator layer and the XDEM parts. This is very advantageous, as basically all isotopes except for  $^{60}\text{Co}$  have decayed since then. Under these assumptions in Figure 6.1 one can see the resulting spectra based on  $A_{meas}$ .  $^{60}\text{Co}$  gives the greatest contribution up to energies of about 2200 keV. Above this,  $^{56}\text{Co}$  dominates and is in fact the only contribution at the  $Q$ -value of  $^{116}\text{Cd}$ . As  $^{56}\text{Co}$  has a rather short half-life of 77 days, the choice of  $t_{cool}$  and  $t_{meas}$  play a large role, as they together amount to about 16 times the half-life resulting in a more than 50 000-fold reduction of activity. If  $t_{meas} = 191$  d is assumed, as is the case for data analyzed in chapter 7, the background can be up to an order of magnitude higher.

## 6 Simulations for the XDEM phase

Not only products of cosmogenic activation but also contamination with primordial decay-chains is important. In the copper sample the activity of the  $^{232}\text{Th}$ -chain is  $(0.10 \pm 0.02)$  mBq/kg and that of the  $^{238}\text{U}$ -chain is  $(0.12 \pm 0.03)$  mBq/kg. Both chains are assumed to be in equilibrium and their activity is conservatively derived from their daughter-isotope with the highest measured activity. Also,  $^{40}\text{K}$  and  $^{137}\text{Cs}$  are present with activities of  $(0.32 \pm 0.08)$  mBq/kg and  $(0.24 \pm 0.05)$  mBq/kg respectively. Again, simulated spectra based on these activities can be seen in Figure 6.2. In the upper panel, the contribution of different isotopes and decay-chains is shown. Both  $^{40}\text{K}$  and  $^{137}\text{Cs}$  are only important at their respective full-energy peaks. As the highest energetic  $\gamma$ -line considered here is at 2615 keV, entries in the spectrum above this energy are mostly coming from coincident events. This is highlighted in the lower panel of Figure 6.2, where the influence of three different cuts is shown.

For the first cut, only events with energy deposition in exactly one detector are considered. For the second cut, the energy has to be deposited in only one sector of a single detector. For the third cut, additionally 90% of all events with more than one interaction per sector are removed. These cuts remove background by more than one order of magnitude at high energies, but are also effective at low energies, where reduction factors around 5 can be achieved. Furthermore, events removed by the interaction depth cut  $0.2 < z < 0.9$  and the guard-ring are always excluded here, as it is assumed that any low-background analysis with the XDEM will make use of these cuts. Details on the implementation of these cuts can be found Ref. [Her18].

The results (in terms of background index  $\pm 100$  keV around the  $Q$ -values of  $^{116}\text{Cd}$  and  $^{130}\text{Te}$ ) from the analysis of activation products are shown in Table 6.3, taking into account the above mentioned cuts. It gives contributions at the level of  $10^{-3}$  cts/kg/keV/yr if no cuts are applied. The background contribution is in general higher at  $Q^{130}\text{Te}$  than at  $Q^{116}\text{Cd}$ . If all three cuts are applied, the contributions are lowered by nearly an order of magnitude and always below  $10^{-3}$  cts/kg/keV/yr. But even the highest value of  $4.0 \cdot 10^{-3}$  cts/kg/keV/yr with no cuts would imply only about 0.26 events on average after 3 years of data-taking in the whole 200 keV region around  $Q^{130}\text{Te}$ . Thus, cosmogenic activation is unlikely to give any relevant contribution to background.

The contributions from contamination of the shielding are much larger, as shown in Table 6.4. Besides the aforementioned simulation of the copper parts, radioisotopes in the lead shielding were also simulated. Activities for the ULA lead are given in Appendix A. The remaining lead is coming from various sources and was not screened prior to installation, consequently its activity is not well known, but assumed here

Table 6.3: Background contribution from cosmogenic activation of copper parts at  $\pm 100$  keV around the  $Q$ -values of  $^{116}\text{Cd}$  and  $^{130}\text{Te}$  with different cuts.  $SD$  denotes only single-detector events,  $SD + SS$  only single-sector events and  $SD + SS + SSE$  additionally assumes that 90% of all multi-site events within one sector can be removed.

ROI	$A^{\text{All}}$	$A^{\text{SD}}$	$A^{\text{SD+SS}}$	$A^{\text{SD+SS+SSE}}$
	[cts/kg/keV/yr]			
<b>Measured Activities</b>				
$^{116}\text{Cd}$	$5.5 \cdot 10^{-4}$	$3.3 \cdot 10^{-4}$	$1.8 \cdot 10^{-4}$	$1.2 \cdot 10^{-4}$
$^{130}\text{Te}$	$1.4 \cdot 10^{-3}$	$7.8 \cdot 10^{-4}$	$3.1 \cdot 10^{-4}$	$2.0 \cdot 10^{-4}$
<b>Calculated Activities</b>				
$^{116}\text{Cd}$	$1.2 \cdot 10^{-3}$	$7.1 \cdot 10^{-4}$	$3.8 \cdot 10^{-4}$	$2.6 \cdot 10^{-4}$
$^{130}\text{Te}$	$4.0 \cdot 10^{-3}$	$2.0 \cdot 10^{-3}$	$6.7 \cdot 10^{-4}$	$4.2 \cdot 10^{-4}$

Table 6.4: The same as Table 6.3, but for contaminants in the copper and lead shielding.

ROI	$A^{\text{All}}$	$A^{\text{SD}}$	$A^{\text{SD+SS}}$	$A^{\text{SD+SS+SSE}}$
	[cts/kg/keV/yr]			
<b>Copper</b>				
$^{116}\text{Cd}$	$1.1 \cdot 10^{-2}$	$5.0 \cdot 10^{-3}$	$5.6 \cdot 10^{-4}$	$3.0 \cdot 10^{-4}$
$^{130}\text{Te}$	$2.8 \cdot 10^{-1}$	$1.8 \cdot 10^{-1}$	$8.2 \cdot 10^{-2}$	$2.4 \cdot 10^{-2}$
<b>Lead</b>				
$^{116}\text{Cd}$	$6.2 \cdot 10^{-4}$	-	-	-
$^{130}\text{Te}$	$2.2 \cdot 10^{-1}$	$1.3 \cdot 10^{-1}$	$5.8 \cdot 10^{-2}$	$2.6 \cdot 10^{-2}$

to be ten times that of the ULA lead. At  $E \leq 1$  MeV, the normal lead is of minor importance anyway, as the ULA lead and the copper shield most of the radiation, while at energies above 2615 keV coincidences are also rare due to geometric effects. This is why the contribution from lead at  $Q^{116\text{Cd}}$  is always negligible, but substantial around  $Q^{130\text{Te}}$ . The copper contributes at both values, but around  $Q^{116\text{Cd}}$  it can be largely suppressed by the cuts, as it is caused mainly by coincident events.

Further simulated background contributions in this work include  $^{210}\text{Pb}$  in the lead shielding and cosmic muons.  $^{210}\text{Pb}$  and its progenies only emit radiation with much lower energy than  $Q^{116\text{Cd}}/Q^{130\text{Te}}$ . A very large number of MC-samples had to be generated to properly account for  $^{210}\text{Pb}$ . On the one hand, both its specific activity and source mass are high, but on the other hand, suppression from the inner shielding is strong. Even though  $5.5 \cdot 10^{10}$  samples were generated in this work, this number is still low, corresponding to only 1/5 year of real data-taking. Generating even more

## 6 Simulations for the XDEM phase

events was not possible due to limited time and computing power.

Regarding muons,  $2 \cdot 10^6$  were generated in a  $3 \times 3\text{m}^2$  area outside of the shielding, corresponding to 20 years of data-taking. In this way, both direct muon interactions and muons interacting with the shielding are taken into account. The resulting spectrum was then scaled to a flux of  $(3.41 \pm 0.01) \cdot 10^{-4}/(\text{m}^2 \text{ s})$  [Bel+12]. Muon induced events can be vetoed effectively by cuts based on event multiplicity [Hei14] or pulse-shape [Zat14] and could thus be largely removed in principle. Without any further measures they give a strong contribution at high energies at the order of some  $10^{-2}$  cts/kg/keV/yr.

The complete background model can be found in Figure 6.3, where all contributions are added. They are shown grouped by primordial decay-chains,  $^{137}\text{Cs}$ ,  $^{40}\text{K}$ , contributions from copper activation,  $2\nu\beta\beta$ -events and muons. Energy resolution is included by adding to each event a Gaussian determined by the energy resolution fit in section 7.2. The background indices from all considered sources without any further cuts are  $5.4 \cdot 10^{-1}$  cts/kg/keV/yr at  $Q^{130\text{Te}}$  and  $3.4 \cdot 10^{-2}$  cts/kg/keV/yr at  $Q^{116\text{Cd}}$ .

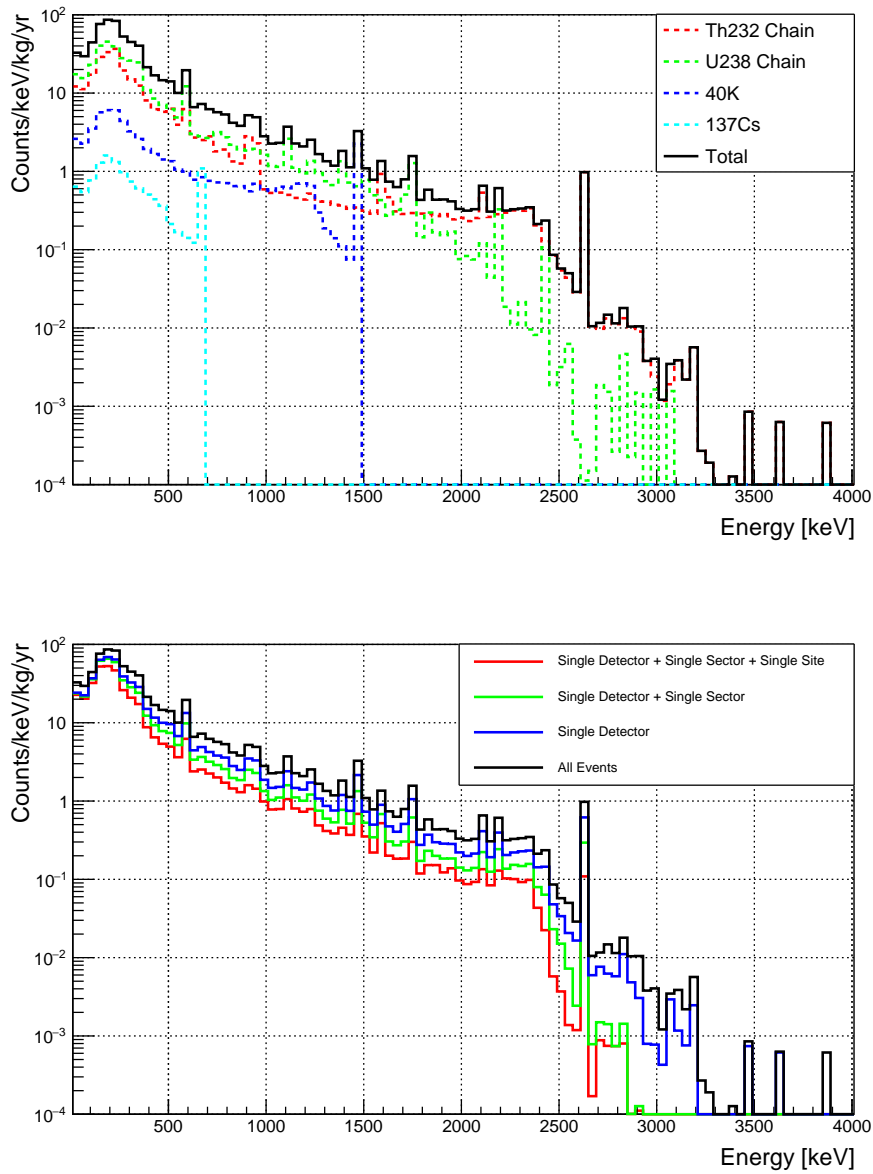


Figure 6.2: The same as Figure 6.1, but for primordial and man-made radioisotopes. In the upper panel, the influence of different components can be seen. The bottom panel shows the reduction of background by using cuts on multi-site events.

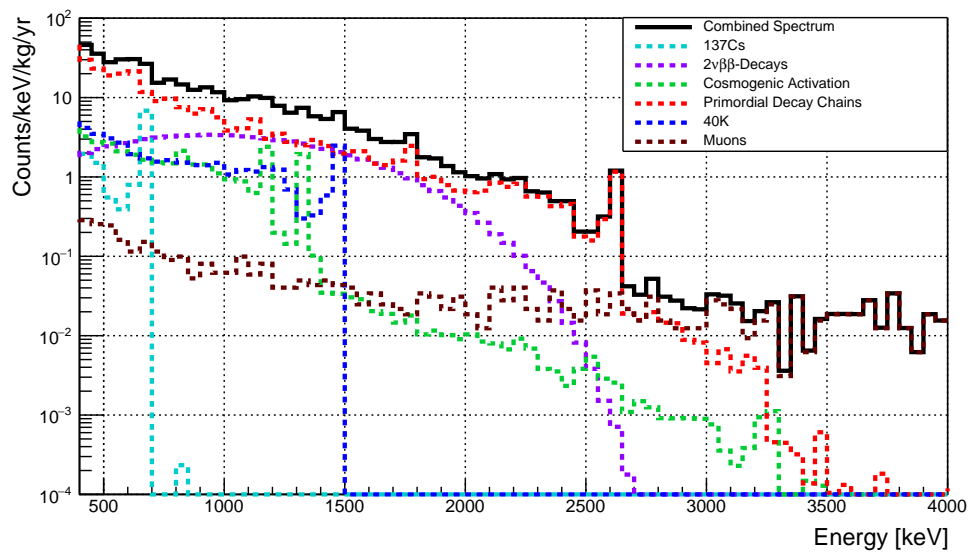


Figure 6.3: Combined spectrum from all simulated background sources for the XDEM in this work and Ref. [Her18] according to their measured activities or known fluxes.

## 7 Performance of the XDEM

The goal of the XDEM project is to determine whether the concept is suitable to search for double  $\beta$ -decays. Even more than with help of laboratory measurements presented in section 5.2, this can be shown assessing the performance in a low-background underground setup. This will be the topic of this chapter. The installation of the detectors into such a setup was explained in section 4.2. Here, several parameters will be investigated, including the linearity and energy resolution as calculated from calibration measurements and the stability of the data-taking. The background spectrum will be investigated with respect to the background index at the  $Q$ -value of  $^{116}\text{Cd}$  and  $^{130}\text{Te}$ . Finally, limits on the neutrinoless double  $\beta$ -decay ( $0\nu\beta\beta$ ) half-lives of both isotopes will be presented based on an exposure of 39.5 kg d.

### 7.1 Data-Taking Conditions

Because of problems with the high-voltage distribution and the NIM-infrastructure (see subsection 4.2.2 and subsection 4.2.3), not all data taken with the XDEM setup are usable for this analysis. Here, only data taken between 02.11.2018 and 13.05.2019 are taken into account, corresponding to a run-time of 191 days. Despite this comparably short run-time, the amount of data should be sufficient to compare the performance of the XDEM to previous COBRA setups and similar experiments in the field. In the following, some details about the conditions during data-taking will be given.

The setup was not continuously operational during the data-taking period. The main reason for this were changes of detector thresholds, since these needed to be adjusted at the start of the period. Near-optimal values can only be found empirically during data-taking as a trade-off between the amount of noise-only triggers and exposure in the low-energy part of the spectrum. As the rate of physical events should be approximately stable in time (for details see section 7.3), this can be done by observing the file size of each four hour long measurement file. This gives an estimate for the number of events per time. But for a change to take effect, data-taking needs to be stopped for some time. A less common occurrence were failures of the VME servers that control

## 7 Performance of the XDEM

flash-analog-digital-converter (FADC) operation. These servers sometimes stopped writing data and needed to be reset manually. Additionally, for technical reasons there has to be a short gap of some minutes between each measurement run. This slightly diminished the live-time of the experiment. In summary, data corresponding to uninterrupted data-taking of about 175 days were recorded. This corresponds to a live-time fraction of 91%.

The average temperature was about 12 °C near the pre-amplifiers and 13 °C near the lead castle. The average humidity was about 11 % and 12 %, respectively (see section 4.1 for details). These values were stable at the level of 2 %. Only the humidity near the lead castle showed larger deviations each time the LN<sub>2</sub>-Dewar was re-filled. The value at no time exceeded 17 %. The numbers indicate, that no significant failures of either the cooling or the LN<sub>2</sub>-flushing occurred. The detector voltages were monitored occasionally. No significant deviations were observed. Consequently, all data were deemed usable under these aspects.

Furthermore, not all detectors and sectors of the XDEM are included in the data shown here. Detector EV 694253-2 is disregarded completely. All sectors of this detector were severely affected by noise. One channel additionally seems to lack any CPG-like pulses, hinting at a failure of the electrical contacts. Three further sectors were disregarded, one from EV 694318-2 (missing CA signal) and two from REDLEN 109031 (missing CA signal and large noise). Three detectors requiring a bulk voltage of 2600 V were not operated at their working point as determined in subsection 5.2.1. As explained in subsection 4.2.3, the maximum voltage was limited to 2200 V to avoid spark-overs. The grid bias on 109031 was also reduced to 60 V as this resulted in more stable operation. Consequently, the yield of sectors used was 29/36  $\approx$  81%. The total active mass was thus 255.0 g. Taking into account both live-time and sector yield, the total accumulated exposure was 39.5 kg d. The lowest trigger threshold was 49.5 keV. The exposure-weighted average threshold was 156.6 keV.

To be able to interpret the data taken to search for double  $\beta$ -decays with COBRA – henceforth called *physics-data* – it is vital to calibrate the detectors in regular intervals with known radioactive sources. A calibration was performed shortly before and after this period, but none in between. In both <sup>22</sup>Na-, <sup>228</sup>Th- and <sup>152</sup>Eu-sources were used. For the results presented here, energy depositions measured in each sector are summed on the detector level. No summing of detector energies is performed<sup>1</sup>.

---

<sup>1</sup>For this, data from different FADCs has to be synchronized manually. This requires additional effort and was deemed beyond the scope of this work. Ref. [Vol18] gives details about this topic in the context of the Demonstrator

Guard-ring signals of the XDEM were read-out, but are not analyzed here. Their utilization for energy reconstruction was briefly tested in earlier works [Arl16; Teb16]. It was also shown that the signals can be used to veto  $\beta$ -particles entering the detectors from the side walls [BD18]. In a future analysis their incorporation may thus prove beneficial, but should not change any of the results presented here except for the background.

## 7.2 Linearity, Energy Resolution, Interaction Depth & Multiplicity

Besides for the actual calibration of the physics-data, calibration-data can also be used to assess the XDEMs performance. Important parameters are linearity of the energy scale, energy resolution and monitoring of interaction depth and event multiplicity which are used for cuts to reduce background in the physics-data. As already mentioned, two calibrations were performed. Only results from the second calibration are shown here as the results of both were similar. One source of bias in the calibration process is that low energetic photons only penetrate some mm into the detectors. Their interactions are consequently not uniformly distributed. The detector response on the other hand varies with position. This effect is largely compensated by the use of the weighting factor  $w$  introduced in Equation 3.6. Also, events from potential  $0\nu\beta\beta$ -decay are high-energetic, where this effect is absent. It is thus deemed not detrimental in the context of this work.

As explained in section 5.2, four parameters per detector are needed to calibrate the data from the COBRA detectors. To be able to interpret more complex spectra, at least approximate knowledge of them is necessary to correctly separate peaks in the spectrum and assign them to their true energy. Thus, a staged approach is used for data-processing. The sources also had a similar nominal activity of 3.65 kBq to 6.95 kBq as of 16.07.2018. An overview of all  $\gamma$ -lines used for calibration in this work can be found in Table 7.1.

The simplest spectrum is that of the  $\beta^+$ -decay of  $^{22}\text{Na}$ . It produces one  $\gamma$ -line due to de-excitation of the daughter nucleus  $^{22}\text{Ne}$  and a second line from the positron annihilation. These are well separated and both have a high intensity. Thus, this source is well suited to determine the relative pre-amplifier gain  $c_2$  and get initial guesses for the remaining calibration parameters  $w$  and  $c_{1,3}$  as introduced in Equation 5.4.

$^{228}\text{Th}$  has numerous  $\gamma$ -lines, but only the three given in Table 7.1 are used here. Its highest energetic line at 2614.5 keV is very important, as no other similar high

## 7 Performance of the XDEM

Table 7.1:  $\gamma$ -lines used for the calibration of the XDEM data. Intensities are given as the average number of photons emitted per initial decay of the given source nucleus. All data from Ref. [Bec19].

Source	Energy [keV]	Intensity [%]
$^{22}\text{Na}$	511.0	180.7
$^{22}\text{Na}$	1 274.5	99.9
$^{228}\text{Th}$	238.6	43.6
$^{228}\text{Th}$	583.2	85.0
$^{228}\text{Th}$	2 614.5	99.8
$^{152}\text{Eu}$	121.8	28.4
$^{152}\text{Eu}$	344.3	26.6
$^{152}\text{Eu}$	778.9	13.0
$^{152}\text{Eu}$	964.1	14.5
$^{152}\text{Eu}$	1 408.0	20.1

energetic line is available. It is also very close to the  $Q$ -value of  $^{116}\text{Cd}$  and can thus be used to estimate cut efficiencies. With the three lines from  $^{228}\text{Th}$  a second estimation of  $w$  is done. Together with the result from the two lines of  $^{22}\text{Na}$  an average  $w$  is calculated and used for all further purposes.

For a more precise calibration of the energy scale via  $c_{1,3}$  lines from  $^{152}\text{Eu}$  are also taken into account. This isotope can actually undergo three different types of decay,  $\beta^-$ ,  $\beta^+$  and electron capture (EC). It has 129 known  $\gamma$ -lines, from which five are used here. Thus, the total number of calibration-points is doubled by using  $^{152}\text{Eu}$ . The spectrum from a  $^{152}\text{Eu}$ -calibration is shown in Figure 7.1 with the lines used for calibration marked. One advantage of using this isotope is its lowest energetic  $\gamma$ -line at 121.7 keV. This lines allows to assess low-energy performance close to the trigger thresholds.

The weighting factor estimation was slightly modified in comparison to earlier COBRA publications or previous sections of this work. Formerly, the optimal  $w$  was defined as the value which minimized the energy resolution of the detector. This criterion is quite natural, as improving the energy resolution is the very purpose of using  $w$ . But, as already explained for the working point optimization in subsection 5.2.1, this is not the proper quantity to be optimized to achieve the best sensitivity for a peak-search in a spectrum with background. A more suitable quantity is thus

$$s_{\max}(w_{\text{opt}}) = \max \frac{\epsilon_{\text{Det}}}{\sqrt{\Delta E}}. \quad (7.1)$$

$\epsilon_{\text{Det}}$  is usually not affected much by changing the weighting factor, as long as  $w$  is

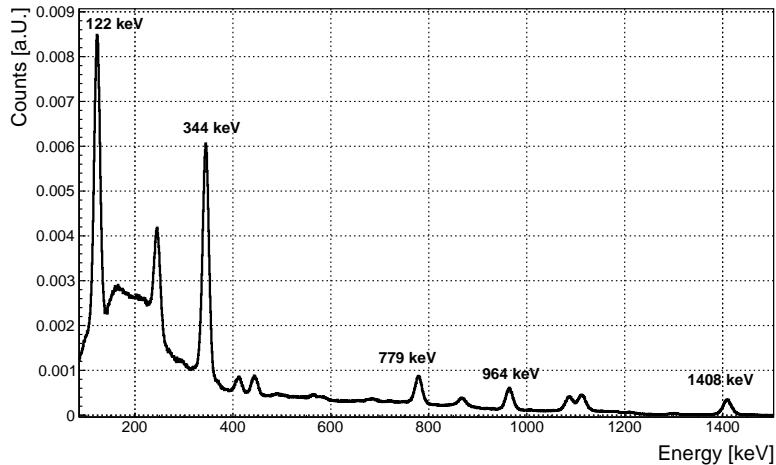


Figure 7.1: Spectrum obtained in the May 2019 calibration with the XDEM and a  $^{152}\text{Eu}$ -source. The peaks which are used for calibration are marked with their respective energy.

close to a value that minimizes the effect of electron trapping. But, as changing  $w$  in general induces a non-linear change in peak-shape, it is possible to produce very non-Gaussian peaks by picking an improper  $w$ . As  $w_{\text{opt}}$  is not known beforehand, it is possible to start the optimization with values of  $w$  that produce very sharp, non-Gaussian peaks containing only few events. With such a peak, a detector appears to have a low  $\Delta E$ , but also indicates a low  $\epsilon_{\text{Det}}$ . The weighting factor optimization has to take  $\epsilon_{\text{Det}}$  into account. Consequently, it is done with respect to  $s$  and not just with respect to  $\Delta E$ .

Another difference to the fitting procedure outlined in section 5.2 is that two different background parameterizations are used. The calibration sources used at the LNGS do not have such a simple spectrum as the  $^{137}\text{Cs}$ -source used in the laboratory. Hence, instead of always assuming a constant background, sometimes also a linear function is used.

A basic performance quantity is the baseline noise of each channel, as it is roughly proportional to the minimally achievable energy resolution. It is defined as the root mean square (RMS) of the baseline far enough away in time from when a trigger occurred. The baseline RMS is shown in Figure 7.2. The magnitude of the noise varies by up to a factor of 8 between the channels. It can be seen that many channels exhibit a noise around 10 ADC channels or less, but an number of channels also shows

## 7 Performance of the XDEM

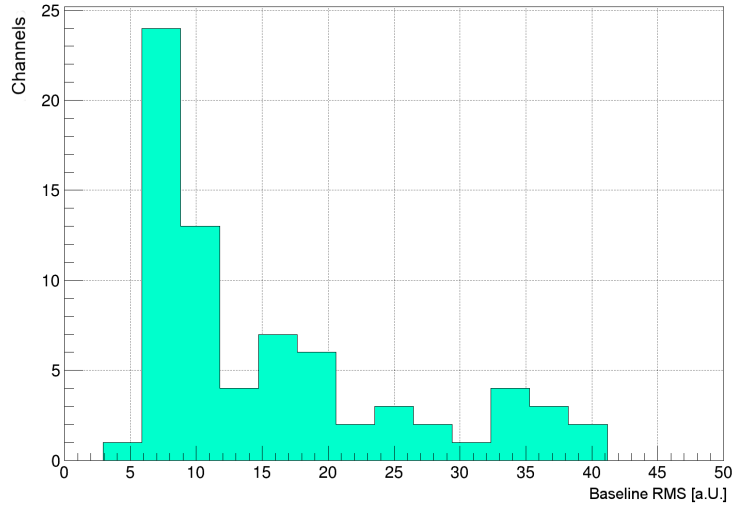


Figure 7.2: Histogram of the baseline RMS as a measure of noise in each channel.

significantly higher values up to 40 ADC channels. As, according to Equation 3.2, noise usually is the most important driver of energy resolution at low energies, this spread indicates a rather large difference in low-energy performance between detectors, It is less important at the  $Q$ -values of  $^{116}\text{Cd}$  or  $^{130}\text{Te}$ .

Another important feature is the linearity of the energy scale. To evaluate this, the centroid of each  $\gamma$ -line is determined, plotted against its known energy and a linear function is fitted to this relation. The result can be seen in Figure 7.3, where the linearity of an unweighted average of all individual detectors is shown. The overall offset of the calibration is smaller than 0.1%. It is thus negligible compared to the energy resolution, which is typically an order of magnitude larger. On the other hand,  $\chi_{red}^2 = 6.4$  indicates a far from perfect fit. Looking at the residuals (normalized difference between reconstructed and true energy) in the lower panel of Figure 7.3, this seems to come mainly from low energetic lines, likely due to the bias in this region mentioned above. Indeed, if those lines are removed  $\chi_{red}^2 = 5.6$  is reached.

As no  $\gamma$ -line has the same energy as the  $Q$ -values of the double-beta isotopes, a fit is conducted to extrapolate energy resolution to the relevant energies. To do this, numerous functions can be found in the literature. Here, a rather simple and often used function of the form

$$\Delta E(E) = \sqrt{a + bE + cE^2} \quad (7.2)$$

is used. Its parameters  $a, b, c$  directly relate to the three fundamental terms in Equa-

## 7.2 Linearity, Energy Resolution, Interaction Depth & Multiplicity

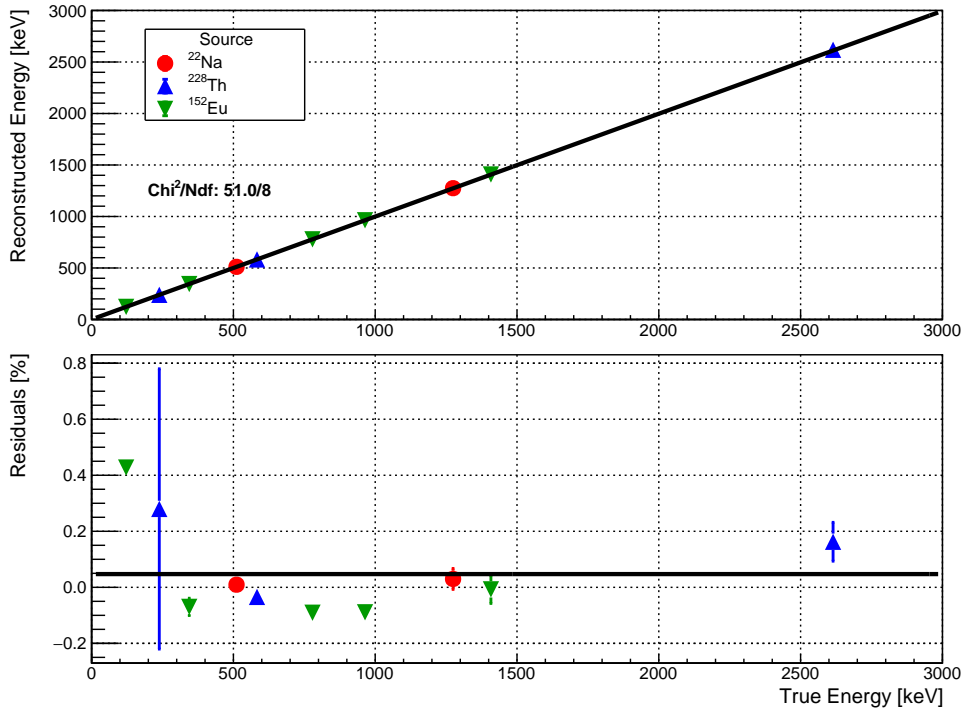


Figure 7.3: Reconstructed energy from the fitted centroid of  $\gamma$ -lines against their known true energy. A combination of all XDEM detectors is shown. In the upper panel a linear function is fitted to the data, showing that the correlation is in fact linear. In the lower panel the residuals are shown, e.g. the normalized difference between reconstructed and true energy. The line indicates the average offset.

tion 3.2. A good fit to CdZnTe-data is often also achieved if  $c$  is omitted. This can be beneficial if the number of lines available for calibration is low, like in Ref. [Ebe+16c]. This case will also be tested here. In Figure 7.4, the FWHM obtained from the fit of individual  $\gamma$ -lines as described in section 5.2 is plotted against their total energy and fitted according to the formula above. Once again, data from the whole XDEM combined is shown.

The fit to Equation 7.2 gives  $\chi_{red}^2 = 6.8$  and  $\chi_{red}^2 = 6.0$  if  $c$  is omitted. This indicates that both functions are able to describe the data to some degree, but neither can do it really well. The three parameter version of the function tends to predict a slightly worse resolution at high energies and will thus be used from here on as a more conservative estimate. Still, the fit underestimates the resolution of the 2615 keV lines from  $^{228}\text{Th}$ . As no other line with similarly high energy is available, it can not be checked if this is a systematic effect. In any case, for the search for  $0\nu\beta\beta$ -decays conducted in section 7.5

## 7 Performance of the XDEM

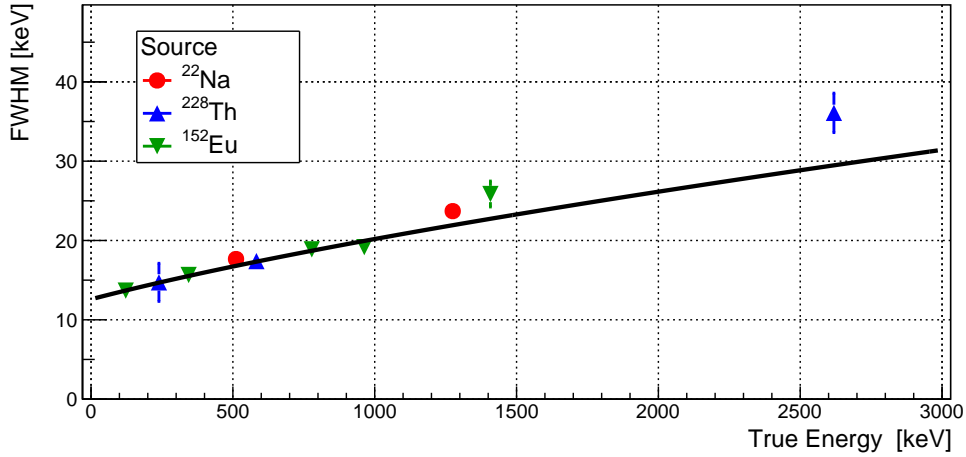


Figure 7.4: Energy resolution of all XDEM detectors combined fitted with a three parameter resolution function as defined in Equation 7.2.

a large region of interest is chosen to account for this fact.

From the fitted function, the energy resolution at different points of interest can be calculated. The first is the resolution at 662 keV. It can be used to compare the results from the low-background setup to the characterization measurements from subsection 5.2.4. The average relative resolution at this energy is  $(2.6 \pm 0.3) \%$ , slightly above the value of  $(2.3 \pm 0.4) \%$  achieved in subsection 5.2.4 and still well below the quality criterion of 4.0%. This is likely due to higher noise at the LNGS. At the  $Q$ -value of  $^{116}\text{Cd}$  at 2814 keV, the resolution is  $(1.1 \pm 0.3) \%$ .

If only events in a restricted depth-range  $0.2 < z < 0.9$  are taken into account, the resolution is improved to  $(1.0 \pm 0.3) \%$ . This is because events from the near-anode region, where the worst performance is expected, are removed. The results do not change significantly whether averages of single sectors, summed energies of all sectors in each detector, or from all data combined into a single histogram are considered. The worst resolution at 2814 keV of a single sector is found to be 2.0%, while the best one is 0.7%. The trend from subsection 5.2.4 of REDLEN detectors having a better energy resolution on average is confirmed.

Another quantity of interest is the distribution of events with respect to interaction depth  $z$ . This is shown exemplary for  $^{228}\text{Th}$  in Figure 7.5 as a plot of energy against depth. It can be seen, that most events fall into the physical region of  $0 < z < 1.0$ . A number of events is found outside of this region due to limited depth resolution and

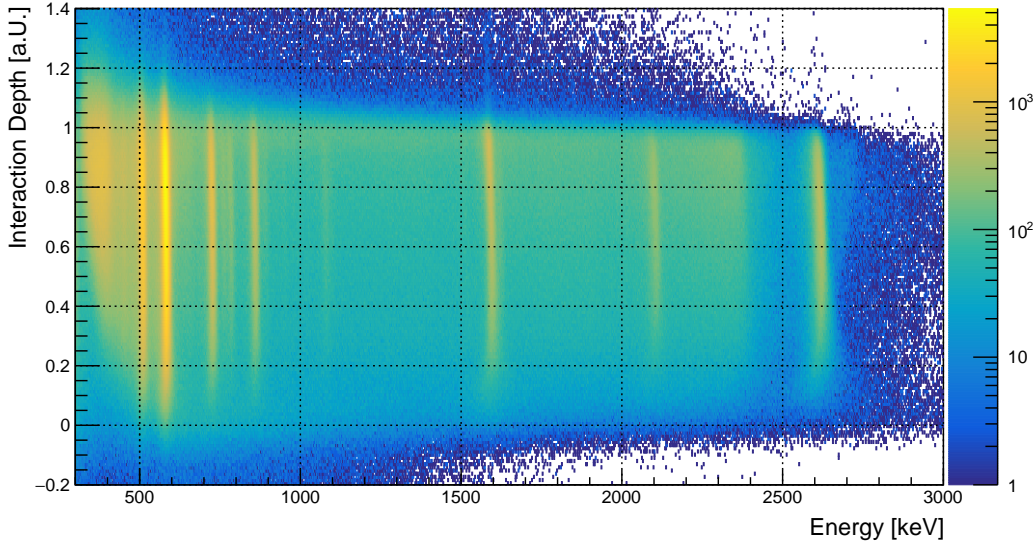


Figure 7.5: Energy versus interaction depth for a calibration with  $^{228}\text{Th}$ . The color indicates the number of events. The vertical lines correspond to the full-energy absorption of photons from  $\gamma$ -lines.

trapping effects. This becomes less pronounced at higher energies, as the signal-to-noise ratio rises, increasing depth resolution. The signal efficiency  $\epsilon_z$  of a cut on the interaction depth is given by  $\epsilon_z = 1 - \frac{N_{\text{cut}}}{N_{\text{all}}}$ , with  $N_{\text{cut}}$  the number of events remaining after the cut is applied and  $N_{\text{all}}$  the total number of events.

$N_{\text{cut}}$  and  $N_{\text{all}}$  are calculated for the line at 2615 keV from  $^{228}\text{Th}$ . This line is the closest to the  $Q$ -values of  $^{116}\text{Cd}$  and  $^{130}\text{Te}$ . All events falling within  $(2615 \pm 26)$  keV, corresponding roughly to  $\pm 1$  FWHM, are selected. If the interaction depth range is restricted to  $0.0 < z < 1.0$ , then  $\epsilon_z \geq 0.99$ . If  $0.2 < z < 0.9$  is used, which should remove all events close the electrodes,  $\epsilon_z = 0.89 \pm 0.01$  is obtained. If the trapping corrected interaction depth  $z_{\text{tc}}$  is used, a higher value of  $\epsilon_{z_{\text{tc}}} = 0.90 \pm 0.04$  is found. As the reason for the much larger deviation is unclear, no trapping correction will be used from here on.

Another parameter of interest is event multiplicity  $m_{\text{sec}}$  within a single detector, e. g. how many sectors have simultaneously measured a significant amount of energy for a given detector. In Figure 7.6 events with arbitrary multiplicity, as well as those with a  $m_{\text{sec}} = 1$  (single sector events) and  $m_{\text{sec}} > 1$  (multi sector events) from a  $^{22}\text{Na}$ -calibration are shown. Events falling into the peak around 511 keV are dominantly

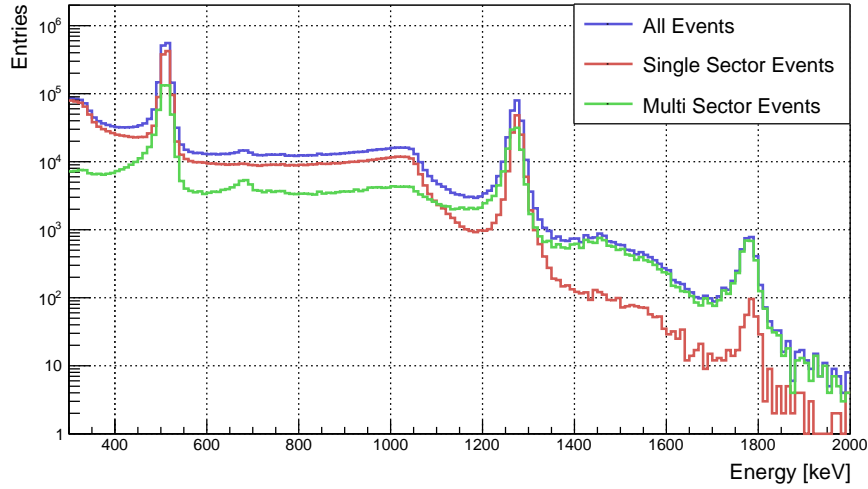


Figure 7.6: Events with different multiplicities  $m_{sec}$  from a  $^{22}\text{Na}$ -calibration. The coincidence peak at high energies has a much higher fraction of multi sector events than the other two peaks.

single sector events, as the cross section for a photon to interact via the photoelectric effect is high at this energy. For the peak around 1275 keV, the fraction of multi sector events is higher. The peak around 1786 keV, caused by the coincident detection of a photon with 1275 keV and one of the annihilation photons, is made up predominantly by multi-sector events. This is because such a coincident detection is likely to be registered in more than a single sector.

It is also possible to estimate the effect of a cut on  $m_{sec}$  based on  $^{228}\text{Th}$ -calibration data. At 2615 keV interaction via pair-production is likely (see Figure 3.1). In this case, two 511 keV photons are emitted following positron annihilation. These can be re-absorbed in the same sector they are created, another one or none at all. If both photons are re-absorbed, the resulting peak is called full energy peak (FEP), if only one photon is absorbed single escape peak (SEP) and if none is detected double escape peak (DEP).

In analogy to the interaction depth cut, an efficiency  $\epsilon_m = 1 - \frac{N_{m=1}}{N_{\text{all}}}$  can be computed for both peaks. The results are  $\epsilon_m^{\text{SEP}} = 0.78 \pm 0.07$  compared to  $\epsilon_m^{\text{DEP}} = 0.95 \pm 0.02$ . In other words, the content of the SEP is reduced by more than 20%, while the content of the DEP is only reduced by about 5% if only single sector events are taken into account. As in solid-state devices double-beta decay usually deposits all its energy in a tiny region of space it will predominantly register as a single-sector process. For

background processes involving high energetic  $\gamma$ -rays, multi sector events are more likely. Thus, such a cut can be used to reduce background.

The conclusion from the calibration measurements is that the XDEMs energy response is linear, allowing the interpolation to energies beyond the calibration lines. The energy resolution of about 1 % FWHM allows to separate two-neutrino double  $\beta$ -decay ( $2\nu\beta\beta$ )- and  $0\nu\beta\beta$ -decay. It is slightly better than that of the *Demonstrator* array with 1.1 % [Ebe+16c]. The resolution at 662 keV is worse by about 10 % compared to the characterization measurements, likely due to noise. Both the interaction depth as well as the sector multiplicity can be used to reduce background. A search for  $0\nu\beta\beta$ -decays with the XDEM is thus feasible.

### 7.3 Stability

As the data presented in this chapter were collected over the course of more than half a year, it is important to judge the stability of data-taking in this period. This can be done in various ways. Ideally, one would have very regular calibrations, but this is not the case here. A simple indirect method is to observe external parameters like temperature and humidity, as these directly affect the setup. Indeed, these values were rather stable at the monitored points in the setup. Another way is to use data generated with the precision pulse-generator. As several thousand pulses are injected per day, their average height can be determined with high accuracy on a daily basis. The drawback of this method is that it only probes the electronics but not the detectors themselves.

A further option is to look at the evolution of trigger thresholds. They depend heavily on noise conditions and thus stable thresholds indicate a stable behavior of noise over time. It is also possible to look for differences in the calibration parameters obtained in the two calibration campaigns. Ideally, these are constant. Finally, the measured rate of physics-data can be checked. This method has worse accuracy than the pulser method, as event rates are threshold-dependent and only few events are measured each day at energies far above the thresholds. Nevertheless, this method gives the most direct representation of data-quality.

The stability of the pulser signal is checked by histogramming the height of all pulses injected on a single day and then fitting a Gaussian to the resulting distribution. Its mean is plotted as a function of time in Figure 7.7. Only channels from detector EV 694318-3 are shown. The other detectors behave very similar. It can be seen that the pulse-height differs from channels to channel. This is a consequence of both the

## 7 Performance of the XDEM

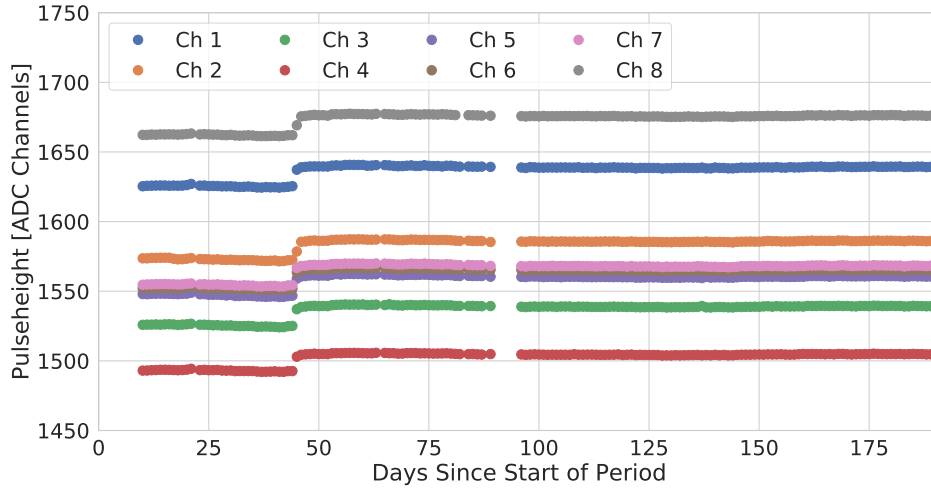


Figure 7.7: Height of artificially injected pulser-signals in eight channels of one detector.

different gains in each channel and the varying capacitance of capacitors used to couple the pulser signal into the amplifiers.

There are also noticeable gaps in the time-series. At the beginning, the pulser was miss-configured and no usable pulses were recorded. Around day 90 no data was collected due to instabilities of the VME-infrastructure and a subsequent failure to restart data-taking immediately. Apart from that, two periods with stable pulse-heights and a transition period in between can be observed. The difference in pulse-heights between the periods is about 15 ADC channels, or slightly below 1%, while the variance within the periods is well below 0.1%. The time of transition corresponds roughly to the installation of the additional cooling in the upper part of the COBRA building. This caused a decrease in temperature of about 10°C at the linear-amplifiers and FADCs over several days. It can be concluded that a single shift of gains occurred during data-taking, but aside from this the electronics showed excellent stability.

Trigger thresholds were constantly adjusted to achieve both stable data-taking and thresholds as low as possible. At the start of the period, a threshold value of 60 ADC channels was used for every sector. This could quickly be lowered as shown in Figure 7.8. After about a month of daily adjustments, values between 11 and 18 ADC channels were reached. Some had to be slightly adjusted later, as they proved to be too low to achieve a stable data-rate. For some detectors, as REDLEN 109033 shown in red in Figure 7.8, this was basically not necessary. For others, like EV 694318-1 shown in blue in Figure 7.8, the values needed to be raised quite significantly. Overall, it was

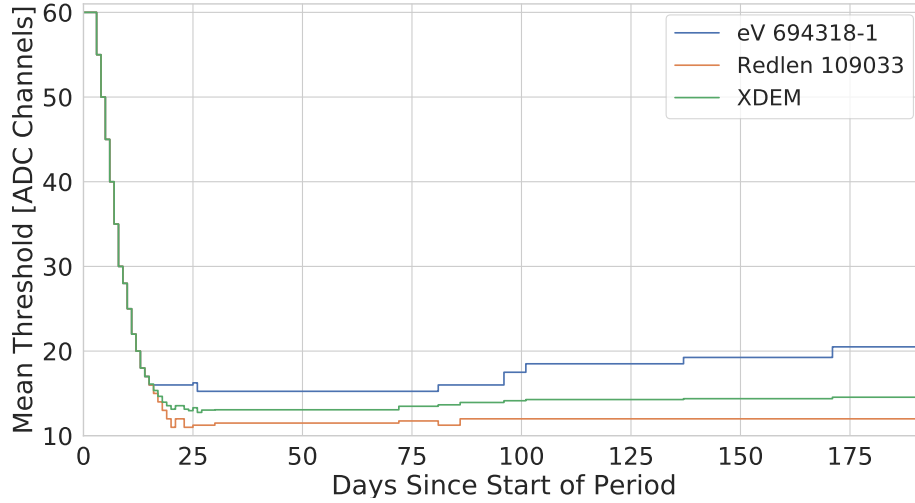


Figure 7.8: Trigger thresholds averaged over individual sectors as a function of time. *XDEM* is the mean of all sectors incorporated in this analysis. The other two lines show the detectors with the highest (EV 694318-1) and lowest (REDLEN 109033) average thresholds.

possible to operate most sectors with stable thresholds over a time of several months.

Another way to judge stability is to look for deviation of the calibration factors, as defined in Equation 5.4, between the first calibration in November 2018 and the second calibration in May 2019. Although some variations exist for single sectors, the average<sup>2</sup> differences of the pre-amplifier gains  $c_2$ , the weighting factors  $w$  and the calibration offsets  $c_3$  are all compatible with zero. Only  $c_1$  shows a significant systematic shift of  $(-0.7 \pm 0.3) \%$ . The reason is presumably the same as given above for the injected pulses. This also explains why the detector and pre-amplifier related parameters  $w, c_2$  are not affected.

To estimate the influence on the final spectrum, the energy corresponding to a pulse with  $A_{CA} = 750$  ADC ch and  $A_{NCA} = 150$  ADC ch is calculated with each set of calibration parameters. These values equal an energy of 2800 keV for a detector with  $c_2 = w = 1$ ,  $c_3 = 0$  keV and  $c_1 = 2.8$  keV/ADC ch at a depth of  $z = 0.5$ . With these parameters, the average difference in energy between the two calibrations is

<sup>2</sup>It might be possible to not use an average set of calibration parameters for the low-background data, but to apply one or the other set of parameters period wise according to Figure 7.7. This might result in a smaller uncertainty on peak positions or effective energy resolution, but it is not straight-forward to handle the transition time. It is also not possible to say for sure that no other circumstance aside from electronics issues also contributed to the shift in parameters.

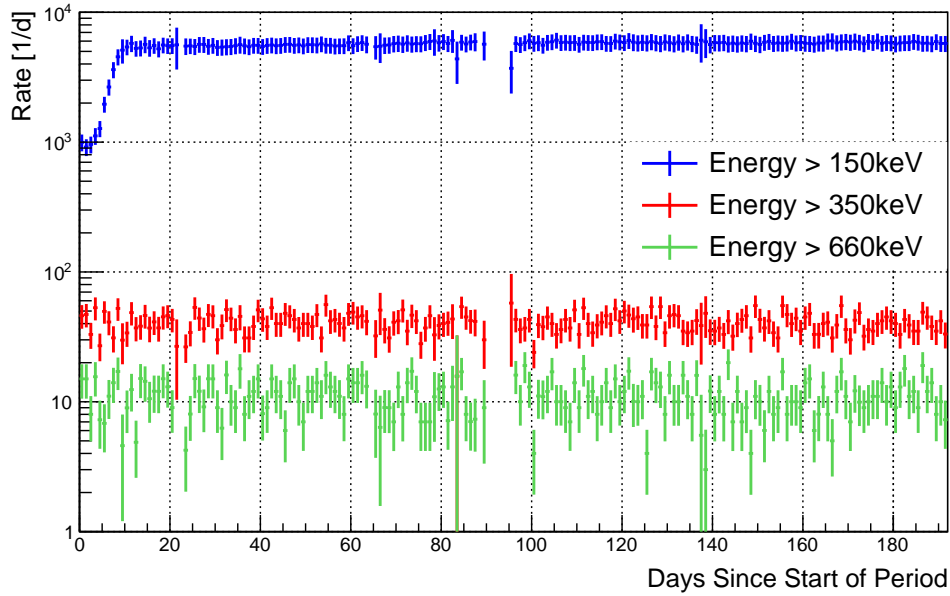


Figure 7.9: Measured daily event rate with different energy thresholds as function of time, corrected for run-time on each day. It can be seen, that, beside a rise in the first two weeks in the lowest-energy region due to changing trigger thresholds, no time-dependence is present in any region.

again ( $-0.7 \pm 0.3$ ) %, the same as for  $c_1$ . If all physics data is pooled together and an average set of calibration parameters is used, the shift is somewhat mitigated. As the overall resolution is much higher and individual factors are added in quadrature, this additional contribution is still be small

Finally, the rate of physics-data in three different energy categories is shown in Figure 7.9. All rates are life-time corrected to allow for better comparison. The lowest range includes all events with  $E > 150$  keV, which corresponds to the average trigger threshold in this period. As such, one can see a rise in rate at the start of data-taking, when thresholds were usually higher. After about two weeks, the rate stabilizes around  $(5725 \pm 63)/d$ . This is compatible with the assumptions that the rate at this energy is caused mainly by the decay of  $^{113}\text{Cd}$ , taking into account the accessible fraction of the  $\beta$ -spectrum.

The second category is  $E > 350$  keV. This value is chosen as it is higher than any threshold in this period. Here, the rate is stable at about  $(39.3 \pm 0.6)/d$ . There is no indication for a significant change over time. The same is true for the category of

## 7.4 Analysis of the Low-Background Spectrum

$E > 660$  keV. This value was chosen to exclude all contributions from  $^{113}\text{Cd}$  even when energy-doubling (see section 3.1) takes places. If some part of the rate in this category would be caused by the decay of an isotope with a half-life comparable to the duration of data-taking, e. g. from cosmic activation overground, it could influence the rate in this category. The rate in this region is only  $(9.8 \pm 0.3)/\text{d}$  and statistical fluctuations dominate day-to-day changes. This means that no hints for the decay of radioisotopes with a half-life comparable to the run-time of this period can be detected.

Overall, the main contribution to instabilities of the data-taking is the change of temperature in the upper part of the setup. This change caused a slight shift in gain in the later stages of the data acquisition chain. Trigger thresholds were decreased quickly in the beginning and only needed small readjustments after about a month. No indications for a change in the rate of recorded data over time was observed in any of the defined categories. Concluding, the data-taking was stable over time in terms of rate. The gain-shift, which effectively degrades energy and depth resolution, is significant but still small compared to the overall energy resolution. Consequently, data from before as well as after the shift will be used.

## 7.4 Analysis of the Low-Background Spectrum

In total, 2 853 031 events not injected by the precision pulser were record, corresponding to a rate of about 0.2 Hz. Of these, 1 671 042 were not identified by the data-cleaning cuts as un-physical. Events flagged as un-physical are removed from the data-set from here on. Only 7 152 events additionally have  $E > 350$  keV, above the end-point of the  $^{113}\text{Cd}$   $\beta$ -decay. Thus, the fraction of physical events well above the end-point is only 0.25 %. Furthermore, if a cut of  $0.2 < z < 0.9$  is applied, only 2 444 events remain, showing the huge importance of removing near-electrode events. This corresponds to a rate of 0.16 mHz, i. e. less than two per day or  $61.6/(\text{kg d})$ . Requiring  $m_{\text{sec}} = 1$  only removes an additional 470 events. Consequently, a restriction on  $m_{\text{sec}}$  will not be discussed further, as the loss in detection efficiency (see section 6.1) associated with such a cut is not outweighed by the small reduction of background. In the following, different contributions to the total number of detected events will be discussed.

In Figure 7.10 the integral number of events is shown for three different data-selections, but on the level of individual detectors<sup>3</sup>. It can be seen, that detectors 1, 2 and 3 give the largest contribution in all selections. In particular, the contribution of events around 662 keV is very concentrated on few detectors and will be discussed in

---

<sup>3</sup>The different fraction of working sectors per detector is not taken into account here.

## 7 Performance of the XDEM

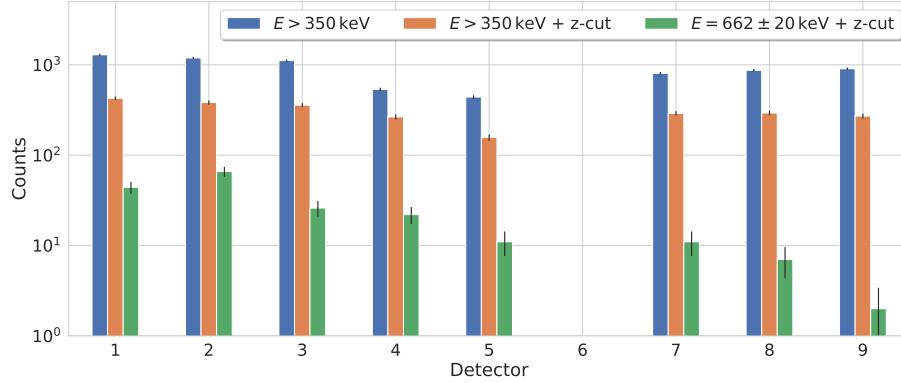


Figure 7.10: Number of events measured by each individual detector with different data selections. Figure 4.6 gives an explanation of detector numbers. Detector 6 was not used in this analysis.

more detail further below. On the other hand, the depth cut removes a large fraction of events for all detectors.

The complete spectrum up to 15 MeV can be seen in Figure 7.11. A number of features can be made out with  $E \geq 2 \text{ MeV}$ . As seen in Figure 7.12, most events at high energies are localized very close to the electrodes. These likely belong to various  $\alpha$ -decays of  $^{190}\text{Pt}$ , analyzed later in more detail, and  $^{222}\text{Rn}$ - or  $^{220}\text{Rn}$ -daughters.  $^{220}\text{Rn}$  itself for example undergoes  $\alpha$ -decay with a  $Q$ -value<sup>4</sup> of 6 288.2 keV. The decay-chain of  $^{222}\text{Rn}$  contains  $\alpha$ -decays with high intensities at energies of e. g. 4 784.3 keV, 5 304.3 keV, 5 489.5 keV and 6 002.4 keV. Around these energies broad, peak-like structures are visible in Figure 7.11. At even higher energies, further decays potentially contributing to background exist, but as events with these energy are mostly registered near the anodes, they are likely caused by the double-energy effect.

As the highest energetic  $\alpha$ -decays, which all are found in the primordial decay-chains before the radon isotopes, seem to be absent,  $\alpha$ -decays are likely caused by  $^{220}\text{Rn}$ ,  $^{222}\text{Rn}$  and their progenies.  $^{220}\text{Rn}$  itself and all its daughters have half-lives of less than 12 hours. Thus, depositions of this chain will decay within a few days. For  $^{222}\text{Rn}$  the situation is different, as it has a longer half life of about 3.8 d, making it more common.

Its daughter  $^{210}\text{Pb}$  even has a half life of about 22 yr and can accumulate on the detector surface. Due to the long half-life of  $^{210}\text{Pb}$ , the  $^{222}\text{Rn}$  will not be in secular

<sup>4</sup>In general,  $\alpha$ -decays will be registered at energies slightly below their  $Q$ -value if they take place on the detectors surface, as part of the energy can be taken away by the recoiling daughter nucleus and some is lost in the metalization and potential dead-layers, see Ref. [Koe12].

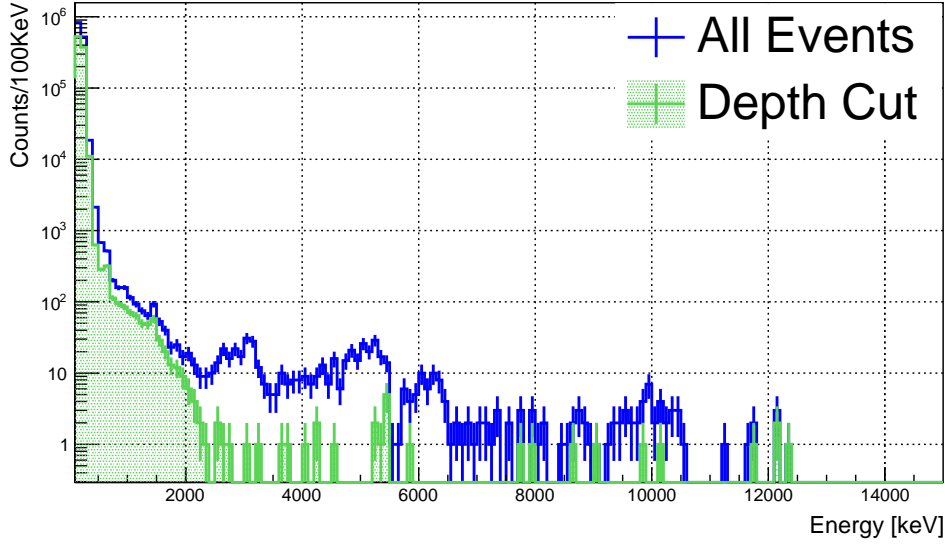
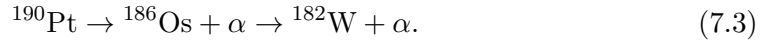


Figure 7.11: Energy spectrum obtained with 0.108 kg d of exposure of the XDEM setup. Events not flagged as un-physical are shown in blue. Events that additionally pass the interaction-depth cut are shown in green.

equilibrium at time-scales relevant here. The rate of events with  $5\,000\text{ keV} < E < 6\,000\text{ keV}$ , where many peaks from Rn-daughters are found, is less than one per day. This makes it hard to investigate the time structure of Rn-decays to determine their origin. All of these features vanish if the above mentioned depth-cut is used. This indicates that the contamination with radioisotopes of the detectors themselves is small.

One unstable isotope known to be present in the electrodes of EV detectors is  $^{190}\text{Pt}$ . It decays according to



with a half-life [Bra+17] of  $(4.97 \pm 0.16) \cdot 10^{11}$  yr and makes up about 0.01% of natural Platinum. The second part of the decay chain can be ignored, as  $^{186}\text{Os}$  has an even longer half-life of  $\geq 1 \cdot 10^{15}$  yr and the decay chain is clearly not in equilibrium given the half-life of  $^{190}\text{Pt}$ . The energy of  $\alpha$ -particles emitted in the decay of  $^{190}\text{Pt}$  is  $(3\,268.6 \pm 0.6)$  keV [Bra+17].

In Figure 7.13 it can be seen that there is a peak in the background spectrum between

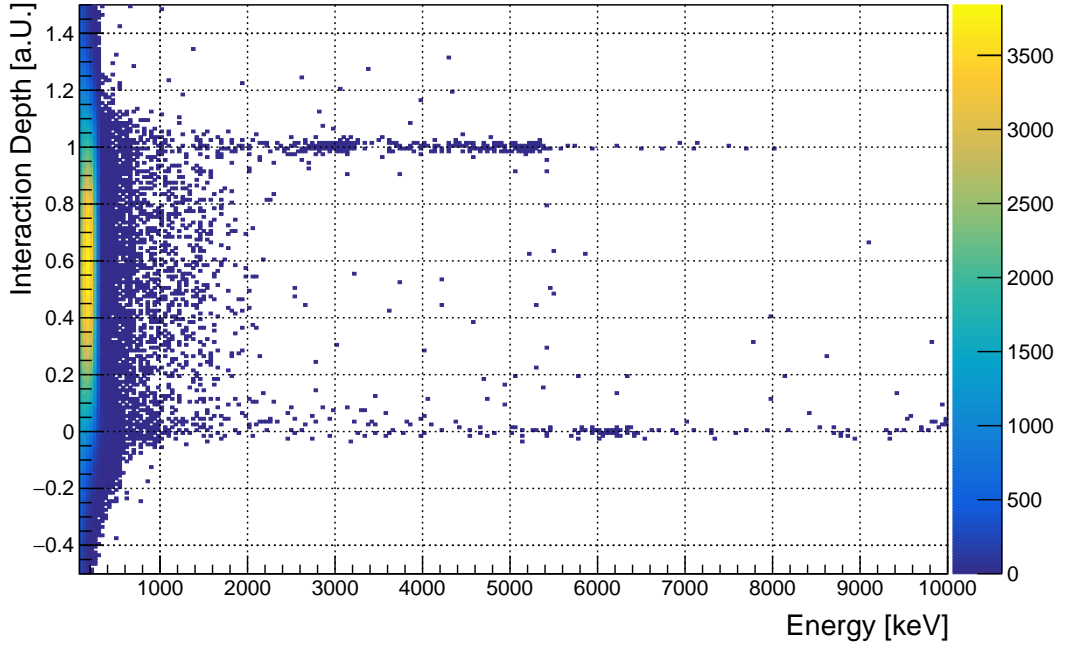


Figure 7.12: Two dimensional representation of the events detected with the XDEM as a function of both energy and interaction-depth. At lower energies events are distributed over the whole depth range. At higher energies events tend to accumulate near depths corresponding to the electrodes.

3 000 keV and 3 200 keV. Most of these events stem from the cathode region<sup>5</sup>, defined as  $0.9 < z < 1.1$ . In Ref. [Koe12]  $(0.12 \pm 0.01)$  cts/day/det were found in a region between 2 800 keV and 3 200 keV for the first 16 Demonstrator detectors. In the same region in the XDEM data-set one finds a total of 95 events, 81 of which are coming from EV detectors. This results in a rate of  $(0.15 \pm 0.02)$  cts/day/det. It must also be taken into account that the cathode area is four-times that of the Demonstrator detectors. Thus, to result in a similar number of cts/day/det there must be a difference in electrode thickness which results in a different number of  $^{190}\text{Pt}$  atoms of about a factor of three.

There are ten events with an energy above 11 000 keV. These are likely caused by muons, as no  $\alpha$ - or  $\beta$ - particles or  $\gamma$ -rays are emitted by natural decay chains with such a high energy. A highly energetic muon (acting as minimal ionizing particle) deposits

<sup>5</sup>At the anode region, energy-doubling causes a similar peak at roughly twice the energy, but more smeared out.

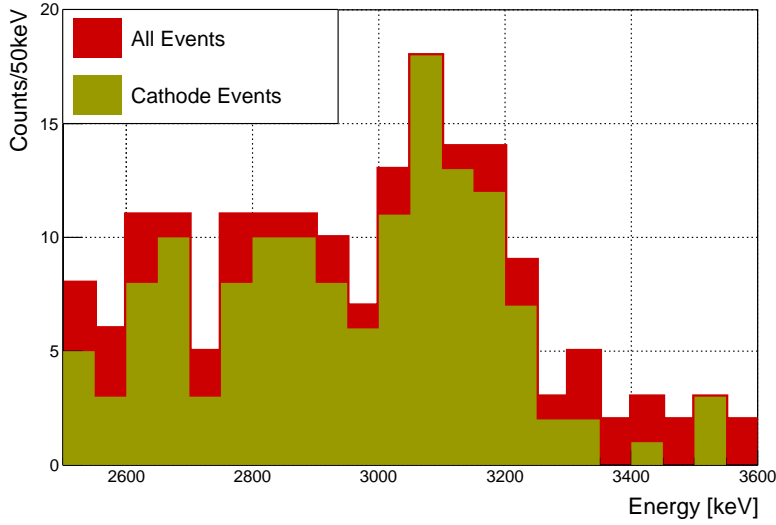


Figure 7.13: Distribution of events around 3100 keV originating near the cathodes (dark yellow) and without depth restriction (red).

about 11 MeV even on the shortest possible path through the crystal. Taking the flux of  $(3.41 \pm 0.01) \cdot 10^{-4}/(\text{m}^2 \text{s})$  [Bel+12], the expected number of direct interactions is 12 events<sup>6</sup>. In reality, muons can also enter a detector under an angle or hit it just partly. Also, muons not always simply pass through a detector, but can also be stopped and create unstable isotopes. Anyway, the numbers found are statistically compatible.

Easily identifiable in the upper plot of Figure 7.14 is a peak around 662 keV. It comes presumably from the decay of  $^{137}\text{Cs}$ . The peak is fitted with a Gaussian over an exponentially falling background. The obtained mean of  $E = (660.1 \pm 1.4)$  keV fits this hypothesis well. The width of  $\Delta E = (21.8 \pm 2.8)$  keV corresponds to a relative resolution of about  $(3.3 \pm 0.4)\%$ . This is slightly worse than the expectation of  $(2.6 \pm 0.3)\%$  based on section 7.2. The fit of signal and background (S+B) gives  $\chi_{\text{red}}^2 = 0.8$ . Fitting only an exponentially falling background (B) gives  $\chi_{\text{red}}^2 = 2.5$ . This is clearly in favor of the S+B hypothesis.

After subtracting the background component, a net count-rate of  $(0.76 \pm 0.04)/\text{d}$  is obtained. The background model from section 6.2 predicts only 0.40/d. This shows that a higher activity of  $^{137}\text{Cs}$  than expected is present. As seen in Figure 7.10, the events in the region around this energy are spread unevenly across detectors, with the

<sup>6</sup>This assumes that the top are of the detector can be used as an effective are for muon interaction. It also takes into account the number of active sectors.

## 7 Performance of the XDEM

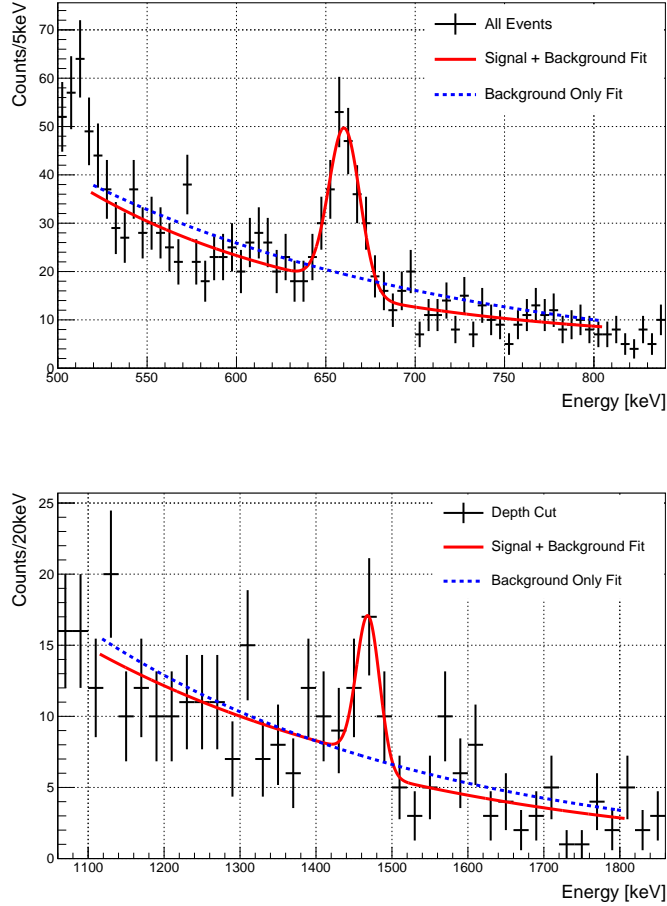


Figure 7.14: Number of events around the  $\gamma$ -lines of  $^{137}\text{Cs}$  (upper plot) and  $^{40}\text{K}$  (lower plot). In both cases, a fit assuming an exponentially falling background and a signal+background hypothesis are shown. The signal around  $^{40}\text{K}$  is only significant if a cut on interaction depth is used to remove other backgrounds.

strongest contribution at detector 2 (EV 694318-2). This hints at a localized source at or near to this detector.

Similarly, around 1460.8 keV one expects (see section 6.2) a peak from  $^{40}\text{K}$ . Indications for this line in the spectrum are weaker, as seen in the lower plot of Figure 7.14. The fit in this case gives  $\chi_{\text{red}}^2 = 1.2$  for S+B and  $\chi_{\text{red}}^2 = 1.7$  for B. The fitted mean  $E = (1469.0 \pm 6.8)$  keV is only  $1.2\sigma$  away from the true mean. The width  $\Delta E = (35.8 \pm 13.1)$  keV is again higher than expected. The net rate of the signal is only  $(0.14 \pm 0.02)/\text{d}$ . This coincides with the background model prediction. No further peaks were identified. Upper limits on the rate of various  $\gamma$ -lines are given in

## 7.4 Analysis of the Low-Background Spectrum

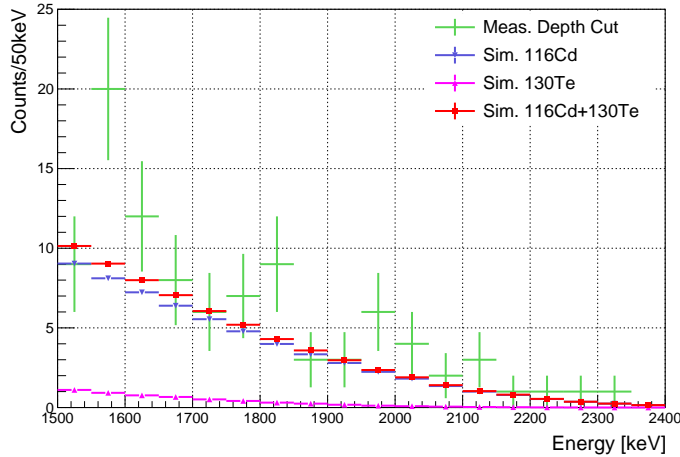


Figure 7.15: Energy spectrum between 1500 keV and 2400 keV overlaid with a simulation of the two-neutrino decays of  $^{116}\text{Cd}$  and  $^{130}\text{Te}$  scaled to half-lives found in literature.

### Appendix B.

Besides these peaks, another known source of events are the  $2\nu\beta\beta$ -decays of  $^{116}\text{Cd}$  and  $^{130}\text{Te}$ . Using the half-life from Ref. [Bar19] of  $t_{1/2}^{116\text{Cd}} = (2.69 \pm 0.12) \cdot 10^{19} \text{ yr}$  on average 4458 events/kg/yr should be registered without taking into account signal efficiencies. With the given exposure this corresponds to 480 events in the complete spectrum. The  $2\nu\beta\beta$  of  $^{130}\text{Te}$  furthermore gives also a contribution, although a smaller one. Even if there is about five times more  $^{130}\text{Te}$  than  $^{116}\text{Cd}$  in the XDEM detectors (see next section for exact values), the half-life (taken from the same reference) is also larger by a factor of about 25, leading to an estimated 82 events in this data-set.

Most of these events will have rather low energy and are thus registered in a part of the spectrum where the background is comparatively high. In Figure 7.15 the measured spectrum is compared to a MC-simulation of both decays. In the energy range from 1500 keV to 2400 keV 96 events are found and 65 events are expected. This corresponds to a signal-to-background ratio of  $2.1 \pm 0.3$ . Thus, a large fraction of events above the  $^{40}\text{K}$ -line are caused by  $2\nu\beta\beta$ -decays. In a later stage of the experiment with a larger exposure this can be exploited to perform an independent measurement of the corresponding half-lives.

Finally, one can compare the measured spectrum with the background model developed in section 6.2. To account for deviations in activity with regard to the external measurements, the model is scaled to the data using `TFRACTIONFITTER` from ROOT.

## 7 Performance of the XDEM

All  $^{232}\text{Th}$ -,  $^{238}\text{U}$ -,  $^{210}\text{Pb}$ -,  $^{40}\text{K}$ -, and  $^{137}\text{Cs}$ -sources are combined into a single histogram for each isotope. Without this simplification, the number of degrees of freedom in the fit would be too large given the number of bins and available statistics. The spectrum from cosmogenic activation of the copper (calculated with  $t_{meas} = 191$  d),  $2\nu\beta\beta$ -decays of  $^{116}\text{Cd}$  and  $^{130}\text{Te}$  combined and the muon spectrum are also included. The fraction of each spectrum is allowed to vary freely. The fit is conducted in an energy range from 400 keV to 4000 keV with a bin width of 100 keV. The result of the fit is presented in Figure 7.16.

Deviations exist mainly above 2000 keV. The fit yields  $\chi^2/Ndf = 0.17/29$ , which is very small. This is likely caused by the the large number of empty bins or bins with only a single event, which have large relative uncertainties. This makes it hard to judge the validity of the model at higher energies. However, taking into account that the model is in principle still incomplete, it seems already able to describe the data well.

### 7.5 Search for $0\nu\beta\beta$ -decays

As a last step in this analysis, the data are used to search for  $0\nu\beta\beta$ -decays of  $^{116}\text{Cd}$  and  $^{130}\text{Te}$ . These are the two  $\beta^-\beta^-$  isotopes with the highest  $Q$ -value. The half-life  $t_{1/2}$  of a decay can be calculated according to

$$t_{1/2} = \frac{\ln(2)NX\epsilon}{\hat{s}} \quad (7.4)$$

with the number of source atoms per kilogram detector mass  $n^{116\text{Cd}} = 1.73 \cdot 10^{23}/\text{kg}$  or  $n^{130\text{Te}} = 8.62 \cdot 10^{23}/\text{kg}$  (see Ref.[Ebe+16c]) for  $\text{Cd}_{0.9}\text{Zn}_{0.1}\text{Te}$  and natural isotopic composition, the exposure  $X = 0.108$  kg yr, the signal efficiency  $\epsilon$ , and  $\hat{s}$  the observed signal strength. In case no signal is observed  $\hat{s}$  is exchanged for an upper limit on the number of signal events which results in a lower limit on  $t_{1/2}$ .

$\epsilon$  can be factorized into an intrinsic efficiency  $\epsilon_{Sum}^{iso}$  (see section 6.1), an efficiency due to the behavior of real detectors  $\epsilon_{Det}$  (see subsection 5.2.3) and the efficiency of the depth cut  $\epsilon_z$  (see section 7.2). The only number that depends on the isotope of interest is  $\epsilon_{Sum}^{iso}$  and consequently it follows that

$$\begin{aligned} \epsilon^{116\text{Cd}} &= \epsilon_{Det} \cdot \epsilon_{Sum}^{116\text{Cd}} \cdot \epsilon_z = 0.50 \pm 0.03 \\ \epsilon^{130\text{Te}} &= \epsilon_{Det} \cdot \epsilon_{Sum}^{130\text{Te}} \cdot \epsilon_z = 0.52 \pm 0.03. \end{aligned}$$

The region of interest (ROI) is defined as  $Q_{\beta\beta} \pm 3\Delta E$  with  $\Delta E^{116\text{Cd}} = 26.1$  keV and

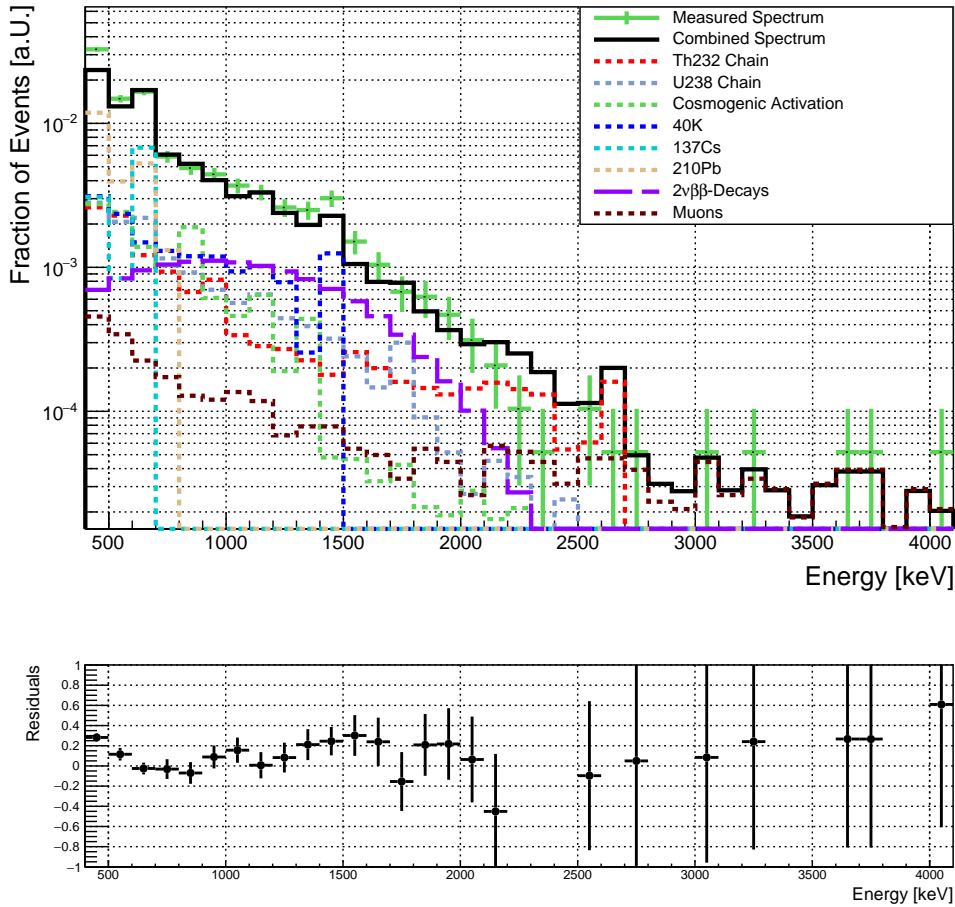


Figure 7.16: Different background contributions scaled to the measured data. In the lower panel the normalized differences between model and data are shown.

$\Delta E^{130\text{Te}} = 25.0\text{keV}$ . The large window of  $3\Delta E$  is chosen so that all events from a potential  $0\nu\beta\beta$ -peak fall into it. This takes account the energy shift described above, the fact that  $\gamma$ -lines in the background spectrum appear somewhat wider than expected from calibration and that width of the 2615 keV-peak is slightly underestimated by the resolution function. This choice is also consistent with earlier COBRA publications [Ebe+16c].

For the estimation of the background contribution  $b_{meas}$  in these regions, a window of  $Q_{\beta\beta} \pm 300\text{keV}$  is applied excluding the signal ROI. This choice is illustrated in Figure 7.17. In the ROIs  $n^{116\text{Cd}} = 1$  and  $n^{130\text{Te}} = 2$  events were found, both compatible with the expected number of background events. In the background region  $b_{meas}^{116\text{Cd}} = 4$

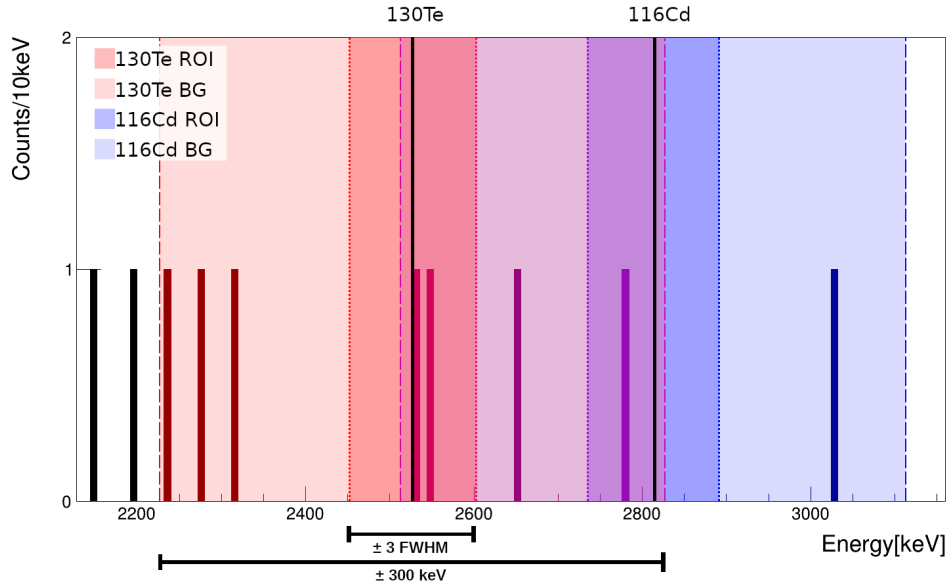


Figure 7.17: Energy spectrum around the  $Q$ -values of  $^{130}\text{Te}$  and  $^{116}\text{Cd}$ . The  $Q$ -values are marked and the regions for background and signal are overlaid in different colors. It can be seen, that in the middle region there is significant overlap between both background regions.

events were found. This results in  $b^{116\text{Cd}} = 1.4 \pm 0.7$  events expected in the ROI. Similarly,  $b_{meas}^{130\text{Te}} = 5$  is found, leading to  $b^{130\text{Te}} = 1.7 \pm 0.7$ . Expressed as a background index  $B$  normalized to exposure and energy<sup>7</sup> the numbers are

$$b^{116\text{Cd}} = (0.08 \pm 0.04) \text{ cts/kg/keV/yr}$$

$$b^{130\text{Te}} = (0.10 \pm 0.05) \text{ cts/kg/keV/yr.}$$

The background model predicted values of  $5.4 \cdot 10^{-1}$  cts/kg/keV/yr at  $Q^{130\text{Te}}$  and  $3.4 \cdot 10^{-2}$  cts/kg/keV/yr at  $Q^{116\text{Cd}}$  prior to the fit to the data.  $b^{116\text{Cd}}$  is thus slightly higher than predicted, but within  $1.2\sigma$  of the expectation, and  $b^{130\text{Te}}$  is much lower.

Based on these numbers  $\hat{s}$  is estimated, or equivalently a limit on the maximum allowed signal strength is set if no signal is found. A number of different approaches exist to deal with this problem, each with different (dis-)advantages. Here, an approach based on a profile likelihood ratio is used. It is implemented under the name TROLKE as part of ROOT 6.14 and explained in detail in Ref. [RLC05].

<sup>7</sup>Without the use of the interaction depth cut,  $B$  would have been  $(1.9 \pm 0.2)$  cts/kg/keV/yr and  $(1.3 \pm 0.2)$  cts/kg/keV/yr.

The implementation used here supports the inclusion of uncertainties in the background level and the signal efficiency as nuisance parameters. Both are rather large at about 50% and 5%. The inclusion of further nuisance parameters with uncertainties at the percent-level, like number of source atoms or uncertainties in the energy scale might be desirable, but with the given exposure the background uncertainty is clearly dominant.

The profile likelihood ratio method itself works by constructing a profile likelihood function

$$\lambda(s|n, b) = \frac{L(s, \hat{b}(s)|n, b)}{L(\hat{s}, \hat{b}|n, b)} \quad (7.5)$$

with  $L$  denoting ordinary likelihood functions – given in this case by two Poisson distributions for  $n + b$  and  $b$  – and  $\hat{s}, \hat{b}$  the most likely values of the respective parameters.  $\hat{s}$  is found by minimizing  $-2 \ln(\lambda(s|n, b))$ , which is approximately  $\chi^2$ -distributed. Confidence intervals can be calculated from the shape of the curve around the minimum. The treatment of the efficiency uncertainty can be included by multiplying a Gaussian probability distribution of the mean efficiency and its standard deviation to  $L$ .

As already naïvely expected from the number of observed events, this method gives no significant signal here. The critical number of events to reject the background only hypothesis at 90% C.L. is in both cases  $n_{\text{crit}} = 5$ . Consequently, limits will be reported. The sensitivities  $S_{\text{avg}}$  of the two peak searches, defined as the average limit obtained with no true signal  $s = 0$  and  $n = b$ , are  $S_{\text{avg}}^{116\text{Cd}} \geq 2.1 \cdot 10^{21}$  yr and  $S_{\text{avg}}^{130\text{Te}} \geq 1.0 \cdot 10^{22}$  yr. The observed lower half-life limits at 90% C.L. are

$$t_{1/2}^{116\text{Cd}} \geq 2.7 \cdot 10^{21} \text{ yr}, \quad (7.6)$$

$$t_{1/2}^{130\text{Te}} \geq 8.8 \cdot 10^{21} \text{ yr}. \quad (7.7)$$

With regard to the quoted sensitivities, the differences reflect a slight under-fluctuation of events with respect to the expected background for  $^{116}\text{Cd}$  and vice versa for  $^{130}\text{Te}$ .

The results were cross-checked with another method, the unified approach by Feldman and Cousins [FC98]. This method is also implemented in ROOT as `TFELDMAN-COUSINS`. The implementation used here does not include the treatment of nuisance parameters. This method yields limits of

$$t_{1/2}^{116\text{Cd}} \geq 2.2 \cdot 10^{21} \text{ yr}$$

$$t_{1/2}^{130\text{Te}} \geq 7.9 \cdot 10^{21} \text{ yr},$$

## 7 Performance of the XDEM

which are slightly lower than the ones obtained with the approach outlined above<sup>8</sup>. In any case, the limits are severely affected by the small available statistics, which not only gives rise to rather large limits on  $\hat{s}$ . It also makes the results sensitive to the definition of background and signal ROIs, as the exclusion of even a single event has a large influence.

### 7.6 Discussion and Outlook

In this section, data taken over the course of half a year with the COBRA XDEM setup were analyzed. Issues with individual sectors and a single detector lead to a sector-yield of 81 %. The lifetime-fraction was 91 % resulting in a total exposure of 39.5 kg d. Calibration measurements showed good linearity of the energy scale and an energy resolution at 2814 keV of about 1.0 % FWHM. The spectrum is steadily decreasing from 350 keV to about 2500 keV and dominated by peaks from  $\alpha$ -decays at higher energies. If a cut on the interaction depth is applied, this component is nearly completely reduced. The resulting background index is  $(0.08 \pm 0.04)$  cts/kg/keV/yr at  $Q_{\beta\beta}^{116\text{Cd}}$ . Statistics are limited, with single-digit numbers of events in the ROIs of  $^{116}\text{Cd}$  and  $^{130}\text{Te}$ . No significant excesses over background were found and half-life limits of  $t_{1/2}^{116\text{Cd}} \geq 2.7 \cdot 10^{21}$  yr and  $t_{1/2}^{130\text{Te}} \geq 8.8 \cdot 10^{21}$  yr were set using a likelihood-based approach. These are the most stringent limits obtained in the context of COBRA for both isotopes.

A previous search performed with the COBRA Demonstrator [Ebe+16c] used a larger exposure of 234.7 kg d. The limit for  $^{116}\text{Cd}$  was less than half as strong at  $1.1 \cdot 10^{21}$  yr. The limit for  $^{130}\text{Te}$  was also significantly weaker at  $6.1 \cdot 10^{21}$  yr. This shows the improvements in the XDEM phase. The background is lowered by a factor of 33 in the  $^{116}\text{Cd}$  ROI. This could be reached by employing the guard-ring method to remove surface events, having a beneficial surface-to-background ratio and using cleaner materials, as well as better protection from radon and advanced cleaning techniques like electro-polishing. These improvements in background are shown in Figure 7.18.

At the same time, signal efficiency is improved by about 50 %. This is due to the larger detectors and employing the guard-ring instead of pulse-shape based cuts. Energy resolution was also slightly improved from 1.1 % to about 1.0 %. In the future, an analysis with more exposure might make use of additional tools for background reduction like spatial- and temporal-anti-coincidence, pulse-shape based methods to

---

<sup>8</sup>The fact, that for very small signals the Feldman-Cousins method tends to give higher limits on  $\hat{s}$ , i. e. lower limits on  $t_{1/2}$ , was already observed in the literature [RL01].

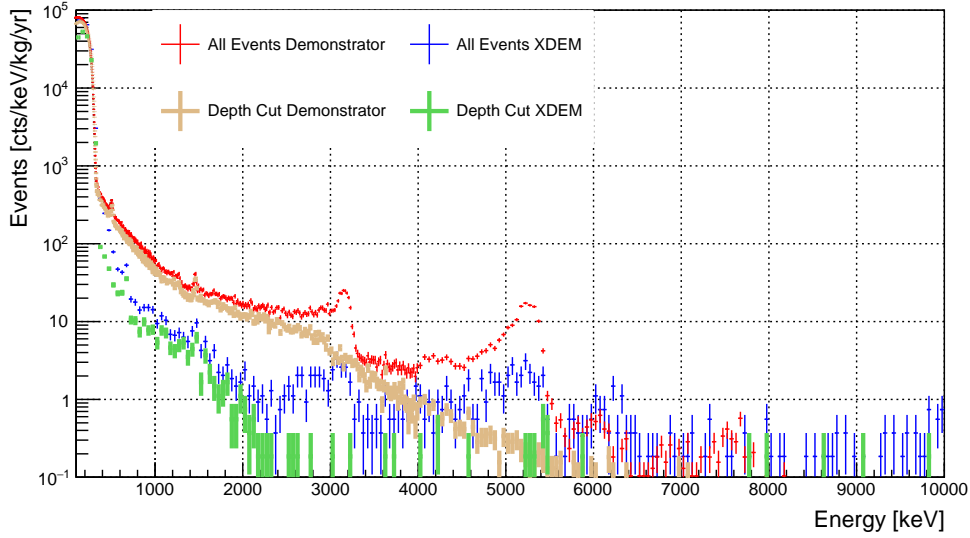


Figure 7.18: Background spectrum of the XDEM and the Demonstrator with and without interaction depth cuts. The XDEM rate is lower in both categories.

recognize multiple-scattering and cuts on the height of the guard-ring signal. For this task, a further development of the background model might prove useful. This would help to gain a better understanding of the background and further estimate possible reductions through the use of cuts. Improvements with regard to the energy resolution might also be possible by using more advance filter techniques and reducing electronic noise. Also, the number of usable sectors should be improved.

Other experiments were able to set much higher bounds on  $t_{1/2}$ . The AURORA experiment [Bar+18], which is based on large  $\text{CdWO}_4$  scintillators, has set a limit of  $t_{1/2}^{116\text{Cd}} \geq 2.2 \cdot 10^{23}$  yr. The reported background was slightly higher and energy resolution much worse. AURORA also had higher detection efficiency and approximately ten times longer data-taking. But foremost, more than 30 times higher number of  $^{116}\text{Cd}$  nuclei were employed due to the use of more massive and enriched crystals. The most recent results of CUORE [Oue18] quote  $t_{1/2}^{130\text{Te}} \geq 1.3 \cdot 10^{25}$  yr, which is even further away from the results presented in this work. In the case of CUORE the detector mass, energy resolution and background are all much more beneficial.



## 8 Conclusion

In this thesis the XDEM was presented as a major upgrade of the COBRA experiment. The upgrade itself was extensively described in chapter 4. During the course of this upgrade, several small improvements to the already existing Demonstrator setup were also conducted. These allowed to lower the trigger thresholds of this experiment significantly. With these it was possible for COBRA to perform a detailed analysis of the spectral shape of the  $\beta^-$ -decay of  $^{113}\text{Cd}$  which gave indications for quenching of the axial-vector coupling  $g_A$ .

In chapter 5 the detector used for the XDEM were investigated. It was shown that the method to calculate the interaction depth had to be slightly modified to be compatible with the novel CPqG detector design. With this modification the method yielded similar results as with a conventional CPG design. After the working point of each detector had been determined, their performance was thoroughly characterized. It could be shown that the detectors have a high mobility-lifetime product  $\mu_e\tau_e = (1.25 \pm 0.44) \cdot 10^2 \text{ cm}^2/\text{V}$  on average. Their mean relative detection efficiency is  $\epsilon_{\text{Det}} = 0.78 \pm 0.04$  if the guard-ring is used to reduce the influence of background sources at the detectors surface. Their energy resolution was found to be much better than the quality criterion of 4% FWHM at 662 keV. It turned out that detector with comparatively bad resolution tend to have higher leakage currents which behave non-linearly with rising bias voltage. Overall, nine detector for the XDEM were chosen which showed a promising performance.

In chapter 6 Monte Carlo simulations were presented that yielded further information about the behavior of the detectors and the XDEM as a whole. For one thing, the intrinsic efficiency to measure neutrinoless double  $\beta$ -decays at their full energy was determined. It turned out to be  $\epsilon_{\text{int}} = 0.714 \pm 0.009$  for  $^{116}\text{Cd}$  and  $\epsilon_{\text{int}} = 0.753 \pm 0.007$  for  $^{130}\text{Te}$ . Furthermore a background model was constructed based on information from external measurements about the radioisotopes content of construction materials used for the XDEM. This model predicts a background of  $3.4 \cdot 10^{-2} \text{ cts/kg/keV/yr}$  at  $Q^{^{116}\text{Cd}}$  and  $5.1 \cdot 10^{-1} \text{ cts/kg/keV/yr}$  at  $Q^{^{130}\text{Te}}$ . The biggest contributions to this are coming from cosmic muons and contamination of the inner parts of the shielding with

## 8 Conclusion

primordial decay-chains.

Based on these results the XDEM setup was commissioned in April 2018. After some initial problems were overcome, data-taking started in November 2018. In chapter 7 first data taken over 191 days was presented. Calibration measurements showed a good linearity of the energy scale of the detectors inside the underground setup. Their relative energy resolution at the  $Q$ -values of the aforementioned double-beta decays was estimated to be about 1.0% FWHM. The stability of the setup during the 191 days was assessed with various methods. A shift in reconstructed energy was found to have occurred after a decrease in temperature at some parts of the read-out electronics. Its magnitude was found to be smaller than the energy resolution and thus not prohibitive for further analyses. The interaction depth cut proved successful in removing a large portion of the background while retaining a fraction  $0.89 \pm 0.01$  of signal-like events. A comparison to the background model showed that a significant fraction of events measured between 350 keV and 2800 keV is coming from two-neutrino double  $\beta$ -decays.

Finally a search for the neutrinoless double  $\beta$ -decays of  $^{116}\text{Cd}$  and  $^{130}\text{Te}$  was conducted with this data. An expected background of  $b^{116\text{Cd}} = (0.08 \pm 0.04)$  cts/kg/keV/yr and  $b^{130\text{Te}} = (0.10 \pm 0.05)$  cts/kg/keV/yr was found for the signal regions showing. No significant excess in events was observed in these regions. Consequently, lower limits on the half-lives of these decays were set at  $t_{1/2}^{116\text{Cd}} \geq 2.7 \cdot 10^{21}$  yr and  $t_{1/2}^{130\text{Te}} \geq 8.8 \cdot 10^{21}$  yr. These are the most stringent limits set in the context of COBRA.

In Figure 8.1 the half-life limit on the neutrinoless decay of  $^{116}\text{Cd}$  and the product of background index and energy resolution  $B \times \Delta E$  is shown for various iterations of the COBRA experiment and other  $^{116}\text{Cd}$ -based experiments. Compared to the first COBRA setup, the half-life limit could be improved by two orders of magnitude and  $B \times \Delta E$  by about four orders of magnitude in the XDEM. Compared to the Demonstrator setup  $B \times \Delta E$  is improved by more than a factor of 36 and stronger limits are obtained with only about 1/6th of the exposure. This demonstrates the success of background reduction techniques like the interaction depth cut and the use of the guard-ring, as well as improved choice of materials and cleaning procedures.

A further reduction in background might be possible by using spatial and time anti-coincidence, cuts on the height of the guard-ring signal and pulse-shapes analysis, things that were in parts already successfully used for the Demonstrator. In the short-term the XDEM will profit from acquiring more exposure through a longer measurement. For this, it would be beneficial to try to raise the number of usable sectors and keep a high live-time fraction. To be competitive with other experiments more source atoms are needed. This could be achieved by both isotopic enrichment and the deployment

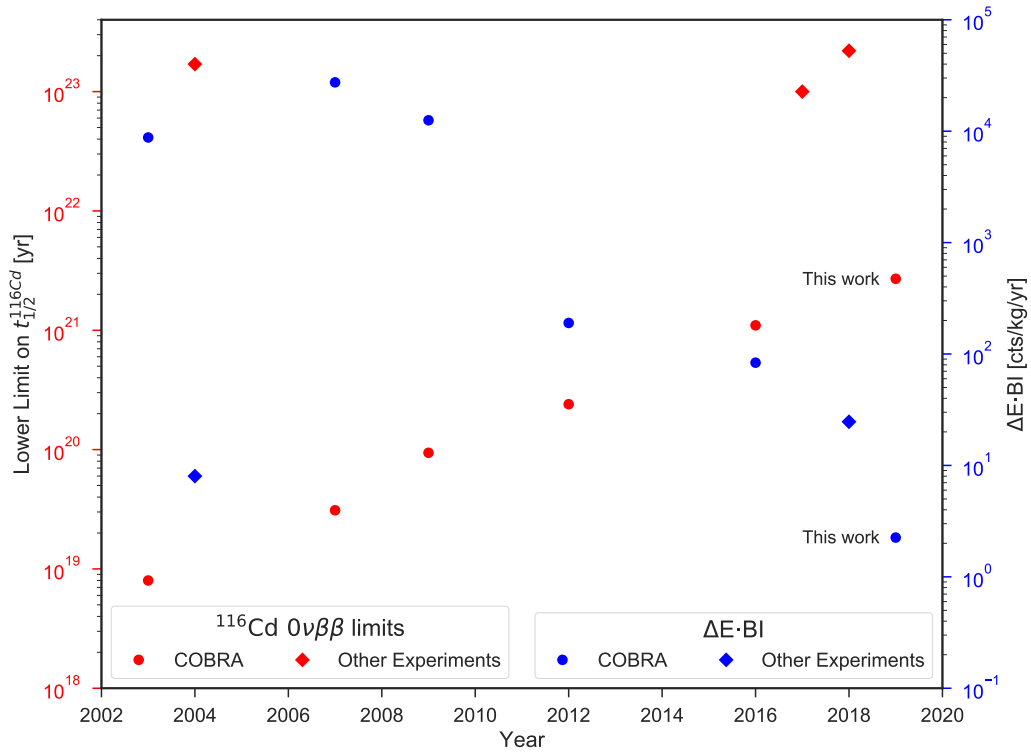


Figure 8.1: Limits on the  $0\nu\beta\beta$  half-life of  $^{116}\text{Cd}$  from different stages of COBRA [KMZ03; Blo+07; Daw+09b; Ebe+16c]. Also shown are the Solotvina- [Dan+03], NEMO-3- [Arn+17] and the AUROA-experiments [Bar+18]. Also shown is the product of background index and FWHM energy resolution.

of more detector mass. With detectors enriched to about 90% of  $^{116}\text{Cd}$ , it would be possible to measure the  $2\nu\beta\beta$ -decay with excellent signal-to-background ratio. The detector mass needed to improve existing limits on the decay of  $^{116}\text{Cd}$  by AURORA would be relatively modest. Only little more than a kilogram of enriched detector mass would be needed, which should be feasible using the current approach. Tackling the limits on the decay of  $^{130}\text{Te}$  set by CUORE would require a very different way of operation, as COBRA would have to be scaled up to several hundred kilogram of detector mass.

# Acknowledgments

The work conducted in this thesis would not have been possible without the help of many people whom I like to thank here.

First of all, I like to thank Prof. Dr. Kevin Kröniger and Prof. Dr. Claus Gößling for granting me the opportunity to work on this interesting experiment and supervising my thesis. I also like to thank Prof. Dr. Wolfgang Rhode for acting as a referee.

I am indebted to my family for supporting me during the work at my thesis. This is especially true for my wife Katharina and my daughter Lea who had to do without me much too often when I got missing behind my computer. I am thanking my parents and parents-in-law for always being interested in the progress of my work and their ongoing support. I also like to thank Judith Stockem for providing me with useful tips concerning the English language.

I also have to thank all people at E4 for many joyful years. I cannot name everyone here, but like to highlight Andrea Teichmann's patience in matters of bureaucracy. Also, Dr. Jens Weingarten and Gregor Geßner were great proof readers which reminded me of the existence of the plural and the difference between then and than.

I was happy to be able to work with many interesting and kind people on the COBRA experiment. Prof. Dr. Kai Zuber often provided me with great insights into nuclear- and neutrino-physics. Dr. Jan Tebrügge supervised me during my B.Sc. and M.Sc. theses and proof-read parts of this thesis. Jan also taught me how to work with CdZnTe detectors in the first place and we had many great discussions designing the XDEM. Thomas Quante was always helpful with any problem regarding IT or coding. The experience that Stefan Zatschler gained in working with the Demonstrator allowed me to successfully operate the XDEM setup. Furthermore, I like to thank all COBRA people who worked with me at the LNGS. The days working in the underground may have been long and stressful, but they were also fun and ultimately very fruitful! Numerous people who worked on COBRA before me paved the way for my thesis. Of these, I like to point out Dr. Oliver Schulz who was always available for questions regarding software tools and acted as our IT coordinator at the LNGS.

Similarly, I like to thank some people working at the LNGS itself: Matthias Junker,

## 8 *Conclusion*

Nicola Rossi and Vincenzo Caracciolo for acting as local contact persons at the LNGS and helping me deal with the language barrier. Marco Balata not only acted as our GLIMOS but was also very helpful in all regards concerning chemistry and cleaning. Stefano Nisi kindly provided ICP-MS measurements of several components for the experiment.

I also like to thank Roberto from the Il Grottino in Assergi for being such a fantastic host. Additional FADCs required for the operation of the XDEM were once again kindly provided by R. Wischnewski.

# Bibliography

- [AA+18] A. A. Aguilar-Arevalo et al. “Significant Excess of ElectronLike Events in the MiniBooNE Short-Baseline Neutrino Experiment”. In: *Phys. Rev. Lett.* 121.22 (2018), p. 221801. DOI: 10.1103/PhysRevLett.121.221801. arXiv: 1805.12028 [hep-ex].
- [Aal+02a] C. E. Aalseth et al. “Comment on ”Evidence For Neutrinoless Double Beta Decay””. In: *Modern Physics Letters A* 17.22 (2002), pp. 1475–1478. DOI: 10.1142/S0217732302007715. eprint: <https://doi.org/10.1142/S0217732302007715>. URL: <https://doi.org/10.1142/S0217732302007715>.
- [Aal+02b] C. E. Aalseth et al. “The IGEX Ge-76 neutrinoless double beta decay experiment: Prospects for next generation experiments”. In: *Phys. Rev. D* 65 (2002), p. 092007. DOI: 10.1103/PhysRevD.65.092007. arXiv: hep-ex/0202026 [hep-ex].
- [Aal+16] J. Aalbers et al. “DARWIN: towards the ultimate dark matter detector”. In: *JCAP* 1611 (2016), p. 017. DOI: 10.1088/1475-7516/2016/11/017. arXiv: 1606.07001 [astro-ph.IM].
- [Abd+94] J. N. Abdurashitov et al. “Results from SAGE”. In: *Phys. Lett.* B328 (1994), pp. 234–248. DOI: 10.1016/0370-2693(94)90454-5.
- [Abe+18] K. Abe et al. “Search for CP Violation in Neutrino and Antineutrino Oscillations by the T2K Experiment with  $2.2 \times 10^{21}$  Protons on Target”. In: *Phys. Rev. Lett.* 121.17 (2018), p. 171802. DOI: 10.1103/PhysRevLett.121.171802. arXiv: 1807.07891 [hep-ex].
- [Abg+16] N. Abgrall et al. “The Majorana Demonstrator radioassay program”. In: *Nucl. Instrum. Meth.* A828 (2016), pp. 22–36. DOI: 10.1016/j.nima.2016.04.070. arXiv: 1601.03779 [physics.ins-det].

## BIBLIOGRAPHY

- [Abg+17] N. Abgrall et al. “The Large Enriched Germanium Experiment for Neutrinoless Double Beta Decay (LEGEND)”. In: *AIP Conf. Proc.* 1894.1 (2017), p. 020027. DOI: 10.1063/1.5007652. arXiv: 1709.01980 [physics.ins-det].
- [Ada+17] P. Adamson et al. “Measurement of the neutrino mixing angle  $\theta_{23}$  in NOvA”. In: *Phys. Rev. Lett.* 118.15 (2017), p. 151802. DOI: 10.1103/PhysRevLett.118.151802. arXiv: 1701.05891 [hep-ex].
- [Ade+18] D. Adey et al. “Measurement of the Electron Antineutrino Oscillation with 1958 Days of Operation at Daya Bay”. In: *Phys. Rev. Lett.* 121 (24 2018), p. 241805. DOI: 10.1103/PhysRevLett.121.241805. URL: <https://link.aps.org/doi/10.1103/PhysRevLett.121.241805>.
- [AEE08] Frank T. Avignone III, Steven R. Elliott, and Jonathan Engel. “Double Beta Decay, Majorana Neutrinos, and Neutrino Mass”. In: *Rev. Mod. Phys.* 80 (2008), pp. 481–516. DOI: 10.1103/RevModPhys.80.481. arXiv: 0708.1033 [nucl-ex].
- [Ago+03] S. Agostinelli et al. “Geant4—a simulation toolkit”. In: *Nuclear Instruments and Methods in Physics Research Section A: Accelerators, Spectrometers, Detectors and Associated Equipment* 506.3 (2003), pp. 250 – 303. ISSN: 0168-9002. DOI: [https://doi.org/10.1016/S0168-9002\(03\)01368-8](https://doi.org/10.1016/S0168-9002(03)01368-8). URL: <http://www.sciencedirect.com/science/article/pii/S0168900203013688>.
- [Ago+18] M. Agostini et al. “Improved Limit on Neutrinoless Double- $\beta$  Decay of  $^{76}\text{Ge}$  from GERDA Phase II”. In: *Phys. Rev. Lett.* 120 (13 2018), p. 132503. DOI: 10.1103/PhysRevLett.120.132503. URL: <https://link.aps.org/doi/10.1103/PhysRevLett.120.132503>.
- [Ahm+02] Q. R. Ahmad et al. “Direct Evidence for Neutrino Flavor Transformation from Neutral-Current Interactions in the Sudbury Neutrino Observatory”. In: *Phys. Rev. Lett.* 89 (1 2002), p. 011301. DOI: 10.1103/PhysRevLett.89.011301. URL: <https://link.aps.org/doi/10.1103/PhysRevLett.89.011301>.
- [Ake+19] M. Aker et al. “An improved upper limit on the neutrino mass from a direct kinematic method by KATRIN”. In: (2019). arXiv: 1909.06048 [hep-ex].

- [Alb+18a] J. B. Albert et al. “Search for Neutrinoless Double-Beta Decay with the Upgraded EXO-200 Detector”. In: *Phys. Rev. Lett.* 120 (7 2018), p. 072701. DOI: 10.1103/PhysRevLett.120.072701. URL: <https://link.aps.org/doi/10.1103/PhysRevLett.120.072701>.
- [Alb+18b] J. B. Albert et al. “Sensitivity and Discovery Potential of nEXO to Neutrinoless Double Beta Decay”. In: *Phys. Rev.* C97.6 (2018), p. 065503. DOI: 10.1103/PhysRevC.97.065503. arXiv: 1710.05075 [nucl-ex].
- [Alb16] M. Albrecht. “Analyse des Rauschverhaltens eines ASIC basierten Auslesesystems für das COBRA-Experiment”. Bachelor’s Thesis. TU Dortmund, 2016.
- [Ald+18] C. Alduino et al. “First Results from CUORE: A Search for Lepton Number Violation via  $0\nu\beta\beta$  Decay of  $^{130}\text{Te}$ ”. In: *Phys. Rev. Lett.* 120.13 (2018), p. 132501. DOI: 10.1103/PhysRevLett.120.132501. arXiv: 1710.07988 [nucl-ex].
- [Ale07] M. Alex. “A microcontroller based solution for remote laboratory data acquisition and control”. Diploma. TU Dortmund, 2007.
- [Ali+17] A. E. Ali et al. “Determining the neutrino mass with cyclotron radiation emission spectroscopy—Project 8”. In: *J. Phys.* G44.5 (2017), p. 054004. DOI: 10.1088/1361-6471/aa5b4f. arXiv: 1703.02037 [physics.ins-det].
- [All+16] J. Allison et al. “Recent developments in Geant4”. In: *Nuclear Instruments and Methods in Physics Research Section A: Accelerators, Spectrometers, Detectors and Associated Equipment* 835 (2016), pp. 186–225. ISSN: 0168-9002. DOI: <https://doi.org/10.1016/j.nima.2016.06.125>. URL: <http://www.sciencedirect.com/science/article/pii/S0168900216306957>.
- [ALL02] M. Amman, J. S. Lee, and P. N. Luke. “Electron trapping nonuniformity in high-pressure-Bridgman-grown CdZnTe”. In: *Journal of Applied Physics* 92.6 (2002), pp. 3198–3206. DOI: 10.1063/1.1502922. eprint: <https://doi.org/10.1063/1.1502922>. URL: <https://doi.org/10.1063/1.1502922>.
- [Alv+19] S. I. Alvis et al. “A Search for Neutrinoless Double-Beta Decay in  $^{76}\text{Ge}$  with 26 kg-yr of Exposure from the MAJORANA DEMONSTRATOR”. In: (2019). arXiv: 1902.02299 [nucl-ex].

## BIBLIOGRAPHY

- [Amm+09a] M. Amman et al. “Detector Module Development for the High Efficiency Multimode Imager”. In: 12/2009, pp. 981–985. DOI: 10.1109/NSSMIC.2009.5402446.
- [Amm+09b] M. Amman et al. “Evaluation of THM-Grown CdZnTe Material for Large-Volume Gamma-Ray Detector Applications”. In: *IEEE Transactions on Nuclear Science* 56.3 (2009), pp. 795–799. ISSN: 0018-9499. DOI: 10.1109/TNS.2008.2010402.
- [Ang+12] G. Angloher et al. “Results from 730 kg days of the CRESST-II Dark Matter search”. In: *The European Physical Journal C* 72.4 (2012), p. 1971. ISSN: 1434-6052. DOI: 10.1140/epjc/s10052-012-1971-8. URL: <https://doi.org/10.1140/epjc/s10052-012-1971-8>.
- [Apr+19a] E. Aprile et al. “Observation of two-neutrino double electron capture in  $^{124}\text{Xe}$  with XENON1T”. In: *Nature* 568.7753 (2019), pp. 532–535. ISSN: 1476-4687. DOI: 10.1038/s41586-019-1124-4. URL: <https://doi.org/10.1038/s41586-019-1124-4>.
- [Apr+19b] E. Aprile et al. “Observation of two-neutrino double electron capture in  $^{124}\text{Xe}$  with XENON1T”. In: *Nature* 568.7753 (2019), pp. 532–535. DOI: 10.1038/s41586-019-1124-4. arXiv: 1904.11002 [nucl-ex].
- [Arl+17] J.-H. Arling et al. “Suppression of alpha-induced lateral surface events in the COBRA experiment using CdZnTe detectors with an instrumented guard-ring electrode”. In: *Journal of Instrumentation* 12.11 (2017), P11025–P11025. DOI: 10.1088/1748-0221/12/11/p11025. URL: <https://doi.org/10.1088/1748-0221/12/11/p11025>.
- [Arl14] J. H. Arling. “Systematische Untersuchung von  $6\text{ cm}^3$ -CdZnTe-Detektorkristallen mit zwei verschiedenen CPG-Designs”. Bachelor thesis. TU Dortmund, 2014.
- [Arl16] J. H. Arling. “Characterization of Coplanar Grid CdZnTe Detectors and Instrumentation of the Guardring for the COBRA Experiment”. Master’s Thesis. TU Dortmund, 2016.
- [Arn+05] R. Arnold et al. “Technical design and performance of the NEMO 3 detector”. In: *Nuclear Instruments and Methods in Physics Research Section A: Accelerators, Spectrometers, Detectors and Associated Equipment* 536.1 (2005), pp. 79–122. ISSN: 0168-9002. DOI: 10.1016/j.nima.2004.

- 07.194. URL: <http://www.sciencedirect.com/science/article/pii/S0168900204016821>.
- [Arn+15] R. Arnold et al. “Results of the search for neutrinoless double- $\beta$  decay in  $^{100}\text{Mo}$  with the NEMO-3 experiment”. In: *Phys. Rev. D* 92 (7 2015), p. 072011. DOI: 10.1103/PhysRevD.92.072011. URL: <https://link.aps.org/doi/10.1103/PhysRevD.92.072011>.
- [Arn+17] R. Arnold et al. “Measurement of the  $2\nu\beta\beta$  decay half-life and search for the  $0\nu\beta\beta$  decay of  $^{116}\text{Cd}$  with the NEMO-3 detector”. In: *Phys. Rev. D* 95 (1 2017), p. 012007. DOI: 10.1103/PhysRevD.95.012007. URL: <https://link.aps.org/doi/10.1103/PhysRevD.95.012007>.
- [Ase+11] V. N. Aseev et al. “An upper limit on electron antineutrino mass from Troitsk experiment”. In: *Phys. Rev. D* 84 (2011), p. 112003. DOI: 10.1103/PhysRevD.84.112003. arXiv: 1108.5034 [hep-ex].
- [Awa+10] S.A. Awadalla et al. “Characterization of detector-grade CdZnTe crystals grown by traveling heater method (THM)”. In: *Journal of Crystal Growth* 312.4 (2010), pp. 507–513. ISSN: 0022-0248. DOI: <https://doi.org/10.1016/j.jcrysgro.2009.11.007>. URL: <http://www.sciencedirect.com/science/article/pii/S002202480900997X>.
- [Azz+18] O. Azzolini et al. “First Result on the Neutrinoless Double- $\beta$  Decay of  $^{82}\text{Se}$  with CUPID-0”. In: *Phys. Rev. Lett.* 120.23 (2018), p. 232502. DOI: 10.1103/PhysRevLett.120.232502. arXiv: 1802.07791 [nucl-ex].
- [Bak+05] A. M. Bakalyarov et al. “Results of the experiment on investigation of Germanium-76 double beta decay: Experimental data of Heidelberg-Moscow collaboration November 1995 - August 2001”. In: *Phys. Part. Nucl. Lett.* 2 (2005). Pisma Fiz. Elem. Chast. Atom. Yadra 2005, No.2, 21 (2005), pp. 77–81. arXiv: hep-ex/0309016 [hep-ex].
- [Ban+19] I. C. Bandac et al. “The  $0\nu 2\beta$ -decay CROSS experiment: preliminary results and prospects”. In: (2019). arXiv: 1906.10233 [nucl-ex].
- [Bar+17] A.S. Barabash et al. “Calorimeter development for the SuperNEMO double beta decay experiment”. In: *Nuclear Instruments and Methods in Physics Research Section A: Accelerators, Spectrometers, Detectors and Associated Equipment* 868 (2017), pp. 98–108. ISSN: 0168-9002. DOI: 10.1016/j.nima.2017.06.044. URL: <http://www.sciencedirect.com/science/article/pii/S0168900217306976>.

## BIBLIOGRAPHY

- [Bar+18] A. S. Barabash et al. “Final results of the Aurora experiment to study  $2\beta$  decay of  $^{116}\text{Cd}$  with enriched  $^{116}\text{CdWO}_4$  crystal scintillators”. In: *Phys. Rev. D* 98.9 (2018), p. 092007. DOI: 10.1103/PhysRevD.98.092007. arXiv: 1811.06398 [nucl-ex].
- [Bar10] A. S. Barabash. “75 years of double beta decay: yesterday, today and tomorrow”. In: *DAE Symp. Nucl. Phys.* 55 (2010), p. I13. arXiv: 1101.4502 [nucl-ex].
- [Bar15] A.S. Barabash. “Average and recommended half-life values for two-neutrino double beta decay”. In: *Nuclear Physics A* 935 (2015), pp. 52–64. ISSN: 0375-9474. DOI: <https://doi.org/10.1016/j.nuclphysa.2015.01.001>. URL: <http://www.sciencedirect.com/science/article/pii/S037594741500010X>.
- [Bar19] A. S. Barabash. “Average and recommended half-life values for two-neutrino double beta decay: upgrade-2019”. In: *Matrix Elements for the Double-beta-decay EXperiments (MEDEX'19) Prague, Czech Republic, May 27-31, 2019*. 2019. arXiv: 1907.06887 [nucl-ex].
- [Bau+15] Laura Baudis et al. “Cosmogenic activation of xenon and copper”. In: *Eur. Phys. J. C* 75.10 (2015), p. 485. DOI: 10.1140/epjc/s10052-015-3711-3. arXiv: 1507.03792 [astro-ph.IM].
- [BD+18] L. Bodenstein-Dresler et al. “Quenching of  $g_A$  deduced from the  $\beta$ -spectrum shape of  $^{113}\text{Cd}$  measured with the COBRA experiment”. In: (06/06/2018). <https://arxiv.org/abs/1806.02254>. arXiv: 1806.02254 [nucl-ex]. URL: <https://arxiv.org/abs/1806.02254>.
- [BD15] L. Bodenstein-Dresler. “Entwicklung einer neuen Detektorhalterung inklusive Inbetriebnahme einer ASIC-basierten Auslese für das COBRA-Experiment”. Bachelor Thesis. TU Dortmund, 2015.
- [BD18] L. Bodenstein-Dresler. “Preparation for the COBRA XDEM phase including design of mechanical parts and tests of electronics and measurements of beta-suppression”. Master’s Thesis. TU Dortmund, 2018.
- [BD76] J. Bahcall and R. Davis. “Solar Neutrinos - a Scientific Puzzle”. In: *Science* 191 (1976), pp. 264–267. DOI: 10.1126/science.191.4224.264.
- [Bec19] Laboratoire National Henri Becquerel. *Nucléide - Lara Library for gamma and alpha emissions*. 2019. URL: <http://www.nucleide.org/Laraweb/index.php> (visited on 07/15/2019).

## BIBLIOGRAPHY

- [Bel+07] P. Belli et al. “Investigation of  $\beta$  decay of  $^{113}\text{Cd}$ ”. In: *Phys. Rev. C* 76 (6 2007), p. 064603. DOI: 10.1103/PhysRevC.76.064603. URL: <https://link.aps.org/doi/10.1103/PhysRevC.76.064603>.
- [Bel+10] P. Belli et al. “New observation of  $2\beta 2\nu$  decay of  $^{100}\text{Mo}$  to the  $0_1^+$  level of  $^{100}\text{Ru}$  in the ARMONIA experiment”. In: *Nuclear Physics A* 846.1 (2010), pp. 143–156. ISSN: 0375-9474. DOI: <https://doi.org/10.1016/j.nuclphysa.2010.06.010>. URL: <http://www.sciencedirect.com/science/article/pii/S037594741000549X>.
- [Bel+12] G Bellini et al. “Cosmic-muon flux and annual modulation in Borexino at 3800 m water-equivalent depth”. In: *Journal of Cosmology and Astroparticle Physics* 2012.05 (2012), pp. 015–015. DOI: 10.1088/1475-7516/2012/05/015. URL: <https://doi.org/10.1088%2F1475-7516%2F2012%2F05%2F015>.
- [Bel+89] P. Belli et al. “Deep underground neutron flux measurement with large BF3 counters”. In: *Il Nuovo Cimento A (1965-1970)* 101.6 (1989), pp. 959–966. ISSN: 1826-9869. DOI: 10.1007/BF02800162. URL: <https://doi.org/10.1007/BF02800162>.
- [Bel88] E. Bellotti. “The Gran Sasso Underground Laboratory”. In: *Nuclear Instruments and Methods in Physics Research Section A: Accelerators, Spectrometers, Detectors and Associated Equipment* 264.1 (1988), pp. 1–4. ISSN: 0168-9002. DOI: [https://doi.org/10.1016/0168-9002\(88\)91093-5](https://doi.org/10.1016/0168-9002(88)91093-5). URL: <http://www.sciencedirect.com/science/article/pii/0168900288910935>.
- [Ber+] M.J. Berger et al. *XCOM: Photon Cross Sections Database*. Ed. by NIST. URL: <https://www.nist.gov/pml/xcom-photon-cross-sections-database> (visited on 07/09/2019).
- [Bil+17] T. Billoud et al. “Characterization of a pixelated CdTe Timepix detector operated in ToT mode”. In: *Journal of Instrumentation* 12.01 (2017), P01018–P01018. DOI: 10.1088/1748-0221/12/01/p01018. URL: <https://doi.org/10.1088%2F1748-0221%2F12%2F01%2Fp01018>.
- [Blo+07] T. Bloxham et al. “First results on double  $\beta$ -decay modes of Cd, Te, and Zn Isotopes”. In: *Phys. Rev. C* 76 (2 2007), p. 025501. DOI: 10.1103/PhysRevC.76.025501. URL: <https://link.aps.org/doi/10.1103/PhysRevC.76.025501>.

## BIBLIOGRAPHY

- [Bol+02] Aleksey E. Bolotnikov et al. “Properties of Pt Schottky type contacts on high-resistivity CdZnTe detectors”. In: *NIM A* 482.1-2 (2002), pp. 395–407. DOI: 10.1016/S0168-9002(01)01506-6. arXiv: physics/0103005 [physics.ins-det].
- [Bol+05] A. E.E. Bolotnikov et al. “Performance studies of CdZnTe detector by using a pulse shape analysis”. In: *Proceedings of SPIE - The International Society for Optical Engineering* 5922 (08/2005). DOI: 10.1117/12.618355.
- [Bol+11] A. E. Bolotnikov et al. “Performance of a Large Volume 20×20×15 mm<sup>3</sup>CPG Detector”. In: *IEEE Transactions on Nuclear Science* 58.6 (2011), pp. 3167–3171. ISSN: 0018-9499. DOI: 10.1109/TNS.2011.2167984.
- [Bol+16] A. E. Bolotnikov et al. “CdZnTe position-sensitive drift detectors with thicknesses up to 5cm”. In: *Applied Physics Letters* 108.9 (2016), p. 093504. DOI: 10.1063/1.4943161. eprint: <https://doi.org/10.1063/1.4943161>. URL: <https://doi.org/10.1063/1.4943161>.
- [Bra+17] M. Braun et al. “A new precision measurement of the  $\alpha$ -decay half-life of 190Pt”. In: *Physics Letters B* 768 (2017), pp. 317–320. ISSN: 0370-2693. DOI: <https://doi.org/10.1016/j.physletb.2017.02.052>. URL: <http://www.sciencedirect.com/science/article/pii/S037026931730165X>.
- [BRJ83] J. Bernabeu, A. De Rujula, and C. Jarlskog. “Neutrinoless double electron capture as a tool to measure the electron neutrino mass”. In: *Nuclear Physics B* 223.1 (1983), pp. 15–28. ISSN: 0550-3213. DOI: [https://doi.org/10.1016/0550-3213\(83\)90089-5](https://doi.org/10.1016/0550-3213(83)90089-5). URL: <http://www.sciencedirect.com/science/article/pii/0550321383900895>.
- [BT04] D. Binosi and L. Theußl. “JaxoDraw: A graphical user interface for drawing Feynman diagrams”. In: *Computer Physics Communications* 161.1 (2004), pp. 76–86. ISSN: 0010-4655. DOI: <https://doi.org/10.1016/j.cpc.2004.05.001>. URL: <http://www.sciencedirect.com/science/article/pii/S0010465504002115>.
- [BW11] M. Berglund and M. E. Wieser. “Isotopic compositions of the elements 2009”. In: *Pure Appl. Chem.* 83.2 (2011), pp. 397–410. DOI: <http://dx.doi.org/10.1351/PAC-REP-10-06-02>.

- [Cah+13] R. N. Cahn et al. “White Paper: Measuring the Neutrino Mass Hierarchy”. In: *Proceedings, 2013 Community Summer Study on the Future of U.S. Particle Physics: Snowmass on the Mississippi (CSS2013): Minneapolis, MN, USA, July 29-August 6, 2013*. 2013. arXiv: 1307.5487 [hep-ex]. URL: <http://www.slac.stanford.edu/econf/C1307292/docs/submittedArxivFiles/1307.5487.pdf>.
- [Car+04] J. M. Carmona et al. “Neutron background at the Canfranc Underground Laboratory and its contribution to the IGEX-DM dark matter experiment”. In: *Astropart. Phys.* 21 (2004), pp. 523–533. DOI: 10.1016/j.astropartphys.2004.04.002. arXiv: hep-ex/0403009 [hep-ex].
- [Car+06] G. A. Carini et al. “Effect of Te precipitates on the performance of CdZnTe detectors”. In: *Applied Physics Letters* 88.14 (2006), p. 143515. DOI: 10.1063/1.2189912. eprint: <https://doi.org/10.1063/1.2189912>. URL: <https://doi.org/10.1063/1.2189912>.
- [Car+07] G. A. Carini et al. “Non-uniformity effects in CdZnTe coplanar-grid detectors”. In: *physica status solidi (b)* 244.5 (2007), pp. 1589–1601. ISSN: 1521-3951. DOI: 10.1002/pssb.200675103. URL: <http://dx.doi.org/10.1002/pssb.200675103>.
- [Ceb+15] S. Cebrián et al. “Radiopurity assessment of the tracking readout for the NEXT double beta decay experiment”. In: *JINST* 10.05 (2015), P05006. DOI: 10.1088/1748-0221/10/05/P05006. arXiv: 1411.1433 [physics.ins-det].
- [Che+08] H. Chen et al. “Characterization of large cadmium zinc telluride crystals grown by traveling heater method”. In: *Journal of Applied Physics* 103.1 (2008), p. 014903. DOI: 10.1063/1.2828170. eprint: <https://doi.org/10.1063/1.2828170>. URL: <https://doi.org/10.1063/1.2828170>.
- [Che+18] H. Chen et al. “Development of large-volume high-performance monolithic CZT radiation detector”. In: vol. 10762. 2018. DOI: 10.1117/12.2321244. URL: <https://doi.org/10.1117/12.2321244>.
- [Chr+64] J. H. Christenson et al. “Evidence for the  $2\pi$  Decay of the  $K_2^0$  Meson”. In: *Phys. Rev. Lett.* 13 (4 1964), pp. 138–140. DOI: 10.1103/PhysRevLett.13.138. URL: <https://link.aps.org/doi/10.1103/PhysRevLett.13.138>.

## BIBLIOGRAPHY

- [Cle+98] T. Cleveland et al. “Measurement of the Solar Electron Neutrino Flux with the Homestake Chlorine Detector”. In: *Astrophys.J.* 496.1 (1998), p. 505. URL: <http://stacks.iop.org/0004-637X/496/i=1/a=505>.
- [CM13] L. Cai and L. Meng. “Hybrid pixel-waveform CdTe/CZT detector for use in an ultrahigh resolution MRI compatible SPECT system”. In: *Nuclear Instruments and Methods in Physics Research Section A: Accelerators, Spectrometers, Detectors and Associated Equipment* 702 (2013). PET/MR and SPECT/MR: New Paradigms for Combined Modalities in Molecular Imaging, pp. 101–103. ISSN: 0168-9002. DOI: <https://doi.org/10.1016/j.nima.2012.08.069>. URL: <http://www.sciencedirect.com/science/article/pii/S0168900212009722>.
- [CM97] J.L. Campbell and J.A. Maxwell. “A cautionary note on the use of the Hypermet tailing function in X-ray spectrometry with Si(Li) detectors”. In: *Nucl. Instrum. Methods Phys. Res., Sect. B* 129.2 (1997), pp. 297–299. ISSN: 0168-583X. DOI: [https://doi.org/10.1016/S0168-583X\(97\)00229-2](https://doi.org/10.1016/S0168-583X(97)00229-2). URL: <http://www.sciencedirect.com/science/article/pii/S0168583X97002292>.
- [Coa+16] I. Coarasa et al. “Cosmogenic and primordial radioisotopes in copper bricks shortly exposed to cosmic rays”. In: *Journal of Physics: Conference Series* 718 (05/2016), p. 042049. DOI: 10.1088/1742-6596/718/4/042049.
- [Col+16] Planck Collaboration et al. “Planck intermediate results - XLVI. Reduction of large-scale systematic effects in HFI polarization maps and estimation of the reionization optical depth”. In: *A&A* 596 (2016), A107. DOI: 10.1051/0004-6361/201628890. URL: <https://doi.org/10.1051/0004-6361/201628890>.
- [Cor] Rogers Corporation. *RO4000 Series High Frequency Circuit Materials Data Sheet*. URL: <http://www.rogerscorp.de/documents/726/acs/R04000-Laminates-R04003C-and-R04350BData-Sheet.pdf> (visited on 05/02/2019).
- [Cow+56] C. L. Cowan et al. “Detection of the free neutrino: A Confirmation”. In: *Science* 124 (1956), pp. 103–104. DOI: 10.1126/science.124.3212.103.
- [Cri+99] M. Cribier et al. “Results of the whole GALLEX experiment”. In: *Nuclear Physics B - Proceedings Supplements* 70.1 (1999). Proceedings of the Fifth

- International Workshop on topics in Astroparticle and Underground Physics, pp. 284–291. ISSN: 0920-5632. DOI: [https://doi.org/10.1016/S0920-5632\(98\)00438-1](https://doi.org/10.1016/S0920-5632(98)00438-1). URL: <http://www.sciencedirect.com/science/article/pii/S0920563298004381>.
- [Dan+03] F. A. Danevich et al. “Search for  $2\beta$  decay of cadmium and tungsten isotopes: Final results of the Solotvina experiment”. In: *Phys. Rev. C* 68 (3 2003), p. 035501. DOI: 10.1103/PhysRevC.68.035501. URL: <https://link.aps.org/doi/10.1103/PhysRevC.68.035501>.
- [Dan+62] G. Danby et al. “Observation of High-Energy Neutrino Reactions and the Existence of Two Kinds of Neutrinos”. In: *Phys. Rev. Lett.* 9 (1 1962), pp. 36–44. DOI: 10.1103/PhysRevLett.9.36. URL: <https://link.aps.org/doi/10.1103/PhysRevLett.9.36>.
- [Dav16] K. David. “Effizienzbestimmung von Quad-Grid-CdZnTe-Detektoren”. Bachelor’s Thesis. TU Dortmund, 2016.
- [Dav55] R. Davis. “Attempt to detect the antineutrinos from a nuclear reactor by the  $\text{Cl}37(\text{anti-}\nu, e^-) \text{A}37$  reaction”. In: *Phys. Rev.* 97 (1955), pp. 766–769. DOI: 10.1103/PhysRev.97.766.
- [Daw+09a] J. V. Dawson et al. “An Investigation into the Cd-113 Beta Decay Spectrum using a CdZnTe Array”. In: *Nucl. Phys.* A818 (2009), pp. 264–278. DOI: 10.1016/j.nuclphysa.2008.12.010. arXiv: 0901.0996 [nucl-ex].
- [Daw+09b] J. V. Dawson et al. “Experimental study of double- $\beta$  decay modes using a CdZnTe detector array”. In: *Phys. Rev. C* 80 (2 2009), p. 025502. DOI: 10.1103/PhysRevC.80.025502. URL: <https://link.aps.org/doi/10.1103/PhysRevC.80.025502>.
- [Dev+06] R. Devanathan et al. “Signal variance in gamma-ray detectors—A review”. In: *Nuclear Instruments and Methods in Physics Research Section A: Accelerators, Spectrometers, Detectors and Associated Equipment* 565.2 (2006), pp. 637–649. ISSN: 0168-9002. DOI: <https://doi.org/10.1016/j.nima.2006.05.085>. URL: <http://www.sciencedirect.com/science/article/pii/S0168900206009089>.
- [DHH68] Raymond Davis, Don S. Harmer, and Kenneth C. Hoffman. “Search for Neutrinos from the Sun”. In: *Phys. Rev. Lett.* 20 (21 1968), pp. 1205–1209.

## BIBLIOGRAPHY

- DOI: 10.1103/PhysRevLett.20.1205. URL: <https://link.aps.org/doi/10.1103/PhysRevLett.20.1205>.
- [DHP12] F. F. Deppisch, M. Hirsch, and H. Päs. “Neutrinoless double-beta decay and physics beyond the standard model”. In: *Journal of Physics G: Nuclear and Particle Physics* 39.12 (2012), p. 124007. DOI: 10.1088/0954-3899/39/12/124007. URL: <https://doi.org/10.1088%2F0954-3899%2F39%2F12%2F124007>.
- [DMV14] S. Dell’Oro, Sm Marcocci, and F. Vissani. “New expectations and uncertainties on neutrinoless double beta decay”. In: *Phys. Rev. D* 90.3 (2014), p. 033005. DOI: 10.1103/PhysRevD.90.033005. arXiv: 1404.2616 [hep-ph].
- [Dot+94] F.P. Doty et al. “Pixellated CdZnTe detector arrays”. In: *Nuclear Instruments and Methods in Physics Research Section A: Accelerators, Spectrometers, Detectors and Associated Equipment* 353.1 (1994), pp. 356–360. ISSN: 0168-9002. DOI: [https://doi.org/10.1016/0168-9002\(94\)91675-6](https://doi.org/10.1016/0168-9002(94)91675-6). URL: <http://www.sciencedirect.com/science/article/pii/0168900294916756>.
- [Dre13] M. Drewes. “The Phenomenology of Right Handed Neutrinos”. In: *Int. J. Mod. Phys. E* 22 (2013), p. 1330019. DOI: 10.1142/S0218301313300191. arXiv: 1303.6912 [hep-ph].
- [DRZ11] A. Dueck, W. Rodejohann, and K. Zuber. “Neutrinoless double beta decay, the inverted hierarchy, and precision determination of  $\theta_{12}$ ”. In: *Phys. Rev. D* 83 (11 2011), p. 113010. DOI: 10.1103/PhysRevD.83.113010. URL: <https://link.aps.org/doi/10.1103/PhysRevD.83.113010>.
- [Ebe+16a] J. Ebert et al. “Characterization of a large CdZnTe coplanar quad-grid semiconductor detector”. In: *Nuclear Instruments and Methods in Physics Research Section A: Accelerators, Spectrometers, Detectors and Associated Equipment* 806 (2016), pp. 159–168. ISSN: 0168-9002. DOI: <https://doi.org/10.1016/j.nima.2015.09.116>. URL: <http://www.sciencedirect.com/science/article/pii/S016890021501205X>.
- [Ebe+16b] J. Ebert et al. “Long-term stability of underground operated CZT detectors based on the analysis of intrinsic  $^{113}\text{Cd}$  beta-decay”. In: *Nucl. Instr. Meth.* 821 (2016), pp. 109–115. ISSN: 0168-9002. DOI: [http :](http://)

- [//dx.doi.org/10.1016/j.nima.2016.03.012](https://dx.doi.org/10.1016/j.nima.2016.03.012). URL: <http://www.sciencedirect.com/science/article/pii/S0168900216300304>.
- [Ebe+16c] J. Ebert et al. “Results of a search for neutrinoless double- $\beta$  decay using the COBRA demonstrator”. In: *Phys. Rev. C* 94 (2 2016), p. 024603. DOI: 10.1103/PhysRevC.94.024603. URL: <http://link.aps.org/doi/10.1103/PhysRevC.94.024603>.
- [Ebe+16d] J. Ebert et al. “The COBRA demonstrator at the LNGS underground laboratory”. In: *Nucl. Instrum. Meth.* A807 (2016), pp. 114–120. DOI: 10.1016/j.nima.2015.10.079. arXiv: 1507.08177 [physics.ins-det].
- [EHM87] S. R. Elliott, A. A. Hahn, and M. K. Moe. “Direct evidence for two-neutrino double-beta decay in  $^{82}\text{Se}$ ”. In: *Phys. Rev. Lett.* 59 (18 1987), pp. 2020–2023. DOI: 10.1103/PhysRevLett.59.2020. URL: <https://link.aps.org/doi/10.1103/PhysRevLett.59.2020>.
- [Epo] Etc. Epoxies. *20-3001 NC EPOXY POTTING AND ENCAPSULATING RESIN - Technical Bulletin*. URL: [https://www.epoxies.com/\\_resources/common/userfiles/file/20-3001NC.pdf](https://www.epoxies.com/_resources/common/userfiles/file/20-3001NC.pdf) (visited on 05/03/2019).
- [Esk+95] J. D. Eskin et al. “The effect of pixel geometry on spatial and spectral resolution in a CdZnTe imaging array”. In: *1995 IEEE Nuclear Science Symposium and Medical Imaging Conference Record*. Vol. 1. 1995, 544–548 vol.1. DOI: 10.1109/NSSMIC.1995.504320.
- [Esp+17] R. Espagnet et al. “Conception and characterization of a virtual coplanar grid for a  $11\times 11$  pixelated CZT detector”. In: *Nuclear Instruments and Methods in Physics Research Section A: Accelerators, Spectrometers, Detectors and Associated Equipment* (03/2017). DOI: 10.1016/j.nima.2017.03.025.
- [Est+19] Ivan Esteban et al. “Global analysis of three-flavour neutrino oscillations: synergies and tensions in the determination of  $\theta_{23}$ ,  $\delta_{\text{CP}}$ , and the mass ordering”. In: *Journal of High Energy Physics* 2019.1 (2019), p. 106. ISSN: 1029-8479. DOI: 10.1007/JHEP01(2019)106. URL: [https://doi.org/10.1007/JHEP01\(2019\)106](https://doi.org/10.1007/JHEP01(2019)106).
- [EV02] Steven R. Elliott and Petr Vogel. “Double beta decay”. In: *Ann. Rev. Nucl. Part. Sci.* 52 (2002), pp. 115–151. DOI: 10.1146/annurev.nucl.52.050102.090641. arXiv: hep-ph/0202264 [hep-ph].

## BIBLIOGRAPHY

- [Fan47] U. Fano. “Ionization Yield of Radiations. II. The Fluctuations of the Number of Ions”. In: *Phys. Rev.* 72 (1 1947), pp. 26–29. DOI: 10.1103/PhysRev.72.26. URL: <http://link.aps.org/doi/10.1103/PhysRev.72.26>.
- [FC98] Gary J. Feldman and Robert D. Cousins. “A Unified approach to the classical statistical analysis of small signals”. In: *Phys. Rev.* D57 (1998), pp. 3873–3889. DOI: 10.1103/PhysRevD.57.3873. arXiv: physics/9711021 [physics.data-an].
- [Fer34] E. Fermi. “Versuch einer Theorie der  $\beta$ -Strahlen.” In: *Zeitschrift für Physik* 88.3 (1934), pp. 161–177. DOI: 10.1007/BF01351864. URL: <https://doi.org/10.1007/BF01351864>.
- [FGM58] R. P. Feynman and Murray Gell-Mann. “Theory of Fermi interaction”. In: *Phys. Rev.* 109 (1958). [417(1958)], pp. 193–198. DOI: 10.1103/PhysRev.109.193.
- [Fri+13] M. Fritts et al. “Analytical model for event reconstruction in coplanar grid CdZnTe detectors”. In: *Nucl.Instrum.Meth.* A708 (2013), pp. 1–6. DOI: 10.1016/j.nima.2013.01.004. arXiv: 1211.6604 [physics.ins-det].
- [Fri+14] M. Fritts et al. “Pulse-shape discrimination of surface events in CdZnTe detectors for the COBRA experiment”. In: *Nuclear Instruments and Methods in Physics Research Section A: Accelerators, Spectrometers, Detectors and Associated Equipment* 749 (2014), pp. 27–34. ISSN: 0168-9002. DOI: <https://doi.org/10.1016/j.nima.2014.02.038>. URL: <http://www.sciencedirect.com/science/article/pii/S0168900214002149>.
- [Fu+15a] J. Fu et al. “Depth sensing technique using time-to-peak of anode signal in CZT detectors”. In: *Nuclear Instruments and Methods in Physics Research Section A: Accelerators, Spectrometers, Detectors and Associated Equipment* 797 (2015), pp. 165–171. ISSN: 0168-9002. DOI: <https://doi.org/10.1016/j.nima.2015.06.048>. URL: <http://www.sciencedirect.com/science/article/pii/S0168900215007986>.
- [Fu+15b] J. Fu et al. “Strengthened electric field technique implemented on CZT detectors”. In: *Nuclear Instruments and Methods in Physics Research Section A: Accelerators, Spectrometers, Detectors and Associated Equipment* 771 (2015), pp. 93–97. ISSN: 0168-9002. DOI: <https://doi.org/>

- 10.1016/j.nima.2014.10.054. URL: <http://www.sciencedirect.com/science/article/pii/S016890021401211X>.
- [Fuk+94] Y. Fukuda et al. “Atmospheric  $\nu_\mu/\nu_e$  ratio in the multi-GeV energy range”. In: *Physics Letters B* 335.2 (1994), pp. 237–245. ISSN: 0370-2693. DOI: [https://doi.org/10.1016/0370-2693\(94\)91420-6](https://doi.org/10.1016/0370-2693(94)91420-6). URL: <http://www.sciencedirect.com/science/article/pii/0370269394914206>.
- [Fuk+98] Y. Fukuda et al. “Evidence for oscillation of atmospheric neutrinos”. In: *Phys. Rev. Lett.* 81 (1998), pp. 1562–1567. DOI: 10.1103/PhysRevLett.81.1562. arXiv: hep-ex/9807003 [hep-ex].
- [Fur39] W. H. Furry. “On transition probabilities in double beta-disintegration”. In: *Phys. Rev.* 56 (1939), pp. 1184–1193. DOI: 10.1103/PhysRev.56.1184.
- [Gan+16] A. Gando et al. “Search for Majorana Neutrinos Near the Inverted Mass Hierarchy Region with KamLAND-Zen”. In: *Phys. Rev. Lett.* 117 (8 2016), p. 082503. DOI: 10.1103/PhysRevLett.117.082503. URL: <https://link.aps.org/doi/10.1103/PhysRevLett.117.082503>.
- [Gan18] A. Gando. *KamLAND-Zen*. 2018. DOI: 10.5281/zenodo.1286895.
- [Gas+17] L. Gastaldo et al. “The electron capture in  $^{163}\text{Ho}$  experiment – ECHO”. In: *The European Physical Journal Special Topics* 226.8 (2017), pp. 1623–1694. ISSN: 1951-6401. DOI: 10.1140/epjst/e2017-70071-y. URL: <https://doi.org/10.1140/epjst/e2017-70071-y>.
- [Geaa] *Physics Lists EM constructors in Geant4 10.4*. URL: <https://geant4.web.cern.ch/node/1731> (visited on 06/27/2019).
- [Geab] *Use Cases - Reference Physics Lists*. URL: <https://geant4.web.cern.ch/node/302> (visited on 06/27/2019).
- [Geh17] D. Gehre. “Investigations on CdZnTe-Semiconductor-Detectors for the Search of the Neutrinoless Double Beta Decay”. PhD thesis. TU Dresden, 2017.
- [Ger+06] G. De Geronimo et al. “Characterization of an ASIC for CPG sensors with grid-only depth of interaction sensing”. In: *IEEE Trans. Nucl. Sci.* 53.2 (2006), pp. 456–461. ISSN: 0018-9499. DOI: 10.1109/TNS.2006.871260.
- [GGS58] M. Goldhaber, L. Grodzins, and A. W. Sunyar. “Helicity of Neutrinos”. In: *Phys. Rev.* 109 (1958), pp. 1015–1017. DOI: 10.1103/PhysRev.109.1015.

## BIBLIOGRAPHY

- [GLZ18] C. Giganti, S. Lavignac, and M. Zito. “Neutrino oscillations: the rise of the PMNS paradigm”. In: *Prog. Part. Nucl. Phys.* 98 (2018), pp. 1–54. DOI: 10.1016/j.pnpnp.2017.10.001. arXiv: 1710.00715 [hep-ex].
- [GM35] M. Goeppert-Mayer. “Double Beta-Disintegration”. In: *Phys. Rev.* 48 (6 1935), pp. 512–516. DOI: 10.1103/PhysRev.48.512. URL: <https://link.aps.org/doi/10.1103/PhysRev.48.512>.
- [Gro19] CUPID Interest Group. “CUPID pre-CDR”. In: (2019). arXiv: 1907.09376 [physics.ins-det].
- [Gys+19] P. Gysbers et al. “Discrepancy between experimental and theoretical  $\beta$ -decay rates resolved from first principles”. In: (2019). DOI: 10.1038/s41567-019-0450-7. arXiv: 1903.00047 [nucl-th].
- [GZ55] S. S. Gershtein and Ya. B. Zeldovich. “Meson corrections in the theory of beta decay”. In: *Zh. Eksp. Teor. Fiz.* 29 (1955). [80(1955)], pp. 698–699.
- [Haf+11] M. Haffke et al. “Background measurements in the Gran Sasso Underground Laboratory”. In: *Nuclear Instruments and Methods in Physics Research A* 643.1 (2011), pp. 36–41. DOI: 10.1016/j.nima.2011.04.027. arXiv: 1101.5298 [astro-ph.IM].
- [He+96] Z. He et al. “1-D position sensitive single carrier semiconductor detectors”. In: *Nuclear Instruments and Methods in Physics Research Section A: Accelerators, Spectrometers, Detectors and Associated Equipment* 380.1 (1996), pp. 228–231. ISSN: 0168-9002. DOI: [http://dx.doi.org/10.1016/S0168-9002\(96\)00352-X](http://dx.doi.org/10.1016/S0168-9002(96)00352-X). URL: <http://www.sciencedirect.com/science/article/pii/S016890029600352X>.
- [He01] Z. He. “Review of the Shockley–Ramo theorem and its application in semiconductor gamma-ray detectors”. In: *Nucl. Instrum. Meth. A* 463.1–2 (2001), pp. 250–267. ISSN: 0168-9002. DOI: [http://dx.doi.org/10.1016/S0168-9002\(01\)00223-6](http://dx.doi.org/10.1016/S0168-9002(01)00223-6). URL: <http://www.sciencedirect.com/science/article/pii/S0168900201002236>.
- [Hec32] K. Hecht. “Zum Mechanismus des lichtelektrischen Primärstromes in isolierenden Kristallen”. In: *Zeitschrift für Physik* 77.3 (1932), pp. 235–245. ISSN: 0044-3328. DOI: 10.1007/BF01338917. URL: <https://doi.org/10.1007/BF01338917>.

- [Hei14] N. Heidrich. “Monte Carlo-based Development of a Shield and Total Background Estimation for the COBRA Experiment”. PhD thesis. Universität Hamburg, 2014.
- [Her15] J. A. Hernando. “Status of NEXT-100 Experiment”. In: *Physics Procedia* 61 (2015). 13th International Conference on Topics in Astroparticle and Underground Physics, TAUP 2013, pp. 251–253. ISSN: 1875-3892. DOI: <https://doi.org/10.1016/j.phpro.2014.12.040>. URL: <http://www.sciencedirect.com/science/article/pii/S1875389214006531>.
- [Her16] C. Herrmann. “Simulation of a 3x3 CZT-Detector-Layer for the COBRA-Experiment”. Bachelor’s Thesis. TU Dortmund, 2016.
- [Her18] C. Herrmann. “Monte-Carlo Based Studies of Potential Background in the XDEM-phase of the COBRA Experiment”. Master’s Thesis. TU Dortmund, 2018.
- [Heu95] G Heusser. “Low-Radioactivity Background Techniques”. In: *Annual Review of Nuclear and Particle Science* 45.1 (1995), pp. 543–590. DOI: 10.1146/annurev.ns.45.120195.002551. eprint: <https://doi.org/10.1146/annurev.ns.45.120195.002551>. URL: <https://doi.org/10.1146/annurev.ns.45.120195.002551>.
- [Hir+89] K. S. Hirata et al. “Observation of  $^8\text{B}$  solar neutrinos in the Kamiokande-II detector”. In: *Phys. Rev. Lett.* 63 (1 1989), pp. 16–19. DOI: 10.1103/PhysRevLett.63.16. URL: <https://link.aps.org/doi/10.1103/PhysRevLett.63.16>.
- [HKS17] M. Haaranen, J. Kotila, and J. Suhonen. “Spectrum-shape method and the next-to-leading-order terms of the  $\beta$ -decay shape factor”. In: *Phys. Rev. C* 95 (2 2017), p. 024327. DOI: 10.1103/PhysRevC.95.024327. URL: <https://link.aps.org/doi/10.1103/PhysRevC.95.024327>.
- [Hon+04] J. Hong et al. “Cathode depth sensing in CZT detectors”. In: *Proc. SPIE 5165, X-Ray and Gamma-Ray Instrumentation for Astronomy XIII* 5165 (2004). DOI: 10.1117/12.506216. URL: <https://doi.org/10.1117/12.506216>.
- [HR13] Julian Heeck and Werner Rodejohann. “Neutrinoless Quadruple Beta Decay”. In: *EPL* 103.3 (2013), p. 32001. DOI: 10.1209/0295-5075/103/32001. arXiv: 1306.0580 [hep-ph].

## BIBLIOGRAPHY

- [HSR05] Z. He, B. W. Sturm, and E. Rhodes. “Investigation of a Large Volume Multi-Pair Coplanar Grid CdZnTe Detector for Improved Detection Efficiency”. In: *IEEE Nuclear Science Symposium Conference Record, 2005*. Vol. 2. 2005, pp. 1159–1162. DOI: 10.1109/NSSMIC.2005.1596456.
- [Hua+17] W.J. Huang et al. “The AME2016 atomic mass evaluation”. In: *Chinese Physics C* 41.3 (2017), p. 03000.
- [Hö18] I. Höfmann. “Effizienzbestimmung von CdZnTe-CPqG-Detektoren für das COBRA-XDEM-Upgrade”. Bachelor’s Thesis. TU Dortmund, 2018.
- [Inca] Cremat Inc. *CR-110-R2 charge sensitive preamplifier: Application guide*. URL: <http://www.cremat.com/CR-110-R2.pdf> (visited on 05/08/2019).
- [Incb] H3D Inc. *H Series H100 Industrial Imaging Spectrometer*. URL: <https://h3dgamma.com/h100.php> (visited on 05/03/2019).
- [Ini+08] K. Iniewski et al. “High Voltage Optimization in CZT Detectors”. In: (05/2008).
- [IR50] M. G. Inghram and J. H. Reynolds. “Double Beta-Decay of  $\text{Te}^{130}$ ”. In: *Phys. Rev.* 78 (6 1950), pp. 822–823. DOI: 10.1103/PhysRev.78.822.2. URL: <https://link.aps.org/doi/10.1103/PhysRev.78.822.2>.
- [JMN16] B. J. P. Jones, A. D. McDonald, and D. R. Nygren. “Single Molecule Fluorescence Imaging as a Technique for Barium Tagging in Neutrinoless Double Beta Decay”. In: *JINST* 11.12 (2016), P12011. DOI: 10.1088/1748-0221/11/12/P12011. arXiv: 1609.04019 [physics.ins-det].
- [KI12] J. Kotila and F. Iachello. “Phase space factors for double- $\beta$  decay”. In: *Phys. Rev.* C85 (2012), p. 034316. DOI: 10.1103/PhysRevC.85.034316. arXiv: 1209.5722 [nucl-th].
- [KK+01a] H. V. Klapdor-Kleingrothaus et al. “Evidence For Neutrinoless Double Beta Decay”. In: *Modern Physics Letters A* 16.37 (2001), pp. 2409–2420. DOI: 10.1142/S0217732301005825. eprint: <https://doi.org/10.1142/S0217732301005825>. URL: <https://doi.org/10.1142/S0217732301005825>.
- [KK+01b] H. V. Klapdor-Kleingrothaus et al. “Latest results from the Heidelberg-Moscow double beta decay experiment”. In: *Eur. Phys. J.* A12 (2001), pp. 147–154. DOI: 10.1007/s100500170022. arXiv: hep-ph/0103062 [hep-ph].

- [KKK06] H. V. Klapdor-Kleingrothaus and I. V. Krivosheina. “The Evidence For The Observation Of  $0\nu\beta\beta$  Decay: The Identification Of  $0\nu\beta\beta$  Events From The Full Spectra”. In: *Modern Physics Letters A* 21.20 (2006), pp. 1547–1566. DOI: [10.1142/S0217732306020937](https://doi.org/10.1142/S0217732306020937). eprint: <https://doi.org/10.1142/S0217732306020937>. URL: <https://doi.org/10.1142/S0217732306020937>.
- [KMZ03] H. Kiel, D. Münstermann, and K. Zuber. “A search for various double beta decay modes of Cd, Te, and Zn isotopes”. In: *Nuclear Physics A* 723.3 (2003), pp. 499–514. ISSN: 0375-9474. DOI: [https://doi.org/10.1016/S0375-9474\(03\)01363-0](https://doi.org/10.1016/S0375-9474(03)01363-0). URL: <http://www.sciencedirect.com/science/article/pii/S0375947403013630>.
- [Kod+01] K. Kodama et al. “Observation of tau neutrino interactions”. In: *Phys. Lett. B* 504 (2001), pp. 218–224. DOI: [10.1016/S0370-2693\(01\)00307-0](https://doi.org/10.1016/S0370-2693(01)00307-0). arXiv: [hep-ex/0012035](https://arxiv.org/abs/hep-ex/0012035) [hep-ex].
- [Koe12] T. Koettig. “Sensitivity Studies of CdZnTe Semiconductor Detectors for the COBRA Experiment”. Ph.D. thesis. TU Dortmund, 2012.
- [Kra+05] Ch. Kraus et al. “Final results from phase II of the Mainz neutrino mass search in tritium beta decay”. In: *Eur. Phys. J. C* 40 (2005), pp. 447–468. DOI: [10.1140/epjc/s2005-02139-7](https://doi.org/10.1140/epjc/s2005-02139-7). arXiv: [hep-ex/0412056](https://arxiv.org/abs/hep-ex/0412056) [hep-ex].
- [Kuv+10] I. Kuvvetli et al. “CZT drift strip detectors for high energy astrophysics”. In: *Nuclear Instruments and Methods in Physics Research Section A: Accelerators, Spectrometers, Detectors and Associated Equipment* 624.2 (2010). New Developments in Radiation Detectors, pp. 486–491. ISSN: 0168-9002. DOI: <https://doi.org/10.1016/j.nima.2010.03.172>. URL: <http://www.sciencedirect.com/science/article/pii/S0168900210008247>.
- [LH09] M. Laubenstein and G. Heusser. “Cosmogenic radionuclides in metals as indicator for sea level exposure history”. In: *Applied Radiation and Isotopes* 67.5 (2009). 5th International Conference on Radionuclide Metrology - Low-Level Radioactivity Measurement Techniques ICRM-LLRMT’08, pp. 750–754. ISSN: 0969-8043. DOI: <https://doi.org/10.1016/j.apradiso.2009.01.029>. URL: <http://www.sciencedirect.com/science/article/pii/S096980430900030X>.

## BIBLIOGRAPHY

- [Li+06] Q. Li et al. “Electrical properties and electrical field in depletion layer for CZT crystals”. In: *Transactions of Nonferrous Metals Society of China* 16 (2006), s75 –s78. ISSN: 1003-6326. DOI: [https://doi.org/10.1016/S1003-6326\(06\)60146-5](https://doi.org/10.1016/S1003-6326(06)60146-5). URL: <http://www.sciencedirect.com/science/article/pii/S1003632606601465>.
- [Li+07] W. Li et al. “Impact of temperature variation on the energy resolution of 3D position sensitive CZT gamma- ray spectrometers”. In: *2007 IEEE Nuclear Science Symposium Conference Record*. Vol. 3. 2007, pp. 1809–1815. DOI: 10.1109/NSSMIC.2007.4436510.
- [LLS14] A. J. Long, C. Lunardini, and E.E. Sabancilar. “Detecting non-relativistic cosmic neutrinos by capture on tritium: phenomenology and physics potential”. In: *JCAP* 1408 (2014), p. 038. DOI: 10.1088/1475-7516/2014/08/038. arXiv: 1405.7654 [hep-ph].
- [Loa+15] P. Loaiza et al. “Obelix, a new low-background HPGe at Modane Underground Laboratory”. In: *AIP Conference Proceedings* 1672.1 (08/2015). ISSN: 0094-243X. DOI: 10.1063/1.4928012.
- [Loa+16] J. C. Loach et al. “A Database for Storing the Results of Material Radiopurity Measurements”. In: *Nucl. Instrum. Meth.* A839 (2016), pp. 6–11. DOI: 10.1016/j.nima.2016.09.036. arXiv: 1604.06169 [physics.ins-det].
- [Luk94] P.N. Luke. “Single-polarity charge sensing in ionization detectors using coplanar electrodes”. In: *Appl. Phys. Lett.* 65.22 (1994), pp. 2884–2886. DOI: <http://dx.doi.org/10.1063/1.112523>. URL: <http://scitation.aip.org/content/aip/journal/apl/65/22/10.1063/1.112523>.
- [Luk95] P. N. Luke. “Unipolar charge sensing with coplanar electrodes-application to semiconductor detectors”. In: *IEEE Transactions on Nuclear Science* 42.4 (1995), pp. 207–213. ISSN: 0018-9499. DOI: 10.1109/23.467848.
- [LY56] T. D. Lee and Chen-Ning Yang. “Question of Parity Conservation in Weak Interactions”. In: *Phys. Rev.* 104 (1956), pp. 254–258. DOI: 10.1103/PhysRev.104.254.
- [Ma+14] Y. Ma et al. “Design and study of a coplanar grid array CdZnTe detector for improved spatial resolution”. In: *Applied Radiation and Isotopes* 94 (2014), pp. 314 –318. ISSN: 0969-8043. DOI: <https://doi.org/10.1016/>

- j.apradiso.2014.09.003. URL: <http://www.sciencedirect.com/science/article/pii/S0969804314003261>.
- [Mau] F. Mauger. *bxdecay0 - C++ port of the legacy Decay0/GENBB FORTRAN library*. URL: <https://github.com/BxCppDev/bxdecay0> (visited on 06/27/2019).
- [MH06] Dongming Mei and A. Hime. “Muon-induced background study for underground laboratories”. In: *Phys. Rev. D* 73 (2006), p. 053004. DOI: 10.1103/PhysRevD.73.053004. arXiv: astro-ph/0512125 [astro-ph].
- [Mic] The Regents of the University of Michigan. *Polaris Technology Summary*. URL: <https://cztlab.engin.umich.edu/summary/> (visited on 05/03/2019).
- [Mis06] MissMJ. *Standard Model of Elementary Particles*. 2006. URL: [https://commons.wikimedia.org/wiki/File:Standard\\_Model\\_of\\_Elementary\\_Particles.svg](https://commons.wikimedia.org/wiki/File:Standard_Model_of_Elementary_Particles.svg) (visited on 04/26/2019).
- [MP+96] G. Martínez-Pinedo et al. “Effective  $g_A$  in the pf shell”. In: *Phys. Rev. C* 53 (6 1996), R2602–R2605. DOI: 10.1103/PhysRevC.53.R2602. URL: <https://link.aps.org/doi/10.1103/PhysRevC.53.R2602>.
- [MPS14] M. Mirea, T. Pahomi, and S. Stoica. “Phase Space Factors for Double Beta Decay: an up-date”. In: (2014). arXiv: 1411.5506 [nucl-th].
- [MS13] J. Maalampi and J. Suhonen. “Neutrinoless Double  $\beta^+$  / EC Decays”. In: *Adv. High Energy Phys.* 2013 (2013), p. 505874. DOI: 10.1155/2013/505874.
- [Ned14] T. Neddermann. “Material screening by means of low-level gamma ray spectrometry with the Dortmund Low Background HPGe Facility”. PhD thesis. TU Dortmund, 2014.
- [Now17] A. Nowak. “Simulation der Kalibration der CZT Detektoren für das COBRA Experiment”. Bachelor’s Thesis. TU Dortmund, 2017.
- [NSS62] M. Nakagawa, S. Sakata, and Z. Sakata. “Remarks on the Unified Model of Elementary Particles”. In: *Progress of Theoretical Physics* 28.5 (11/1962), pp. 870–880. ISSN: 0033-068X. DOI: 10.1143/PTP.28.870. eprint: <http://oup.prod.sis.lan/ptp/article-pdf/28/5/870/5258750/28-5-870.pdf>. URL: <https://doi.org/10.1143/PTP.28.870>.

## BIBLIOGRAPHY

- [OG18] G. Orebi Gann. *SNO+*. 2018. DOI: 10.5281/zenodo.1286908.
- [Oue18] J. Ouellet. *Latest Results from the CUORE Experiment*. 2018. DOI: 10.5281/zenodo.1286904.
- [Pau30] W. Pauli. *Brief an die Radioaktiven*. 1930. URL: [http://www.neutrino.uni-hamburg.de/sites/site\\_neutrino/content/e45939/e48540/e48541/e48544/infoboxContent48545/material-vorlesung1-moessbauer-pauli.pdf](http://www.neutrino.uni-hamburg.de/sites/site_neutrino/content/e45939/e48540/e48541/e48544/infoboxContent48545/material-vorlesung1-moessbauer-pauli.pdf).
- [PBJ98] M.A.J. van Pamelan and C. Budtz-Jørgensen. “Novel electrode geometry to improve performance of CdZnTe detectors”. In: *Nuclear Instruments and Methods in Physics Research Section A: Accelerators, Spectrometers, Detectors and Associated Equipment* 403.2 (1998), pp. 390–398. ISSN: 0168-9002. DOI: [https://doi.org/10.1016/S0168-9002\(97\)01120-0](https://doi.org/10.1016/S0168-9002(97)01120-0). URL: <http://www.sciencedirect.com/science/article/pii/S0168900297011200>.
- [Pon57] B. Pontecorvo. “Mesonium and anti-mesonium”. In: *Sov. Phys. JETP* 6 (1957). [*Zh. Eksp. Teor. Fiz.*33,549(1957)], p. 429.
- [Pon58] B. Pontecorvo. “Inverse beta processes and nonconservation of lepton charge”. In: *Sov. Phys. JETP* 7 (1958). [*Zh. Eksp. Teor. Fiz.*34,247(1957)], pp. 172–173.
- [Pon68] B. Pontecorvo. “Neutrino Experiments and the Problem of Conservation of Leptonic Charge”. In: *Sov. Phys. JETP* 26 (1968). [*Zh. Eksp. Teor. Fiz.*53,1717(1967)], pp. 984–988.
- [Pon91] B. Pontecorvo. “Inverse beta process”. In: *Camb. Monogr. Part. Phys. Nucl. Phys. Cosmol.* 1 (1991). [,97(1946)], pp. 25–31.
- [PRTV10] G. Pagliaroli, F. Rossi-Torres, and F. Vissani. “Neutrino mass bound in the standard scenario for supernova electronic antineutrino emission”. In: *Astropart. Phys.* 33 (2010), pp. 287–291. DOI: 10.1016/j.astropartphys.2010.02.007. arXiv: 1002.3349 [hep-ph].
- [Ram39] S. Ramo. “Currents Induced by Electron Motion”. In: *Proceedings of the IRE* 27.9 (1939), pp. 584–585. ISSN: 0096-8390. DOI: 10.1109/JRPROC.1939.228757.

- [RL01] W. A. Rolke and A. M. López. “Confidence intervals and upper bounds for small signals in the presence of background noise”. In: *Nuclear Instruments and Methods in Physics Research Section A: Accelerators, Spectrometers, Detectors and Associated Equipment* 458.3 (2001), pp. 745–758. ISSN: 0168-9002. DOI: [https://doi.org/10.1016/S0168-9002\(00\)00935-9](https://doi.org/10.1016/S0168-9002(00)00935-9). URL: <http://www.sciencedirect.com/science/article/pii/S0168900200009359>.
- [RLC05] Wolfgang A. Rolke, Angel M. Lopez, and Jan Conrad. “Limits and confidence intervals in the presence of nuisance parameters”. In: *Nucl. Instrum. Meth.* A551 (2005), pp. 493–503. DOI: 10.1016/j.nima.2005.05.068. arXiv: physics/0403059 [physics].
- [Rod11] Werner Rodejohann. “Neutrino-less Double Beta Decay and Particle Physics”. In: *Int. J. Mod. Phys.* E20 (2011), pp. 1833–1930. DOI: 10.1142/S0218301311020186. arXiv: 1106.1334 [hep-ph].
- [Roh16] K. Rohatsch. “Charakterisierung von großvolumigen CdZnTe-Detektoren mit segmentierter CPG-Anodenkonfiguration für das COBRA-Experiment”. Diploma Thesis. TU Dresden, 2016.
- [RS92] M. Richter and P. Siffert. “High resolution gamma ray spectroscopy with CdTe detector systems”. In: *Nuclear Instruments and Methods in Physics Research Section A: Accelerators, Spectrometers, Detectors and Associated Equipment* 322.3 (1992), pp. 529–537. ISSN: 0168-9002. DOI: [https://doi.org/10.1016/0168-9002\(92\)91227-Z](https://doi.org/10.1016/0168-9002(92)91227-Z). URL: <http://www.sciencedirect.com/science/article/pii/016890029291227Z>.
- [Rö14] D. Röttges. “Interaktionstiefenrekonstruktion in CZT-Quad-Detektoren des COBRA Experiments”. Bachelor Thesis. TU Dortmund, 2014.
- [SB88] David N. Spergel and John N. Bahcall. “The mass of the electron neutrino: Monte Carlo studies of SN 1987A observations”. In: *Physics Letters B* 200.3 (1988), pp. 366–372. ISSN: 0370-2693. DOI: [https://doi.org/10.1016/0370-2693\(88\)90790-3](https://doi.org/10.1016/0370-2693(88)90790-3). URL: <http://www.sciencedirect.com/science/article/pii/0370269388907903>.
- [Sch+01] T.E Schlesinger et al. “Cadmium zinc telluride and its use as a nuclear radiation detector material”. In: *Materials Science and Engineering: R: Reports* 32.4 (2001), pp. 103–189. ISSN: 0927-796X. DOI: [https://doi.org/10.1016/S0927-796X\(01\)00001-1](https://doi.org/10.1016/S0927-796X(01)00001-1).

## BIBLIOGRAPHY

- [//doi.org/10.1016/S0927-796X\(01\)00027-4](http://doi.org/10.1016/S0927-796X(01)00027-4). URL: <http://www.sciencedirect.com/science/article/pii/S0927796X01000274>.
- [Sch+06] S. Schael et al. “Precision electroweak measurements on the  $Z$  resonance”. In: *Phys. Rept.* 427 (2006), pp. 257–454. DOI: 10.1016/j.physrep.2005.12.006. arXiv: hep-ex/0509008 [hep-ex].
- [Sch+11] M. Schwenke et al. “Exploration of Pixelated detectors for double beta decay searches within the COBRA experiment”. In: *Nuclear Instruments and Methods in Physics Research Section A: Accelerators, Spectrometers, Detectors and Associated Equipment* 650.1 (2011). International Workshop on Semiconductor Pixel Detectors for Particles and Imaging 2010, pp. 73–78. ISSN: 0168-9002. DOI: <https://doi.org/10.1016/j.nima.2010.12.128>. URL: <http://www.sciencedirect.com/science/article/pii/S0168900210029086>.
- [Sch11] O. Schulz. “Exploration of new Data Acquisition and Background Reduction Techniques for the COBRA Experiment”. PhD thesis. TU Dortmund, 2011. URL: <http://hdl.handle.net/2003/29108>.
- [Sch16] C. Schleich. “Untersuchung der Energiedeposition von Alphastrahlung bei  $6\text{ cm}^3$  CdZnTe Detektoren bei unterschiedlichen Konfigurationen von CA und NCA”. Bachelor’s Thesis. TU Dortmund, 2016.
- [Sch17] K.s Scholberg. “Supernova signatures of neutrino mass ordering”. In: *Journal of Physics G: Nuclear and Particle Physics* 45.1 (2017), p. 014002. DOI: 10.1088/1361-6471/aa97be. URL: <https://doi.org/10.1088/1361-6471/aa97be>.
- [SG01] C. Scheiber and G. C. Giakos. “Medical applications of CdTe and CdZnTe detectors”. In: *Nucl. Instrum. Methods Phys. Res. A* 458.1 (2001). Proc. 11th Int. Workshop on Room Temperature Semiconductor X- and Gamma-Ray Detectors and Associated Electronics, pp. 12–25. ISSN: 0168-9002. DOI: [https://doi.org/10.1016/S0168-9002\(00\)01032-9](https://doi.org/10.1016/S0168-9002(00)01032-9). URL: <http://www.sciencedirect.com/science/article/pii/S0168900200010329>.
- [Sho38] W. Shockley. “Currents to Conductors Induced by a Moving Point Charge”. In: *Journal of Applied Physics* 9.10 (1938), pp. 635–636. DOI: 10.1063/1.1710367. eprint: <https://doi.org/10.1063/1.1710367>. URL: <https://doi.org/10.1063/1.1710367>.

- [SK16] M. Salathe and T. Kihm. “Optimized digital filtering techniques for radiation detection with HPGe detectors”. In: *Nucl. Instrum. Meth.* A808 (2016), pp. 150–155. DOI: 10.1016/j.nima.2015.11.051. arXiv: 1504.02039 [physics.ins-det].
- [Smi16] A. Yu. Smirnov. “Solar neutrinos: Oscillations or No-oscillations?” In: (2016). arXiv: 1609.02386 [hep-ph].
- [Sor+09] S. Sordo et al. “Progress in the Development of CdTe and CdZnTe Semiconductor Radiation Detectors for Astrophysical and Medical Applications”. In: *Sensors (Basel, Switzerland)* 9 (05/2009), pp. 3491–526. DOI: 10.3390/s90503491.
- [SSS18] A. Saxena, P. C. SriSaxena, and T. Suzuki. “Ab initio calculations of Gamow-Teller strengths in the  $sd$  shell”. In: *Phys. Rev. C* 97 (2 2018), p. 024310. DOI: 10.1103/PhysRevC.97.024310. URL: <https://link.aps.org/doi/10.1103/PhysRevC.97.024310>.
- [Stu07] B. W. Sturm. “Gamma-ray spectroscopy using depth-sensing coplanar grid cadmium zinc tellurium semiconductor detectors”. PhD thesis. University of Michigan, 2007. URL: <http://hdl.handle.net/2027.42/126569>.
- [Suh17a] J. Suhonen. “Impact of the quenching of  $g_A$  on the sensitivity of  $0\nu\beta\beta$  experiments”. In: *Phys. Rev. C* 96 (5 2017), p. 055501. DOI: 10.1103/PhysRevC.96.055501. URL: <https://link.aps.org/doi/10.1103/PhysRevC.96.055501>.
- [Suh17b] Jouni T. Suhonen. “Value of the Axial-Vector Coupling Strength in  $\beta$  and  $\beta\beta$  Decays: A Review”. In: *Front.in Phys.* 5 (2017), p. 55. DOI: 10.3389/fphy.2017.00055. arXiv: 1712.01565 [nucl-th].
- [SV82] J. Schechter and J. W. F. Valle. “Neutrinoless double- $\beta$  decay in  $SU(2)\times U(1)$  theories”. In: *Phys. Rev. D* 25 (11 1982), pp. 2951–2954. DOI: 10.1103/PhysRevD.25.2951. URL: <https://link.aps.org/doi/10.1103/PhysRevD.25.2951>.
- [Sys] Struck Innovative Systeme. *SIS3300 8 Channel 100 MHz 12-bit ADC*. Ed. by Matthias Kirsch. URL: <https://www.struck.de/sis3300.htm> (visited on 05/08/2019).

## BIBLIOGRAPHY

- [Sö11] A. Sörensen. “Ortsaufgelöste Effizienzbestimmung von CdZnTe Halbleiterdetektoren mit kollimierter Gammastrahlung für das COBRA-Experiment”. Diploma thesis. 2011.
- [Tan+18] M. Tanabashi et al. “Review of Particle Physics”. In: *Phys. Rev. D* 98 (3 2018), p. 030001. DOI: 10.1103/PhysRevD.98.030001. URL: <https://link.aps.org/doi/10.1103/PhysRevD.98.030001>.
- [Teb16] J. Tebrügge. “Commissioning of the COBRA demonstrator and investigation of surface events as its main background”. PhD thesis. TU Dortmund, 2016.
- [Tem13] R. Temminghoff. “Interaktionstiefenabhängige Charakterisierung von Pulsen in CPG-Detektoren”. Bachelor Thesis. TU Dortmund, 2013.
- [Tem15] R. Temminghoff. “Characterization and Simulation of the Properties of CPqG Detectors for the COBRA Experiment”. Master Thesis. TU Dortmund, 2015.
- [Tem16] R. Temminghoff. “Spatially resolved investigation of large CdZnTe detectors with a coplanar quad-grid”. In: *2016 IEEE NSS/MIC/RTSD*. 2016, pp. 1–4. DOI: 10.1109/NSSMIC.2016.8069959.
- [Tem17] R. Temminghoff. “Investigation of the Depth Reconstruction and Search for Local Performance Variations With a Large Coplanar-Quad-Grid CdZnTe Detector”. In: *IEEE Transactions on Nuclear Science* 64.7 (2017), pp. 1934–1941. ISSN: 0018-9499. DOI: 10.1109/TNS.2017.2711922.
- [The14] R. Theinert. “Performance and efficiency studies of CdZnTe semiconductor detectors for the COBRA experiment”. Master thesis. TU Dortmund, 2014.
- [Tim15] J. H. K. Timm. “Studien seltener neutroneninduzierter Prozesse und Koinzidenzanalysen zur Bestimmung und Reduktion von Untergrundbeiträgen im COBRA-Experiment”. Universität Hamburg, Diss., 2015. Dr. Hamburg: Universität Hamburg, 2015, p. 130. DOI: 10.3204/DESY-THESIS-2015-047. URL: <https://bib-pubdb1.desy.de/record/288372>.

- [Vas+90] A. A. Vasenko et al. “New Results in the Itep / Yepi Double Beta Decay Experiment With Enriched Germanium Detector”. In: *Mod. Phys. Lett. A* 5 (1990). [1061(1989)], pp. 1299–1306. DOI: 10.1142/S0217732390001475.
- [Vol18] J. Volkmer. “Prospects of the investigation of EC/beta+ decays with the COBRA experiment”. TU Dresden, 2018.
- [Wei67] S Weinberg. “A Model of Leptons”. In: *Phys. Rev. Lett.* 19 (21 1967), pp. 1264–1266. DOI: 10.1103/PhysRevLett.19.1264. URL: <https://link.aps.org/doi/10.1103/PhysRevLett.19.1264>.
- [Wes12] T. Wester. “Characterization of CdZnTe Coplanar Grid Detectors and Pulse Shape Analysis for the COBRA Experiment”. PhD thesis. TU Dresden, 2012.
- [Wil73] D.H. Wilkinson. “Renormalization of the axial-vector coupling constant in nuclear  $\beta$ -decay (II)”. In: *Nuclear Physics A* 209.3 (1973), pp. 470–484. ISSN: 0375-9474. DOI: [https://doi.org/10.1016/0375-9474\(73\)90840-3](https://doi.org/10.1016/0375-9474(73)90840-3). URL: <http://www.sciencedirect.com/science/article/pii/0375947473908403>.
- [Win55] Rolf G. Winter. “Double  $K$  Capture and Single  $K$  Capture with Positron Emission”. In: *Phys. Rev.* 100 (1 1955), pp. 142–144. DOI: 10.1103/PhysRev.100.142. URL: <https://link.aps.org/doi/10.1103/PhysRev.100.142>.
- [Wis+02] K. Wisshak et al. “Neutron capture cross sections for stellar Cd production”. In: *Phys. Rev. C* 66 (2 2002), p. 025801. DOI: 10.1103/PhysRevC.66.025801. URL: <https://link.aps.org/doi/10.1103/PhysRevC.66.025801>.
- [Wu+57] C. S. Wu et al. “Experimental Test of Parity Conservation in Beta Decay”. In: *Phys. Rev.* 105 (1957), pp. 1413–1414. DOI: 10.1103/PhysRev.105.1413.
- [WZ05] M. Wójcik and G. Zuzel. “Low-<sup>222</sup>Rn nitrogen gas generator for ultra-low background counting systems”. In: *Nuclear Instruments and Methods in Physics Research Section A: Accelerators, Spectrometers, Detectors and Associated Equipment* 539.1 (2005), pp. 427–432. ISSN: 0168-9002. DOI: <https://doi.org/10.1016/j.nima.2004.10.023>. URL: <http://www.sciencedirect.com/science/article/pii/S0168900204023356>.

## BIBLIOGRAPHY

- [WZ13] C. Weinheimer and K. Zuber. “Neutrino Masses”. In: *Annalen Phys.* 525.8-9 (2013), pp. 565–575. DOI: 10.1002/andp.201300063. arXiv: 1307.3518 [hep-ex].
- [Yan+16] G. Yang et al. “Electropolishing of surfaces: theory and applications”. In: *Surface Engineering* 33 (07/2016), pp. 1–18. DOI: 10.1080/02670844.2016.1198452.
- [Zat14] S. Zatschler. “Identification of Multi-Site Events in Coplanar-GridCdZnTe Detectors for the COBRA-Experiment”. Diploma Thesis. TU Dresden, 2014.
- [Zat16] S. Zatschler. “Discrimination of single-site and multi-site events in CZT-CPG detectors for the COBRA experiment”. In: *2016 IEEE Nuclear Science Symposium, Medical Imaging Conference and Room-Temperature Semiconductor Detector Workshop (NSS/MIC/RTSD)*. 2016, pp. 1–5. DOI: 10.1109/NSSMIC.2016.8069958.
- [ZDT02] Yu.G Zdesenko, F.A Danevich, and V.I Tretyak. “Has neutrinoless double  $\beta$  decay of  $^{76}\text{Ge}$  been really observed?” In: *Physics Letters B* 546.3 (2002), pp. 206–215. ISSN: 0370-2693. DOI: [https://doi.org/10.1016/S0370-2693\(02\)02705-3](https://doi.org/10.1016/S0370-2693(02)02705-3). URL: <http://www.sciencedirect.com/science/article/pii/S0370269302027053>.
- [ZH12] Y. Zhu and Z. He. “Performance of a 2-keV digitizer ASIC for 3-D position-sensitive pixellated semiconductor detectors”. In: *2012 IEEE Nuclear Science Symposium and Medical Imaging Conference Record (NSS/MIC)*. 2012, pp. 4109–4112. DOI: 10.1109/NSSMIC.2012.6551939.
- [Zha+12] F. Zhang et al. “Characterization of the H3D ASIC Readout System and  $6.0\text{ cm}^3$ -D Position Sensitive CdZnTe Detectors”. In: *IEEE Transactions on Nuclear Science* 59.1 (2012), pp. 236–242. ISSN: 0018-9499. DOI: 10.1109/TNS.2011.2175948.
- [Zha+13] Qiushi Zhang et al. “Progress in the Development of CdZnTe Unipolar Detectors for Different Anode Geometries and Data Corrections”. In: *Sensors (Basel, Switzerland)* 13 (02/2013), pp. 2447–74. DOI: 10.3390/s130202447.
- [Zhe+11] Q. Zheng et al. “Influence of surface preparation on CdZnTe nuclear radiation detectors”. In: *Applied Surface Science* 257.20 (2011), pp. 8742–8746. ISSN: 0169-4332. DOI: <https://doi.org/10.1016/j.apsusc.2011.05>.

## BIBLIOGRAPHY

098. URL: <http://www.sciencedirect.com/science/article/pii/S0169433211008105>.
- [Zsi18] Anna Julia Zsigmond. *New results from GERDA Phase II*. 2018. DOI: 10.5281/zenodo.1287604.
- [Zub01] K. Zuber. “COBRA: Double beta decay searches using CdTe detectors”. In: *Phys. Lett. B* 519 (2001), pp. 1–7. DOI: 10.1016/S0370-2693(01)01056-5. arXiv: nucl-ex/0105018 [nucl-ex].
- [ZW12] G. Zuzel and M. Wójcik. “Removal of the long-lived  $^{222}\text{Rn}$  daughters from copper and stainless steel surfaces”. In: *Nuclear Instruments and Methods in Physics Research Section A: Accelerators, Spectrometers, Detectors and Associated Equipment* 676 (2012), pp. 140–148. ISSN: 0168-9002. DOI: <https://doi.org/10.1016/j.nima.2011.12.043>. URL: <http://www.sciencedirect.com/science/article/pii/S0168900211022522>.

# A Measurement of Radioisotopes in Materials Used for XDEM

It is important to assess the content of radioactive impurities in all materials used for detector construction to achieve a low background. These numbers are also vital for the construction of the background model. The activities or concentrations were assessed with different techniques at various facilities. All results are presented as reported by the respective facilities and no corrections are applied.

- $\gamma$ -spectroscopy with HPGe-detectors. This technique allows to assess the content of any isotope that emits  $\gamma$ -rays. Also, it is possible to detect equilibrium-breaking in decay chains. To achieve high sensitivity, the detector must have a very low background. The technique is non-destructive.
  - DLB - a 60% relative efficiency detector at a shallow overburden site at TU Dortmund
  - Stella - a number of detectors with different efficiencies and backgrounds at the LNGS
  - Obelix - a 160% relative efficiency detector at the Laboratoire Souterrain de Modane, France (4800m.w.e overburden)
- inductively coupled plasma mass spectrometry is a destructive technique to analyze trace impurities of many elements in the range of ppt to ppb. It is a destructive technique. Two facilities were used.
  - VKTA – Strahlenschutz, Analytik & Entsorgung Rossendorf, Dresden
  - Chemical laboratory at the LNGS
- $\beta$ -spectroscopy was performed at the PTB, Braunschweig to assess the  $^{210}\text{Pb}$  content of ULA lead bricks.

Technique	Facility	Manufacturer	Year	Specific Activity [mBq/kg]					
				<sup>22</sup> Na	<sup>40</sup> K	<sup>60</sup> Co	<sup>137</sup> Cs	<sup>232</sup> Th-chain	<sup>238</sup> U-chain
$\gamma$ -spect.	LNGS	eV	2006	-	$\leq 260$	-	$40 \pm 8$	$\leq 51$	$\leq 47$
ICP-MS	Redlen	Redlen	2015	-	$\leq 6.2$	-	$\leq 2.0$	-	$\leq 6.2$
$\gamma$ -spect.	DLB	Redlen	2015	$\leq 9.4$	$\leq 420$	$\leq 4.8$	$\leq 6.6$	$\leq 27$	$\leq 74$
$\gamma$ -spect.	DLB	eV	2015	$\leq 15.5$	$\leq 510$	$\leq 9.1$	$\leq 13.7$	$\leq 34$	$\leq 67$

Table A.1: Specific Activity CdZnTe detector materia. For each entry, the measurement technique and facility, the year of the measurement and the manufacturer of the CdZnTe is listed. If multiple isotopes from a decay chain were analyzed, in case of detection an average is calculated and in case of upper limits the lowest limit is quoted. If a specific isotope was not analyzed it is indicated with a "-".

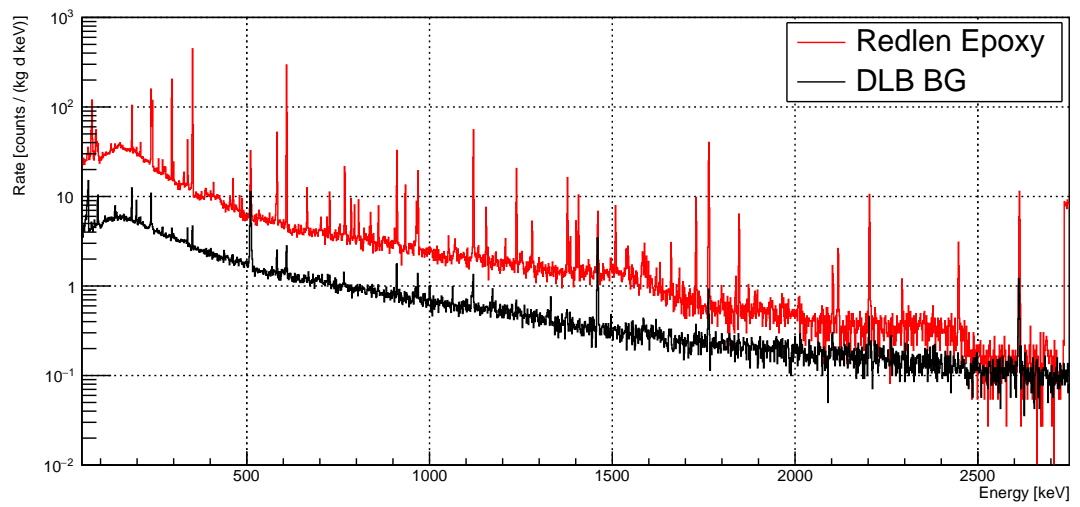


Figure A.1:  $\gamma$ -spectrum of REDLEN-epoxy measured at DLB.

Product	Technique	Facility	Specific Activity [mBq/kg]				
			Used in	$^{40}\text{K}$	$^{137}\text{Cs}$	$^{232}\text{Th}$ -chain	$^{238}\text{U}$ -chain
Red Paint	$\gamma$ -spect.	LNGS	Prototypes	$6.9 \pm 0.8 \cdot 10^3$	$\leq 15$	$900 \pm 100$	$2.0 \pm 0.1 \cdot 10^3$
Clear Paint	$\gamma$ -spect.	LNGS	?	$\leq 1 \cdot 10^3$	$\leq 56$	$\leq 180$	$\leq 140$
	ICP-MS	LNGS	?	$51 \pm 12$	-	$0.59 \pm 0.06$	$1.4 \pm 0.1$
Glyptal	$\gamma$ -spect.	DLB	Both	$\leq 1.7 \cdot 10^3$	$\leq 5.8$	$\leq 25.1$	$200 \pm 50$
	$\gamma$ -spect.	LNGS	Both	$32 \pm 11$	$\leq 1.6$	$5 \pm 1$	$16 \pm 2$
	$\gamma$ -spect.	Obelix	Both	$\leq 291$	-	$\leq 15$	$41 \pm 14$
Redlen Epoxy	$\gamma$ -spect.	DLB	Laboratory	$230 \pm 70$	-	$500 \pm 50$	$5.7 \pm 0.6 \cdot 10^3$
Epoxies etc. 20-3001	$\gamma$ -spect.	Obelix	XDEM	1.2	-	3.0	6.1

Table A.2: Specific Activity of various materials used as detector coating. For each entry, the measurement technique and the setup it was used for is listed. If multiple isotopes from a decay chain were analyzed, in case of detection an average is calculated and in case of upper limits the lowest limit is quoted. If a specific isotope was not analyzed it is indicated with a ”-”. Note that the value for the  $^{238}\text{U}$ -chain in Glyptal measured at the DLB only comes from a single isotope in the chain and is only  $0.5\sigma$  above the decision threshold, which might hint at a statistical fluke. The results for Epoxies etc. 20-3001 were given without uncertainties in the original analysis.

Material	Technique	Facility	Specific Activity [mBq/kg]					
			<sup>40</sup> K	<sup>60</sup> Co	<sup>137</sup> Cs	<sup>210</sup> Pb	<sup>232</sup> Th-chain	<sup>238</sup> U-chain
Copper	$\gamma$ -spect.	Obelix	$0.32 \pm 0.08$	$\leq 0.01$	$0.24 \pm 0.05$	-	$0.10 \pm 0.02$	$0.12 \pm 0.03$
Copper	$\gamma$ -spect.	DLB	$\leq 3.2$	$\leq 0.39$	$\leq 0.57$	-	$\leq 1.17$	$\leq 2.17$
ULA lead I	ICP-MS	Plombum	$2.0 \pm 0.7$	-	-	$\leq 3 \cdot 10^3$	$\leq 0.158$	$0.35 \pm 0.14$
ULA lead II	$\beta$ -spect.	PTB	-	-	-	$3.4 \pm 2.6 \cdot 10^3$	-	-
PE+B	$\gamma$ -spect.	LNGS	$\leq 64$	-	$\leq 4$	-	$7.0 \pm 2.7$	$12 \pm 3$

Table A.3: Specific Activity of various materials used as components of the shielding. For each entry, the measurement technique and the setup it was used for is listed. If multiple isotopes from a decay chain were analyzed, in case of detection an average is calculated and in case of upper limits the lowest limit is quoted. If a specific isotope was not analyzed it is indicated with a "-". The values for short living isotopes are given as average over the measurement time

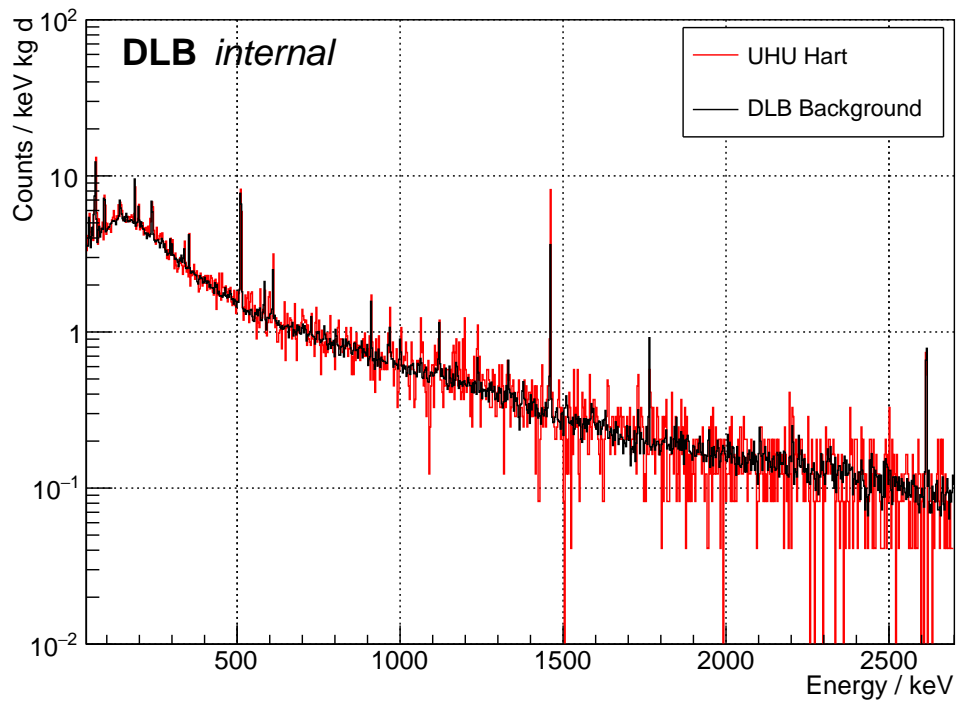


Figure A.2:  $\gamma$ -spectrum obtained with the DLB measuring *UHU-hart* glue that was used to attach the signal wires to the electrodes of the demonstrator detectors. A large amount of  $^{40}\text{K}$  is contained in the glue, as can be easily seen by the high peak at 1460 keV.

Material	Technique	Used in	Specific Activity [mBq/kg]					
			$^{40}\text{K}$	$^{137}\text{Cs}$	$^{108m}\text{Ag}$	$^{110m}\text{Ag}$	$^{232}\text{Th}$ -chain	$^{238}\text{U}$ -chain
UHU hart	$\gamma$ -spect.	Demo.	$890 \pm 120$	$\leq 30.3$	-	-	$\leq 5.0$	$\leq 43$
LS 200	$\gamma$ -spect.	Demo.	$\leq 71$	$\leq 4.4$	$101.0 \pm 3.9$	$4.9 \pm 2.2$	$\leq 4.0$	$\leq 8$
TRA-DUCT 2902	ICP-MS	XDEM	$17.2 \pm 0.3$	-	-	-	$0.23 \pm 0.03$	$0.82 \pm 0.10$
RG 178	$\gamma$ -spect.	Demo.	$300 \pm 80$	$\leq 28$	-	-	$\leq 44$	$\leq 55$
Medikabel	$\gamma$ -spect.	Both	$26 \pm 4$	$0.8 \pm 0.2$	$0.32 \pm 0.08$	-	$0.4 \pm 0.2$	$0.5 \pm 0.2$
POM plate	Both	Both	$\leq 31$	$3 \pm 1$	-	-	$0.12 \pm 0.02$	$2.3 \pm 0.4$
PA 6.6 screw	ICP-MS	Both	-	-	-	-	$0.17 \pm 0.03$	$0.34 \pm 0.07$
PTFE tube	ICP-MS	Both	-	-	-	-	$0.028 \pm 0.012$	$\leq 0.062$
PTFE plate	ICP-MS	none	-	-	-	-	$0.045 \pm 0.016$	$0.074 \pm 0.037$

Table A.4: Specific Activity of various materials used as construction materials in COBRA. For each entry, the measurement technique and the setup it was used for is listed. If multiple isotopes from a decay chain were analyzed, in case of detection an average is calculated and in case of upper limits the lowest limit is quoted. If a specific isotope was not analyzed it is indicated with a ”-”.

# B Peak Contents in Background Spectrum

Table B.1: Count-rate of various  $\gamma$ - and  $\alpha$ -peaks in the XDEM spectrum. An interaction depth cut  $0.2 < z < 0.9$  is used. For limit setting TROLKE is used, for details see section 7.5.

Isotope	Energy [keV]	$R_{zcut}$ [1/d]
$^{22}\text{Na}$	1 274.5	$\leq 0.07$
$^{40}\text{K}$	1 460.8	$0.08 \pm 0.04$
$^{56}\text{Co}$	846.8	$\leq 0.07$
	1 238.3	$\leq 0.05$
	2 598.4	$\leq 0.009$
$^{60}\text{Co}$	1 173.2	$\leq 0.02$
	1 332.5	$\leq 0.04$
$^{88}\text{Y}$	898.0	$\leq 0.10$
	1 836.1	$\leq 0.05$
$^{110m}\text{Ag}$	657.8	$0.67 \pm 0.09$
	884.7	$\leq 0.09$
	1 505.0	$\leq 0.04$
$^{113}\text{Cd}(n, \gamma)$	558.5	$\leq 0.11$
$^{124}\text{Sb}$	1 690.9	$\leq 0.05$
$^{137}\text{Cs}$	661.6	$0.65 \pm 0.09$
$^{208}\text{Tl}$	583.2	$\leq 0.16$
$^{208}\text{Tl}$	2 614.5	$\leq 0.009$
$^{210}\text{Pb-}\alpha$	5 407.5	$0.009 \pm 0.008$
$^{214}\text{Bi}$	609.3	$\leq 0.05$
$^{228}\text{Th}$	911.2	$\leq 0.09$
Anni.	511.0	$\leq 0.13$

## C Zn Content of CdZnTe Detectors

The determination of the exact content  $x$  of Zn in the  $\text{Cd}_x\text{Zn}_{1-x}\text{Te}$  detectors used in the COBRA experiment is a problematic issue. On the one hand, as the exact Zn content is an important degree of freedom in crystals growth, the manufacturers are usually reluctant in giving away to much information about it and also it tends to vary across the length of a crystal ingot and also between bulk and surface of a single detector. On the other hand, the exact amount of Zn is important for any analysis concerned with the decay-rate of isotopes included in CdZnTe as the amount of Zn directly influence the number of atoms of each Cd and Zn isotope within a detector. Thus, imprecise knowledge of  $x$  translates in an uncertainty of rate.

This problem was discussed in some detail for the Demonstrator detectors[Geh17]. For the XDEM this will be done here. Fortunately both EV and REDLEN send crystal samples along with the detectors, that are supposed to be cut from the ingot close to the place the detectors were also cut from. These samples were analyzed by ICP-MS at the LNGS. The device was calibrated with Zn standard solutions prior to the measurements. The results are shown in Table C.1. The amount of CdZnTe from the EV sample was sufficient to perform more than one analysis and revealed some spread. It should be noted, that the results are reported in % by weight (w.t.) a need to be converted taking into account the atomic weights of the elements in CdZnTe to obtain the stoichiometric zinc content  $x$ .

If Cd, Zn and Te were to be considered individually, the conversion would be not possible, as only the % w.t. of Zn is known from the measurement and only the % of atoms of Te is known to be 50% a priori and additionally the molecular weight of the CdZnTe is also unknown, as is it itself a function of the individual fraction, thus the system is underconstrained. The calculation is thus performed by imagining CdZnTe as a mixture of CdTe ( $M = 240.01$  g/mol) and ZnTe ( $M = 192.99$  g/mol). If the weight fraction of Zn ( $M = 65.38$  g/mol) is  $f_{\text{Zn}}^{w.t.}$  the weight fraction of the virtual ZnTe molecules  $f_{\text{ZnTe}}^{w.t.}$  can be calculated by using the fact, that the molecular weight of ZnTe is about three times the atomic weight of Zn and thus the weight fraction is also about three times as large, which means that  $f_{\text{ZnTe}}^{w.t.} = f_{\text{Zn}}^{w.t.} \frac{M_{\text{ZnTe}}}{M_{\text{Zn}}}$  and  $f_{\text{CdTe}}^{w.t.} = 1 - f_{\text{ZnTe}}^{w.t.}$ .

Table C.1: Zn fraction measured by ICP-MS from two CdZnTe samples. The uncertainties of the individual measurements are given as 68% confidence level.

Sample	Zn [% w.t.]
EV 1	$2.83 \pm 0.20$
EV 2	$2.62 \pm 0.20$
EV 3	$4.16 \pm 0.30$
EV 4	$3.14 \pm 0.25$
EV 5	$3.54 \pm 0.30$
EV avg.	$3.26 \pm 0.61$
REDLEN	$2.90 \pm 0.20$

The conversion can then be performed using the relation

$$f_A^{at.} = \frac{f_A^{w.t.}/M_A}{f_A^{w.t.}/M_A + f_B^{w.t.}/M_B} \quad (\text{C.1})$$

which gives values  $f_{ZnTe}^{at.} = 11.7\%$  using the mean value of the EV sample and  $f_{ZnTe}^{at.} = 10.4\%$  for the REDLEN sample. These value then directly translate into corresponding values for  $x$ , as it makes not quantitative difference if CdZnTe is as a mixture of CdTe and ZnTe or or CdTe with a part of Cd atoms replaced with Zn atoms. It turns out, that the obtained values are in agreement with  $x = 0.1$ , as it is conventionally reported for CdZnTe detectors, taking into account the uncertainties, although there is some tendency to slightly higher values, as only one single measurement had a mean value corresponding to  $x \leq 0.1$ . The values are also in agreement with the measurements reported in Ref. [Geh17], if the ICP-MS results are taken as % w.t. instead of the atom fraction stated in the reference.





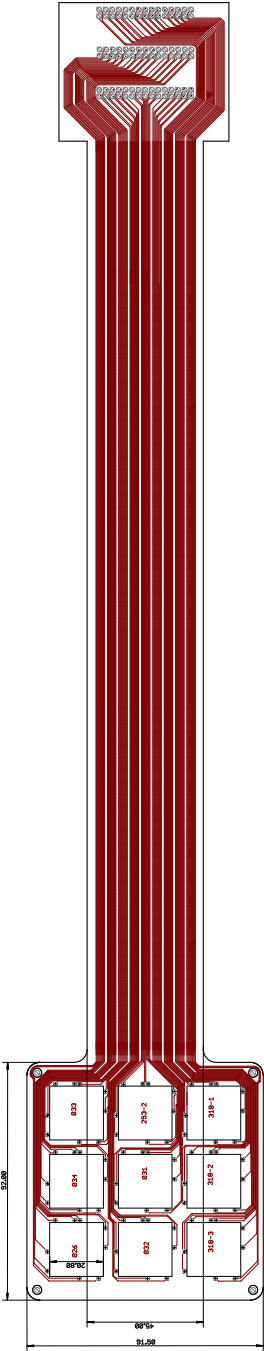


Figure D.2: Drawing of the XDEM signal PCB.

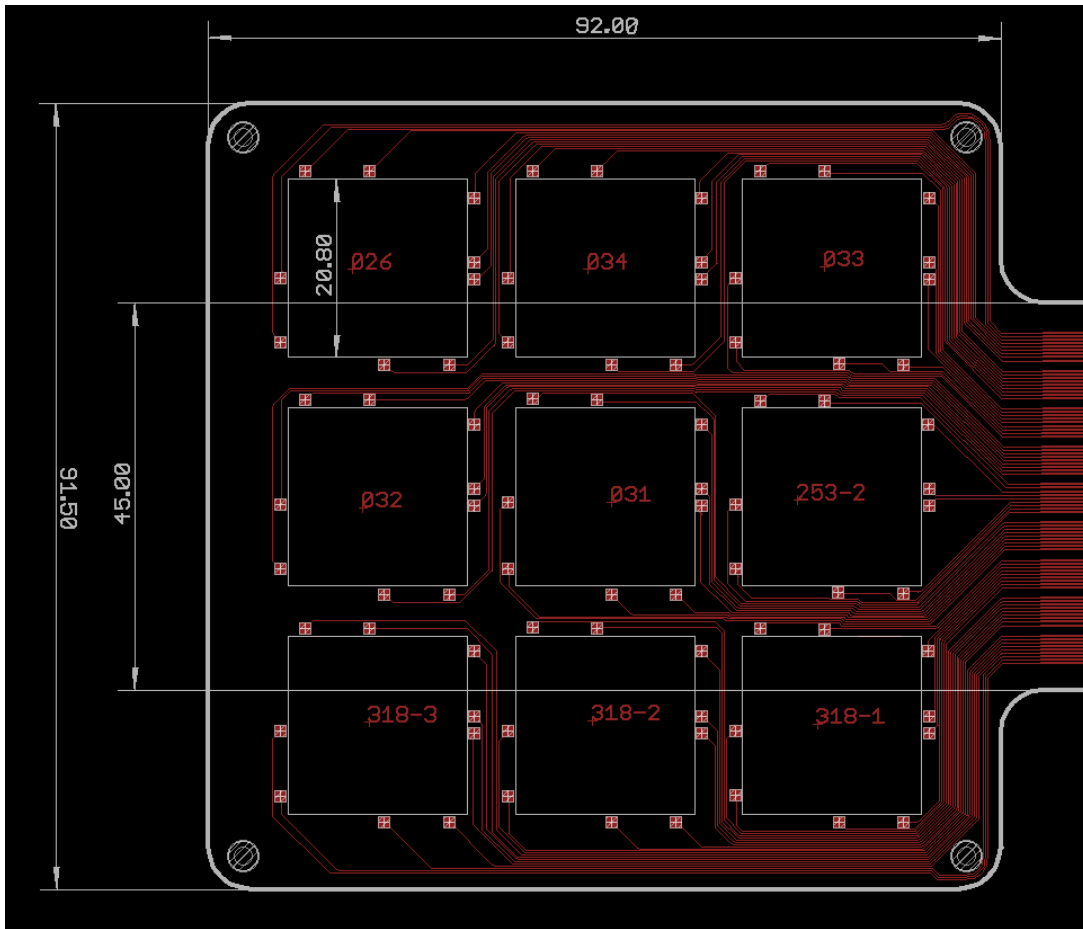


Figure D.3: Closeup of detector region of the same PCB as above

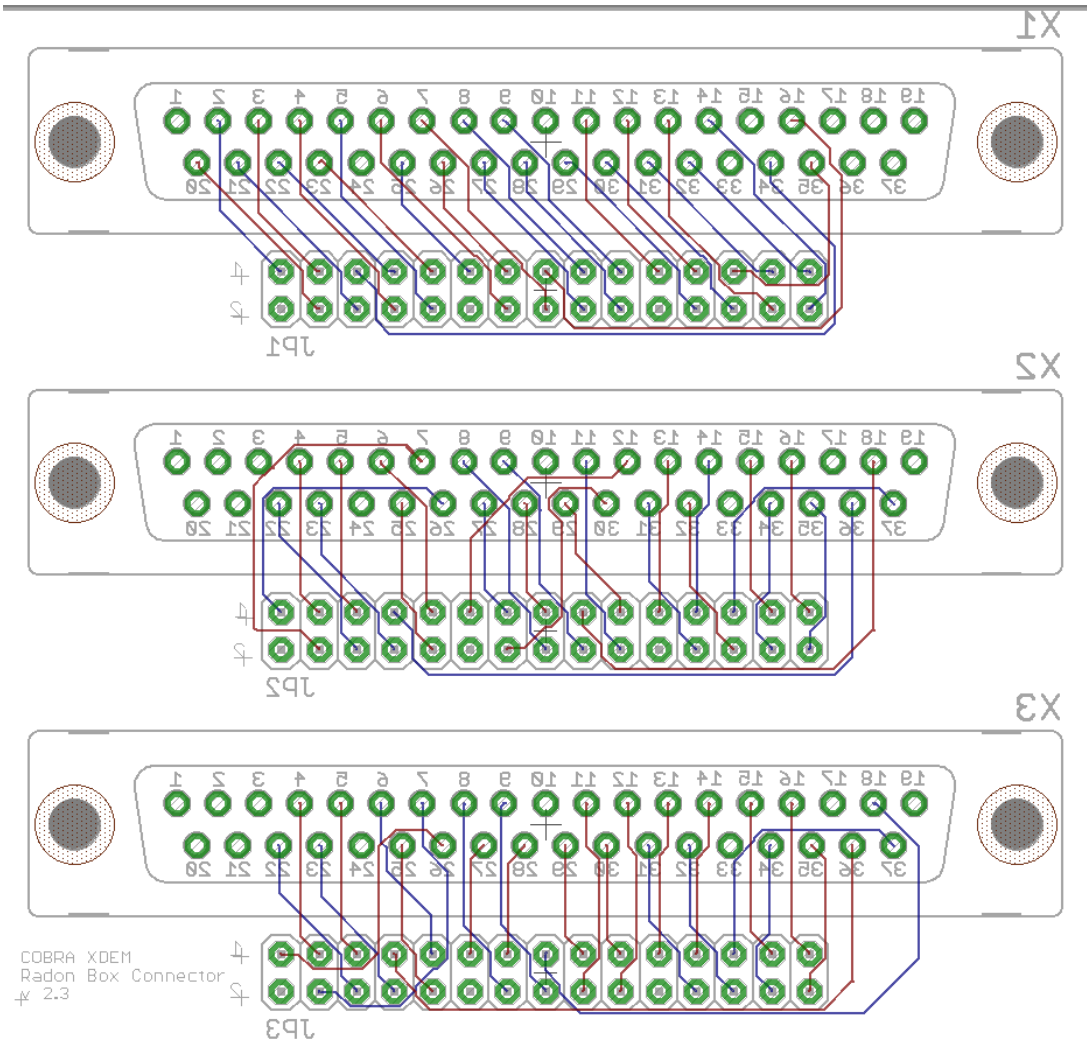


Figure D.4: Drawing of the feed-through PCB connecting the signal PCB to cables outside the gas-tight enclosure.

# List of Publications and Conference Contributions

## Publications

- R. Temminghoff. “Spatially resolved investigation of large CdZnTe detectors with a coplanar quad-grid”. In: *2016 IEEE NSS/MIC/RTSD*. 2016, pp. 1–4. DOI: 10.1109/NSSMIC.2016.8069959
- R. Temminghoff. “Investigation of the Depth Reconstruction and Search for Local Performance Variations With a Large Coplanar-Quad-Grid CdZnTe Detector”. In: *IEEE Transactions on Nuclear Science* 64.7 (2017), pp. 1934–1941. ISSN: 0018-9499. DOI: 10.1109/TNS.2017.2711922
- J.-H. Arling et al. “Suppression of alpha-induced lateral surface events in the COBRA experiment using CdZnTe detectors with an instrumented guard-ring electrode”. In: *Journal of Instrumentation* 12.11 (2017), P11025–P11025. DOI: 10.1088/1748-0221/12/11/p11025. URL: <https://doi.org/10.1088/1748-0221/12/11/p11025>
- L. Bodenstein-Dresler et al. “Quenching of  $g_A$  deduced from the  $\beta$ -spectrum shape of  $^{113}\text{Cd}$  measured with the COBRA experiment”. In: (06/06/2018). <https://arxiv.org/abs/1806.02254>. arXiv: 1806.02254 [nucl-ex]. URL: <https://arxiv.org/abs/1806.02254>

## Talks at Conferences

- Robert Temminghoff  
*Untersuchung von  $2\text{ cm} \times 2\text{ cm} \times 1.5\text{ cm}$  CdZnTe Detektoren mit coplanarer Quad Grid Struktur für das COBRA Experiment*  
Spring Meeting, German Physical Society, Wuppertal, 09.03.2015

## List of Publications and Conference Contributions

- Robert Temminghoff for the COBRA collaboration  
*Status and Prospects of the COBRA  $0\nu\beta\beta$  Experiment*  
Spring Meeting, German Physical Society, Darmstadt, 16.03.2016
- Robert Temminghoff on behalf of the COBRA collaboration  
*Spatially Resolved Investigation of Large CdZnTe Detectors with a Coplanar Quad-Grid*  
IEEE International Symposium on Room-Temperature Semiconductor Detectors (RTSD), Strasbourg, 02.11.2016
- Robert Temminghoff for the COBRA collaboration  
*Status of the COBRA Experiment*  
Spring Meeting, German Physical Society, Bochum, 01.03.2018
- Robert Temminghoff for the COBRA collaboration  
*Detector Evaluation for the COBRA XDEM*  
Spring Meeting, German Physical Society, Würzburg, 20.03.2018
- Robert Temminghoff for the COBRA collaboration  
*The COBRA Double Beta Decay Experiment*  
Spring Meeting, German Physical Society, Aachen, 26.03.2019

## Posters at Conferences

- Robert Temminghoff for the COBRA collaboration  
*Interaction Depth Reconstruction in  $(20 \times 20 \times 15)\text{mm}^3$  Coplanar-Quad-Grid CdZnTe Detectors*  
Spring Meeting, German Physical Society, Münster, 28.03.2017
- Robert Temminghoff for the COBRA collaboration  
*The COBRA Extended Demonstrator*  
Neutrino 2018, Heidelberg, 04.06.2018  
<http://doi.org/10.5281/zenodo.1300875>

## List of (Co-)Supervised Theses

- C. Schleich. “Untersuchung der Energiedeposition von Alphastrahlung bei  $6\text{ cm}^3$  CdZnTe Detektoren bei unterschiedlichen Konfigurationen von CA und NCA”. Bachelor’s Thesis. TU Dortmund, 2016
- M. Albrecht. “Analyse des Rauschverhaltens eines ASIC basierten Auslesesystems für das COBRA-Experiment”. Bachelor’s Thesis. TU Dortmund, 2016
- K. David. “Effizienzbestimmung von Quad-Grid-CdZnTe-Detektoren”. Bachelor’s Thesis. TU Dortmund, 2016
- C. Herrmann. “Simulation of a  $3\times 3$  CZT-Detector-Layer for the COBRA-Experiment”. Bachelor’s Thesis. TU Dortmund, 2016
- J. H. Arling. “Characterization of Coplanar Grid CdZnTe Detectors and Instrumentation of the Guardring for the COBRA Experiment”. Master’s Thesis. TU Dortmund, 2016
- A. Nowak. “Simulation der Kalibration der CZT Detektoren für das COBRA Experiment”. Bachelor’s Thesis. TU Dortmund, 2017
- L. Bodenstein-Dresler. “Preparation for the COBRA XDEM phase including design of mechanical parts and tests of electronics and measurements of beta-suppression”. Master’s Thesis. TU Dortmund, 2018
- I. Höfmann. “Effizienzbestimmung von CdZnTe-CPqG-Detektoren für das COBRA-XDEM-Upgrade”. Bachelor’s Thesis. TU Dortmund, 2018
- C. Herrmann. “Monte-Carlo Based Studies of Potential Background in the XDEM-phase of the COBRA Experiment”. Master’s Thesis. TU Dortmund, 2018